Fluctuations du champ paléomagnétisme terrestre enregistrée par les laves de l'Archipel des Kerguelen (partie australe de l'Océan Indien) et détermination de leur direction de mise en place.

Guillaume Plenier

UNIVERSITÉ MONTPELLIER II
SCIENCES ET TECHNIQUES DU LANGUEDOC

Num : _____

THESE

pour obtenir le grade de
DOCTEUR DE L'UNIVERSITE MONTPELLIER II

Discipline : **Structure et Evolution de la Terre et des Planètes**
Formation doctorale : **Structure et évolution de la lithosphère**
Ecole doctorale : **Sciences de la Terre et de l'Eau**

Fluctuations du champ paléomagnétique terrestre enregistrées par les laves de l'Archipel des Kerguelen (partie australe de l'Océan Indien) et détermination de leur direction de mise en place.

a été présentée et soutenue publiquement

par
Guillaume Plenier

le 20 décembre 2002

Devant le Jury composé de :

MM.	**Marc DAIGNIERES**, Professeur, Université Montpellier II	Président
	Annick CHAUVIN, Professeur, Université Rennes I	Rapporteur
	Pierre ROCHETTE, Professeur, Université Aix Marseille III	Rapporteur
	Pierre CAMPS, Chargé de Recherche, Université Montpellier II	Examinateur
	Bernard HENRY, Chargé de Recherche, IPG Paris	Examinateur
	Mireille PERRIN, Directeur de Recherche, Université Montpellier II	Directeur de thèse

A Moune,

Remerciements

Ces trois dernières années d'étude n'auraient pas pu aboutir au présent manuscrit sans le concours de l'ensemble des personnes que je voudrais évoquer ici. Chacune à sa façon aura contribué à ce que je m'épanouisse pleinement au cours de ma thèse et me sente à l'aise dans mon travail.
Je tiens à remercier en premier lieu toute l'équipe de paléomagnétisme qui m'aura supporté au cours de cette aventure : Lili pour les innombrables essais de réglage du KT ; Thierry pour sa patience et son merveilleux VTM-télécran de Patagonie ; Brigitte pour sa gentillesse et son soutien ; Michel pour ses conseils avisés, souvent déstabilisants, qui m'auront toujours amené à appréhender mes problèmes sous un angle plus intéressant ; Mireille pour m'avoir montré une autre façon d'interpréter les diagrammes de paléointensité et son courage mis à rude épreuve au cours du périple Val Travers-Val Studer ; et enfin Pierre, parfois dur mais toujours juste, qui m'aura remarquablement encadré et guidé durant ces trois années. Nos expériences communes à Kerguelen, en particulier celles de la plaine Ampère, resteront bien longtemps gravées dans ma mémoire. Je tiens aussi à faire un petit clin d'oeil à Joël, pour avoir notamment solidifié l'étagère à échantillon qui menaçait de s'effondrer, et Patrick, que j'aurais finalement épargné.
Je pense aussi aux personnes qui ont passé quelques temps au sein de notre équipe alors que je m'y trouvais ou qu'il m'a été donné de rencontrer par la suite : Avto pour tout l'intérêt qu'il témoigne à mes travaux et sa présence bienveillante ; Bernard Henry pour m'avoir accueilli au laboratoire de Saint Maur et initié à l'analyse de la fabrique magnétique, Charly Aubourg pour le temps qu'il m'aura accordé à Nice suite à mon exposé de l'EGS et pour ses conseils et commentaires qui m'auront grandement servi lors de la rédaction de mon troisième article ; Maxime le Goff pour ses petits programmes et les mesures de cycles d'hysteresis, il semblerait aussi qu'il s'occupe de mon dossier à l'ANPE (véridique !) ; Andreï Kosterov pour son attention ; Lisa Schnepp pour avoir parfumé le four à paléointensité ; Claire pour ces nombreux mails et que j'ai hâte de retrouver autour d'une bière (ou plutôt entourée de bière !) ; Mouloud toujours à fond ; Stéphanie disparue depuis dans le monde impitoyable de l'informatique et enfin Edouard avec qui j'aurais eu l'immense plaisir de partager le bureau des étudiants en paléomagnétisme.
Ceci m'amène tout naturellement à évoquer Rob Coe que j'aurais eu la chance d'accompagner durant son séjour à Montpellier. Cette expérience quotidienne à ses côtés m'aura été particulièrement bénéfique, au niveau de l'anglais tout d'abord, même si j'ai apparemment encore beaucoup de progrès à faire, mais aussi et surtout du point de vue scientifique. Comme convenu, je garde précieusement sa bouteille de Cognac pour une grande occasion à laquelle j'aurais plaisir de l'associer.
Je tiens à citer également : Frédéric Bouchette pour son aide précieuse en général, et en particulier avec les programmes TCL-TK, awk et latex, rien d'étonnant à ce que nos manuscrits se ressemblent après qu'il m'ai généreusement proposé d'utiliser ses fichiers types ; Henry de la Boisse pour m'avoir donné l'occasion d'effectuer de nombreuses vacations dont celle de tuteur lors de la mise en place du modules de méthodologie ; Jean-Patrick Respaut qui lors d'un stage de terrain en License m'a convaincu de faire des études plus longues ; Jean-Marie Dautria pour sa traduction exceptionnelle de "flood basalts" ; Anne Delplanque, terroriste attachante à la bombe à colle, pour ses coups de mains sous Adobe illustrator et

durant mes combats avec la Calcomp ; Christophe Nevado pour m'avoir préparé mes lames minces en toute urgence et les secrétaires Nathalie, Martine, et Céline, elles aussi souvent sollicitées au dernier moment que ce soit pour les ordres de mission, les bons de commande ou autres envois de courrier importants. Merci à Marie-France pour sa participation lors de l'organisation de la journée des doctorants. J'aimerais remercier aussi Benoît Ildefonse auquel j'ai fait appel pour le traitement de mes lames minces, et à travers lui les membres du laboratoire de Tectonophysique qui dès mon D.E.A. se sont montrés très sympathiques à mon égard et ce bien avant le rapprochement prochain avec notre équipe.
Je tiens également à remercier comme il se doit l'Institut Polaire Français pour avoir financé le programme paléomagne 310 qui m'aura permis de me rendre par deux fois dans les Terres Australes et Antarctiques françaises pour y prélever mes échantillons. Sans leur soutien financier et logistique, ce travail n'aurait bien évidemment pas été possible.
Ces deux voyages fantastiques à destination des îles Kerguelen m'ont permis de faire connaissance au cours des transferts sur le Marion Dufresne II ou sur les bases militaires avec des personnes non moins extraordinaires : Alain Lamalle, chef des opérations mais surtout roi de la BLU ; Roland Pagny et ses parallèles (halte au feu !) ; Roland Gauthier, commandant du Marion, qui à deux reprises nous aura ramenés à bon port avec son équipage ; Denis le chef des cuisines fou du Marion dont la lettre et les saucissons me font encore chaud au coeur ; Tonton qui m'aura offert un merveilleux baptême de l'air en hélicoptère ; Jean-Marc et ses équipages de la Curieuse, qui a bien failli devenir un bateau à bulle ; Bernard et ses bois de cerf ; Guillaume, l'autre malchanceux ; Jessy ; Fabianna le miss Ker99 en compétition avec miss moule sur le Marion ; Johann le géophy de Crozet qui m'aura fait beaucoup rire ; Florence de Lyon ; Serge ; Hubert le bout de bois alsacien ; David le gener ; Sylvestre dit Léon pour les chats et les lapins ; Patrick l'artiste de la Mortadelle ; Anne la botachoux ; John le bibou ; Testos ; François plus connu sous le surnom de popy ; les militaires de la base de Port aux Français aux cuisines, à la cop, à l'hôpital, au BCR (tchao Jacky) ou plus souvent à "Totoche" ; les petits oiseaux Florence et Francesco ; les petits poissons Patrice, Philippe et Xavier (merci à l'ensemble du banc pour les chocolats de Noël !) ; les petits cailloux Bertrand, Christophe, Thomas et Jean-Yves ; les petits choux Jacques, Albert-Jean et Irène ; Christophe et Laurent qui traînaient cette fois dans la boue et enfin Kirsten qui aura eu le mérite de nous supporter Pierre et moi durant un mois complet à la pleine Ampère.
Autre lieu, mais une ambiance toute aussi chaleureuse, je tiens à remercier mes compagnons du grand voyage initiatique qu'est la thèse. Tout d'abord ceux qui m'auront souvent attendu au resto U : Marc, Florence, Laure, Eric, Xavier, Jérôme V., Dirk, Jérôme B., Benoît, Maggy, Olivier, Aurélien, Philippe et Florence. Mais aussi ceux qui auront été assez sages pour manger plus tôt ou ailleurs, Sébastien, Benoît, Ghislain, Loic, Philippe, Aude, Youri, Gwladys, Julie et Marianne.
J'ai une pensée toute particulière pour ma famille et mes proches qui m'auront toujours soutenu même si je sais que dans le fond, mon travail sera resté un grand mystère pour la plupart d'entre eux. Merci à Marie-Eve pour son soutien quotidien et son écoute, ma mère, mon père, Nicolas et Géraldine (et ...), Anne-Sophie, Olivier, Fabienne, mes grands parents paternels, Anne, Alain et ses enfants, Benoît, Thomas, mais aussi David de Paris, David et ses petits suisses, Dominique, Lilian, Stéphane, Christophe, Jérôme, Arnaud, Marc, Katia, Céline et JP, Ben, Pierre, Jean, Céline, Bertrand, Antoine et tous les autres... pour m'avoir entouré durant ces années d'études.

Je remercie enfin Annick Chauvin, Marc Daignières, Bernard Henry et Pierre Rochette qui m'ont fait l'honneur de juger ce travail.

Table des matières

Introduction

0.1 Etude des Fluctuations du champ

0.1.1 La dynamo terrestre

Dès 1839, Gauss démontrait que le champ magnétique terrestre (CMT) était généré principalement à partir de sources localisées à l'intérieur de la Terre. L'hypothèse la plus largement répandue à l'heure actuelle est que celui-ci est entretenu par une dynamo auto-excitée mettant en oeuvre la convection de fluides de forte conductivité électrique au niveau de la couche externe liquide du noyau de la Terre, entre 2900 et 5100 km de profondeur [voir Buffet (2000) pour un état des connaissances]. La modélisation de cette dynamo terrestre est particulièrement ardue car la solution recherchée doit satisfaire simultanément les équations de Maxwell (forces electromagnétiques), de Navier-Stokes (écoulement des fluides), de Poisson (forces gravitationnelles) ainsi que l'équation généralisée des transferts de chaleur. Les dynamos numériques, encore limitées par le calcul, sont loin de correspondre à la dynamo terrestre. Par exemple, une viscosité plus importante que celle actuellement estimée pour le noyau liquide est introduite dans les modèles dans le but d'assurer leur stabilité numérique. Le paramètre d'Ekman, rapport de la viscosité cinématique par rapport aux forces de Coriolis, se retrouve ainsi un milliard de fois plus important que celui estimé pour la Terre (Dormy et al., 2000). La dynamique interne du noyau imposant des variations, en direction et en intensité, au champ magnétique terrestre, l'observation de ces fluctuations à la surface du globe permet de contrôler, et de ce fait contribue à augmenter, la validité des modèles de dynamo Terrestre.

0.1.2 Les variations du champ

Les fluctuations du CMT peuvent être classées schématiquement selon trois catégories.

La variation séculaire

La première est appelée variation séculaire. Elle se manifeste par une variation non uniforme du CMT en surface, avec des changements à la fois en direction et en intensité pour des périodes de l'ordre de 10 à 10 000 ans. Cette variation prend très probablement naissance dans la partie supérieure du noyau liquide externe (Le Mouël, 1984). Ainsi par

exemple, les pôles géomagnétiques, pôles calculés pour un dipôle centré qui correspondrait au mieux au CMT observé à un moment donné, évoluent continuellement autour de l'axe de rotation de la terre avec une amplitude de mouvement pouvant atteindre trente à quarante cinq degrés. Cette variation est éliminée si le champ est moyenné sur une période de temps de l'ordre de 10 000 ans.

Les renversements de polarité magnétique

La seconde catégorie de fluctuations du CMT est constituée par les renversements de polarité magnétique. Ceux-ci, observés tout d'abord par David (1904) et Brunhes (1906), ne seront communément admis qu'après une étude menée par Wilson (1962) sur des latérites doublement cuites, montrant que leur réaimantation dans une direction quasi opposée au contact d'un dyke ne peut plus être expliquée par des phénomènes d'auto-inversion au moment de l'enregistrement du champ ambiant. L'origine de tels renversements de polarité magnétique reste mal connue. Le modèle de géodynamo de Glatzmaier (1995) révèle que ces inversions du champ peuvent survenir de façon chaotique. L'existence de l'alternance de périodes stables de polarité magnétique et de sens opposé s'explique mathématiquement par la symétrie des équations gouvernant la dynamique du noyau (Merrill et al., 1979). Ces changements de polarité s'effectuent pendant des périodes de transition qui durent quelques milliers d'années durant lesquelles on observe une chute de l'intensité du champ. Cumuler les informations sur les renversements est primordial pour expliquer leur mécanisme mais permet aussi de mieux comprendre les périodes de stabilité du champ qui précèdent et suivent ces événements.

Les excursions

La troisième catégorie de fluctuations à considérer est intermédiaire entre les deux précédentes et comprend les excursions du CMT. On peut les interpréter comme étant soit l'expression d'une super variation séculaire (avec des écarts des pôles géomagnétiques de plus de quarante cinq degrés par rapport à l'axe de rotation de la Terre), soit des renversements avortés de polarité magnétique (retour rapide à la polarité initiale). Selon Gubbins (1999), les excursions seraient dues au fait que le champ changerait deux fois de polarité dans la partie externe liquide du noyau, avant qu'il n'ait eu le temps de s'inverser à son tour par diffusion dans la graine (période nécessaire de l'ordre de 3 000 ans). Le champ n'aurait alors pas le temps de changer sa polarité magnétique initiale.

0.1.3 Les Observations du champ

Afin de décrire au mieux ces fluctuations, il est important de disposer d'enregistrements du champ magnétique terrestre répartis le plus uniformément possible à la surface

du globe à différentes époques. On utilise pour cela des mesures directes du champ, effectuées depuis 1837 dans les observatoires magnétiques ainsi que des mesures indirectes provenant d'études archéomagnétiques (jusqu'à 10 000 ans environ) et paléomagnétiques. Ces dernières proviennent de roches ayant enregistré le champ magnétique ambiant au moment de leur formation et permettent d'observer les fluctuations du champ sur de grandes périodes de temps. D'une manière générale, les roches sédimentaires possèdent une aimantation rémanente détritique acquise par l'orientation mécanique des minéraux magnétiques selon la direction du champ ambiant au moment de leur dépôt. Elles fournissent un bon enregistrement temporel du champ paléomagnétique, compte tenu de la continuité des dépôts sédimentaires. Celui-ci peut cependant être biaisé du fait de la gravité (erreur sur l'inclinaison) ou de la présence de courants perturbateurs au moment du dépôt (erreur sur la déclinaison), mais encore par l'acquisition d'une aimantation rémanente post-détritique (plus importante pour les grains fins) au moment de la compaction. Les roches volcaniques, quant à elles, acquièrent une aimantation thermo-rémanente durant leur mise en place. Les minéraux magnétiques enregistrent la direction du champ ambiant avec une intensité qui lui est proportionnelle dès l'instant où ils atteignent leur température dite de blocage en se refroidissant. L'enregistrement du champ magnétique est dans ce cas quasi instantané à l'échelle des temps géologiques, mais beaucoup plus fiable et permet surtout, dans des conditions favorables, de retrouver l'intensité du champ ancien. Or dans le but de définir le vecteur champ total, il est nécessaire que les enregistrements puissent renseigner à la fois sur la direction et l'intensité du champ magnétique, sujettes toutes deux aux fluctuations. Par conséquent les roches volcaniques fournissent des enregistrements de meilleure qualité du champ et sont plus appropriées pour l'étude des fluctuations du champ magnétique.

0.1.4 Répartition des données disponibles et objectif initial

La Figure 1 présente la distribution géographique des sites où des données directionnelles de roches volcaniques d'âge oligocène (23-33 Ma) ont été obtenues [Global Paleomagnetic Database - version 4.3 McElhinny and Lock (1996)]. On y observe un déséquilibre important du nombre de données disponibles entre l'hémisphère Nord et l'hémisphère Sud et ce en particulier pour les latitudes relativement élevées. La Figure 2 présente quant à elle la distribution temporelle des moments dipôlaires virtuels (MDVs), valeur du moment d'un dipôle qui fournirait l'intensité du champ magnétique observé en un lieu et à une époque donnée, calculés à partir de déterminations de paléointensité disponibles pour des âges compris entre 23 et 33 Ma. On remarque alors que les données y sont encore plus rares, du fait de la difficulté à obtenir des estimations de paléointensité, et ne couvrent pas uniformément la période de temps observée. Comme pour les données directionnelles, la distribution géographique est extrêmement inégale avec plus de 80% des données pro-

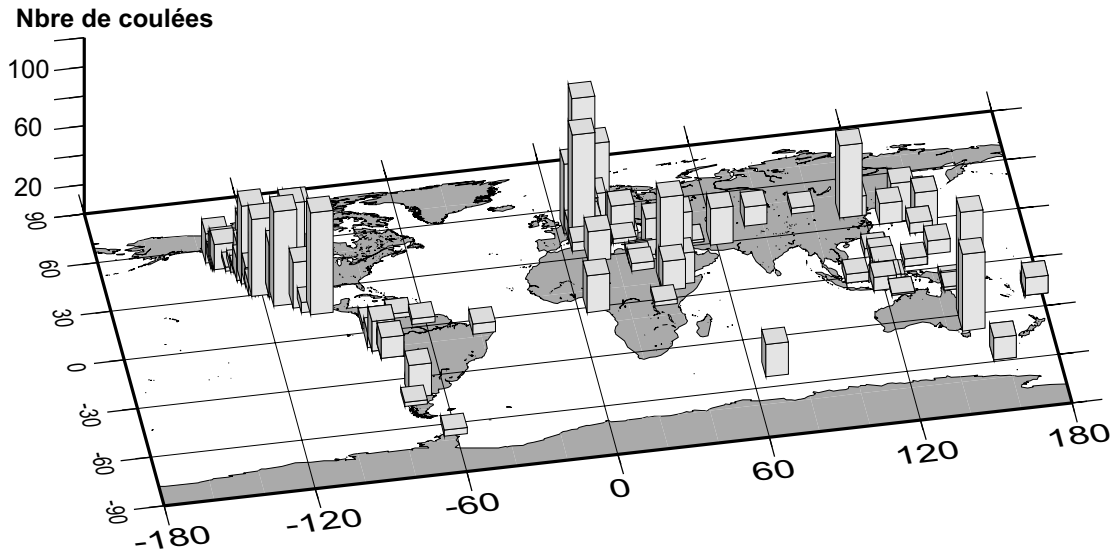

FIG. 1 – Distribution géographique des données directionnelles provenant des roches volcaniques d'âge oligocène [Global Paleomagnetic Database - version 4.3 McElhinny and Lock (1996)].

venant de l'hémisphère Nord.

Par conséquent, des enregistrements à la fois de direction et de paléointensité du CMT, issus de roches volcaniques localisées dans l'hémisphère Sud à des latitudes relativement élevées pour la période Oligocène étendue (20-40 Ma) manquaient encore au moment où cette thèse débutait.

L'objectif initial de mon doctorat, qui sera développé dans la première partie de ce manuscrit, consistait donc à effectuer une étude paléomagnétique complète (direction et paléointensité) de séquences volcaniques d'âge oligocène provenant de l'archipel des Kerguelen, situé à 49°20' de latitude Sud et 70°20' de longitude Est. Cela m'a amené à participer à deux campagnes de prélèvement, financées dans le cadre du programme paléomagne 310 par l'Institut Polaire Français (IPF) durant les hivers 1999-2000 et 2001-2002 (cf. Figure 3). Les données issues de ces travaux devaient par la suite compléter les bases de données internationales existantes et contribuer ainsi indirectement à une meilleure comprehension de la dynamique interne du noyau terrestre. Cette étude, dans la lignée des analyses entreprises sur d'autres sections prélevées auparavant (Camps et al., 2003), visait dans le même temps à prospecter d'éventuels enregistrements détaillés d'inversions du CMT.

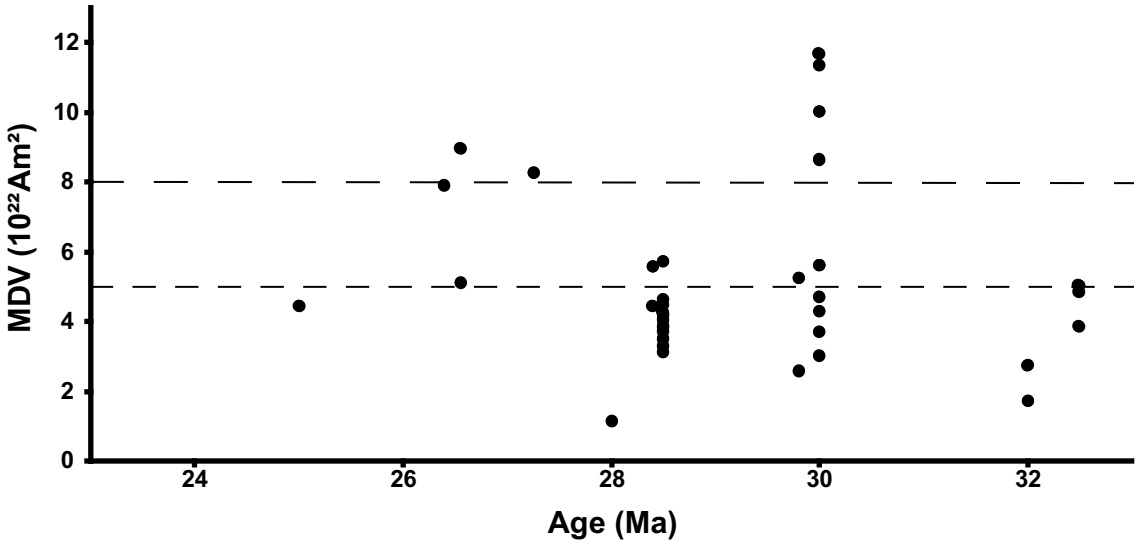

FIG. 2 – Distribution temporelle des moments dipôlaires virtuels (MDVs) calculés à partir d'estimations de paléointensité oligocènes, disponibles dans la base de données internationale de paléointensité de l'IAGA fin 1999. La ligne en pointillés espacés (resserrés) souligne la valeur du MDV moyen déterminé pour la période 0-0.3 Ma (0.3-300 Ma).

0.2 Contribution à la géologie de Kerguelen

0.2.1 Historique

Depuis sa découverte le 12 Février 1772 par le chevalier Yves de Kerguelen-Tremarec, l'archipel des Kerguelen, d'une superficie de 7 215 km^2, a été sujet à de nombreuses études géologiques. Parmis les explorations les plus importantes, on retiendra notamment les expéditions du *Résolution* et du *Discovery* menées par le capitaine Cook (1776), de l'*Erebus* et du *Terror* menées par Sir Ross (1840), du *Challenger* menée par le capitaine Nares (1874), et enfin les expéditions allemandes de *la Gazelle* (1874-76) et du *Gauss* (1902). Ce n'est qu'à partir de 1908 que la France effectua ses premiers repérages suite à une initiative privée des frères Rallier du Baty qui sillonnèrent les côtes et effectuèrent les premiers relevés hydrographiques. Jusqu'au milieu des années vingt, la géologie de Kerguelen demeurait très sommaire et c'est Aubert de la Rüe (1932) qui en publiant la première carte géologique contribua à une meilleure description de l'ensemble de l'archipel. A partir de 1951, la France dispose d'une station permanente à Port aux Français permettant aux recherches géologiques, entre autres, d'être plus poussées et de progresser plus rapidement. En 1970, Jacques Nougier est alors en mesure de proposer une carte de reconnaissance au 1/200 000^e de la géologie des îles Kerguelen (cf. Figure 4). Plus récemment, donnant suite à l'étude d'une zone test centrée sur les presqu'îles Jeanne d'Arc et Ronarc'h (Leyrit et al., 1990), un programme scientifique pluri-annuel mené sous la responsabilité d'André Giret (Université de Saint-Etienne) avait pour objectif de dresser une carte géologique détaillée au 1/100 000^e de l'archipel. L'élaboration de cette nouvelle carte géologique (publication

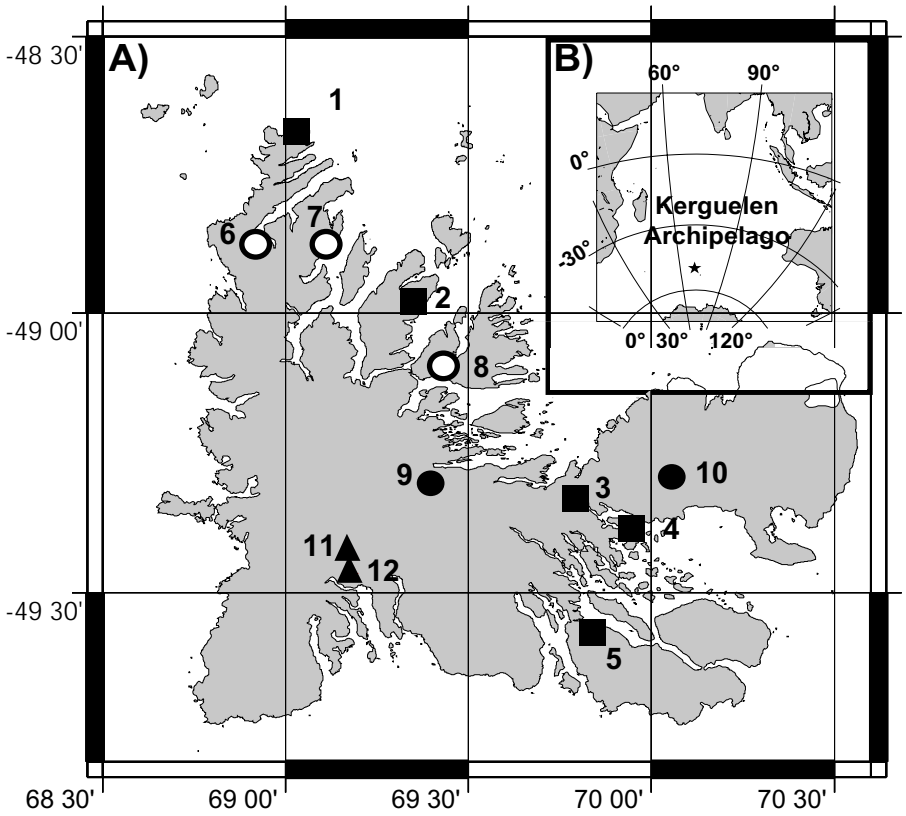

FIG. 3 – A) Récapitulatif des sections prélevées sur l'archipel des Kerguelen dans le cadre du programme paléomagne 310 financé par l'Institut Polaire Français : 1) Port Christmas : 16 coulées (48.67°S,69.02°E), 2) Mont Bureau : 18 coulées (48.97°S,69.35°E), 3) Port Raymond : 9 coulées (49.34°S,69.80°E), 4) Ile Haute : 29 coulées (49.39°S,69.94°E), 5) Port Jeanne d'Arc : 23 coulées (49.57°S,69.84°E), 6) Mont des Ruches : 18 coulées (48.87°S,68.91°E), 7) Mont des Tempêtes : 20 coulées (48.88°S,69.11°E), 8) Mont de la Rabouillère : 19 coulées (49.09°S,69.44°E), 9) Mont de la Tourmente : 33 coulées (49.30°S,69.40°E), 10) Mont Amery : 8+8 coulées (49.29°S,70.06°E), 11) Les trois Ménestrels : 45 coulées (49.43°S,69.17°E) et 12) Les Sentinelles : 13 coulées (49.47°S,69.18°E). Les sections 1 à 5 (carrés noirs) ont été échantillonnées durant l'été austral 1997-1998. Les sections 6 à 10 ont été prélevées durant la campagne d'été 1999-2000 et ont fait l'objet d'une étude directionnelle seulement (ronds noirs) ou combinée à une étude de paléointensité (ronds blancs). Enfin les sections 11 et 12 (triangles noirs) ont été échantillonnées durant la dernière campagne de prélèvement 2001-2002. B) localisation de l'archipel des Kerguelen dans l'Océan Indien.

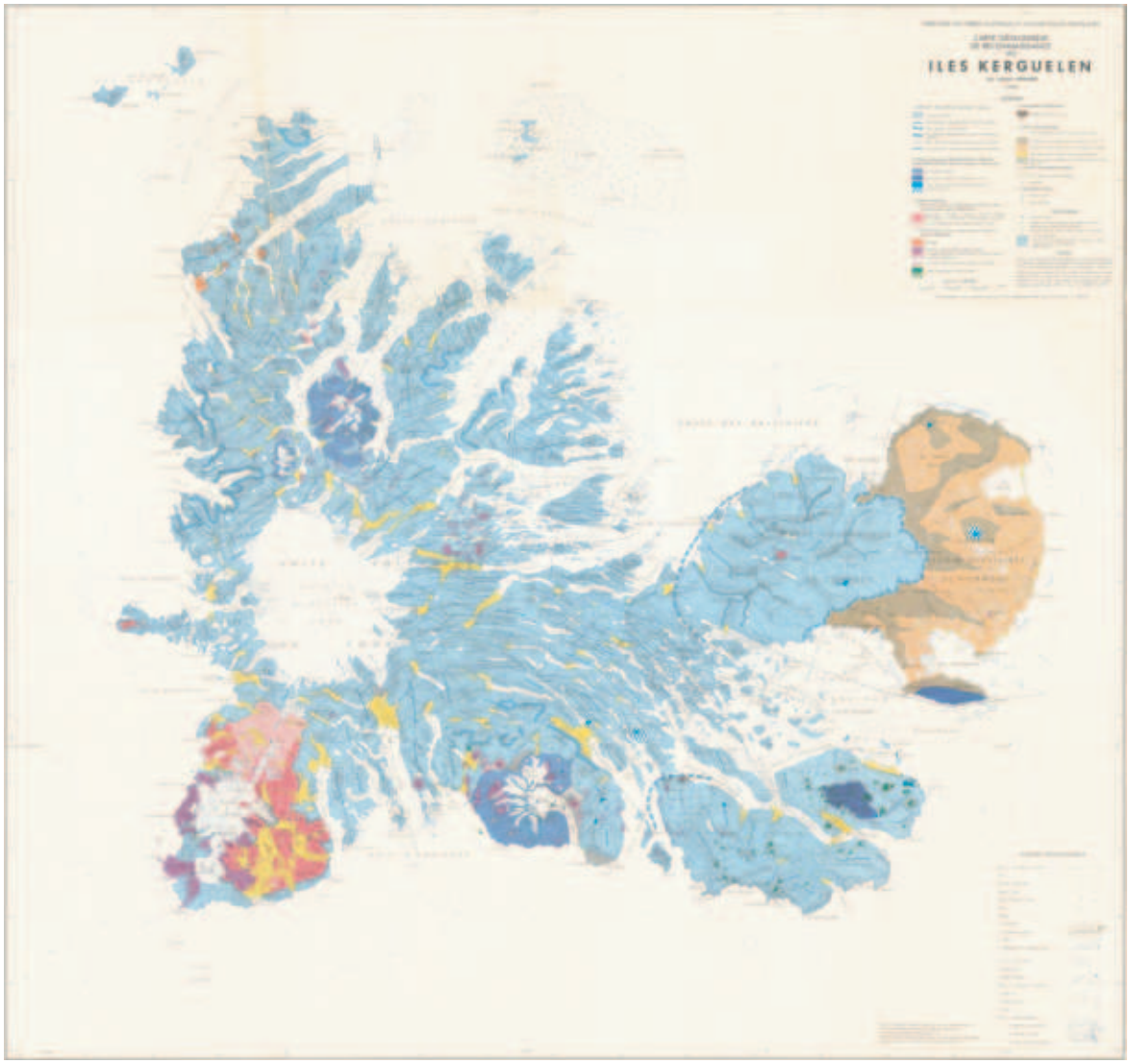

FIG. 4 – Carte géologique de reconnaissance des îles Kerguelen au 1/200 000^{e} (Nougier, 1970b).

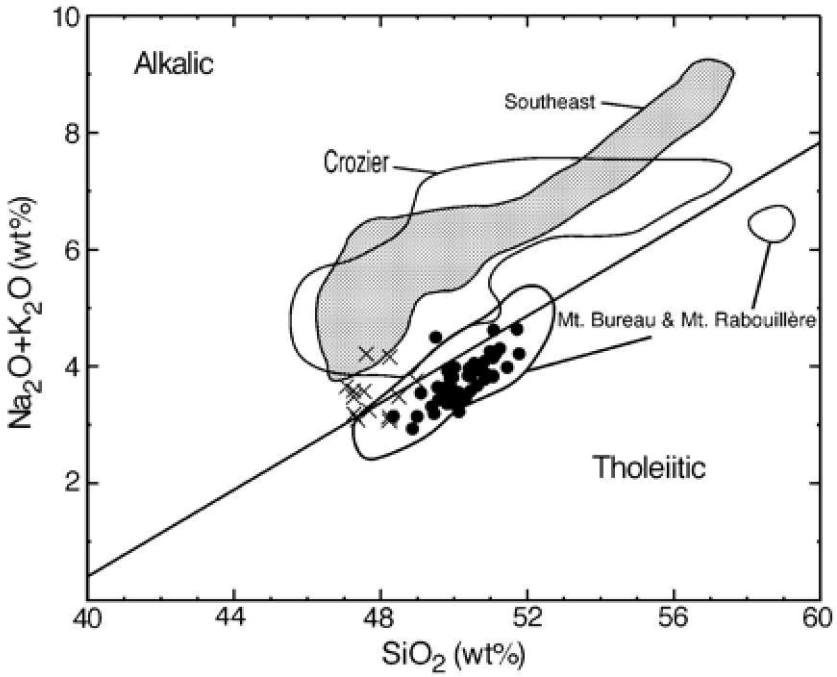

FIG. 5 – Graphique SiO_2 en fonction de $Na_20 + K_2O$ illustrant les différents types de basalte exprimés pour les sections de Port Jeanne d'Arc (Southeast), du Mont Amery (Crozier), du Mont Bureau (Ile Foch), du Mont de la Rabouillère et du Mont de la Tourmente, d'après Frey et al. (2002).

prévue en 2003) s'est accompagné d'études pétrographiques et géochimiques (Gautier et al., 1990; Giret, 1990; Schlich and Giret, 1994; Weis and Giret, 1994; Weis et al., 1998; Frey et al., 2000) ainsi que de nombreuses datations absolues (Yang et al., 1998; Nicolaysen et al., 2000; Doucet et al., 2002) qui ont permis d'orienter nos différentes campagnes d'échantillonnage paléomagnétique. L'ensemble des travaux publiés à ce jour permet de retracer de façon détaillée l'histoire géologique des îles Kerguelen.

0.2.2 Géologie de l'Archipel

L'archipel des Kerguelen repose sur la partie Nord du plateau océanique de Kerguelen-Gaussberg. Il est constitué à plus de 90% de roches volcaniques correspondant à la continuation aérienne oligocène (24-30 Ma) de l'activité du point chaud de Kerguelen, à laquelle s'ajoute ponctuellement des apports de la ride océanique Sud-Ouest indienne. Ce volcanisme fissural de type tholéitique a évolué progressivement vers une seconde phase de volcanisme, à caractère alcalin cette fois, qui prend place à partir de 25 Ma et jusqu'à l'actuel (Frey et al. (2002) et Figure 5). Cette seconde phase fait suite à une période de rémission volcanique ayant entraînée de l'érosion et la formation de niveaux conglomératiques. Les différents épanchements volcaniques (flood basalts) ont entraîné la formation de plateaux basaltiques représentant aujourd'hui des reliefs de 600 à 900 m d'altitude,

suite à une érosion glacière relativement importante. Des intrusions volcano plutoniques alcalines (gabbros, granites et syenites), dont le diamètre varie de 1 à 15 km, ont perforé plus tardivement ces reliefs, provoquant de nombreuses fractures dont le jeu vertical est resté cependant limité.

0.2.3 Magnétostratigraphie et fabrique magnétique

Afin d'apporter une contribution à la compréhension globale de la géologie de Kerguelen, nous avions prévu dès le début de cette thèse d'utiliser les résultats de l'étude directionnelle pour établir une magnétostratigraphie détaillée du volcanisme oligocène de Kerguelen. Vous la trouverez exposée dans le premier chapitre de ce manuscrit. L'objectif était de mieux estimer les intervalles de temps de mise en place de chacune des sections étudiées, à l'aide des datations absolues disponibles et de corrélations géochimiques. Ce travail nous a permis de réviser consécutivement les estimations des taux d'éruption proposées auparavant (Nicolaysen et al., 2000).

Bien qu'elles n'aient pas été prévues initialement, les études de la fabrique magnétique des séquences volcaniques se sont avérées particulièrement intéressantes pour contribuer de façon plus importante encore aux études géologiques menées à Kerguelen. La seconde partie de cette thèse présente l'apport de ce type d'analyses que ce soit dans le cadre d'une étude locale dans les environs de Port Jeanne d'Arc (chapitre 3) où d'un point de vue plus global afin de mieux localiser les centres éruptifs des provinces volcaniques de Kerguelen (Chapitre 4). Une étude de l'anisotropie de susceptibilité de la section du Mont de la Tourmente est également incluse dans le premier chapitre de cette thèse. Elle visait à vérifier si des corrections de pendages devaient être effectuées pour cette séquence volcanique, présentant un pendage de 15° selon un azimut de plus grande pente de 88°, pour l'analyse de ses directions magnétiques.

Bibliographie

Aubert de la Rüe, E., 1932. Etude géologique et géographique de l'archipel de Kerguelen. Rev. Géogr. Géol. Dyn. 5, 231 pp.

Brunhes, B., 1906. Recherches sur la direction d'aimantation des roches volcaniques. J. Phys. 5, 705–724.

Buffet, B., 2000. Earth's core and the Geodynamo. Science 288, 2007–2012.

Camps, P., Henry, B., Plenier, G., 2003. Statistical properties of paleomagnetic directions in Kerguelen lava flows. Geochem. Geophys. Geosystems in preparation.

David, P., 1904. Sur la stabilité de la direction d'aimantation dans quelques roches volcaniques. C. R. Acad. Sci. Paris 138, 41–42.

Dormy, E., Valet, J., Courtillot, V., 2000. Numerical models of the geodynamo and observational constraints. Geochem. Geophys. Geosystems 1 (2000GC000062).

Doucet, S., Weis, D., Scoates, J., Nicolaysen, K., Frey, F., Giret, A., 2002. The depleted mantle component in Kerguelen Archipelago basalts : Petrogenesis of tholeiitic-transitional basalts from the Loranchet Peninsula. J. Petrol. 43 (7), 1341–1366.

Frey, F., Weis, D., Yang, H.-J., Nicolaysen, K., Leyrit, H., Giret, A., 2000. Temporal geochemical trends in Kerguelen Archipelago basalts : evidence for decreasing magma supply from the Kerguelen plume. Chem. Geol. 164, 61–80.

Frey, F., Nicolaysen, K., Kubit, B.K., Weis, D., Giret, A., 2002. Flood basalt from Mont Tourmente in the central Kerguelen Archipelago : the change from transitional to alcalic basalt at ≈25 Ma. J. Petrol. 43, 7, 1367-1387.

Gautier, I., Weis, D., Mennessier, J., Vidal, P., Giret, A., Loubet, M., 1990. Petrology and geochemistry of the Kerguelen Archipelago basalts (south Indian Ocean) : evolution of the mantle sources from ridge to intraplate position. Earth Planet. Sci. Letts 100, 59–76.

Giret, A., 1990. Typology, evolution, and origin of the Kerguelen plutonic series, Indian ocean : a review. Geol. J. 25, 239–247.

Glatzmaier, G., Robets, P.H., 1995. A three-dimensional self-consistent computer simulation of a geomagnetic field reversal. Nature 377, 203–209.

Gubbins, D., 1999. The distinction between geomagnetic excursions and reversals. Geophys. J. Int. 137 (1), F1–F3.

Le Mouël, J., 1984. Outer core geostrophic flow and secular variation of Earth's geomagnetic field. Nature 311, 734–735.

Leyrit, H., Bardintzeff, J., Verdier, O., Giret, A., Brousse, R., 1990. Les presqu'îles Jeanne d'Arc et Ronarc'h : zone test pour une cartographie géologique au 1/100 000 des îles Kerguelen. Compt. Rend. Acad. Sci. Paris 311 (II), 561–566.

McElhinny, M., Lock, J., 1996. IAGA paleomagnetic databases with access. Surv. Geophys. 17 (5), 575–591.

Merrill, R., McElhinny, M., Stevenson, D., 1979. Evidence for long-term asymmetries in the Earth's magnetic field and possible implications for dynamo theories. Phys. Earth Planet. Inter. 20, 75–82.

Nicolaysen, K., Frey, F., Hodges, K., Weis, D., Giret, A., 2000. $^{40}Ar/^{39}Ar$ geochronology of flood basalts from the Kerguelen Archipelago, southern Indian Ocean : implications for Cenozoic eruption rates of the Kerguelen plume. Earth Planet. Sci. Letts. 174, 313–328.

Nougier, J., 1970. Terres Australes et Antarctique Françaises (T.A.A.F.), Kerguelen Islands reconnaissance map, 1 :200 000. Instit. Geograph. Nat'l., Paris .

Schlich, R., Giret, A., 1994. Géologie, géochimie et géophysique des Kerguelen. Mem. Soc. Géol. Fr., 108p, 11 contributions.

Weis, D., Damasceno, D., Frey, F., Nicolaysen, K., Giret, A., 1998. Temporal isotopic variations in the Kerguelen plume : evidence from the Kerguelen Archipelago. Miner. Mag. 62A, 1643–1644.

Weis, D., Giret, A., 1994. Kerguelen plutonic complexes : Sr, nd, pb isotopic study and inferences about their sources, age and geodynamic setting. Mem. Soc. Géol. Fr. 166, 47–59.

Wilson, R., 1962. The paleomagnetism of baked contact rocks and reversals of the earth's magnetic field. Geophys. J. Roy. Astron. Soc. 7, 194–202.

Yang, H.-J., Frey, F., Weis, D., Giret, A., Pyle, D., Michon, G., 1998. Petrogenesis of the flood basalts forming the northern Kerguelen Archipelago : Implications for the Kerguelen plume. J. Petrol. 39 (4), 711–748.

Première partie

Fluctuations du champ magnétique terrestre enregistrées par les laves de Kerguelen

Avant propos

Cette première partie s'articule autour de deux articles. Le premier a été publié très récemment dans un volume spécial de *Physique of the Earth and Planetary Interior* traitant, du champ paléomagnétique selon différents aspects tels que les observations et modèles, les méthodes et résultats appliqués à la détermination de paléointensité, la variation paléoséculaire et les nouveaux progrès relatifs aux études de magnétostratigraphie. Ce volume spécial regroupe des contributions qui donnent suite à quatre sessions présentées durant le congrès scientifique commun IAGA-IASPEI qui s'est tenu à Hanoï en Août 2001. Notre travail présente en particulier les résultats d'une étude directionnelle menée sur les cinq sections d'âge oligocène ($\approx$100 coulées) prélevées durant la campagne d'été 1999-2000. Une estimation de la variation séculaire y est reportée et confrontée au modèle G de (McFadden et al., 1991). La magnétostratigraphie établie pour chacune des sections nous a permis d'y inclure une révision de l'estimation de leurs taux d'éruption respectifs. Cet article contient également des études de magnétisme des roches qui, associées aux résultats de l'étude directionnelle, constituaient les travaux préliminaires nécessaires à l'étude de paléointensité qui suit.

Le second manuscrit qui vient d'être soumis au *Geophysical Journal International* détaille l'étude de paléointensité menée sur trois des cinq sections étudiées en direction. Les sections du Mont de la Tourmente et du Mont Amery, que nous n'auront pas eu le temps de traiter au cours de cette thèse, pourrait faire l'objet d'une nouvelle étude similaire à celle-ci. Tout d'abord, le lecteur trouvera dans ce travail la présentation de résultats expérimentaux obtenus à partir d'échantillons pilotes repérés à partir des cinq critères de sélection *a priori* suivants :

- un écart angulaire entre aimantation rémanente naturelle (ARN0) et aimantation rémanente caractéristique $\leq 15^\circ$ (ou une aimantation secondaire rapidement détruite) ;
- des coefficients de viscosité $\leq 5\%$ (10% pour les échantillons provenant de coulées intermédiaires) ;
- une évolution constante de la susceptibilité magnétique mesurée en champ faible à température ambiante après chaque palier de désaimantation thermique ; dans

le cas d'échantillons traités par champ alternatif, l'évolution de la susceptibilité magnétique d'un autre échantillon de la même coulée traité thermiquement a été observée par défaut ;

- une dispersion intra-coulée faible de l'ARN0 ;
- enfin une courbe k-T réversible témoignant de la stabilité thermique d'un échantillon caractéristique de chaque coulée.

Ensuite, 12 estimations moyennes de paléointensité à l'échelle de la coulée sont rapportées. Leur qualité technique est assurée par l'utilisation de 7 critères *a posteriori* :

- quatre points successifs considérés au minimum pour définir un intervalle de température d'interprétation ;
- un rapport $z \leq 15\%$, qui permet de prendre en compte les problèmes d'aimantations rémanentes secondaires acquises pendant les expériences au laboratoire ;
- un rapport DRAT $\leq 10\%$ pour vérifier la reproductibilité des mesures ;
- une fraction d'ARN0 f ≥ 0.3 pour que l'interpretation soit significative ;
- une déviation angulaire maximum (MAD) $\leq 10^\circ$ pour éviter de prendre en compte plusieurs composantes dans la détermination ;
- un angle α entre la direction caractéristique et la moyenne vectorielle $\leq 10^\circ$ pour s'assurer que la composante sur laquelle porte l'estimation est bien la composante primaire ;
- enfin des test dits «de la queue» dans les cas où plusieurs déterminations étaient possibles pour aider à discriminer les différentes interprétations.

Ce second article présente enfin une confrontation de ces nouvelles déterminations avec les données oligocènes, disponibles dans les bases de données internationales (Perrin and Schnepp, 2003), répondant aux mêmes critères de qualité.

Chapitre 1

Palaeomagnetic study of Oligocene (24-30 Ma) lava flows from the Kerguelen Archipelago (Southern Indian Ocean): Directional analysis and magnetostratigraphy

G. Plenier, P. Camps, B. Henry & K. Nicolaysen

Publié dans Phys. Earth Planet. Int., 133 (2002) 127-146

We report palaeomagnetic determinations in order to estimate the palaeosecular variation of the geomagnetic field for the upper Oligocene period from a southern site. We measured the anisotropy of magnetic susceptibility (AMS) of basalts from five sections to check the reliability of applying tectonic correction and concluded that no stratigraphic corrections were needed. A positive reversal test implies that secondary components were sufficiently removed from the characteristic remanent magnetization. Also, the sampling was sufficiently random to accurately reflect upper Oligocene palaeosecular variation. Calculations of the between-flow angular standard deviation (S_B) from the geographic pole show values between 21.2° and 21.8°. This palaeosecular variation estimate agrees with Model G for palaeosecular variation (McFadden et al., 1991), which is axisymmetric and assumes an equatorial symmetry of the geomagnetic field. The virtual geomagnetic poles (VGPs) from the Mont des Ruches section seem to exhibit two polarity changes : reverse-normal (R-N) first, and in more detail a second normal-reverse (N-R) one. Finally, assuming that no polarity chrons are missed by any of the sections, we compare the magnetostratigraphy we defined to the global geomagnetic polarity scale of Huestis and Acton (1997) using previously obtained radiometric dates to correlate the sections (Yang et al., 1998; Nicolaysen et al., 2000; Doucet et al., 2002). The precise age constraints furnished by these correlations allow an estimation of eruption rates from 0.30 to at least 1.31 km/my, with wide variations from section to section and an increase of eruption rate for younger sections. However, due to the non uniqueness of the correlations, the age limits of the sections and consequently the extrusion rate estimations can vary. Moreover, assuming the Mont des Ruches section has probably recorded all the magnetic polarity intervals, the

Mont de la Rabouillère and Mont de la Tourmente intermediate VGP directions may indicate unrecorded polarity chrons. The eruption rates calculated can thus be overestimated.

Keywords : Oligocene palaeosecular variation ; Anisotropy of magnetic susceptibility ; Virtual geomagnetic poles

1.1 Introduction

Because there is no way to observe the composition and dynamics of the Earth's core directly, one indirect method is to study the Earth's magnetic field fluctuations recorded or observed at the Earth's surface. These fluctuations, which include secular variation, reversals, and excursions, are principally related to the fluid dynamics of the outer core. An accurate understanding of core dynamics can be obtained by the use of geomagnetic field modeling,(see Dormy et al. (2000) for a review). However, these simulations require more experimental constraints to define the robust characteristics of the Earth's magnetic field against which they can be tested. Thus, numerous records more or less uniformally distributed at the Earth's surface for consecutive time windows on the geological time scale are needed (Merrill and McFadden, 1999). Unfortunately, owing to the non-uniform distribution of the continents, a sampling bias between the northern and southern hemisphere, particularly at high latitudes, affects the palaeomagnetic data currently available. Only few studies present volcanic sequences located in the southern hemisphere. A question that arises is whether the main palaeomagnetic field is equatorially symmetric, as used for some models of palaeosecular variation (McFadden et al., 1991, e.g.), or whether it is more complicated as currently observed.

This report presents a palaeomagnetic study carried out on samples from five stratigraphic sections of Oligocene lava flows from the Kerguelen Archipelago (49.9°S, 70°E). Our objectives were to add new magnetic data in a poorly defined area, to prospect for flows recording transitions, and to check the symmetry of the geomagnetic field between the northern and southern hemisphere. Finally, by comparing the magnetostratigraphy of the five studied sections with previous geochemical studies and geochronological dating (Gautier et al., 1990; Nicolaysen et al., 2000; Frey et al., 2000; Doucet et al., 2002), we discuss the correlation between disparate stratigraphic sections and more precisely constrain calculated eruption rates.

1.2 Geological setting

The Kerguelen Archipelago is located in the southern Indian Ocean (49.9°S, 70°E) on the northern part of the Kerguelen-Gaussberg Plateau (Fig. 1.1). This large oceanic plateau, with its conjugate Broken Ridge, is a manifestation of intensive Cretaceous (119-95 Ma) volcanism due to the Kerguelen hotspot (Duncan (2002) and references therein). The Kerguelen Archipelago represents the continuation of this hotspot volcanism for the

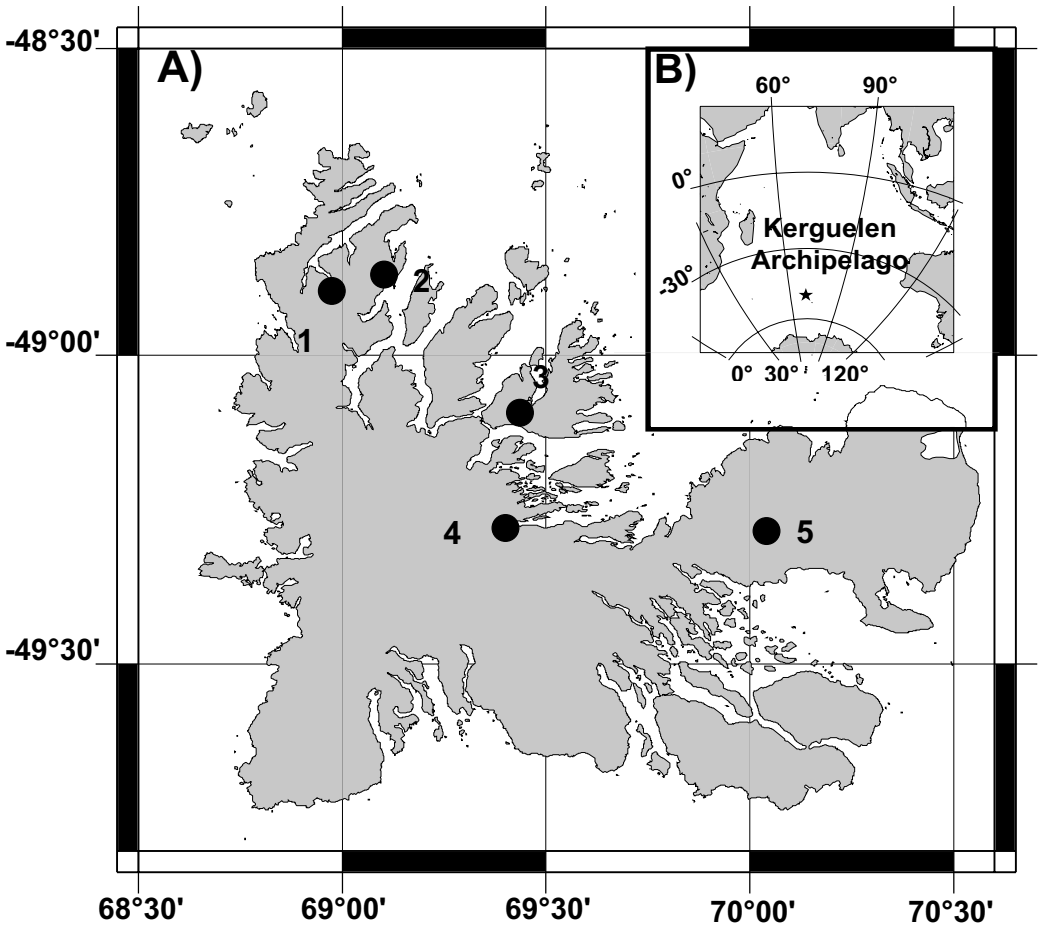

FIG. 1.1 – A) Locations of sampled sections : **1** Mont des Ruches : 18 flows, **2** Mont des Tempêtes : 20 flows, **3** Mont de la Rabouillère : 19 flows, **4** Mont de la Tourmente : 33 flows and **5** Mont Amery : 8 flows. B) Location of the Kerguelen Archipelago in the Indian Ocean.

last 30 Ma (Yang et al., 1998; Weis et al., 1998; Nicolaysen et al., 2000), but some magmatic contribution from the Southeast Indian Ridge (SEIR) during the early Cenozoic is not excluded (Doucet et al., 2002). More than 85% of the archipelago is composed of basalt flows which form valley walls (400 to 900 m high) exposed by glacial erosion. Intrusions (gabbro, granite, and syenite) from 1 to 15 km diameter also occur. Isotopic chemistry links the origin of the plutons to Kerguelen plume melts (Giret, 1990; Weis and Giret, 1994).

1.3 Palaeomagnetic sampling

In recent geochemical study of seven volcanic sections located principally in the northern part of the Kerguelen archipelago, Nicolaysen et al. (2000) and Doucet et al. (2002) determined $^{40}Ar/^{39}Ar$ isochron ages on acid leached groundmass. To benefit from these available dates, the strategy was to sample the same sections. Then, we looked for the thickest studied sections, recovering the maximum number of successive and minimally-altered lava flows. We also searched for sampling areas not affected by significant tectonism or by subsequent intrusions. Based on geologic, geochemical, and logistical criteria, we decided to target the five sections presented in Fig. 1.1. In addition to a previous palaeomagnetic study (Camps et al., in preparation), this allowed us to completely sample the Oligocene basalts exposed on the archipelago. Except for the Mont de la Tourmente section, we were unable to sample the previously-dated sections in exactly the same locations. For the Mont des Ruches section, syenite and dyke intrusions close to the original geochimical section led us to sample the opposite valley wall (800 m westward), assuming the two sections are correlated. For the Mont des Tempêtes section, we were not able to cross a major river to reach the 3 km distant Mont Fontaine section. Here again, we sampled the opposite valley wall assuming the lavas correlate between the two sections. For the Mont Rabouillère section, we preferred to take a nearby section (400 m away) which was less altered and undisturbed by dykes. In this case, there is no doubt of the lateral continuity between the two sections. Finally, for the Mont Amery section, we chose to continue the previous magnetic sampling of Henry and Plessard (1997), starting at the next flow upward, rather than to resample the dated Mont Crozier section (about 2 km away) which is more difficult to reach.

In all, almost a hundred lava flows with seven samples per flow on average were drilled using a gas-powered drill, and the samples were oriented with both solar sightings and magnetic compass plus a clinometer. Because of the particular field trip conditions encountered on Kerguelen, the possibility to return to the same place is always uncertain. For this reason, we decided to sample each successive lava flow, in order to recover any existing magnetic transitional directions.

1.4 Rock Magnetic properties

1.4.1 Low-field susceptibility versus temperature

Experimental procedure

We performed continuous measurements of the low-field (100 μT) magnetic susceptibility versus temperature (KT curves) during heating and cooling cycles to characterize the magnetic mineralogy of samples and to estimate their thermal stability. We used the method of Prévot et al. (1983) to estimate the mean Curie temperature of magnetic minerals revealed by a reversible fall in the KT curves. The measurements were performed in vacuum ($< 10^{-2}$ mbar) using a modified Bartington susceptibility meter MS2 associated to a home made furnace. The rock sample is a cylindrical core of $\approx$1 cm^3. One sample per flow for the Mont des Ruches, Mont des Tempêtes and Mont Rabouillère sections was heated to its Curie temperature with a heating and cooling rate of 7°/mn. Unfortunately, some technical problems did not permit analysis of all the flows, but the shape of the curves we obtained are independent of the corresponding section. The two treated flows from the Mont de la Tourmente section make us confident to expect that the two remaining sections will qualitatively provide similar results.

Results and interpretation

The primary magnetic carrier is presumed to be a titanomagnetite ($Fe_{3-x}Ti_xO_4$) with an x value of 0.6-0.7 as generally expected for basaltic lava flows. Two distinct types of KT behaviour were observed. The first case, sample 123C in Fig. 2.2, illustrates the irreversible and complex thermomagnetic behaviour observed for almost 60% of the samples. This sample presents three susceptibility falls at $\approx$100-150°C, near 350°C and finally around 400°C. We suggest that the first susceptibility decrease correspond to the original titanomagnetites. However, titanomagnetites are supposed to stay stable during heating under vacuum and should be observed in the cooling curve. Therefore, it is not excluded that the first fall indicate slightly oxidized titanomaghemites, resulting from low temperature oxydation of the original titanomagnetites. Heating-cooling cycles at various intermediate temperatures performed on some other specimens lead us to interpret the second fall as due to the presence of titanomaghemites with higher degree of oxidation or different mineral size but also at the same time to dissociation effects of the metastable titanomaghemites present in the sample. Because inversion of titanomaghemites is an irreversible phenomenon, the third susceptibility fall might not exist before heating in the laboratory. Titanomaghemites are known to invert in two stages during heating-cooling cycles, with a first unstable inversion product which produces the third susceptibility decrease near 400°C, and a final stable inversion product which depends on the degree of oxidation of the starting titanomaghemite (Özdemir, 1987). These final products usually consist of a titanomagnetite-ilmenite as-

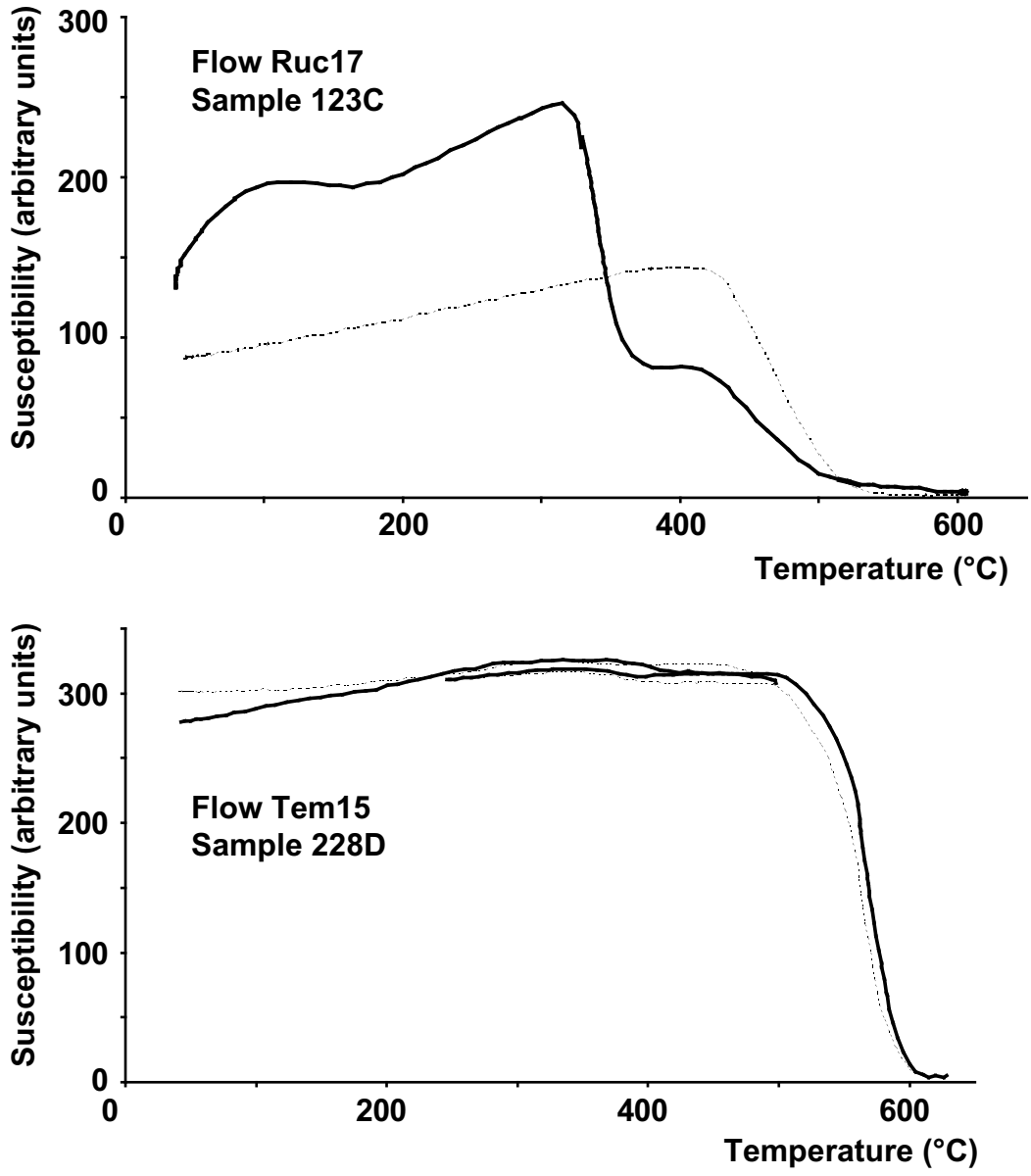

FIG. 1.2 – Low-field susceptibility versus temperature curves displaying the two typical behaviour observed for the Kerguelen basalts. Bold (dashed) lines correspond to heating (cooling) phases.

semblage, or haematite and pseudobrookite for the most highly oxidized titanomaghemite (Özdemir, 1987). No matter which is the degree of oxidation because as it is often observed, haematite is reduced under vacuum to yield a Ti-poor titanomagnetite ($\sim$ 400°C). In case of total oxidation, the susceptibility measured during cooling might only reflect this titanomagnetite. Thus, whatever the degree of oxidation considered, the shoulder in the susceptibility curve observed during cooling might relate the presence of a stable titanomagnetite with a 460 $\pm$ 25°C Curie temperature. All samples showing this complex behaviour yield qualitatively the same KT-curve with some differences due probably to varying degrees of oxidation of the original titanomaghemite.

For the second case, sample 228D in Fig. 2.2, the reversibility of the curve indicates that the primary mineral phase is a non maghemitized titanomagnetite with a mean Curie temperature of 560 $\pm$ 15 °C. This low-Ti titanomagnetite quite probably results from high temperature oxyexsolution during the flow emplacement of the original titanomagnetite.

Unfortunately, the two behaviours describe above cannot be related to macroscopic flow characteristics as for example, the flow thickness, the color of the samples or the presence of phenocrysts. Thus, a complete study of each flow is needed to detect the thermally stable second case which could correspond to samples well suited for palaeointensity determinations (Plenier et al., in preparation).

1.4.2 Viscosity index

Experimental procedure

Before magnetic cleaning, the viscosity index ν (Thellier and Thellier, 1944; Prévot, 1981) was first determined on the entire collection in order to estimate the Viscous Remanent Magnetization (VRM) possibly acquired by the samples since the beginning of the Brunhes polarity epoch. We measured the specimens after 2 weeks in the ambient magnetic field oriented along the z core axis and again, after 2 weeks storage in a zero field. The difference between this two measurements yields the VRM acquired during 15-days in the present geomagnetic field (Thellier and Thellier, 1944). We calculate the viscosity index ν using :

$$\nu = \frac{\Delta_z}{\sqrt{x_0^2 + y_0^2 + z_0^2}} \times 100$$

where Δ_z represents the difference in the magnetization intensity parallel to the magnetizing field between the two measurements, and x_0, y_0 and z_0 represent the cartesian components in core coordinate of the magnetization after 2 weeks storage in a field-free space. The viscosity index, expressed as a percentage, corresponds approximately to 25% of the VRM acquired *in situ* since the last reversal of polarity (780 kyr)(Prévot, 1981).

Results and interpretations

The mean geometric viscosity indices ($\bar{\nu}$) for each flow are reported in Table B.1.

TAB. 1.1 – Cleaned average directions of magnetization of the lava flows.

Flow	n/N	Inc	Dec	α_{95}	κ	Plat	Plong	polar.	ν%	J_{20}	Alt
Mont des Ruches section (48.87°S, 68.91°E)											
Ruc18	7/7	72.7	175.7	4.3	197.7	-80.5	82.8	R	9.13	0.37	230
Ruc17	7/7	65.6	192.6	5.6	116.4	-81.6	336.2	R	9.85	0.53	220
Ruc16	4/4	79.9	183.3	6.5	201.6	-68.4	65.9	R	2.48	0.50	180
Ruc15[1]	7/7	74.5	159.2	3.9	244.8	-73.1	105.3	R	4.6	1.17	160
Ruc14[1]	7/7	76.4	149.5	4.5	183.8	-67.7	104.5	R	5.8	1.15	150
Ruc13	7/7	64.0	237.6	11.1	30.5	-51.8	356.7	R	32.45	0.33	140
Ruc12	7/7	64.0	69.4	6.0	102.3	-22.2	113.8	T	65.81	0.45	120
Ruc11	7/7	81.3	144.1	8.0	58.2	-61.2	89.8	R	0.23	1.73	100
Ruc10	7/7	78.3	92.7	5.3	130.5	-45.1	101.7	R	1.25	1.08	90
Ruc9	11/11	-14.4	15.0	8.1	32.4	46.6	90.8	N	35.88	1.10	85
Ruc8	8/8	-60.8	15.9	2.5	474.4	76.8	132.5	N	17.11	0.59	80
Ruc7	6/7	-62.0	345.1	4.9	188.2	78.3	1.9	N	21.2	0.85	70
Ruc6[2]	8/8	-68.7	358.2	4.1	180.1	86.6	268.0	N	2.57	3.69	60
Ruc5[2]	7/7	-59.1	0.6	13.1	22.2	81.0	71.9	N	9.36	1.80	55
Ruc4[2]	7/7	-66.2	10.1	5.5	120.6	83.3	160.3	N	4.45	2.92	50
Ruc3[2]	8/8	-70.6	356.6	3.9	203.2	83.7	267.0	N	4.28	5.37	40
Ruc2	7/7	-60.9	58.2	3.3	329.2	49.6	171.8	N	5.21	1.08	25
Ruc1	8/8	52.5	195.1	5.3	108.6	-70.6	290.0	R	4.11	1.28	10
Mont des Tempêtes section (48.88°S, 69.11°E)											
Tem20	7/8	67.4	165.3	5.1	139.9	-80.4	145.5	R	25.52	0.16	246
Tem19	6/7	73.4	142.8	7.2	88.1	-66.2	119.3	R	72.64	0.20	224
Tem18	8/8	60.7	177.0	3.5	248.7	-82.5	231.6	R	2.73	9.47	172
Tem17	7/7	62.0	186.0	4.0	224.8	-83.0	287.7	R	3.36	13.40	160
Tem16	5/7	64.2	178.1	4.2	328.6	-86.8	224.6	R	5.57	3.62	152
Tem15[3]	4/4	64.5	188.1	2.8	1109.8	-84.0	317.3	R	4.04	5.80	145
Tem14[3]	7/7	57.1	190.3	7.9	59.3	-76.6	286.6	R	2.06	15.10	140
Tem13	7/7	55.5	180.5	5.0	146.0	-77.2	250.9	R	2.99	1.76	130
Tem12[4]	7/7	59.8	175.0	5.2	136.0	-81.1	223.9	R	10.48	1.23	120
Tem11[4]	7/7	58.5	185.1	4.3	199.5	-79.7	271.7	R	3.91	0.45	110
Tem10[4]	7/7	60.6	188.0	7.0	75.6	-80.8	289.7	R	2.56	0.75	105
Tem9	7/7	58.7	186.7	7.2	70.5	-79.4	278.5	R	11.64	0.47	100
Tem8	6/7	88.4	106.2	4.1	269.4	-49.7	73.9	R	47.41	0.17	90
Tem7[5]	7/7	77.3	219.9	4.3	193.6	-63.4	33.1	R	5.28	0.22	80
Tem6[5]	5/5	77.1	221.2	2.4	979.6	-63.0	31.9	R	4.94	0.53	75
Tem5	5/5	80.9	251.2	4.4	308.3	-51.5	41.5	R	5.93	0.39	68
Tem4	7/7	78.3	232.9	3.2	360.7	-58.0	34.0	R	9.00	0.33	60
Tem3[6]	7/7	74.4	203.1	14.4	18.5	-69.2	42.4	R	21.44	1.38	50
Tem2[6]	7/7	64.6	215.7	4.4	193.1	-66.1	347.0	R	41.99	1.10	30
Tem1	7/7	-67.3	356.6	2.8	464.7	87.5	309.2	N	5.87	3.20	5
Mont de la Tourmente section (49.30°S, 69.39°E)											
Tou1	7/7	-69.9	358.0	4.9	150.0	85.3	264.1	N	13.21	1.15	580
Tou2	7/7	-47.7	3.8	4.1	222.0	69.3	78.9	N	2.97	0.57	525
Tou3	7/7	-49.6	6.2	4.9	152.6	70.6	85.6	N	4.63	8.33	520
Tou4	7/7	-69.6	358.3	5.3	131.4	85.8	263.4	N	23.08	0.72	510
Tou5	9/9	-56.1	332.0	3.9	174.9	66.1	0.8	N	53.48	1.10	505
Tou6[7]	7/7	-62.6	356.4	5.5	123.6	84.1	43.2	N	8.82	1.15	495

Flow	n/N	Inc	Dec	α_{95}	κ	Plat	Plong	polar.	ν%	J_{20}	Alt
Tou7[7]	4/4	-63.9	346.2	11.1	69.0	80.0	355.9	N	37.93	0.86	490
Tou8[7]	7/7	-64.3	359.6	6.8	80.5	86.8	64.5	N	110.17	0.29	480
Tou9	7/7	-76.6	131.0	5.8	108.3	30.0	227.4	T	54.67	1.24	465
Tou10[8]	7/7	-65.0	11.9	3.5	306.5	81.7	147.6	N	9.47	1.20	430
Tou11[8]	6/6	-72.1	6.5	4.3	247.0	81.3	225.5	N	20.26	2.12	420
Tou12	7/7	-52.6	22.4	7.6	63.9	71.2	120.8	N	52.44	0.80	410
Tou13	7/7	-55.6	34.4	6.1	98.4	61.8	144.6	N	6.35	1.78	390
Tou14	3/4	-77.8	304.0	16.2	58.8	57.2	286.8	N	65.6	0.41	380
Tou15[9]	7/7	-66.6	23.9	5.7	112.1	74.5	167.8	N	37.13	0.95	370
Tou16[9]	7/7	-73.7	33.3	2.8	462.8	68.4	200.6	N	26.48	0.39	360
Tou17	6/7	-39.8	285.7	42.5	3.4	27.0	335.5	T	172.63	5.97	340
Tou18	7/7	-59.6	323.8	2.0	883.5	63.2	344.8	N	26.72	0.29	330
Tou19	7/7	-75.5	14.2	5.5	121.7	74.6	224.4	N	4.74	2.51	320
Tou20	7/7	-72.0	6.6	3.7	267.6	79.1	225.5	N	18.80	1.33	305
Tou21	7/7	-56.7	2.6	7.0	75.8	77.8	79.3	N	148.60	0.18	290
Tou22	6/7	-84.4	8.7	10.7	39.9	52.6	256.5	N	96.79	0.30	280
Tou23	7/7	-67.8	24.6	5.0	144.3	74.2	174.1	N	11.33	3.05	250
Tou24	7/7	-69.5	10.8	5.5	121.6	82.2	193.5	N	10.99	0.43	240
Tou25	7/7	-79.3	16.4	7.0	76.0	68.5	233.6	N	18.11	1.60	220
Tou26	8/8	-64.6	18.2	6.1	83.0	77.5	153.2	N	59.41	0.42	210
Tou27	7/7	-65.4	26.7	2.6	551.0	72.3	163.8	N	24.75	0.55	200
Tou28	7/7	-67.2	35.4	7.2	71.0	67.3	174.6	N	26.07	1.68	190
Tou29	5/5	-52.0	100.7	8.7	78.1	17.9	189.0	T	22.44	2.12	180
Tou30	7/7	-77.6	41.2	2.6	551.1	63.1	213.6	N	18.62	2.13	160
Tou31	7/7	-60.0	6.2	5.7	112.8	80.5	99.1	N	30.38	0.24	135
Tou32	7/7	-66.1	38.5	4.3	199.1	64.9	172.3	N	12.51	0.34	120
Tou33	7/7	-59.6	34.4	3.9	243.9	64.3	152.4	N	54.88	0.94	110
Mont Amery section (49.29°S, 70.06°E)											
Ame8	7/7	-77.7	350.8	3.2	347.2	72.2	262.1	N	2.33	2.56	345
Ame7	7/7	-74.9	326.0	6.6	83.4	67.5	294.0	N	32.09	0.14	340
Ame6	7/7	-57.2	37.1	4.1	220.5	61.1	150.8	N	14.51	2.48	330
Ame5	7/7	-60.8	29.5	5.4	125.0	68.2	151.2	N	13.28	0.69	280
Ame4	7/7	-52.9	9.6	5.3	129.3	72.6	97.9	N	18.73	0.87	270
Ame3	7/7	-75.2	9.4	3.7	265.3	76.1	231.5	N	19.14	0.56	250
Ame2	7/7	-60.4	22.3	6.4	89.7	72.5	141.5	N	7.05	0.12	225
Ame1	7/7	-60.5	1.7	4.3	195.5	82.1	79.4	N	17.45	0.63	200
Mont Rabouillère section (49.09°S, 69.44°E)											
Rab19	7/7	-72.54	2.63	2.8	471.0	81.1	240.6	N	8.8	3.72	280
Rab18	7/7	-78.14	2.63	4.3	196.0	71.6	246.3	N	2.4	1.49	270
Rab17	7/7	-63.17	109.68	4.4	187.0	22.1	203.4	T	9.0	0.30	250
Rab16	8/8	-73.07	354.00	2.0	922.0	79.8	267.4	N	9.3	1.99	230
Rab15	7/7	75.27	173.30	4.1	220.0	-76.1	82.8	R	13.8	0.33	190
Rab14	7/7	69.52	173.53	3.7	269.0	-84.1	111.1	R	10.7	0.20	170
Rab13	7/7	48.40	134.43	2.3	714.0	-50.4	172.0	R	4.8	1.06	160
Rab12	7/7	68.19	140.23	4.2	207.0	-64.8	138.7	R	1.8	0.84	150
Rab11	7/7	56.93	193.60	3.7	266.0	-74.9	295.0	R	2.6	1.85	130
Rab10	6/7	48.70	178.36	1.5	2014.0	-70.5	245.2	R	1.5	1.67	120
Rab9	7/7	71.72	177.11	2.7	494.0	-82.3	81.8	R	23.4	0.22	100
Rab8	7/7	68.22	176.29	2.8	476.0	-86.6	112.7	R	18.3	0.18	80
Rab7	7/7	69.85	198.78	1.9	1017.0	-77.4	8.3	R	11.2	0.59	60
Rab6	6/7	59.00	185.50	4.1	273.0	-80.0	274.2	R	4.9	3.41	45
Rab5	7/7	67.96	180.88	3.1	375.0	-87.9	55.7	R	9.9	1.06	30
Rab4	8/8	54.53	188.27	1.7	1073.0	-74.7	276.0	R	5.7	3.63	20

Flow	n/N	Inc	Dec	α_{95}	κ	Plat	Plong	polar.	ν%	J_{20}	Alt
Rab3$^{(10)}$	8/8	81.02	160.99	3.1	319.0	-65.1	82.7	R	0.9	2.67	14
Rab2$^{(10)}$	7/7	81.71	152.27	4.0	234.0	-62.5	85.7	R	2.5	1.34	8
Rab1$^{(10)}$	7/7	78.38	145.84	2.5	600.0	-64.7	99.4	R	7.8	0.94	2

$^{(i\ =\ 1\text{-}10)}$ indicates flows which can be grouped together (see discussion). n/N is the number of samples used in the analysis/total number of samples collected. Inc and Dec are the mean inclination, positive downward, and the declination east of north, respectively. α_{95} is the 95% confidence envelope for the average direction. κ is the precision parameter of Fisher distribution. Plat/Plong is the latitude/longitude of VGP position, respectively. The polarity of the flow (polar.) is normal (N) if Plat $> 45°$, reverse (R) if Plat $< -45°$, and intermediate (T) for the other cases. ν% is the geometric mean viscosity index (Thellier and Thellier, 1944). J_{20} is the geometric mean remanence intensity after cleaning at 20 mT (for AF demagnetized samples only). Alt is the altitude of the flow in meter.

Calculated for the whole collection, $\bar{\nu}_{all}$ is relatively high (10.3%) compared to the mean value of 6.1% for subaerial volcanic rocks found by Prévot (1981). Only 33% of the specimens have a viscosity index $< 5\%$ or $< 10\%$ for intermediate polarity. Surprisingly, the mean geometric viscosity index calculated for the reverse polarity units alone ($\bar{\nu}_R$) is lower than for normal ones ($\bar{\nu}_N$), 5.8% and 16.4% respectively, which contradicts normal expectations (Prévot, 1981).

However, the high normal polarity $\bar{\nu}_N$ indices and the difference in $\bar{\nu}$ values for normal and reverse polarity flows are due to the Mont de la Tourmente section only. As observed in Fig. 1.3 A), the four other localities present more expected values of ν, with more than 50% of the samples displaying a viscosity index lower than 10%. For the Mont de la Tourmente section, only 20% of the samples display a similar ν value. Moreover, we can observe that almost 15% of the samples from this section present viscosity indices greater than 100%. Fig. 1.3 B) and C) illustrate that these huge values are associated to samples providing low magnetization intensity, after two weeks storage in a shielded room, combined with larger viscous component, after 15 days under the present geomagnetic field.

The particular behaviour of the Mont de la Tourmente samples is quit difficult to explain. According to Prévot (1981), VRMs in basalts can arise in two ways. VRMs hard with respect to alternating fields (AF) demagnetization are carried by single domain magnetite grains with sizes near the superparamagnetism threshold, resulting from high-temperature oxidation of originally homogeneous titanomagnetite. AF-soft VRMs are carried by multidomain grains of low Curie point homogeneous titanomagnetite. Because the ratio of VRM on the total remanent magnetization is supposed to increase with the grain size of magnetic mineral, our results may indicate a larger magnetic grain size for the Mont de la Tourmente lava flows than for classical subaerial lavas. As already deduced from the KT analysis, both low Curie temperature (first case) and high temperature oxidation (second case) are observed in Kerguelen samples. We will demonstrate that the VRM carried by the samples is soft (removed at 20 mT), favoring the hypothesis of larger multidomain grains of low Curie

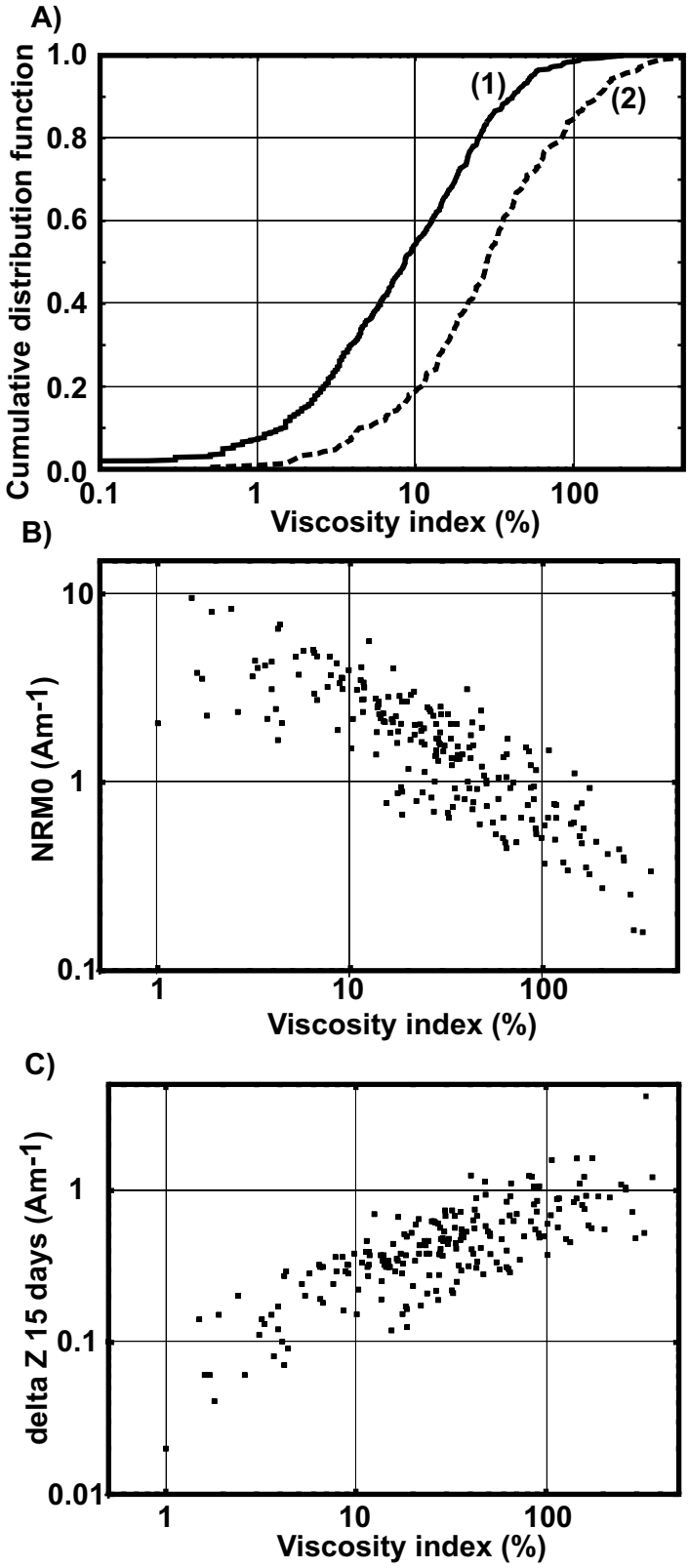

FIG. 1.3 – A) Cumulative distribution function of the viscosity indices (ν) from (1) the Mont des Ruches, Mont des Tempêtes, Mont de la Rabouillère, and Mont Amery sections combined, (2) the Mont de la Tourmente section. B) Magnetization intensity after two weeks storage in a shielded room (NRM0) as a function of ν. C) Magnetization intensity of the viscous component acquired during 15 days under the geomagnetic field (delta z 15 days) as a function of ν.

point titanomagnetites to explain the high normal polarity values.

1.5 Palaeodirection determinations

1.5.1 Tectonic corrections

No significant dip has been observed for four of our sections. On the contrary, the whole Mont de la Tourmente section presents an eastward dip of 15°. According to the geological map (Nougier, 1970a), only east-west trending fractures are present in the neighborhood of this section, and there is no direct evidence for a tilting of the entire section after flow emplacement.

Anisotropy of magnetic susceptibility (AMS)

It is possible to discriminate paleotopography and associated flow direction from post-emplacement tectonic tilting by comparing the flowing direction, determined using anisotropy of magnetic susceptibility (AMS) and the present dip direction. We measured the AMS of the samples from the Mont de la Tourmente section to know if the tectonic corrections were needed. In order to recover the initial flow direction (Cañón Tapia et al., 1995, e.g.), all the samples, with regular standard shape (n=221 of 224), were analyzed using the KLY2 Kappabridge in the IPG Paris palaeomagnetic laboratory at Saint Maur. In order to eliminate statistically indistinct values, we filtered the individual data using both F statistics and the three sigma limit on the A and B factors as described by Cañón Tapia et al. (1995). Doing thus, 33 samples were eliminated. The confidence regions for the mean direction of each axis were calculated using linear perturbation analysis (Hext, 1963; Jelinek, 1978; Lienert, 1991), bootstrap method (Constable and Tauxe, 1990) and the bivariate extension of Fisher's statistics (Henry and Le Goff, 1995). A difficulty in AMS study of volcanic flows is the possible occurrence of permutation of maximum-intermediate susceptibility axis. Such permutations of the principal susceptibility axis are sometimes observed in samples from a same flow, possibly giving wrong mean directions (Cañón Tapia et al., 1996). We therefore determined the density contour of the maximum (Kmax), intermediate (Kint), and minimum (Kmin) principal susceptibility axis to look for possible discrepancies between orientation of the axis clusters and mean directions.

AMS measurement of fewer than 10 specimens per flow yields quite large statistical uncertainty of the susceptibility tensor (Cañón Tapia et al., 1997). Although all our samples were drilled from the lower part of each flow, the sampling strategy was not designed for AMS analysis. Because only seven samples were taken per flow, AMS mean directions per flow are of weak significance, showing large uncertainties. However, the aim of our study was not to constrain the flowing direction of each flow, because it can be related to the local flowing disturbances, but to determine the mean flowing direction. The low significance of the data per flow does not allow

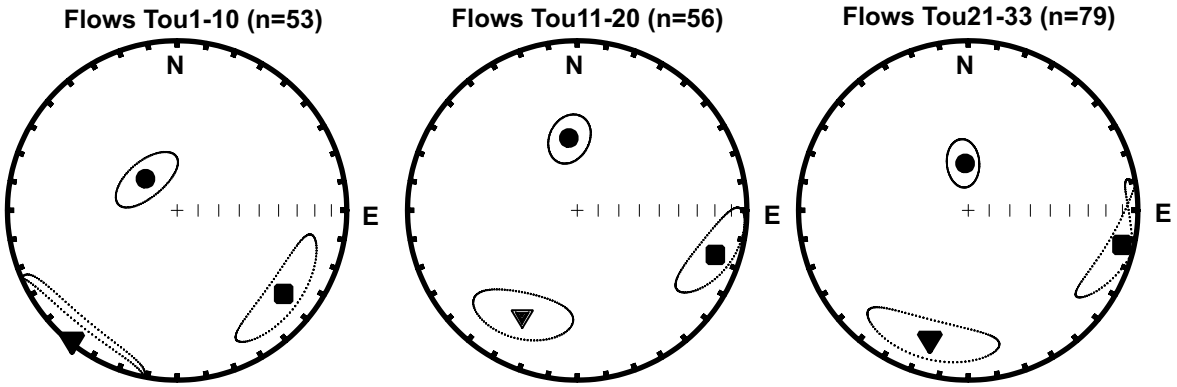

FIG. 1.4 – Mean principal susceptibility axis of three consecutive parts from the Mont de la Tourmente section and their 95% confidence ellipses (Constable and Tauxe, 1990), square K_{max}, triangle K_{int} and circle K_{min}.

TAB. 1.2 – Directions of the mean principal susceptibilities and sizes of the confidence regions around them for the Mont de la Tourmente section.

		$\bar{s}$	$\delta\bar{s}$	Dec	Inc	ζ	d_ζ	i_ζ	η	d_η	i_η
Flows 1-10	Max	0.336	0.0005	128.2	21.0	9.6	295.8	68.5	26.0	36.5	4.2
N = 53	Int	0.334	0.0005	219.1	2.4	14.9	73.9	87.1	27.9	309.1	1.7
	Min	0.330	0.0006	315.3	68.8	8.7	140.7	21.1	17.7	50.0	1.8
Flows 11-20	Max	0.336	0.0005	107.9	16.0	9.6	355.7	52.8	21.8	208.4	32.5
N = 56	Int	0.334	0.0003	207.4	30.2	12.4	346.4	52.3	22.0	105.0	20.3
	Min	0.330	0.0004	353.7	55.0	9.3	104.8	14.1	12.6	203.5	31.3
Flows 21-33	Max	0.336	0.0003	103.0	7.9	7.6	359.4	59.4	27.4	197.5	29.3
N = 79	Int	0.334	0.0003	196.1	21.3	11.3	8.0	68.5	27.4	105.1	2.8
	Min	0.330	0.0004	353.8	67.2	7.6	85.0	0.5	11.8	175.2	22.8
whole section	Max	0.336	0.0003	113.6	16.1	5.7	351.0	61.9	14.0	210.4	22.4
N = 188	Int	0.334	0.0002	209.3	18.9	7.5	348.5	65.7	14.0	114.1	14.7
	Min	0.330	0.0003	345.9	64.8	5.7	107.7	13.9	7.5	203.0	20.6

N is the number of sample per data-set. $\bar{s}$ is the eigenvalue of normalized mean susceptibility tensor. $\delta\bar{s}$ corresponds to the 95% confidence region for $\bar{s}$. Dec and Inc are the declination and the inclination of the mean susceptibility axis, respectively. ζ and η are the semiangles of minor and major axis of the 95% confidence ellipse, respectively. $d_{\zeta,\eta}$ is the declination of minor,major axis direction. $i_{\zeta,\eta}$ is the inclination of minor,major axis direction.

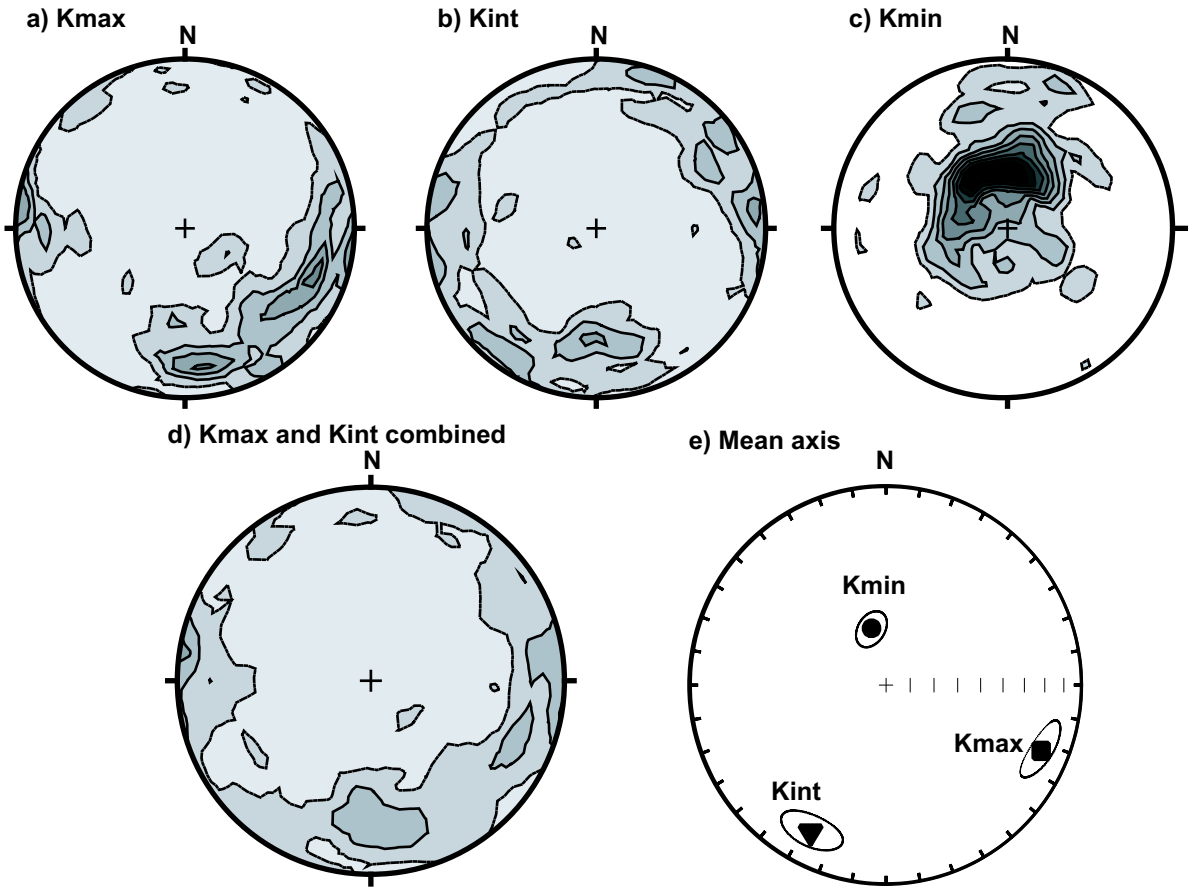

FIG. 1.5 – a), b), c) and d) : Density diagrams of the principal susceptibility axis K_{max} (a), K_{int} (b), K_{min} (c) and K_{max}-K_{int} (d) combined for the Mont de la Tourmente section (n = 188). Mean principal axis (e) and their 95% confidence ellipses (Constable and Tauxe, 1990), square K_{max}, triangle K_{int} and circle K_{min}.

determination of this mean flowing direction from running direction in the different flows. The lack of observed discordances between the flows suggests that the flowing conditions were relatively constant for the whole section, and we therefore merged all the AMS data.

To verify that such a merging is justified, a comparison of the mean data was made dividing the section in three subsets. The coherent results obtained in these parts (Fig. 1.4 and Table 1.2) clearly show the constant flowing conditions during emplacement of the whole section. The three statistical methods used to define the mean directions and their associated confidence zones, provided approximately the same results, for each part as for the whole data. Fig. 1.5A), B), C) and D) displays for all the samples the Kmax, Kint, Kmin and Kmax-Kint density diagrams, respectively. Kmax, Kint and Kmax-Kint density contours present bipolar diagrams. For Kmax, the two maxima of density are ESE and S oriented. Kint own a comparable S trend but the second maximum is E in this case. The combination of the Kmax and Kint leads to decrease the density contrasts, with a maximum of W-E to WNW-ESE main direction and another one, weaker, of S azimuth. The Kmin density diagram displays a well defined mean direction, with a maximum of density strongly dipping northwestward.

Discussion

The bipolarity of the Kmax and Kint density diagrams clearly show that Kmax-Kint axis permutation is important in this section. However, one of the maximum density of Kmax and the maximum density of Kmin perfectly agree with the mean Kmax and Kmin, determined using the other statistical approaches. This indicates that permutations do not significantly affects the mean tensor directions. The consistency of the mean directions for the different parts of the section and the relatively small 95% confidence areas for the whole section yield a strong and coherent signal among the section. The mean tensor directions can be therefore used for the determination of the flowing direction.

The interpretation of these data is unfortunately questionable. In fact, because of axis permutation, Kmax or Kint could represent the flowing direction. Moreover, both mean Kmax and mean Kint present a significant inclination. Kmin is not in the vertical plane including Kmax or Kint. On the one hand, Kmax corresponds to the strongest maximum density and should be a good candidate. In this case, the flowing direction agrees with the present dip direction and probably no tilting occurred after lava emplacement. On the other hand, if Kint represents the flowing direction, the flows were tilted after emplacement. Untilting leads to horizontal Kmax, and to Kmin and Kint in a same vertical plane. No decisive argument yields choice between these two possibilities. The VGPs from the five sections (see Table 2) are more axially distributed without tectonic corrections on the Mont de la Tourmente section. This argues for a eastward dip of topographic

origin before the lava flowing. AMS data being compatible with a lack of tilting after lava emplacement, we chosen to not apply dip correction to the paleomagnetic data from the Mont de la Tourmente section.

1.5.2 Palaeomagnetic cleaning

We performed demagnetizations of the samples in two steps. First, two pilot samples per flow were stepwise demagnetized, one in alternating fields (AF) using a laboratory-built AF demagnetizer (up to 140 mT) and the other thermally in a non-inductive PYROX furnace with a residual magnetic field of less than 20 nT. Remanent magnetizations were measured using a JR-5A spinner magnetometer after each demagnetization step (7 to 16). The behaviour of the pilot specimens guided our choice of the best demagnetization procedure for the remaining samples from the same flow. When the two demagnetization methods yield almost the same results, we preferred to proceed with the thermal treatment because the separation of components is usually more efficient for volcanic rocks. Moreover, the thermal demagnetizations reveal the spectrum of remanence unblocking temperatures, used later to define the demagnetization steps of a pilot palaeointensity experiment (Plenier et al., in preparation).

1.5.3 Results

For almost all of the samples, the individual Characteristic Remanent Magnetization (ChRM) was clearly isolated. Nearly all samples are contaminated by a small secondary component, oriented along the present field, which is removed entirely below 20 mT or 350°C. The softness of this secondary component indicates a viscous origin. The relatively high viscosity indices we found, especially for the Mont de la Tourmente section, support this interpretation. Considering a limit of $\pm$ 45° for the latitude of the virtual geomagnetic poles (VGPs) during stable polarity, examples of orthogonal vector plots for normal, reverse, and intermediate polarity are presented in Fig. 1.6. We determined the individual ChRM directions by means of the least-squares method (Kirschvink, 1980) using at least three consecutive demagnetization steps. If the individual ChRM could not be isolated or if the sample was possibly misoriented (as indicated by field notes and by a direction significantly different than the other samples from the same flow) the sample was excluded from further analysis. This is the case for 11 samples on the 684 analysed. The determinations are of sufficiently good quality since the maximum angular deviation (MAD) is lower than 2° for 80% of the samples. Moreover, only seven flows have an $\alpha_{95} > 10°$, four of them being of intermediate polarity. The directional results are presented in Table 2. Of 98 lava flows, 51% are normal polarity, 44% are reversed polarity, and 5% display intermediate directions. Except for the mont des Ruches section (18 flows), where the normal and reverse polarity flows are equally represented, the percentage of reversed units varies a lot. For the Mont des Tempêtes and the Mont Rabouillère

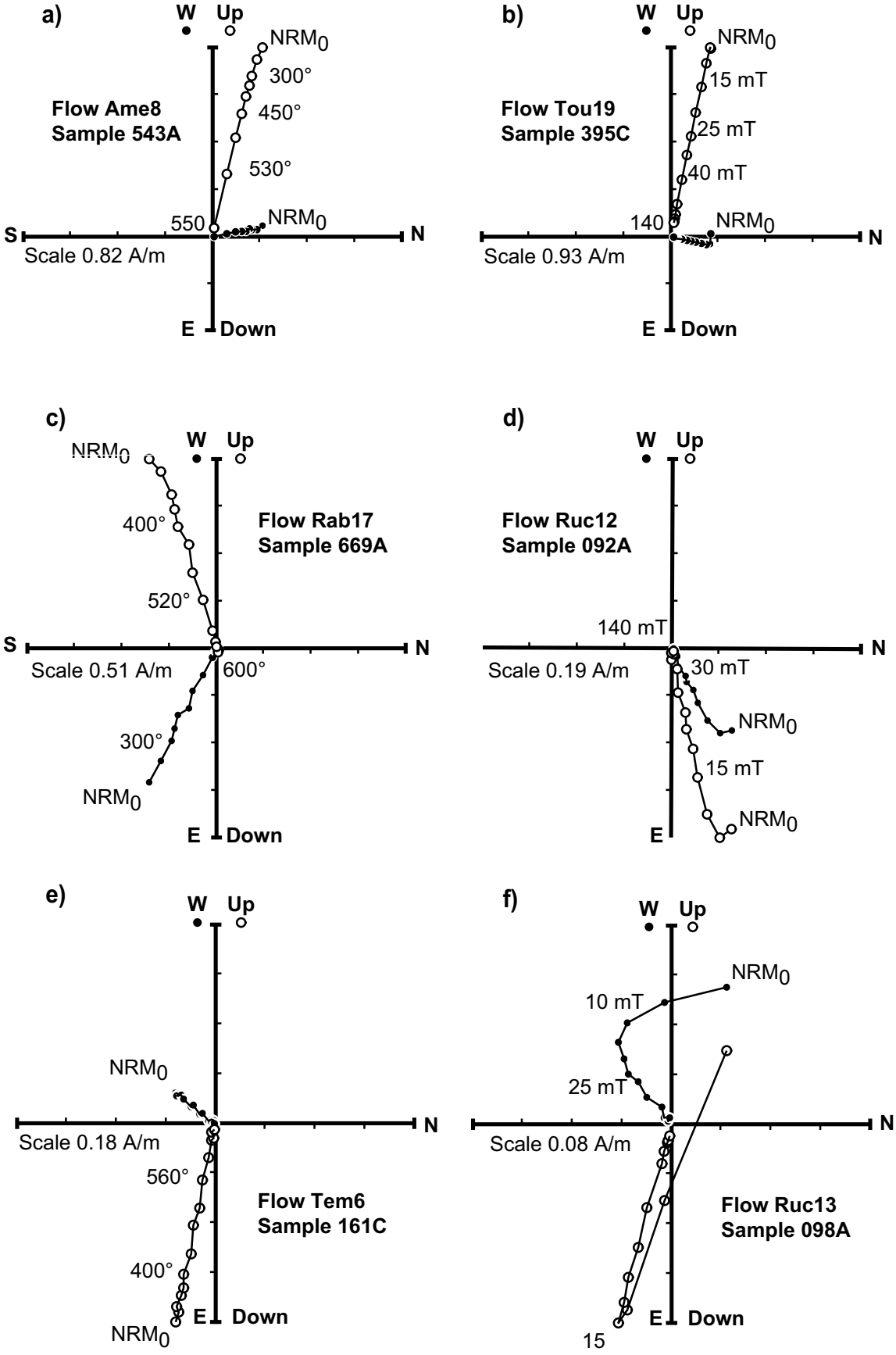

FIG. 1.6 – Orthogonal plots for normal, reversed and intermediate flows for differently demagnetized samples in geographic coordinates. The black (white) points correspond to the horizontal (vertical) plane.

sections (20 and 19 flows, respectively), it is greater than 75%, whereas it is zero for the Mont de la Tourmente and the Mont Amery sections (33 and 8 flows, respectively).

1.6 Discussion

1.6.1 Magnetostratigraphy and extrusion rates

The polarity intervals measured in the five Kerguelen Archipelago sections are shown as a function of elevation in Fig. 1.7. We propose to discuss the correlations between these magnetostratigraphy informations and the reference polarity time scale (Huestis and Acton, 1997) using the absolute age determinations obtained on the corresponding previously dated sections (Yang et al., 1998; Nicolaysen et al., 2000; Doucet et al., 2002), and also the geochemical compositional variations of basalts. For example, the D group signature defined by Yang et al. (1998) in the upper part of the Mont de la Rabouillère section and observed by Doucet et al. (2002) for the lower part of the Mont des Ruches and Mont des Tempêtes sections helps to place these sections stratigraphically with respect to each other. For the Mont Amery section, we sampled upward from the last units studied by Henry and Plessard (1997). We thus included their palaeomagnetic data, which describe the first 200 meters of the section, to furnish a more complete magnetostratigraphy.

In order to check the relationship between the initiation of Kerguelen flood basalts and the conjunction of the Kerguelen Plume with the Southeast Indian ridge, Nicolaysen et al. (2000) used lava accumulation rates to evaluate the location of the Kerguelen Archipelago when it began to form. The magnetostratigraphy correlated to the global geomagnetic polarity time scale allow to better constrain the age limits of each section and then recalculate more accurate extrusion rates for each section. We calculated the extrusion rate (exr) as follow :

$$exr = \frac{\Delta H}{\Delta t - ref}$$

where ΔH is the analyzed stratigraphic thickness and $\Delta t - ref$ the duration of the chrons the lavas correlate to.

The correlations are made using the working hypothesis that all the polarity chrons spanning the emplacement of the volcanic sequence were recorded. This assumption seems reasonable because the volcanic activity of the Kerguelen hotspot is acknowledged to be vigourous. We did not see for example erosion surfaces between the lava flows, only thin sediment layers were sometimes observed. However, the volcanic activity of the Kerguelen plume may differ from place to place and the thickness of the sedimentary layers is not directly related to the time span between two successive flows, their absence does not necessary evidence a rapid succession. Without rigorous arguments, we tentatively considered that no hidden polarity chrons are missing from the volcanic sequences.

Because of the errors on age determinations, several correlations remain possible

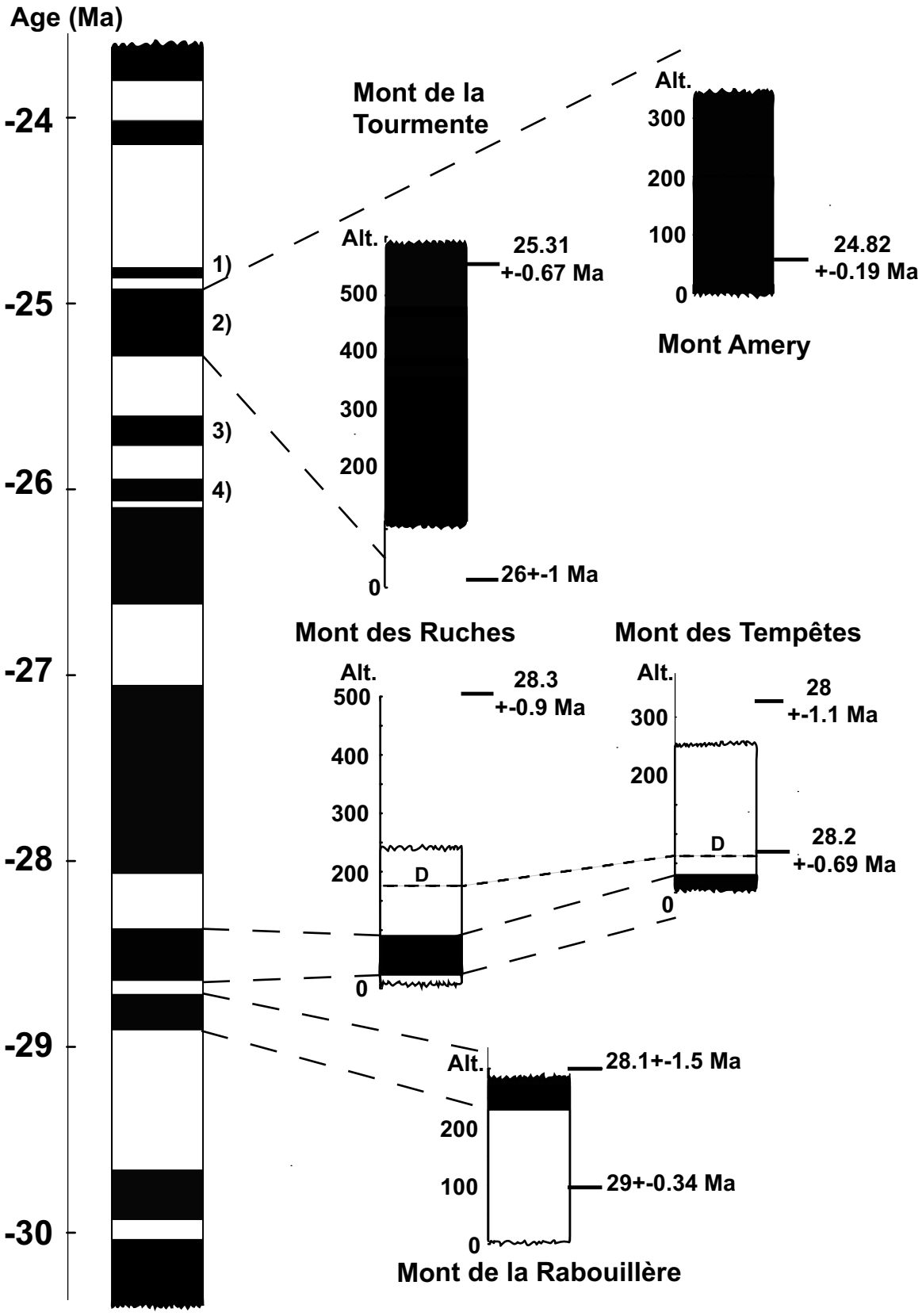

FIG. 1.7 – Magnetostratigraphic correlations with the global geomagnetic polarity time scale (Huestis and Acton, 1997) interpreted using radiometric dates and geochemical observations (Yang et al., 1998; Nicolaysen et al., 2000; Doucet et al., 2002). We assume that all the polarity chrons are recorded at each section. 1), 2), 3), and 4), are the possible correlations allowed for the Mont de la Tourmente section.

for each section. To overcome these uncertainties, we kept the nearest solution from the best radiometric dates available. For instance, the 26±1 Ma date obtained at the base of the less constrained Mont de la Tourmente section is not directly related to a polarity boundary and the precision is not sufficiently accurate to allow a firm correlation. On the contrary, the 25.31±0.67 Ma date at the top of the section is of quite good quality, but 4 correlations can be made considering the error bars (1-4 in Fig. 1.7). The correlation 2) corresponding to a normal polarity chron between 24.92 and 25.28 Ma is the nearest to 25.31 Ma and was kept as our preferred interpretation. One can argue that using dates determined on sections not sampled exactly at the same place can also introduce some bias, but as explained in the paleomagnetic sampling description (section 3), we are quite confident about the stratigraphic relation between the dated sections and the palaeomagnetic ones.

Concerning the extrusion rate calculations, depending on the interpretation made to correlate the sections to the global geomagnetic polarity scale, the results can vary significantly. For this reason, we will give both a lower and upper estimate. It is also important to notice that because the sections do not span the entire chrons, the time elapsed to produce each section is necesseraly shorter than the one used for the calculation. Therefore, both values of the extrusion rate are actually lower bounds of the true eruption rates. These limitations should be kept in mind to appreciate correctly the estimate proposed.

The interpretation, based on the nearest solution from the best radiometric dates, furnish the following constraints on the age limits. The Mont de la Rabouillère section accumulated between 29.7 and 28.7 Ma, the Mont des Ruches section between 28.7 and 28.1 Ma, the Mont des Tempêtes section between 28.6 and 28.1 Ma, the Mont Amery section between 24.9 and 24.8 Ma, and the Mont de la Tourmente section between 25.3 and 24.9 Ma. For the Mont de la Rabouillère, Mont des Ruches, and Mont des Tempêtes sections, we calculated an average extrusion rate of 0.33 km/my (0.70 km/my). But the well constrained normal polarity interval in between two reversed chrons observed on the Mont des Ruches section allows estimation of a more realistic eruption rate of 0.27 km/my (0.39 km/my) for this section. The upper limit of the D geochemical signature combined with the magnetic results indicate that the eruption rate for the Mont des Tempêtes section is almost two times lower than for the Mont des Ruches (between 0.16 and 0.23 km/my). For the youngest Mont de la Tourmente and Mont Amery sections, our first interpretation yields eruption rates of 1.31 km/my (8.55 km/my) and 6.27 km/my (0.96 km/my), respectively.

However, this last eruption rate seems unlikely because very high. Thus, we suggest that Mont de la Tourmente and Mont Amery sections erupted during the same normal polarity chron C7n.2n. This alternative interpretation still agrees with the radiometric dates within error. The age li-

mits of the C7n.2n chron, between 25.3 and 24.9 Ma., yield a more acceptable eruption rate of 0.96 km/my for the Mont Amery section. This second interpretation is our preferred. Fig. 1.7 summarizes the retained correlations of each section with respect to the reference polarity timescale (Huestis and Acton, 1997).

Therefore, the Mont de la Tourmente and Mont Amery sections present smaller values, but within the incertitude interval, than the mean 1.6 ± 0.9 km/my proposed by Nicolaysen et al. (2000) for the same sections. The eruption rates calculated by means of the magnetic remanence seem very different from section to section and confirm higher extrusion rates for youngest sections as supposed by Nicolaysen et al. (2000) from geochronological ages considerations. The major assumption used to obtain these conclusions is that all the polarity chrons are recorded at each section. If this is not the case, the extrusion rates are overestimated.

1.6.2 Intermediate directions

In the present study, we define arbitrarly a palaeomagnetic direction as intermediate if its corresponding VGP has a latitude between $\pm 45°$. Intermediate directions can indicate polarity reversals as well as excursions of the geomagnetic field. Unfortunately, assuming that the magnetostratigraphy is complete at every sampling locality, the presented Kerguelen basalt sections did not record reversals because all the intermediate directions occurred within stable polarity intervals. Concerning the Mont des Ruches section, the preceding and following VGPs of the intermediate polarity flow possess a palaeopole latitude 30° or more away from the closest geographic pole. Thus it is possible to consider this intermediate direction as a rebound during a normal to reverse (N-R) polarity change. A similar remark can be made for the Ruc2 VGP location which might correspond to an intermediate position between the reverse to normal (R-N) polarity change. The successive VGPs from the Mont des Ruches section, connected together with a great circle, are shown in Fig. 1.8. The fact that some VGPs can describe a reversal path lead us to consider, as a simplest interpretation, that all the reversals are recorded at least for the Mont des Ruches section. For the Mont de la Tourmente and Rabouillère sections, because any preceding and following VGPs are not deviated toward theses positions, the intermediate VGP seem isolated. Thus, they can either represent super palaeosecular variation, as well as excursions or true intermediate directions during a reversal not recorded. The assumption made for correlate these sections to a global geomagnetic polarity scale may be unsuitable.

1.6.3 Palaeosecular variation

We included in the present statistical analysis the palaeomagnetic results of Henry and Plessard (1997) for the Port Jeanne d'Arc, Port Couvreux and Mont Amery (Val Studer) sections in order to increase the number of upper Oligocene data. In a second step, we removed the transi-

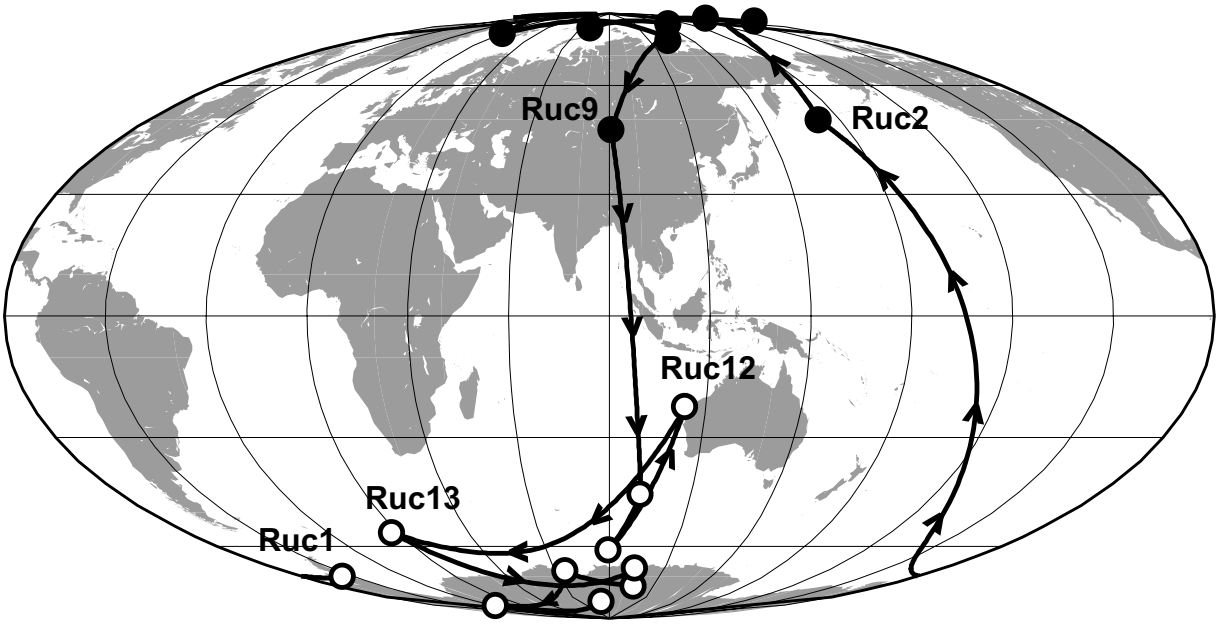

FIG. 1.8 – Locations of VGPs from the Mont des Ruches section.

tional data presenting VGPs with latitude less than ±45°(n=9). The palaeomagnetic directions of individual flow for this global dataset are displayed in Fig. 2.1 with their bootstrapped means and associated 95% confidence ellipses (Tauxe, 1998).

Bootstrap reversal test

In order to check the reliability of the data for palaeosecular variation study, we processed them by separating the mean directions into two polarity datasets and by inverting the normal polarity dataset to its antipode. Then we applied the bootstrap test for a common mean (Tauxe, 1998) for the two datasets in order to perform a reversal test. The statistical analysis of flow-average directions for these two dataset are presented in Table 1.3. Because the confidence intervals of the bootstrapped means for the two distributions overlap for each cartesian coordinate (Fig. 1.10), we concluded that the two means are statistically identical at the 95% level of confidence. Such a positive reversal test implies further, first, that the individual ChRMs are not disturbed by secondary components, next that these ChRMs are primary TRMs, and finally that the palaeomagnetic directions reasonably average the secular variation during the upper Oligocene.

Flow grouping

A random sampling with sufficient time elapsed between successive field recordings is require to estimate the variability of the paleofield due to the secular variation (PSV). Because the present paleomagnetic sampling consists of successive lava flows in a vertical sequence, a risk to introduce a bias in the statistical analysis by giving a spurious weight to a single direction recorded by successive lava flows emplaced in a short time exists. To shed light on this

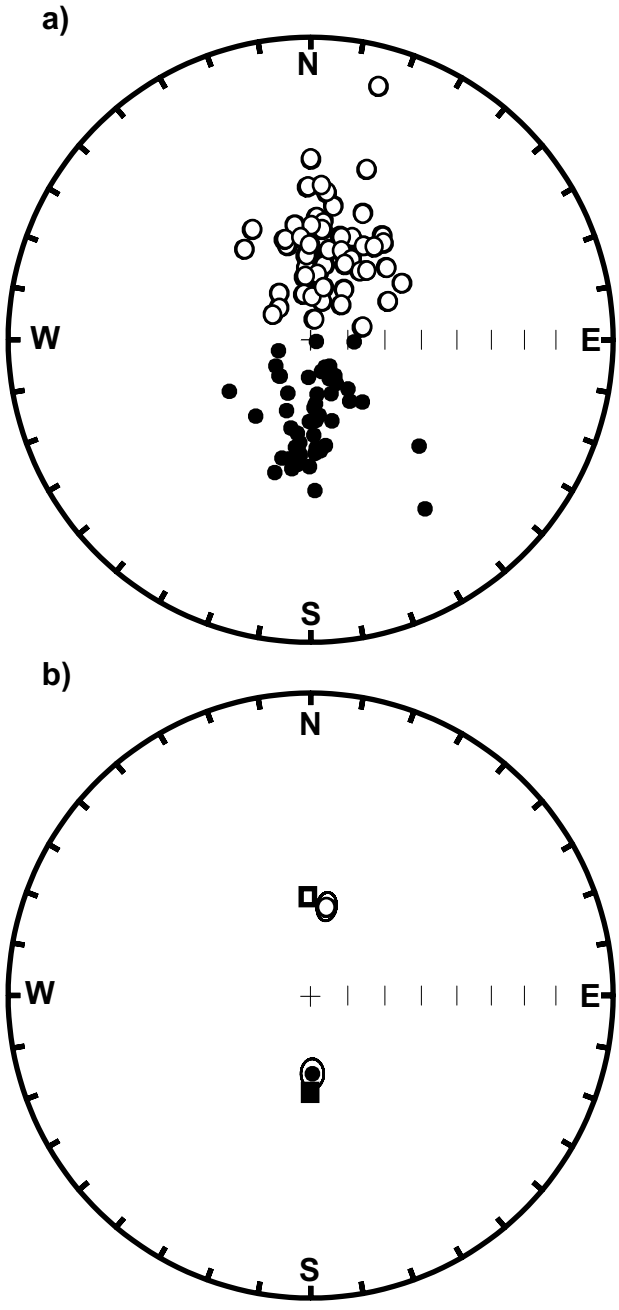

FIG. 1.9 – a) Palaeomagnetic directions of individual flow (Henry and Plessard (1997) and this study combined), and b), their bootstrapped means with 95% confidence ellipses (Tauxe, 1998), after removing of the transitional data. The dipole field directions (squares) are given for comparison. In Black (white) circles and squares are positive (negative) inclinations.

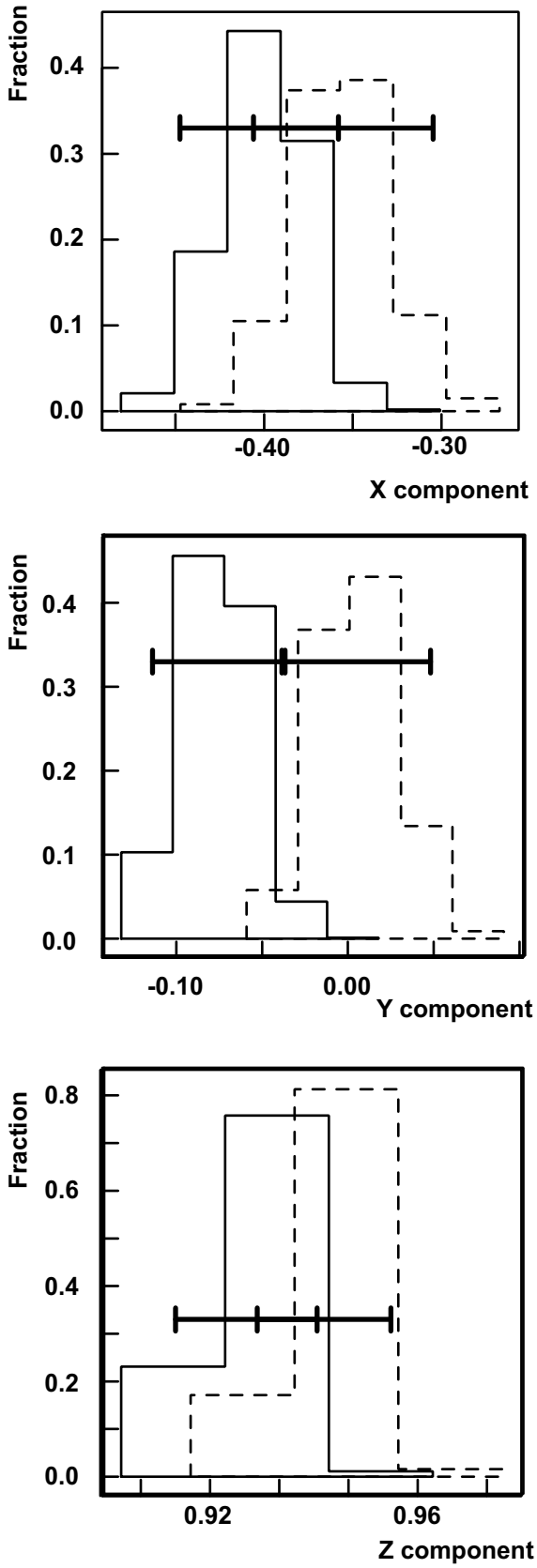

FIG. 1.10 – Histograms of cartesian coordinates of the mean bootstrapped normal and reverse polarity directions and their 95% confidence intervals (Tauxe, 1998).

TAB. 1.3 – Statistical analysis of flow-average direction.

	Dec	Inc	N	R	κ	α_{95}
Ungrouped directions						
Normal	10.2	-65.6	60	58.0849	30.8	3.4
Reverse	178.7	68.9	49	47.5284	32.6	3.6
all combined	5.4	-67.2	109	105.4908	30.8	2.5
Grouped directions						
Normal	11.1	-65.3	53	51.1493	28.1	3.8
Reverse	177.2	68.5	41	39.7268	31.4	4.0
all combined	5.5	-66.9	94	90.7407	28.5	2.8

Dec, Inc are the mean Declination and inclination, respectively. N is the number of lava flow used in the analysis. R is the vector sum of N unit vectors. κ is the precision parameter of Fisher distribution. α_{95} is the 95% confidence envelope for the average direction.

problem, we use the quantitative bootstrap test for a common mean (Tauxe, 1998) to identify non independent successive directions. When two or more succesive flows yield directions with a common mean, we used the field notes to check the geological evidences for elapsed time between the flows (conglomerates, red sediments, coal,...). The flows which cannot be distinguished using these two criteria are then grouped together as indicated in Table 2. Nonetheless, it is important to keep in mind that the palaeomagnetic field itself can stay stable during emplacement of successive lava flow with time elapsed between eruption long enough compared to the rate of secular variation (Love, 2000). In such a case, grouping the data will overestimate the variability of the paleofield. To quantify this potential problem, we estimated the palaeosecular variation using two extreme cases : with (n=94) and without (n=109) grouping of similar successive directions.

Estimation of the palaeosecular variation

We processed the combined data, by reversing the VGPs of reversed polarity. The total angular standard deviation (asd) is calculated using :

$$S_T = (N-1)^{-\frac{1}{2}}(\sum_{i=1}^{N}\theta_i^2)^{\frac{1}{2}}$$

where N is the number of data and θ_i the angle between the ith VGP and the reference position. The total asd is then corrected for experimental error by removing the within-flow asd :

$$S_B^2 = S_T^2 - \frac{S_W^2}{\overline{n}}$$

where $\overline{n}$ is the mean number of samples per unit, $S_W \approx 81^\circ/\sqrt{\overline{k}}$ is the within-flow asd, and $\overline{k}$ the mean precision parameter. Results of these calculations are reported in Table 1.4. Because of the low number of grouped flows, the two different data-sets considered do not change significantly the results. The real palaeosecular variation is estimated in the range of 19.4 and 24.3°, which corresponds to the lower and upper bounds of the two extreme cases.

Comparison with palaeosecular variation model

In Fig. 1.11, we report the VGP scatter and the associated 95% confidence interval

TAB. 1.4 – Dispersion statistics of VGP

	VGPs> 45°	grouped VGPs> 45°
N	109	94
Mean latitude	85.6	85.8
Mean longitude	202.0	197.7
precision parameter K	15.5	14.6
A_{95}	3.6	4.0
within flow asd (S_W)	5.00	4.98
Dispersion from the Earth's rotation axis		
Total asd (S_T)	21.3	21.9
Between flow asd (S_B)	21.2	21.8
95% confidence limits on S_B	19.4-23.4	19.8-24.3

N number of flow for calculations. S_B , S_T, and S_W are the between, total, and within flow angular standard deviations, respectively. The 95% confidence limits on S_B are calculated using the table of 95% confidence limits for angular standard deviation (Cox, 1969).

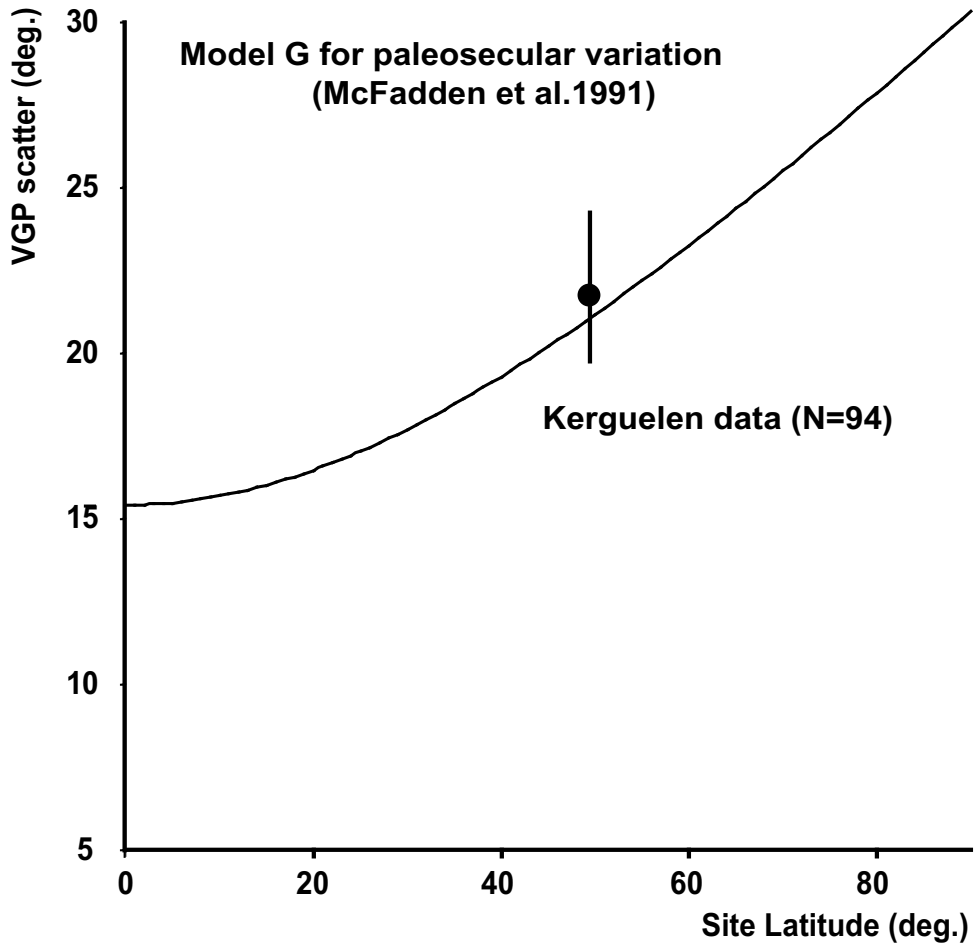

FIG. 1.11 – VGP scatter and 95% confidence interval about spin axis of data (n=94) from Henry and Plessard (1997) and the present study combined (with grouping of magnetically identical flows) compared to the Model G for palaeosecular variation (McFadden et al., 1991).

about the spin axis (n=94) to compare it with the Model G for palaeosecular variation (McFadden et al., 1991). We used this model because it is the only one which can be applied for the 24-30 Ma time window. Obviously, the data fit nicely the model. This substantiates the model G of McFadden et al. (1991) for the approximation of the palaeosecular variation during the 22.5-45 Ma time interval. The equatorial symmetry of the main geomagnetic field assumed in PSV model G is then coherent with our southern hemisphere dataset.

1.7 Conclusions

We present a paleomagnetic analysis of five lava sections from the Kerguelen Archipelago. We use the AMS technique to determine the initial flow direction and conclude that no tectonic corrections to sample orientations are needed for this study. The magnetic carriers have been identified using low-field susceptibility evolution curves and include : 1) original titanomagnetite or slightly oxidized titanomaghemite, 2) titanomaghemite with higher Curie temperature, more or less thermally stable due to low temperature oxidation at a different level, and 3) poor-Ti titanomagnetite produced by high temperature oxidation. Surprisingly, the calculated viscosity index of the Mont de la Tourmente section is larger than expected for subaerial lavas. After laboratory treatment, the primary remanent magnetization is well isolated, as shown by little within flow dispersion and a positive bootstrap reversal test. This test also assures that the Oligocene palaeosecular variation is well averaged by the sampling. If we assume that no reversals are missed by the sections, and considering our interpretation of correlation to the Huestis and Acton (1997) global geomagnetic polarity scale, the magnetostratigraphy permits us to improve the dates of each section – between 29.7 and 28.7 Ma for The Mont de la Rabouillère section, 28.7 and 28.1 Ma for the Mont des Ruches section, 28.6 and 28.1 Ma for the Mont des Tempêtes section, and between 25.3 and 24.9 Ma for the Mont Amery and Mont de la Tourmente sections – and calculate more precisely the eruption rates. These extrusion rates – 0.35 km/my for the Mont des Ruches section, 0.43 km/my for the Mont des Tempêtes, and lower bound values of 0.3 km/my, 0.96 km/my and 1.31 km/my for the Mont de la Rabouillère, Mont Amery and the Mont de la Tourmente respectively – present important variations from section to section with an increase for the younger sections. Thus, the assumption by Nicolaysen et al. (2000) of a constant eruption rate for the Eocene-Oligocene activity of the Kerguelen plume is an oversimplification. The intermediate data from the Mont des Ruches section is considered as a rebound during a normal to reverse polarity change. The VGP direction provided by the Ruc2 flow can also be considered as an intermediate position between the reverse to normal polarity change. These observations leads to consider that at least the Mont des Ruches section recorded all the reversals. Some doubts exist

for the Mont de la Rabouillère and Mont de la Tourmente sections. Their intermediate VGP directions could signal unrecorded reversals, and thus the eruption rates calculated on these sections may be exaggerated. Finally, the estimated palaeosecular variation substantiates an axially symmetric palaeomagnetic field with equatorial symmetry since they are coherent with the model G of palaeosecular variation proposed for the Oligocene period (McFadden et al., 1991).

1.8 Acknowledgments

We are grateful to the "Institut Polaire Paul Emile Victor" for providing all transport facilities and for the support of this project. Special thanks to Alain Lamalle, Roland Pagny and all our field friends. We thank Mireille Perrin for her help during sampling, Michel Prévot for scientific discussions, and Rob Coe for reading the manuscript and for helpful comments. The authors also want to thanks Scott Bogue and two anonymous reviewer for their constructive remarks. They help to clarify and improve the quality of this article. This work was partially supported by CNRS-INSU programme intérieur Terre.

Bibliographie

Cañón Tapia, E., Walker, G., Herrero-Bervera, E., 1995. Magnetic fabric and flow direction in basaltic pahoehoe lava of Xitle volcano, Mexico. J. Volcanol. Geotherm. Res. 65, 249–263.

Cañón Tapia, E., Walker, G., Herrero-Bervera, E., 1996. The internal structure of lava flows – insights from AMS measurements I : Near-vent a'a. J. Volcanol. Geotherm. Res. 70, 21–36.

Cañón Tapia, E., Walker, G., Herrero-Bervera, E., 1997. The internal structure of lava flows – insights from AMS measurements II : Hawaiian pahoehoe, toothpaste lava and 'a'$\bar{a}$. J. of Volcanol. and Geother. Res. 76 (1-2), 19–46.

Constable, C., Tauxe, L., 1990. The bootstrap for magnetic susceptibility tensors. J. Geophys. Res. 95 (8), 383,395.

Cox, A., 1969. Confidence limits for the precision parameter k. Geophys. J. R. astr. Soc. 18, 545–549.

Dormy, E., Valet, J., Courtillot, V., 2000. Numerical models of the geodynamo and observational constraints. Geochem. Geophys. Geosystems 1 (2000GC000062).

Doucet, S., Weis, D., Scoates, J., Nicolaysen, K., Frey, F., Giret, A., 2002. The depleted mantle component in Kerguelen Archipelago basalts : Petrogenesis of tholeiitic-transitional basalts from the Loranchet Peninsula. J. Petrol. 43 (7), 1341–1366.

Duncan, R., 2002. A time frame for construction of the Kerguelen Plateau and Broken Ridge. J. Petrol. 43, 1109–1119.

Frey, F., Weis, D., Yang, H.-J., Nicolaysen, K., Leyrit, H., Giret, A., 2000. Temporal geochemical trends in Kerguelen Archipelago basalts : evidence for decreasing magma supply from the Kerguelen plume. Chem. Geol. 164, 61–80.

Gautier, I., Weis, D., Mennessier, J., Vidal, P., Giret, A., Loubet, M., 1990. Petrology and geochemistry of the Kerguelen Archipelago basalts (south Indian Ocean) : evolution of the mantle sources from ridge to intraplate position. Earth Planet. Sci. Letts 100, 59–76.

Giret, A., 1990. Typology, evolution, and origin of the Kerguelen plutonic series, Indian ocean : a review. Geol. J. 25, 239–247.

Henry, B., Le Goff, M., 1995. Application of the bivariate extension of Fisher's statistics to the magnetic susceptibility anisotropy data : integration of the measurment uncertainties on the orientation of the principal directions. C.R. Acad. Sci. Paris 320 (IIa), 1037–1042.

Henry, B., Plessard, C., 1997. New palaeomagnetic results from the Kerguelen Islands. Geophys. J. Int. 128 (1), 73–83.

Hext, G., 1963. The estimation of second-

order tensors, with related tests and designs. Biometrika 50, 353–373.

Huestis, S., Acton, G., 1997. On the construction of geomagnetic timescales from non-prejudicial treatment of magnetic anomaly data from multiple ridges. Geophys. J. Int. 129 (1), 176–182.

Jelinek, V., 1978. Statistical processing of magnetic susceptibility measured in groups of specimens. Stud. Geophys. Geod. 22, 50–62.

Kirschvink, J., 1980. The least-squares line and plane and the analysis of paleomagnetic data. Geophys. J. R. Astr. Soc. 62, 699–718.

Lienert, B., 1991. Monte Carlo simulation of errors in the anisotropy of magnetic susceptibility : a second-rank symmetric tensor. J. Geophys. Res. 96, 19,539–19,544.

Love, J., 2000. Statistical assessment of preferred transitional vgp longitudes based on paleomagnetic volcanic data. Geophys. J. Int. 140, 211–221.

McFadden, P., Merrill, R., McElhinny, M., Sunhee, L., 1991. Reversals of the Earth's magnetic field and temporal variations of the dynamo families. J. Geophys. Res. 96 (B3), 3923–3933.

Merrill, R., McFadden, P., 1999. Geomagnetic polarity transitions. Rev. Geophys. 37 (2), 201–226.

Nicolaysen, K., Frey, F., Hodges, K., Weis, D., Giret, A., 2000. $^{40}Ar/^{39}Ar$ geochronology of flood basalts from the Kerguelen Archipelago, southern Indian Ocean : implications for Cenozoic eruption rates of the Kerguelen plume. Earth Planet. Sci. Letts. 174, 313–328.

Nougier, J., 1970. Contribution a l'étude géologique et géomorphologique des iles Kerguelen. Bull. Com. Nation. Fr. Rech. Antarct. Paris 27, 696pp.

Özdemir, O., 1987. Inversion of titanomaghemites. Phys. Earth Planet. Int. 46, 184–196.

Prévot, M., 1981. Some aspects of magnetic viscosity on subaerial and submarine volcanic rocks. Geophys. J. R. Astr. Soc. 66, 169–192.

Prévot, M., Mankinen, E., Grommé, C., Lecaille, A., 1983. High paleointensities of the geomagnetic field from thermomagnetic studies on rift valley pillow basalts from the mid-Atlantic ridge. J. Geophys. Res. 88, 2316–2326.

Tauxe, L., 1998. Paleomagnetic Principles and Practice. Kluwer, Dordrecht.

Thellier, E., Thellier, O., 1944. Recherches géomagnétiques sur des coulées volcaniques d'Auvergne. Ann. Geophys. 1, 37–52.

Weis, D., Damasceno, D., Frey, F., Nicolaysen, K., Giret, A., 1998. Temporal isotopic variations in the Kerguelen plume : evidence from the Kerguelen Archipelago. Miner. Mag. 62A, 1643–1644.

Weis, D., Giret, A., 1994. Kerguelen plutonic complexes : Sr, nd, pb isotopic study and inferences about their sources, age and geodynamic setting. Mem. Soc. Géol. Fr. 166, 47–59.

Yang, H.-J., Frey, F., Weis, D., Giret, A., Pyle, D., Michon, G., 1998. Petrogenesis

of the flood basalts forming the northern Kerguelen Archipelago : Implications for the Kerguelen plume. J. Petrol. 39 (4), 711–748.

Chapitre 2

Absolute palaeointensity of Oligocene (28-30 Ma) lava flows from the Kerguelen Archipelago (southern Indian Ocean)

G. Plenier, P. Camps, R.S. Coe & M. Perrin

Soumis au Geophys. J. Int.

We report palaeointensity estimates obtained from three Oligocene volcanic sections from the Kerguelen Archipelago (Mont des Ruches, Mont des Tempêtes, and Mont Rabouillère). Of 402 available samples, 102 were suitable for a palaeofield strength determination after a preliminary selection, among which 49 provide a reliable estimate. Application of strict a posteriori criteria make us confident about the quality of the 12 new mean-flow determinations, which are the first reliable data available for the Kerguelen Archipelago. The VDMs calculated for these flows vary from 2.78 to 9.47 with an arithmetic mean value of 6.15±2.1 $10^{22} Am^2$. Compilation of these results with a selection of the 2002 updated IAGA palaeointensity database lead to a higher (5.4±2.3 $10^{22} Am^2$) Oligocene mean VDM than previously reported (Goguitchaichvili et al., 2001; Riisager, 1999), identical to the 5.5±2.4 $10^{22} Am^2$ mean VDM obtained for the 0.3-5 Ma time window. However, these Kerguelen palaeointensity estimates represent half of the reliable Oligocene determinations and thus a bias toward higher values. Nonetheless, the new estimates reported here strengthen the conclusion that the recent geomagnetic field strength is anomalously high compared to that older than 0.3 Ma.

Keywords : Palaeointensity, Paleointensity, Kerguelen, Tail test, Oligocene.

2.1 Introduction

Numerous studies have been made to increase our knowledge of geodynamo physics, but even so we still do not know the detailed mechanism of the generation of the Earth's magnetic field, and even less about the processes that produce secular variation, excursions and reversals (e.g. Jacobs (1994); Merrill and McFadden (1999)). To better understand the geomagnetic field we need to be able to go

back in time in order to observe its changes and to obtain long-term global characteristics. This is possible with some rocks which recorded the Earth's palaeomagnetic field during their formation or emplacement. Volcanic rocks, in particular, furnish a global knowledge of the geomagnetic field because they contain information on both the direction (inclination and declination) and the strength of the palaeofield. However, the most reliable methods for absolute palaeointensity determination, Thellier and Thellier (1959) and its modified version proposed by Coe (1967b), are time consuming because of the strict conditions which have to be checked to validate the determinations. Moreover, many volcanic rocks turn out to be unsuitable for palaeointensity determination. For these reasons, reliable palaeointensity data are difficult to obtain and are particularly rare. Only 1.5 determinations per million years between 0 and 300 Ma (Selkin and Tauxe, 2000) are available when combining the updated IAGA 1999 data-set and the Scripps submarine basaltic glass databases. Thus more palaeointensity data are needed for a global understanding of the the geomagnetic field.

This study on three basaltic sections sampled in the Kerguelen Archipelago (49.9°S, 70°E) aims to estimate more accurately the palaeomagnetic strength of the geomagnetic field in the 27 and 30 Ma time interval recorded by these lavas. It thus complements the palaeomagnetic direction study recently completed on the same sections (Plenier et al., 2002). Integration of the determinations of this study with selected records issued from preexisting palaeomagnetic databases (Tanaka et al. (1995), updated by Perrin and Shcherbakov (1997) and Perrin et al. (1998)) will allow a better estimation of the Oligocene palaeofield strength and discussion of long-term characteristics of the geodynamo.

2.2 Geology and sampling

The Kerguelen Archipelago lies on the northern part of the Kerguelen-Gaussberg Plateau (southern Indian Ocean). This archipelago is the subaerial continuation of Kerguelen hotspot volcanism for the last 30 Ma (Yang et al., 1998; Weis et al., 1998; Nicolaysen et al., 2000). The lava flows form the tabular reliefs (400 to 900 m high) observed today after glacial erosion, and represent more than 85% of the archipelago surface (Giret, 1990). The rest of the archipelago is composed of intrusions (gabbro, granite, and syenite) issued from Kerguelen plume melts (Weis and Giret, 1994) and quaternary glacial sediments. We studied samples taken on from Mont des Ruches, Mont des Tempêtes, and Mont Rabouillère sections (Fig. 2.1). For the reasons developed in Plenier et al. (2002), we sampled a short distance away from the previously-dated basalt sections (Yang et al., 1998; Nicolaysen et al., 2000; Doucet et al., 2002), but they appear to be correlated. Usually, we drilled seven samples in each successive lava flow using a gas-powered drill and oriented them with both solar sightings

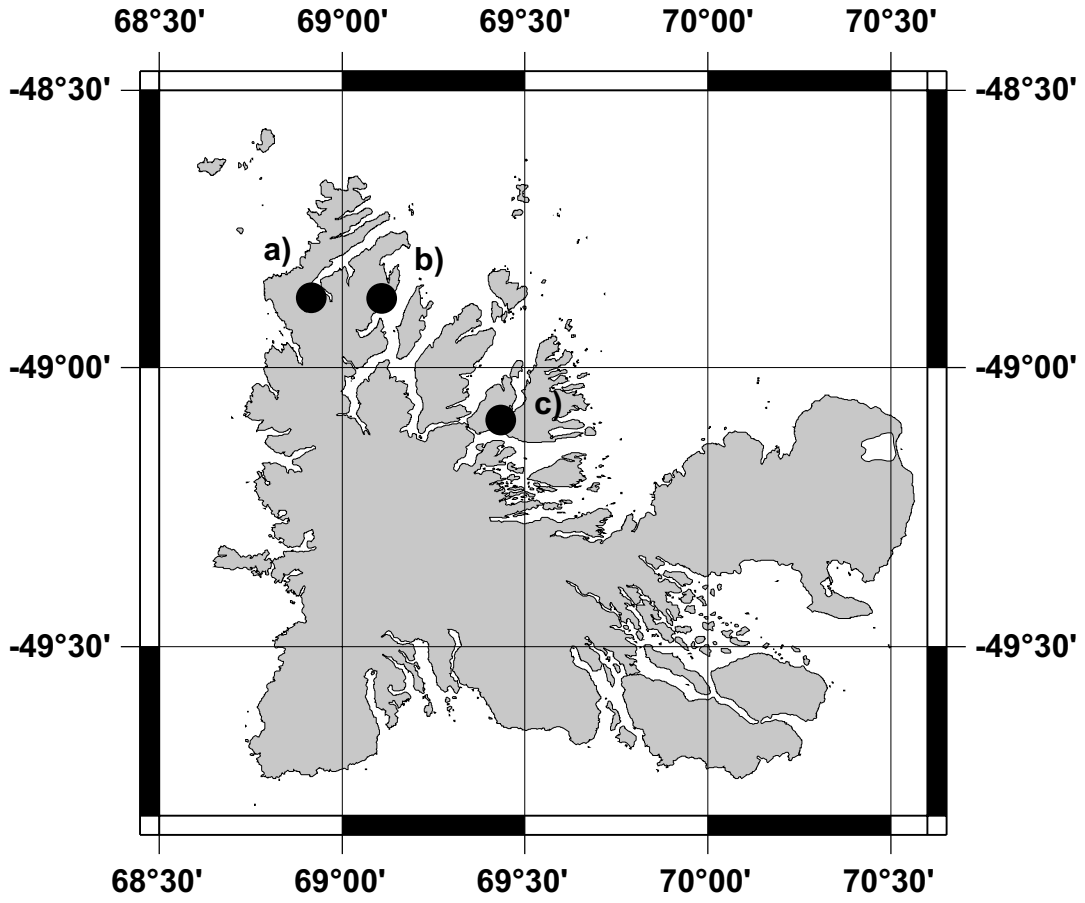

FIG. 2.1 – Location of the studied sections : a) Mont des Ruches : 18 flows (48.87°S,68.91°E), b) Mont des Tempêtes : 20 flows (48.88°S, 69.11°E), c) Mont Rabouillère : 19 flows (49.09°S, 69.44°E).

and magnetic compass with a clinometer. We took care to sample the bottom part of the least altered flows, and as far away as possible from intrusions.

2.3 Rock magnetism and sample selection

For field intensities comparable to those of the Earth, there is a proportionality between thermoremanent magnetization (TRM) intensity measured at 20°C and the strength of the ambient magnetic field applied during cooling through the blocking temperatures for almost all natural rocks. Thus, for some particular rock samples cooling in the geomagnetic field during their formation, it is possible to estimate the palaeomagnetic field strength recorded by comparing their natural remanent magnetization (NRM) with an artificial TRM acquired in the laboratory under a known ambient field. However, the coefficient of proportionality (A) depends on grain size, shape distribution, and blocking temperatures as well as on the amount and type of ferromagnetic material the rock contains. Thus, this coefficient may have changed since the formation of the rock or during heating in the laboratory. For this last reason, a procedure using numerous successive heatings with increasing temperature steps has been developed (Thellier and Thellier, 1959) in order to limit the field strength estimates to the temperature range preceding change of A. The strict conditions to be respected by the samples for correct palaeointensity determination are the following :

(i) The primary remanent magnetization recorded by the studied specimen has to be a thermoremanent magnetization (TRM), acquired at a known epoch in the geomagnetic field.

(ii) The primary remanent magnetization should not be disturbed by large secondary magnetizations.

(iii) The physical, chemical and crystallographical properties of the magnetic minerals must not have changed since the initial TRM was acquired nor changed during the successive heatings imposed by the method.

(iv) The independence and additivity laws of partial thermoremanent magnetization (pTRM) enunciated by Thellier (1938) have to be respected. That is, the total TRM must be equivalent to a sum of pTRMs, each associated with its own blocking temperature interval and not dependent on the remanence carried in every other interval. This generally means that the magnetic carriers have to be single domain (SD) or in favorable cases pseudo single domain (PSD) grains.

Numerous samples can not fulfill these conditions, thus preliminary studies are necessary to check the suitability of the specimens for this method.

2.3.1 Viscosity indices and demagnetizations

In order to assess the importance of the secondary component carried by each sample, we analysed the results from demagnetization experiments performed pre-

viously on sister specimens (Plenier et al., 2002). First, those samples with an angle between the NRM and the characteristic remanent magnetization (ChRM) of 15° or more or with a resistant secondary component (up to 20 mT or 300°C) were excluded. Likewise, we kept only those flows for which the natural remanent magnetization (NRM) of all samples was well grouped (60% of the flows). For these flows, only the samples with a demagnetization curve as undisturbed as possible and presenting unblocking temperatures as high as possible, or median-demagnetization field of at least 20 mT, were retained. Secondly, we estimated the capacity of the specimens to gain a secondary viscous remanent magnetization (VRM) by measuring them first after at least two-week storage in zero field and then after a two-week storage with the ambient field parallel to the cylindrical axis of the specimens. This enables determination of the viscosity index (Thellier and Thellier, 1944) for each sample, which is reported in Table 2.1.

The viscosity index corresponds to about 25% of the VRM acquired since the last reversal 780 ky ago (Prévot, 1981). In order to select the samples, we arbitrarily choose a viscosity index of 10% as an upper limit for intermediate polarity flow specimens and 5% for the others (Prévot et al., 1985).

2.3.2 Susceptibility at room temperature and k-T curves

To be sure of the thermal stability of the samples during successive heating in the laboratory, we measured the room-temperature low-field magnetic susceptibility (k_0) under uncontrolled atmosphere after each thermal demagnetization step of the sister specimen previously studied for palaeodirection determination (Plenier et al., 2002). A favorable sample for palaeointensity determination study should have a relatively constant k_0 value during most of the demagnetization. However, this is not a sufficient criterion because thermally unstable samples may nonetheless display low variations in the susceptibility measured at room temperature. Thus to complete this approach, we measured continuously the low-field susceptibility under vacuum of one sample from each flow usually during two successive heating-cooling cycles, the first up to 350°C and the second up to the Curie temperature. Fig. 2.2 presents two representative k-T curves (susceptibility as a function of temperature) encountered during this study. The first case (Fig. 2.2a) illustrates the irreversible and complex thermomagnetic behaviour observed for almost 60% of the samples. The magnetic carriers are interpreted as original titanomagnetite associated with titanomaghemite, a product of their low temperature oxidation. We rejected the flows yielding this behaviour because of their thermal instability. The second case (Fig. 2.2b) illustrates the re-

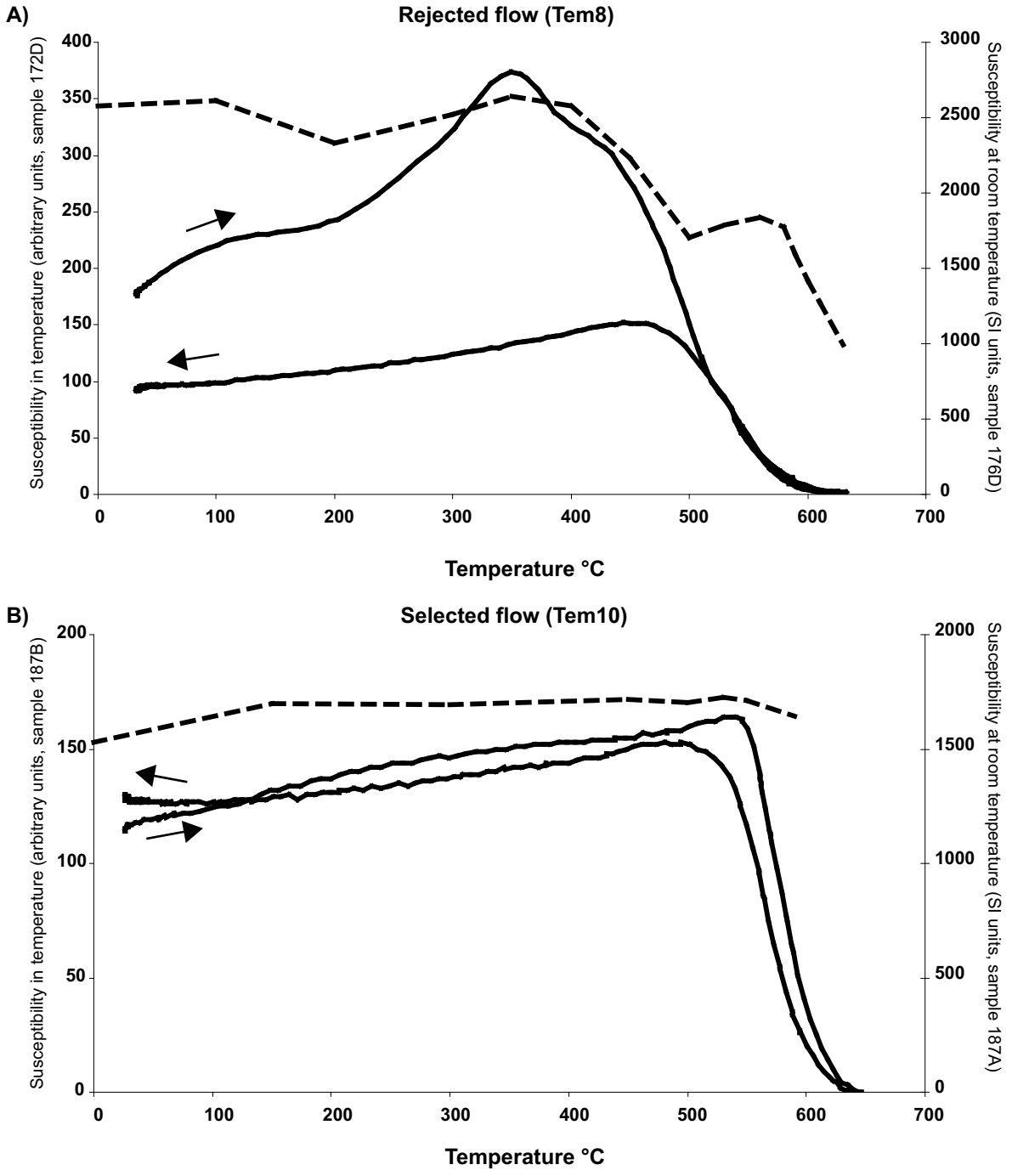

FIG. 2.2 – k-T (solid line) and k_0-T (dashed line) curves of a rejected (A) and a selected (B) flow.

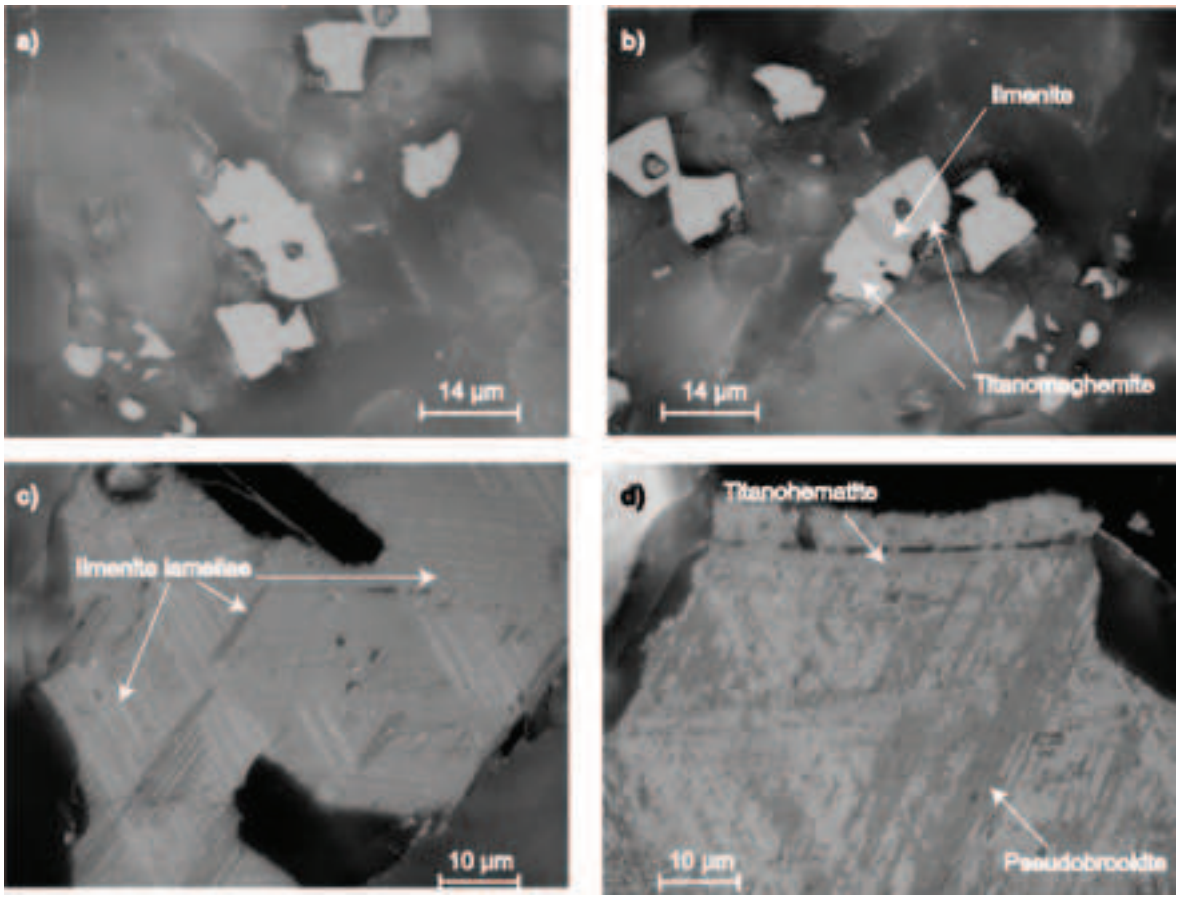

FIG. 2.3 – Reflected light microphotographs using an oil immersion objective. The crossed nicols are at 90°. a),b) : sample 269b (Tou2) in natural light with different orientations ; c),d) : two characteristic minerals from sample 234c (Temp16) in polarised light.

TAB. 2.1 – Cleaned average directions of magnetization of the lava flows (Plenier et al., 2002).

Flow	Chron	n/N	Inc	Dec	α_{95}	κ	Plat	Plong	polar.	ν%	Alt
Mont des Ruches section (48.87°S, 68.91°E)											
Ruc14$^{(1)}$	C9r	7/7	76.4	149.5	4.5	183.8	-67.7	104.5	R	5.80	150
Ruc15$^{(1)}$	C9r	7/7	74.5	159.2	3.9	244.8	-73.1	105.3	R	4.60	160
Ruc16	C9r	4/4	79.9	183.3	6.5	201.6	-68.4	65.9	R	2.48	180
Mont des Tempêtes section (48.88°S, 69.11°E)											
Tem1	C10n.1n	7/7	-67.3	356.6	2.8	464.7	87.5	309.2	N	5.87	5
Tem6	C10n.1n	5/5	77.1	221.2	2.4	979.6	-63.0	31.9	R	4.94	75
Tem10	C9r	7/7	60.6	188.0	7.0	75.6	-80.8	289.7	R	2.56	105
Tem13	C9r	7/7	55.5	180.5	5.0	146.0	-77.2	250.9	R	2.99	130
Tem15	C9r	4/4	64.5	188.1	2.8	1109.8	-84.0	317.3	R	4.04	145
Tem16	C9r	5/7	64.2	178.1	4.2	328.6	-86.8	224.6	R	5.57	152
Tem17	C9r	7/7	62.0	186.0	4.0	224.8	-83.0	287.7	R	3.36	160
Tem18	C9r	8/8	60.7	177.0	3.5	248.7	-82.5	231.6	R	2.73	172
Mont Rabouillère section (49.09°S, 69.44°E)											
Rab12	C10r	7/7	68.2	140.2	4.2	207.0	-64.8	138.7	R	1.80	150

$^{(1)}$ indicates flows which can be grouped together. Chron corresponds to the polarity chron during which the flow emplaced as interpreted by Plenier et al., 2002. n/N is the number of samples analysed/total number of samples collected. Inc and Dec are the mean inclination, positive downward, and the declination east of north, respectively. α_{95} is the 95% confidence envelope for the average direction. κ is the precision parameter of Fisher distribution. Plat/Plong is the latitude/longitude of VGP position, respectively. The polarity of the flow (polar.) is normal (N) if Plat $> 45°$, reverse (R) if Plat $< -45°$, and intermediate (T) for the other cases. ν% is the geometric mean viscosity index (Thellier and Thellier, 1944). Alt is the altitude of the flow in meter.

versible behaviour observed for the rest of the samples. The magnetic carriers are low-Ti titanomagnetites probably produced by high temperature oxyexsolution of the original titanomagnetites. We considered flows presenting this second reversible behaviour as suitable for palaeointensity determination experiments.

In order to complement this thermomagnetic approach, we observed one thin section from each k-T curve type using an oil immersion objective. Fig. 2.3 a) and b) show photomicrographs in natural light of sample 269b (flow Tou2), which displayed irreversible behaviour. We saw an isotropic phase sometimes associated with a pleochroic ilmenite, as showed here. Because titanomagnetite and titanomaghemite are difficult to distinguish under the microscope, it is hard to conclude about the nature of the isotropic phase. These two minerals are certainly both present, but the existence of cracks almost omnipresent in this phase suggest a larger amount of titanomaghemite. This observation agrees well with the k-T curve interpretation. Fig. 2.3 c) and d) show two minerals from a thermally stable sample (234c, Temp16). They illustrate two different advanced stages of deuteric oxidation with ilmenite or titanohematite lamellae exsolved from a residual titanomagnetite almost entirely altered. Again this observation confirms the interpretation of the k-T curves.

2.3.3 Pilot analysis

We kept only flows having at least three samples from different cores which fit all the previously enumerated criteria for the palaeointensity experiments (32 out of the

initial 57). We performed a pilot analysis with one or two samples from each of these flows in order to identify the flows able to give reliable determinations and to define the more appropriate demagnetization steps for the next series. After applying *a posteriori* criteria which will be presented later, 5 flows from the Mont des Ruches section, 9 from the Mont des Tempêtes section and 1 from the Mont de la Rabouillère section seemed suitable. Because a sample which did not pass all the *a priori* selection criteria may sometimes furnish a reliable determination (Perrin, 1998; Coe, 1967a), they should be regarded as serving only for selecting the most appropriate flows for palaeointensity determination. For this reason, the remaining samples from the suitable flows underscored by the pilot analysis have been incorporated in the following two determination series (68 specimens), including the samples which did not pass all the *a priori* criteria first.

2.4 Palaeointensity experiments

2.4.1 Experimental procedure

We used the method of Thellier and Thellier (1959) in its classical form to estimate the palaeointensity of the geomagnetic field. We also followed a sliding pTRM checks procedure (Prévot et al., 1985) every two demagnetization steps in order to verify the coherence in the measure of the partial thermoremanent magnetization (pTRM) gained. Because of the nonlinearity of acquisition of TRM in multidomain grains (Levi, 1977), applying a laboratory field far from the recorded one may lead to underestimation of the ancient field (Tanaka and Kono, 1984; Coe, 1967a). Thus, to increase the quality of the data, we took care to apply, along the vertical axis of the samples, a constant field of 50 μT (with a precision of 0.1 μT), which we supposed to correspond approximately to the strength of the mean Oligocene field for Kerguelen latitude. We also carried out the heating-cooling cycles under a vacuum better than 10^{-4} mbar to limit possible oxidation during experiments. We performed demagnetizations up to 580°C, with 13 steps ranging from 50 to 10°C, using a home made furnace (temperature reproduced within 2°C) in the palaeomagnetic laboratory of the University of Montpellier. Before the treatment, and after each heating-cooling cycle, we measured the remanence with a JR5-A spinner magnetometer. To ensure the reproducibility of the procedure at the same demagnetization step (pair of heating-cooling cycles and pTRM check), we always kept the specimens in the same place in the oven.

2.4.2 Preliminary selection of palaeointensity data

Because palaeointensity determinations are subjective, as many other data interpretations, *a posteriori* criteria help to ensure the technical quality and objectivity of the results and their comparison from study to study. It is noteworthy to point out that except the number of data used for each individual determination, which has

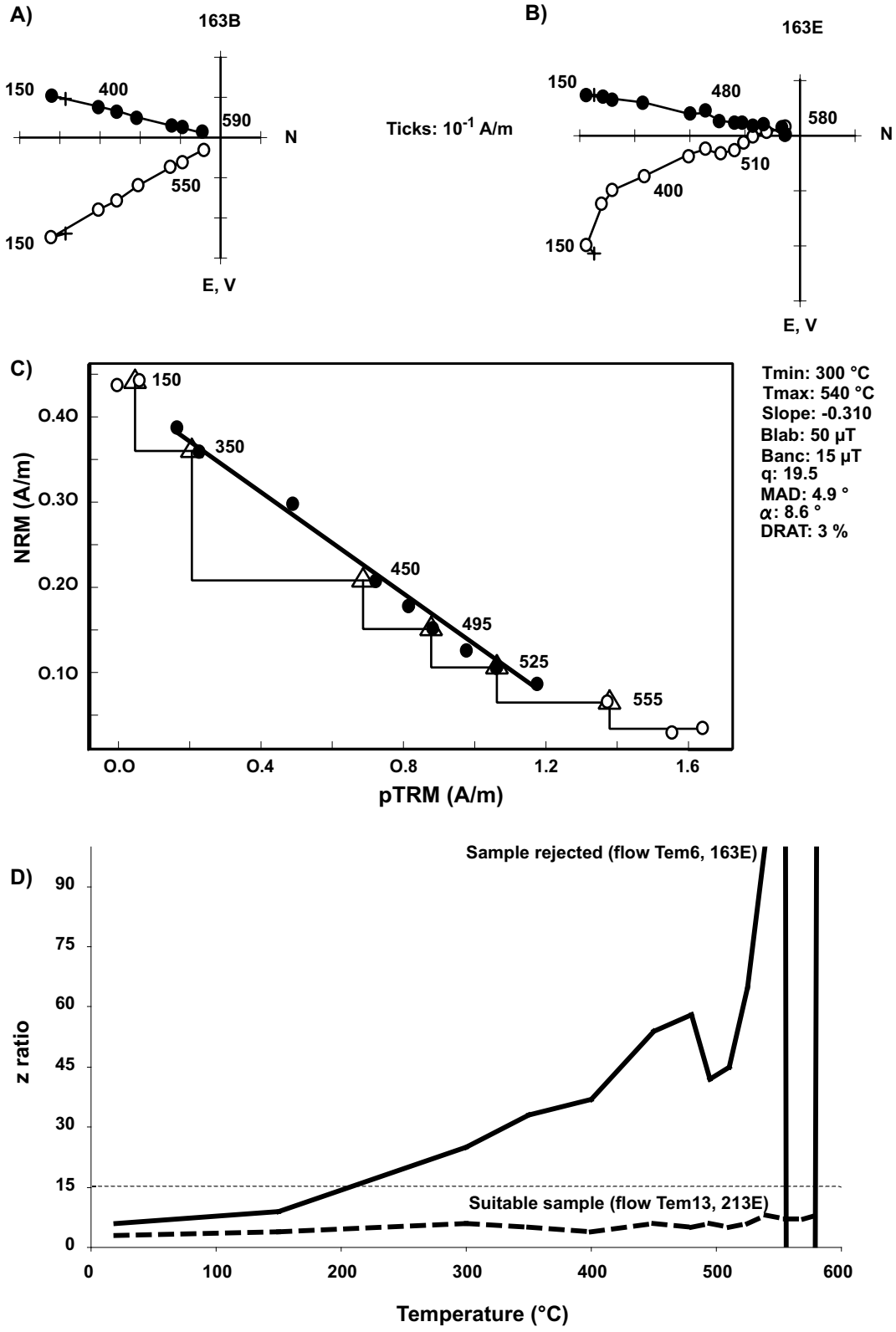

FIG. 2.4 – A) Orthogonal projection of the sister specimen demagnetization, B) Orthogonal projection of the studied sample demagnetization, calculated from the palaeointensity experiment, C) NRM-TRM diagram of the same specimen, and D) Evolution of its z ratio compared to the evolution of the suitable sample 213E.

been fixed to four consecutive points, the other *a posteriori* criteria were not used directly to reject a determination. When only one or two *a posteriori* criteria failed, we kept the determination choosing the nearest temperature interval for which the corresponding criteria stay as close as possible from the exclusion bounds fixed. The data with more than three independent criteria unfulfilled have been considered as unable to furnish a reliable palaeointensity estimate and thus have been excluded.

(i) z ratio :
The heating remanent magnetizations (HRM) (Calvo et al., 2002), acquired under a constant weak field during palaeointensity experiments lead to erroneous data. Hopefully, the field applied during the treatment is uniaxial along the Z axis of our specimens. Thus acquisition of HRM appears as a deviation of the demagnetization curve in the vertical plane towards the vertical axis direction. Such a phenomenon is observed in Fig. 2.4 comparing the orthogonal projections of a rejected sample and its sister specimen.
An "HRM check" is allowed using the ratio (Goguitchaichvili et al., 1999b) :

$$z = \frac{HRM_T}{NRM_T} \times 100$$

where HRM_T and NRM_T are the HRM created in the sample and the NRM left in the ChRM direction, at a given temperature. Similar ratios exists (e.g. R or R', Coe et al. (1984)) but the z ratio allows to monitor the evolution of alterations during treatment. Calculating this ratio supposes that one knows the ChRM direction, which requires demagnetization of a sister specimen before the palaeointensity experiment. For the interpretation, we defined the upper limit of the accepted temperature interval as the one preceding a z >20%. However, we extended the interval over this limit when the ratio NRM left/TRM gained did not change in the new interval. In this case some transformations are present but do not change the estimate. A limitation of the z ratio is that it depends on the angle between the ChRM and the applied field direction (direction of the HRM). The more this angle tends to 90°, the bigger the deviation. Unfortunately, the tray we used to place the specimens in the oven did not permit us to orient their ChRM at 90° to the applied field. However, the z we calculated is a minimum z, thus these steps had to be rejected. Another limitation of this criterion is that some unexpected fluctuations may appear at high temperature when the NRM left is too low. For this reason, we completed this approach by observing the evolution of the demagnetization on an equal area projection. In Fig. 2.4, the z-T curve of a rejected sample 163E (Temp06) is compared to one accepted sample 213E (Temp13).

(ii) Difference ratio :
The sliding pTRM checks we performed, allow us determine the reproducibility of the measurements. Commonly, the difference between repeated pTRM steps should be lower than 5%. However, the variation of pTRM is greater for low-

temperature steps, for which the pTRM acquired is rather small. Therefore, we used the difference ratio (DRAT) (Selkin and Tauxe, 2000), which normalizes the difference between repeated pTRM steps performed on the temperature interval used for the determination by the length of the corresponding NRM-pTRM segment. We fixed a maximum acceptable value of 10% for this criterion. However, this ratio reveals possible alterations on the estimate interval only, whereas physical and chemical alterations of the heated samples can appear as soon as the first demagnetization steps (Kosterov and Prévot, 1998). Therefore, we also monitored the lower temperature pTRM checks by determining the DRAT from ambient to maximum temperature of the interval used to estimate the palaeointensity. It is noteworthy that the sample 163E (Fig. 2.4), rejected because of its z ratio, has a DRAT of only 3%. Also five samples which give an estimate in Table 2.4 possess a DRAT >10%, thus these two alteration criteria are complementary.

(iii) f criterion :
A classical way of representing palaeointensity data is to use the Arai plot (Arai, 1963; Nagata et al., 1963). In this NRM left versus pTRM gained diagram, the slope of the least squares fit line through the data considered gives an estimate of the palaeofield strength. Thus criteria have to be defined to constrain the determination of this best fit line and to quantify the reliability of the palaeointensity estimates.

We already fixed the minimum number of successive points used for the determinations to four. The other criteria used is the NRM fraction f given by the ratio of the NRM in the temperature interval used to estimate the paleointensity to the total NRM (Coe et al., 1978). We consider that a value of 0.3 is the minimum NRM fraction for acceptable determination. Note that a quality factor q (Coe et al., 1978; Prévot et al., 1985) inferior to 5 can also indicate a determination of the palaeofield strength of lower quality. However, because q is not independent of f, this lead to reject the same samples in this study. Thus we did not use it as a rejection criterion.

(iv) Control on Zijderveld plots :
Because a straight line in the Arai plot can involve more than one component, we checked their existence in the orthogonal diagram of the NRM demagnetization. To complete this observational approach, we quantified the dispersion of the points regarding to the best fit line by the maximum angular deviation (MAD) (Kirschvink, 1980) and chose a maximum value of 10° for this criterion.
Another quality criterion is given by the angle α between the best fit line (anchored to the center of mass) and the vector average (anchored to the origin) of the selected data in the orthogonal plot. If the data correspond to the initial NRM, α should be inferior to say 10°, in the opposite, they are certainly biased by the presence of a secondary unknown component.

(v) High temperature pTRM tail test :
Unfortunately, 56% of the samples present a more or less pronounced curvature in their NRM-TRM diagrams and some specimens provide two acceptable estimates regarding the selection criteria. Because independence and additivity laws of partial thermoremanent magnetizations (Thellier, 1938) are violated for MD but maybe also for PSD grains, determination of the domain structure can be used to choose between the two acceptable palaeointensity estimates.
In case of thermally stable samples, a thermomagnetic criterion exist to determine the domain structure of ferrimagnetics (Bol'shakov and Scherbakova, 1979; Shcherbakova et al., 2000; Shcherbakov et al., 2001) :

$$A_{HT}(T_1,T_2) = \frac{tail_{HT}[pTRM(T_1,T_2)]}{pTRM(T_1,T_2)} \times 100$$

where $pTRM(T_1,T_2)$ is the pTRM gained between T1 and T2 during cooling from the Curie Temperature (Tc) in a 100μT field, $tail_{HT}[pTRM(T_1,T_2)$ is the part of the $pTRM_b(T_1,T_2)$ not demagnetized at T_1 ($pTRM(T_1,T_2)$ tail). The above authors inferred that for $A(T_1,T_2)$ <4%, the remanent carrier are predominantly SD grains, for 4% <$A(T_1,T_2)$ <(15-20)%, they behave as pseudo single domain (PSD) grains, and for $A_{HT}(T_1,T_2)$ >20% they are predominantly MD grains.
We thus decided to determine the coefficients $A(T_1,T_2)$ at increasing temperature intervals for one thermally stable sample per flow in order to determine the best temperature interval to estimate the paleointensity. Because the heatings were performed in air, we repeated the determination of the coefficient A(300,T_r) two times, at the beginning and at the end of the treatment, in order to monitor alterations appearing during the experiments. Unfortunately, the vibrating thermal magnetometer (VTM) we used broke before we could measure all the representative samples of each studied flow. The results available are reported in Table 2.2.

Even though all the flows have not been studied, the global trend observed confirms that with increasing temperature, the magnetic carrier behaviour is more SD-like (Carvallo et al., 2002; Shcherbakova et al., 2000). Thus, in cases where two coexisting palaeointensity estimates are allowed (n=5), the pTRM tail test favors acceptance of the higher temperature interval determination, as for sample 187E showed in Fig. 2.5.
(v) Low temperature pTRM tail test :
According to Fabian (2001), the pTRM tail is not a direct measure for a sample's tendency to yield a curved Arai plot. The common concave-up shape of MD Arai diagrams is rather well accounted for by the low temperature tail (Low-T tail) of each pTRM segment acquired during cooling from the Curie temperature ($pTRM(T_1,T_2)$. This Low-T tail is due to the grains with unblocking temperature less than blocking temperature. In order to compare the results obtained from the two tail tests and validate the choice of the temperature intervals for the interpretation, we

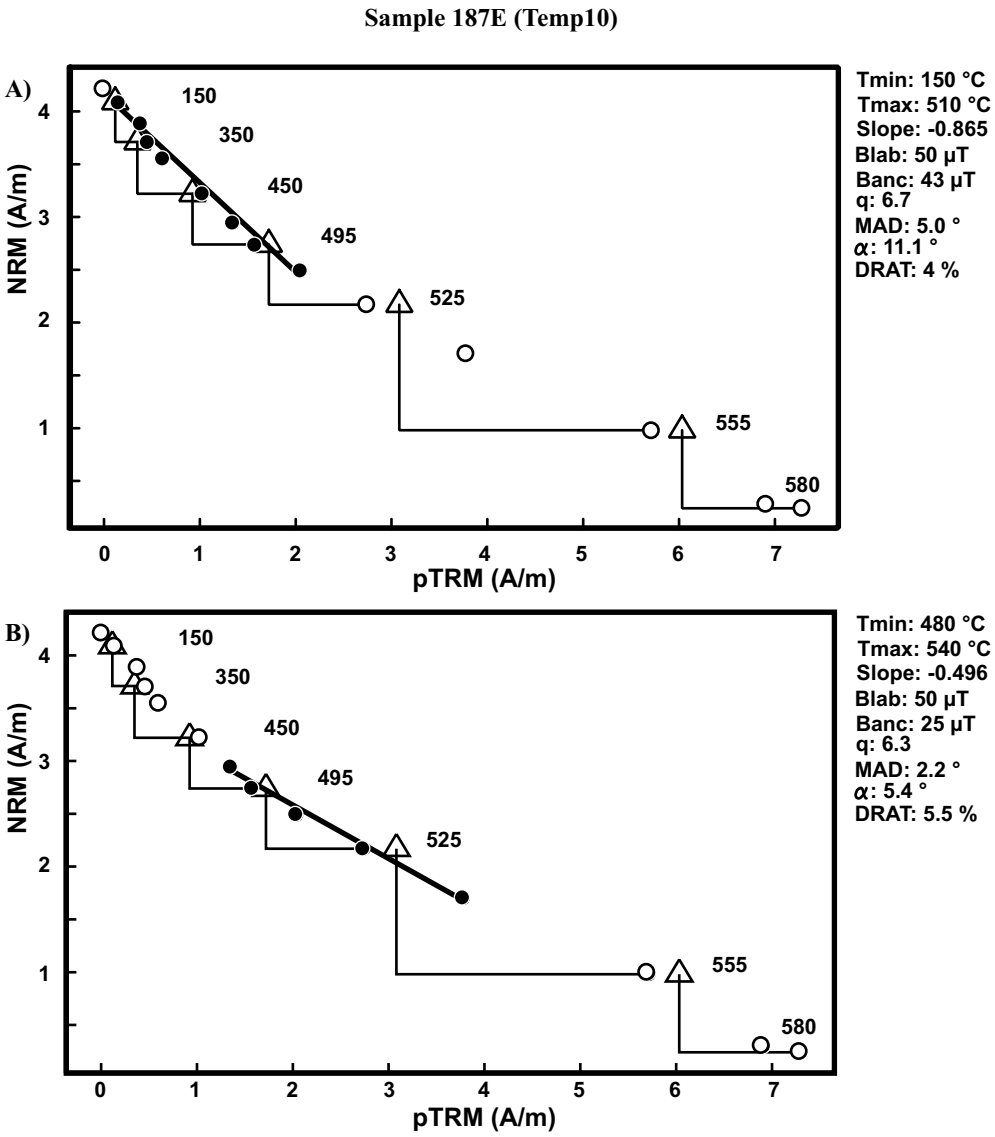

FIG. 2.5 – A) rejected estimate regarding the pTRM-tail test, B) Higher temperature determination for the same sample 187E (Temp10). Black (White) circles are the step used (not used) for the palaeointensity estimate, the triangles represent the pTRM checks.

TAB. 2.2 – High Temperature pTRM tail tests

Flow (sample)	A_{HT}	pTRM (300,T_r)	A_{HT}	pTRM (400,300)	A_{HT}	pTRM (500,400)	A_{HT}	pTRM (550,500)	A_{HT}	pTRM (300,T_r)*
Ruc10 (076B)	25.2	6.3	33.1	2.8	32.7	2.0	6.8	4.4	20.3	6.9
Ruc14 (101C)	20.8	7.9	29.8	5.1	13.3	18.8	4.0	35.7	17.3	8.6
Ruc15 (111C)	48.8	8.7	48.1	10.3	30.6	20.9	13.9	49.7	50.7	16.6
Ruc16 (117B)	17.0	5.6	34.6	3.1						
Tem1 (201B)	12.4	20.6	15.5	3.6	16.6	25.2	3.7	68.7	8.8	25.7
Tem6 (160B)	32.8	4.3	17.4	4.8	28.6	5.8	11.5	14.0	30.7	4.0
Tem10 (187B)	23.9	11.6	25.5	11.9	11.6	35.5	5.0	52.5	21.3	11.2
Tem10 (189B)	29.8	7.9	34.1	5.7	21.7	14.9	5.3	49.6	26.4	8.0
Tem13 (216C)	14.4	8.0	30.1	6.9	9.5	22.7	10.3	32.4	21.1	8.7
Rab10 (620D)	15.2	18.7	35.0	7.4	11.4	38.2	7.6	45.4	16.8	16.5

$A_{HT}(300,T_r)$, $A_{HT}(400,300)$, $A_{HT}(500,400)$, and $A_{HT}(550,500)$ are the coefficients defined by Shcherbakov et al. (2001). $pTRM(300,T_r)$, $pTRM(400,300)$, $pTRM(500,400)$, and $pTRM(550,500)$ are the corresponding pTRM intensities (in A.m^2). $A_{HT}(300,T_r)$* and $pTRM(300,T_r)$*are A_{HT}(300,T_r) and pTRM(300,T_r) repeated at the end of the treatment to control the thermal stability of the sample. For $A_{HT}(T_1,T_2)$ <4%, the remanent carrier are predominantly SD grains, for 4% <$A_{HT}(T_1,T_2)$ <(15-20)%, they present a pseudo single domain behaviour (PSD), and for $A_{HT}(T_1,T_2)$ >20% they are predominantly MD grains.

decided to evaluate the Low-T tail of some characteristic samples used during the palaeointensity experiment. For this aim, we define the coefficient :

$$A_{LT}(T_1,T_2) = \frac{tail_{LT}[pTRM(T_1,T_2)]}{pTRM(T_1,T_2)} \times 100$$

where $pTRM(T_1,T_2)$ is the pTRM gained between T_1 and T_2 in a 50μT field during cooling from the Curie temperature (580°C in practice) and $[pTRM_a(T_1,T_2)]$ the Low-T tail of $pTRM_a(T_1,T_2)$. This coefficient is analogous to the A_a coefficient defined by Shcherbakov et al. (2001) but the relation between the magnitude of the two tails is not clear. We can expect from Dunlop and Özdemir (2001) that A_{alt} is equal to A_a because the unblocking temperature distributions are almost symmetric for a given blocking temperature, but this may be quite different for hundred-degree temperature intervals. In the absence of a quantitative study, only the evolution of the A_{alt} ratio for increasing temperature intervals will be considered.

The A_{alt} coefficients for the (450,350) and (550,450) temperature intervals are reported in Table 2.3.

The main result is that A_{alt}(550,450) is always smaller than A_{alt}(450,350) ; thus the Low-T tail test again favors the higher temperature interval in case of two acceptable determinations. In order to estimate the alteration which may occur during the required preliminary heating up to the Curie temperature, the untreated samples 187D and 201C have been incorporated in the experiment. Comparing their results with the data from the corresponding sister samples 187E and 201E, we can observe that, even though these samples appear thermally stable (reversible k-T curves), A_{alt}(450,350) is greater for the sample used in the palaeointensity estimate and on the contrary A_{alt}(550,450) is greater for the "virgin" sample. Nonetheless, for the five samples that allowed two accep-

TAB. 2.3 – Low Temperature pTRM tail tests

Flow (sample)	A_{LT}(450,350)	%TRM$_{tot}$	A_{LT}(550,450)	%TRM$_{tot}$
Tem1 (201E)	18.30	3.32	2.21	72.03
Tem1 (201C)	10.07	6.31	2.37	73.88
Tem6 (161F)	3.84	11.69	1.52	42.88
Tem10 (187E)	12.95	6.98	2.31	65.13
Tem10 (187D)	8.81	7.15	2.38	54.82
Tem10 (189E)	12.92	5.05	2.31	57.93
Tem13 (213E)	6.86	7.58	2.34	31.75
Tem13 (214D)	23.49	7.73	3.86	18.81
Tem13 (215F)	3.57	8.11	3.36	22.62
Tem13 (217D)	5.65	6.52	2.86	43.40
Tem15 (229C)	12.34	9.35	5.07	59.77
Tem15 (230D)	7.32	8.21	3.07	43.19
Tem16 (237E)	8.21	9.28	2.00	74.13
Tem18 (251C)	15.72	8.95	2.94	64.60

A_{LT}(450,350) and *A_{LT}(550,450)* are coefficients analogous to A_a defined by Shcherbakov et al. (2001). *%TRM$_{tot}$* is the percentage of the corresponding pTRM on the total TRM (pTRM(580,T_r)).

table interpretations, we choose the higher temperature interval, which determination is more coherent with the other samples from the same flow. It is also noteworthy that the A_{alt} ratio are systematically almost two times smaller than the corresponding A_b coefficients, which are supposed to be two times smaller again than the A_a coefficients (Shcherbakov et al., 2001).

2.4.3 Palaeointensity results

Out of the 402 samples from the Mont des Ruches, Mont des Tempêtes, and Mont Rabouillère sections, 102 have been choose using *a priori* criteria. After selection following *a posteriori* criteria, 49 samples furnish a technically acceptable determination (Table 2.4).

The quality factor q varies from 1.6 to 54.3 with a mean value of 12.1 for estimates made on a mean of 7 points. However, some α angles are relatively large, which could be due to an overprint of viscous origin, even though the samples are not strongly viscous, or to a secondary component acquired during the treatment, as shown by the angle β between the ChRMs of the sample and its sister specimen. Altough secondary HRM exists, we consider its effect negligible on the determination, considering the z criterion, the linearity of the Arai diagram and the evolution of the demagnetization in an equal area projection. Therefore, as evidenced by the MAD, which is the most widely satisfied *a posteriori* criterion, we are confident about these interpretations. Moreover, as is commonly done in palaeointensity studies, we distinguished two types of determination : class A for the samples which passed successfully all the criteria and class B for those in which one to three criteria were unfulfilled. However, as observed with flows Rab12 or Temp6, there is no single relation between the field estimate and its classification. Thus, the interpretations made with a few unsatisfied

TAB. 2.4 – Palaeointensity determinations

Flow	Spl	Grade	Fe±σFe	ΔT	n	f	g	q	MAD	α	β	DRAT	Fe±s.d.	VDM
Ruc14	101F	B	38.6±1.1	20-480	8	0.37	0.81	10.8	4.1	(15.7)	12.9	2.7	37.2±2.7	5.18
	102D	B	39.6±1.0	150-495	7	0.39	0.80	12.6	2.5	(12.2)	10.5	2.4		
	103D	B	33.5±1.8	300-495	6	0.33	0.75	4.5	2.2	(12.1)	5.9	8.1		
Ruc15	108C	B	43.0±2.9	20-400	5	(0.25)	0.73	2.7	4.2	8.8	7.8	0.4	40.0±4.3	5.69
	110E	B	37.8±1.1	350-540	8	0.37	0.81	10.2	4.4	(19.8)	16.7	4.1		
	111F	B	45.0±1.1	20-400	6	(0.23)	0.79	4.9	4.6	11.2	10.8	1.7		
	114D	B	34.2±0.9	150-480	6	0.53	0.79	15.9	1.8	(16.4)	11.0	5.2		
Ruc16	115C	B	34.0±1.4	20-400	5	0.32	0.72	5.5	6.2	(11.7)	7.9	0.7	34.8±0.9	4.69
	116C	B	34.2±2.6	150-400	4	(0.22)	0.58	1.6	3.5	7.9	5.7	0.4		
	117F	B	34.8±2.2	150-400	5	(0.23)	0.62	2.2	2.2	7.5	3.0	4.1		
	118F	B	36.3±1.3	20-400	5	0.32	0.68	6.2	1.7	(16.6)	14.8	3.5		
Temp1	201E	B	55.9±4.9	150-480	7	0.31	0.82	2.9	6.1	(16.9)	13.2	1.8	61.0±3.6	9.47
	203E	B	62.9±2.6	20-495	8	0.42	0.84	8.6	3.8	(11.0)	9.8	7.3		
	205E	B	64.1±3.2	150-510	8	0.35	0.82	5.7	4.7	9.9	6.6	(13.1)		
Temp6	160E	B	21.4±0.5	20-500	9	0.57	0.83	21.4	9.4	(14.9)	6.7	6.0	20.1±1.7	2.78
	161F	A	21.2±0.9	150-525	9	0.53	0.85	10.6	3.6	6.0	2.8	4.0		
	162E	B	17.8±0.5	20-525	10	0.52	0.80	16.7	(10.6)	(14.0)	6.1	5.5		
Temp10	187E	A	24.8±1.0	480-540	5	0.35	0.71	6.3	2.2	5.4	2.5	5.5	25.0±1.7	4.23
	188E	A	27.2±1.4	510-555	4	0.47	0.53	4.8	4.1	4.7	3.2	5.1		
	189E	A	23.0±0.5	525-570	4	0.66	0.62	17.5	3.4	1.1	6.3	6.1		
Temp13	213E	A	32.8±1.0	525-580	5	0.41	0.72	9.8	2.2	0.9	2.8	2.0	39.7±5.7	7.18
	214D	A	34.7±1.7	20-555	12	0.48	0.85	8.1	3.5	5.8	6.5	2.5		
	215F	A	36.6±1.5	20-555	12	0.58	0.85	12.4	5.1	2.2	4.6	2.4		
	216F	A	40.0±1.9	20-500	9	0.52	0.85	9.1	7.8	8.5	4.0	5.4		
	217D	A	45.9±3.3	20-555	12	0.74	0.85	8.7	1.9	3.3	2.7	3.2		
	218C	A	48.3±3.1	20-555	12	0.50	0.82	6.3	3.5	6.4	7.3	5.2		
Temp15	228D	A	34.3±0.8	480-580	8	0.76	0.76	25.3	3.1	1.8	2.6	7.7	36.6±1.6	5.89
	229C	B	38.2±1.7	150-495	7	0.30	0.82	5.4	7.2	(17.5)	13.4	2.1		
	230D	A	37.1±0.4	480-580	6	0.78	0.71	54.3	1.6	0.3	5.1	5.8		
Temp16	232D	A	35.2±0.8	20-540	11	0.54	0.87	20.8	2.8	8.0	1.0	4.2	30.5±3.8	4.95
	233C	B	30.4±0.4	350-540	8	0.69	0.84	40.5	2.3	2.5	1.9	(10.7)		
	234E	B	24.6±0.4	300-540	9	0.73	0.84	35.3	3.4	1.3	3.0	(15.1)		
	237E	A	31.6±0.6	350-540	6	0.54	0.66	18.1	2.5	1.5	4.3	2.3		
Temp17	238D	B	48.4±2.5	150-495	7	(0.28)	0.82	4.5	3.4	(14.7)	11.5	5.7	51.8±6.8	8.62
	239D	B	58.8±2.1	150-480	6	(0.25)	0.78	5.4	5.1	(19.4)	14.0	(10.1)		
	240E	B	39.2±0.9	150-500	8	0.40	0.79	13.1	5.1	(11.1)	5.7	5.3		
	241D	B	56.6±1.1	150-495	7	0.36	0.82	15.1	3.3	(12.5)	7.2	6.3		
	243E	B	57.3±3.5	150-450	5	(0.23)	0.73	2.7	4.9	(26.3)	27.5	6.6		
	244E	B	50.3±0.9	150-510	8	0.35	0.84	16.0	5.0	(10.1)	5.2	2.2		
Temp18	245D	A	65.4±2.1	20-510	9	0.44	0.86	11.8	4.2	8.2	2.6	5.5	55.0±6.9	9.30
	246C	B	43.9±0.8	300-495	6	(0.27)	0.78	11.5	2.7	(18.2)	10.1	7.6		
	248D	B	51.6±1.8	150-500	8	(0.29)	0.82	7.2	5.7	(13.0)	10.0	4.2		
	249D	A	53.0±4.2	20-400	5	0.36	0.71	3.2	2.6	7.3	1.9	0.1		
	251C	A	54.8±1.5	150-525	9	0.51	0.85	15.8	3.2	4.9	3.9	4.1		
	252D	B	61.2±1.6	20-495	8	0.52	0.81	16.0	3.0	(10.1)	6.4	(13.8)		
Rab12	628B	A	35.5±0.6	225-500	7	0.53	0.77	24.4	3.3	5.7	4.3	5.2	37.7±2.4	5.76
	629B	A	38.0±2.0	150-480	7	0.54	0.75	7.7	2.1	8.1	5.2	7.1		
	630C	A	41.4±1.1	150-555	11	0.57	0.72	7.8	2.2	5.8	6.7	1.5		
	631C	B	35.8±1.6	150-450	5	0.30	0.68	4.5	5.3	(16.1)	11.9	3.3		

Grade : classification based on the number of *a posteriori* criteria checked (A all, B except at least one evidenced with parenthesis) ; $Fe \pm \sigma Fe$: individual palaeofield strength determination (in μT) and standard error associated (Prévot et al., 1985) ; ΔT : temperature interval of determination ; n : number of consecutive points used for the determination ; f, g and q : fraction of NRM, gap factor and quality factor, respectively (Coe et al., 1978; Prévot et al., 1985) ; MAD : maximum angular deviation ; α : angle between ChRM and origin ; β : angle between ChRMs of the sample and its sister specimen (Plenier et al., 2002) ; $DRAT$: difference ratio (Selkin and Tauxe, 2000) ; $\bar{Fe} \pm s.d.$: mean palaeofield strength of the flow and the standard deviation associated ; VDM : virtual dipole moment ($*10^{22} Am^2$).

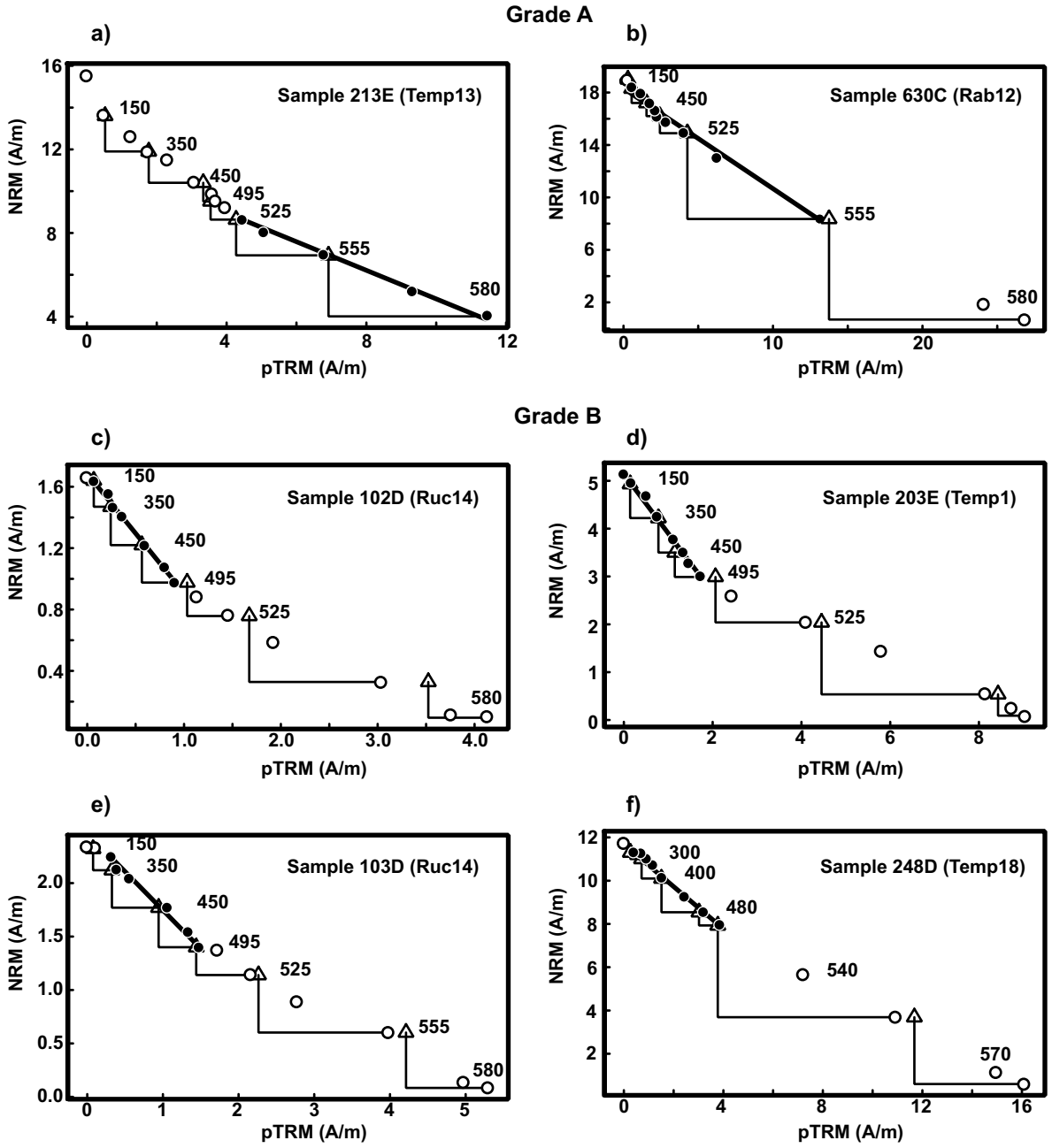

FIG. 2.6 – Characteristic examples of palaeointensity estimates from this study. a) and b) correspond to grade A estimates, c), d), e) and f) to grade B estimates. Black (White) circles are the step used (not used) for the palaeointensity estimate, the triangles represent the pTRM checks.

a posteriori criteria we can also consider to be reliable. Fig. 2.6 shows some characteristic examples of palaeointensity determinations.

Additionally, in Table 2.4, the mean palaeofield strength, with its associated standard deviation is given for each flow. The three consecutive Mont des Ruches flows (Ruc14, 15, and 16) present a well defined palaeointensity on the order of 35-40 μT. This value is comparable with the only reliable flow from the Mont Rabouillère section (Rab12) and with the flows Temp13 and Temp15 of the Mont des Tempêtes. For the last section we also observe three particularly high values around 50-60 μT (Temp 1, 17 and 18) and two well defined lower field strengths of only 20.1 and 25.0$\pm$1.7 μT (Temp6 and 10). These observations and the 15% or less standard deviation of the estimates, make us quite confident about the reliability of these estimations.

In a previous study (Plenier et al., 2002), we performed a quantitative bootstrap test for a common mean on successive magnetic directions in order to identify non-independent records. We concluded that the Ruc14-Ruc15 and temp14-temp15 flows may represent two contemporaneous records of the palaeofield (Table 2.1). Because the palaeomagnetic field may remain constant for a relatively long time (Love, 2000), however, we will nevertheless consider each of the 12 reliable palaeointensity estimates as distinct records.

Concerning the samples 101F, 111F, 201E, 160E, 161F and 229C, for which pTRM tail tests were performed, we decided to keep the lower rather than the higher temperature interval estimates because the latter was sometimes impossible to define owing to alteration of the pTRM spectra (101F, 160E, 201E and 229C) or meaningless compared to the other determinations from the same flow (111F, 161F).

2.5 Discussion

2.5.1 Toward an improvement of palaeointensity determination

Because of the strict conditions imposed by the commonly used palaeointensity determination method of Thellier and Thellier (1959), numerous checks are needed to ensure reliable estimates. For this reason, palaeointensity experiments are time consuming and at the end many samples do not furnish reliable determinations. Consequently, the number of reliable estimates is very low and studies dealing with palaeointensity determinations are relatively rare. Then, effective selection followed by careful palaeointensity determination method are desirable to increase the productivity of the experiments and largely implement the number of palaeointensity estimates in the databases.

However, no ideal selection criteria exist to select suitable specimens and flows for palaeointensity experiments. For example, Shcherbakov et al. (2001) proposed to use a pTRM tail check as a systematic procedure before the experiments to discriminate the samples with

MD grains. Since $A_{AF}(300, T_r)$ is comparable to $A_b(300, T_r)$, we tried to apply this selection procedure to the specimens for which we performed pTRM tail tests to check its reliability. However, all the samples furnishing suitable estimates in this study will not have been selected if this selection was made (c.f. Table 2.2). Thus,we do not recommend to use the thermomagnetic criterion for selection but rather in a case to case basis to define the best temperature interval for thermally stable specimens exhibiting two slopes in the NRM/TRM diagram. For the selection based on k-T curve shapes, the temperature intervals used for the estimates (c.f. Table 2.4) can change at the flow scale (flow Temp13 or Temp15) without important deviation in the palaeofield strength. Therefore, the thermal behaviour of the samples varies within a flow and this criterion applied to a supposedly representative sample is not totally effective.

A study of each successful sample, at the end of the palaeofield strength determination procedure, up to the maximum temperature reached for the palaeointensity estimate would be more interesting. Whatever the numerous *a priori* precautions we took in this study, only 48% of the selected samples gave a reliable estimate. Thus in the absence of an easy to determine and convenient *a priori* criteria, it is preferable to reduce the preliminary experiments to the determination of the viscosity index, which is an already rapid and reliable way to discriminate the specimens disturbed by a viscous secondary component, followed by a directional analysis, needed for careful palaeointensity estimates and giving enough information to discard possibly problematic flows because of large NRM scatter, poor demagnetization curves and so on.

Concerning the determination procedure itself, some modifications of the Thellier's method have been proposed recently (Calvo et al., 2002; Riisager and Riisager, 2001). They include an additional heating at each demagnetization step in order to control the HRM creation and/or a "pTRM tail check". However, the lack of suitable selection criteria lead to more failure of the palaeointensity experiment and these more time consuming procedures are consequently not helpful for systematic studies. Orienting the samples so that their ChRM is perpendicular to the direction of the applied field is less time consuming and sufficient to check for possible HRM creation. Likewise, at the end of the treatment, complementary experiments like k-T curve shape determination, extended Thellier's method (Fabian, 2001) for thermally stable samples or "pTRM tail checks" can be done to ensure the quality and sharpen the reliable estimates, but such supplementary processes must concern the acceptable samples only. Thus, good determinations do not necessarily need supplementary heatings nor burdensome procedures to be performed; this should be limited to the problematic samples only. Reducing the selection and placing the control procedures at the end of the treatment is thus a way to perform reliable palaeointensity estimates

more quickly, without lowering the quality of the determinations.

2.5.2 Comparison with previous palaeointensity results

Five Oligocene flows from the Ile Haute section (49.4°S, 69.9°E) have been processed for palaeointensity study (Derder et al., 1990). Of the 24 samples analysed, 11 yielded a determination, but only one flow provided more than three estimates of the palaeofield strength. Moreover, the uncertainty of the mean palaeointensity is equal to 36% and consequently, these data cannot be considered as reliable. The 12 distinct mean flow estimates presented in this paper are thus the only reliable determinations available for the Kerguelen Archipelago.

However, data well distributed on the Earth's surface are needed to provide a correct idea of the palaeomagnetic field behaviour. It is then important to pool the Oligocene Kerguelen results with other reliable determinations already achieved. For this aim, we used the updated IAGA 2002 palaeointensity database available at the following adress :

ftp ://www.isteem/pub/paleointdb/

This database presents estimates obtained with different quality determinations. However, inclusion of lower quality data leads to higher average values of the geomagnetic field (Juarez and Tauxe, 2000; Goguitchaichvili et al., 1999a), thus a selection using identical criteria to those used in this study is needed before we can combine them meaningfully with the Kerguelen results. For this reason we discarded estimates based on intermediate polarity flows, obtained with other determination methods than the Thellier and Thellier (1959) associated with pTRM checks, presenting less than 3 individual samples from the same unit (except for basaltic submarine glasses) and a standard deviation of the mean $\geq$20%. Application of these drastic selection criteria led to the rejection of 660 determinations out of the 910 estimates contained in the database between 0.3 and 50 Ma (Fig. 2.7a). Then we sharpened the selection to a time window between 20 and 40 Ma, which resulted in 11 suitable estimates among the 74 initial extended Oligocene records of the data base (Fig. 2.7a)).

In order to compare the Kerguelen determinations with the selected estimates issued from various locations and recording different time, we calculated the virtual dipole moment (VDM) (see e.g. Tauxe (1998)), which corresponds to the moment of a dipole field producing the estimated palaeointensity at the considered palaeolatitude. Results of the calculations are reported in Table 2.4 and the 12 suitable determinations are plotted in Fig. 2.7.

Even though we performed careful estimates in order to avoid any possible MD effects in the interpretations, which could lead to systematic higher determinations, the arithmetic mean obtained with the Kerguelen data, $6.15 \pm 2.1\ 10^{22} Am^2$, is definitely higher than the other Oligocene estimates already achieved (Goguitchaichvili

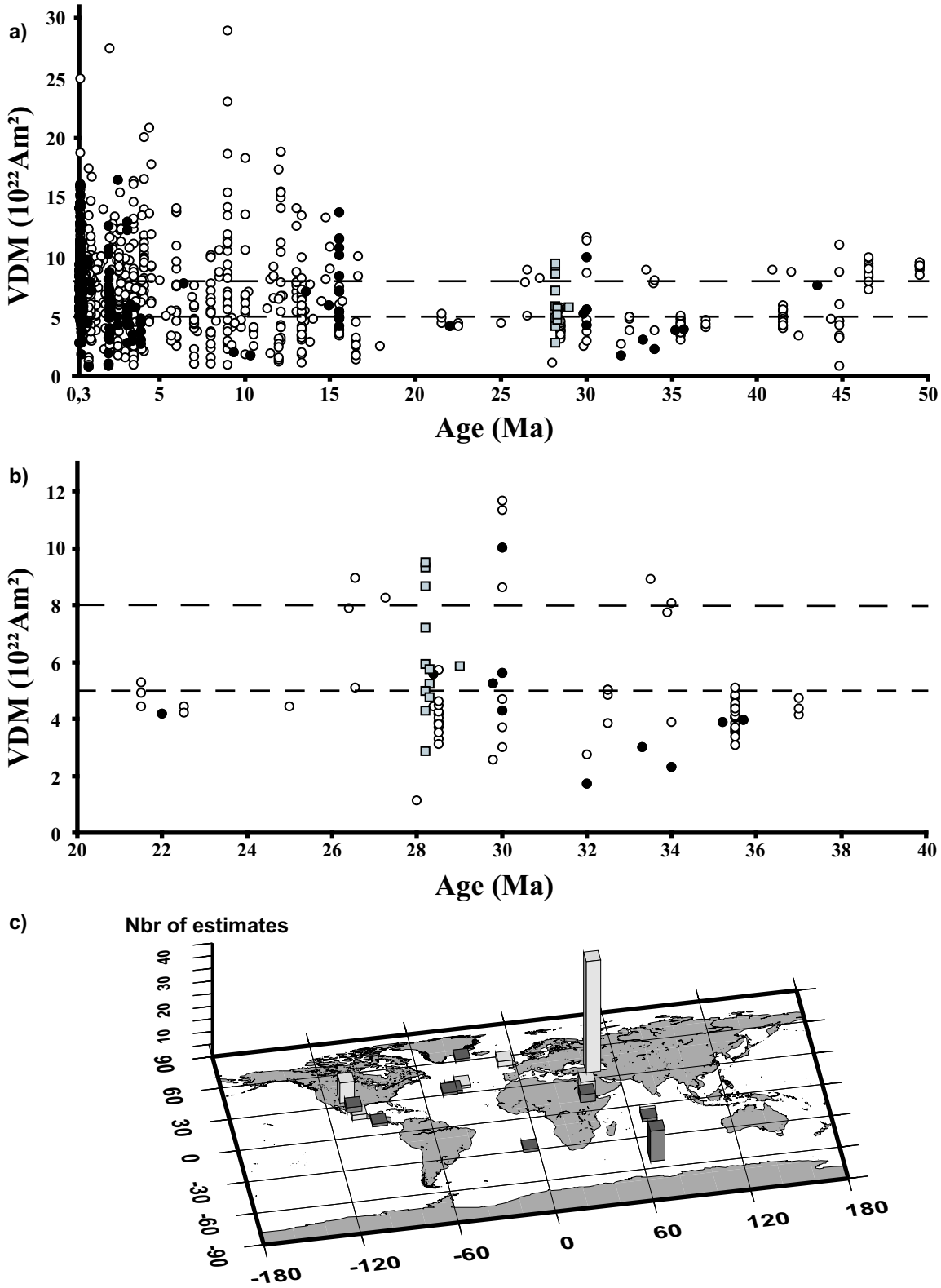

FIG. 2.7 – a) open(black) circles are (selected) VDMs from the IAGA 2002 updated data-set between 0.3 and 50 Ma. Gray squares are the data from this study which pass the selection criteria. Long (short) dashed line indicates the 0-0.3 Ma (0.3-300 Ma) mean VDM value. b) same as a) but for the extended Oligocene (20-40 Ma) time window. c) Location of the palaeointensity records between 20 and 40 Ma. Light(dark) gray column are (selected) estimates from the IAGA 2002 updated data-set for the time window considered.

et al., 2001; Riisager, 1999; Juarez et al., 1998). Including Kerguelen determinations leads to an increase of the Oligocene mean VDM from 4.1±0.5 to 5.4±2.3 $10^{22} Am^2$. The new Oligocene mean VDM is closer to the mean VDM estimated for the 0.3 and 5 Ma interval (Juarez and Tauxe, 2000) and higher than the mean VDM defined between 0.3 and 300 Ma (Fig. 2.7). Thus these selected Oligocene estimates favor a relatively stable field between 0.3 and 40 Ma and reinforce the idea of an exceptionally high recent geomagnetic field strength. However, the lack of good palaeointensity data didn't allow us to go further in our interpretation. As illustrated in Fig. 2.7 c), the Oligocene data do not uniformly cover the Earth's surface even though the Kerguelen results equilize the number of estimates available for each hemisphere. More reliable determinations are needed to better constrain the evolution of the palaeofield with geological time. It is important to note that the Kerguelen results represent half of the reliable palaeointensity estimates available for the Oligocene, which could lead to a bias towards higher values. Moreover, only 3 extended Oligocene determinations are from normal polarity flows. Thus even if the 12 new estimates are supposed to be independent, the Oligocene palaeomagnetic field may not be sufficiently time-averaged.

2.6 Conclusion

We carried out the results of a palaeointensity estimate study on three Oligocene (24-30 Ma) volcanic sections from the Kerguelen Archipelago (southern Indian Ocean). It complements the palaeosecular variation directional study already achieved on these Mont des Ruches, Mont des Tempêtes, and Mont Rabouillère sections (Plenier et al., 2002). Out of the 57 studied units, we considered 32 suitable for palaeofield strength determination experiments when at least three of their samples pass the following selection criteria : angle between NRM and ChRM $\leq 15°$ (or secondary component quickly demagnetized), NRM dispersion not too large, viscosity index <5 % (10% for transitional polarity flows), stable susceptibility at room temperature after each demagnetization step of a sister sample and reversible susceptibility in temperature curves. After preliminary experiments, we studied all samples from 12 favorable flows. We considered only the determinations made with at least 4 successive steps, a z ratio (Goguitchaichvili et al., 1999b) $\leq$ 15%, a DRAT (Selkin and Tauxe, 2000) $\leq$ 10%, f factors (Coe et al., 1978) $\geq$ 0.3, a MAD $\leq 10°$ (Kirschvink, 1980) and an angle α between the best fit line and the vector average $\leq 10°$ to be of good technical quality. In cases of two acceptable estimates, pTRM tail tests were used to choose the temperature interval corresponding to the more SD like behaviour. This careful interpretation of the data leads to 49 reliable estimates. The VDMs calculated for the 12 flows vary from 2.78 to 9.47 with an arithmetic mean value of 6.15±2.1 $10^{22} Am^2$. This study gives the first reliable palaeointensity estimates

from the Kerguelen Archipelago and significantly increases the number of Oligocene data of comparable quality. The new Oligocene mean VDM calculated, 5.4±2.3 $10^{22} Am^2$, is very close to the 0.3-5 Ma value of Juarez and Tauxe (2000) (5.5±2.4 $10^{22} Am^2$), and suggests little evolution of the geomagnetic field between 0.3 and at least 40 Ma. Thus the present intensity of the field (8 $10^{22} Am^2$) is confirmed to be exceptionally high. However, the lack of reliable data limits the interpretation and we discuss practical solutions to speed the selection of suitable samples for careful determination procedures in order to facilitate systematic studies and increase existing palaeointensity databases with high-quality estimates.

2.7 Acknowledgments

We are grateful to the "Institut Polaire Paul Emile Victor" for providing all transport facilities and for the support of this project. Special thanks to Alain Lamalle, Roland Pagny and all our field friends. We thanks Michel Prévot for scientific discussions, Thierry Poidras and Liliane Faynot for technical help during k-T, VTM and palaeointensity experiments. This work was partially supported by CNRS-INSU programme intérieur Terre.

Bibliographie

Arai, Y., 1963. Secular variation in the intensity of the past geomagnetic field. Master's thesis, Univ. of Tokyo, Tokyo, Japan.

Bol'shakov, A., Scherbakova, V., 1979. Thermomagnetic criterion for determining the domain structure of ferrimagnetics. Izvest. Earth Phys. 15, 111–116.

Calvo, M., Prévot, M., Perrin, M., Riisager, J., 2002. Investigating the reasons for the failure of palaeointensity experiments : A study on historical lava flows from Mt. Etna (Italy). Geophys. J. Int. 149 (1), 44–63.

Carvallo, C., Camps, P., Ruffet, G., Henry, B., Poidras, T., 2002. Mono lake or Laschamp geomagnetic event recorded from lava flows in Amsterdam Island (southeastern Indian Ocean). Geophys. J. Int. submitted.

Coe, R., 1967a. The determination of paleointensities of the earth's magnetic field with emphasis on mechanisms which could cause non-ideal behaviour in thellier's method. J. Geomag. Geoelect. 19, 157–179.

Coe, R., 1967b. Paleointensities of the earth's magnetic field determined from tertiary and quaternary rocks. J. Geophys. Res. 72, 3247–3262.

Coe, R., Grommé, S., Mankinen, E., 1978. Geomagnetic paleointensities from radiocarbon-dated lava flows on Hawaii and the question of the Pacific nondipole low. J. Geophys. Res. 83, 1740–1756.

Coe, R., Grommé, S., Mankinen, E., 1984. Geomagnetic paleointensities from excursion sequences in lavas on oahu, hawaii. J.Geophys.Res. 89, 1059–1069.

Derder, M., Plessard, C., Daly, L., 1990. Mise en évidence d'une transition de polarité du champ magnétique terrestre dans les basaltes miocènes des îles Kerguelen. C. R. Acad. Sci. Paris 310 (II), 1401–1407.

Doucet, S., Weis, D., Scoates, J., Nicolaysen, K., Frey, F., Giret, A., 2002. The depleted mantle component in Kerguelen Archipelago basalts : Petrogenesis of tholeiitic-transitional basalts from the Loranchet Peninsula. J. Petrol. 43 (7), 1341–1366.

Dunlop, D., Özdemir, O., 2001. Beyond Néel's theories : thermal demagnetization of narrow-band partial thermoremanent magnetizations. Phys. Earth Planet. Int. 126, 43–57.

Fabian, K., 2001. A theoritical treatment of paleointensity determination experiments on rocks containing pseudo-single or multi domain magnetic particles. Earth Planet. Sci. Letts. 188, 45–58.

Giret, A., 1990. Typology, evolution, and origin of the Kerguelen plutonic series, Indian ocean : a review. Geol. J. 25, 239–247.

Goguitchaichvili, A., Alva-Valdivia, L., Urrutia-Fucugauchi, J., Zesati, C., Caballero, C., 2001. Paleomagnetic and paleointensity study of Oligocene volcanic rocks from Chihuahua (northern Mexico. Phys. Earth Planet. Int. 124, 223–236.

Goguitchaichvili, A., Prévot, M., Camps, P., 1999a. No evidence for strong fields during the R3-N3 icelandic geomagnetic reversal. Earth Planet. Sci. Lett. 167, 15–34.

Goguitchaichvili, A., Prévot, M., Thompson, J., Roberts, N., 1999b. An attempt to determine the absolute geomagnetic field intensity in Southwestern Iceland during the Gauss-Matuyama reversal. Phys. Earth Planet. Int. 115, 53–66.

Jacobs, J., 1994. Reversals of the Earth's magnetic field, Cambridge University Press Edition. the Press Syndicate of the University of Cambridge.

Juarez, M., Tauxe, L., 2000. The intensity of the time-averaged geomagnetic field : the last 5Myr. Earth Planet. Sci. Lett. 175, 169–180.

Juarez, M., Tauxe, L., Gee, J., Pick, T., 1998. The intensity of the Earth's magnetic field over the past 160 million years. Nature 394, 878–881.

Kirschvink, J., 1980. The least-squares line and plane and the analysis of paleomagnetic data. Geophys. J. R. Astr. Soc. 62, 699–718.

Kosterov, A., Prévot, M., 1998. Possible mechanism causing failure of the Thellier paleointensity experiments in some basalts. Geophys. J. Int. 134, 554–572.

Levi, S., 1977. The effect of magnetite particle size on paleointensity determinations of the geomagnetic field. Phys. Earth Planet. Int. 13, 245–259.

Love, J., 2000. Statistical assessment of preferred transitional vgp longitudes based on paleomagnetic volcanic data. Geophys. J. Int. 140, 211–221.

Merrill, R., McFadden, P., 1999. Geomagnetic polarity transitions. Rev. Geophys. 37 (2), 201–226.

Nagata, T., Arai, Y., Momose, K., 1963. Secular variation of the geomagnetic total force during the last 5,000 years. J. Geophys. Res. 68, 5277–5282.

Nicolaysen, K., Frey, F., Hodges, K., Weis, D., Giret, A., 2000. $^{40}Ar/^{39}Ar$ geochronology of flood basalts from the Kerguelen Archipelago, southern Indian Ocean : implications for Cenozoic eruption rates of the Kerguelen plume. Earth Planet. Sci. Letts. 174, 313–328.

Perrin, M., 1998. Paleointensity determination, magnetic domain structure, and selection criteria. J. Geophys. Res. 103, 30591–30600.

Perrin, M., Schnepp, E., Shcherbakov, V., 1998. Paleointensity database updated. EOS 79 (16), 198.

Perrin, M., Shcherbakov, V., 1997. Paleointensity of the Earth's magnetic field for the past 400 ma : Evidence for a dipole structure during the mesozoic low. J. Geomag. Geoelect. 49, 601–614.

Plenier, G., Camps, P., Henry, B., Nicolaysen, K., 2002. Palaeomagnetic study of

Oligocene (24-30 Ma) lava flows from the Kerguelen Archipelago (southern Indian Ocean) : directional analysis and magnetostratigraphy. Phys. Earth Planet. Int. 133, 127–146.

Prévot, M., 1981. Some aspects of magnetic viscosity on subaerial and submarine volcanic rocks. Geophys. J. R. Astr. Soc. 66, 169–192.

Prévot, M., Mankinen, E., Coe, R., Grommé, C., 1985. The Steens Mountain (Oregon) geomagnetic polarity transition. 2. field intensity variations and discussion of reversal models. J. Geophys. Res. 90, 10417–10448.

Riisager, J., 1999. Variation en direction et en intensité du champ magnétique terrestre a la fin du Mesozoique et au Cenozoique. Ph.D. thesis, University of Montpellier, 168 pp.

Riisager, P., Riisager, J., 2001. Detecting multidomain magnetic grains in Thellier palaeointensity experiments. Phys. Earth Planet. Int. 125, 111–117.

Selkin, P., Tauxe, L., 2000. Long-term variations in palaeointensity. Phil. Trans. R. Soc. Lond. 358 (A), 1065–1088.

Shcherbakov, V., Shcherbakova, V., Vinogradov, Y., Heider, F., 2001. Thermal stability of pTRMs created from different magnetic states. Phys. Earth Planet. Int. 126, 59–73.

Shcherbakova, V., Shcherbakov, V., Heider, F., 2000. Properties of partial thermoremanent magnetization in pseudosingle domain and multidomain magnetite grains. J. Geophys. Res. 105 (B1), 767–781.

Tanaka, H., Kono, M., 1984. Analysis of the thelliers' method of paleointensity determination, 2. applicability to high and low magnetic fields. J. Geomag. Geoelect. 36, 285–297.

Tanaka, H., Kono, M., Uchimura, H., 1995. Some global features of paleointensity in geological time. Geophys. J. Int. 120, 97–102.

Tauxe, L., 1998. Paleomagnetic Principles and Practice. Kluwer, Dordrecht.

Thellier, E., 1938. Sur l'aimantation des terres cuites et ses applications géophysiques. Ann. Inst. Physique du Globe, Univ. Paris 16, 157–302.

Thellier, E., Thellier, O., 1944. Recherches géomagnétiques sur des coulées volcaniques d'Auvergne. Ann. Geophys. 1, 37–52.

Thellier, E., Thellier, O., 1959. Sur l'intensité du champ magnétique terrestre dans le passé historique et géologique. Ann. Geophys. 15, 285–376.

Weis, D., Damasceno, D., Frey, F., Nicolaysen, K., Giret, A., 1998. Temporal isotopic variations in the Kerguelen plume : evidence from the Kerguelen Archipelago. Miner. Mag. 62A, 1643–1644.

Weis, D., Giret, A., 1994. Kerguelen plutonic complexes : Sr, nd, pb isotopic study and inferences about their sources, age and geodynamic setting. Mem. Soc. Géol. Fr. 166, 47–59.

Yang, H.-J., Frey, F., Weis, D., Giret, A., Pyle, D., Michon, G., 1998. Petrogenesis of the flood basalts forming the northern

Kerguelen Archipelago : Implications for the Kerguelen plume. J. Petrol. 39 (4), 711–748.

Deuxième partie

Etude de la fabrique magnétique

Avant propos

Pour les roches volcaniques, la fabrique magnétique, *i.e.* l'anisotropie de susceptibilité magnétique (ASM), est relativement faible, presque comparable à celle obtenue pour les sédiments, malgré une susceptibilité magnétique élevée. Elle est cependant intimement liée aux forces s'exerçant durant leur emplacement (Tarling and Hrouda, 1993; Borradaile and Henry, 1997; Merle, 1998; Bouchez, 2000), que ce soit de façon directe (anisotropie de forme), avec l'axe d'allongement des minéraux magnétiques dans la direction de l'écoulement (Hrouda, 1982; Cañón Tapia et al., 1995; Morris, 2000), ou de façon indirecte (anisotropie de distribution et phénomènes d'interaction), avec une cristallisation intersticielle tardive autour de phases préexistantes orientées dans la direction de l'écoulement (Hargraves et al., 1991; Rochette et al., 1992, 1999; Ferré et al., 2002). Par conséquent, bien qu'elle nécessite des appareils très sensibles et précis, la mesure de l'ASM peut théoriquement permettre de retrouver la direction et même le sens de mise en place du corps étudié (Knight and Walker, 1988; Cañón Tapia et al., 1997; Tauxe et al., 1998; Geoffroy et al., 2002).

Le premier chapitre de cette partie rapporte les résultats d'une étude (soumise au *J. Volcanol. Geotherm. Res.*) de la fabrique magnétique d'une section située à proximité de Port Jeanne d'Arc, au Sud Est de l'archipel de Kerguelen (cf. Figure 2.8). Cette étude

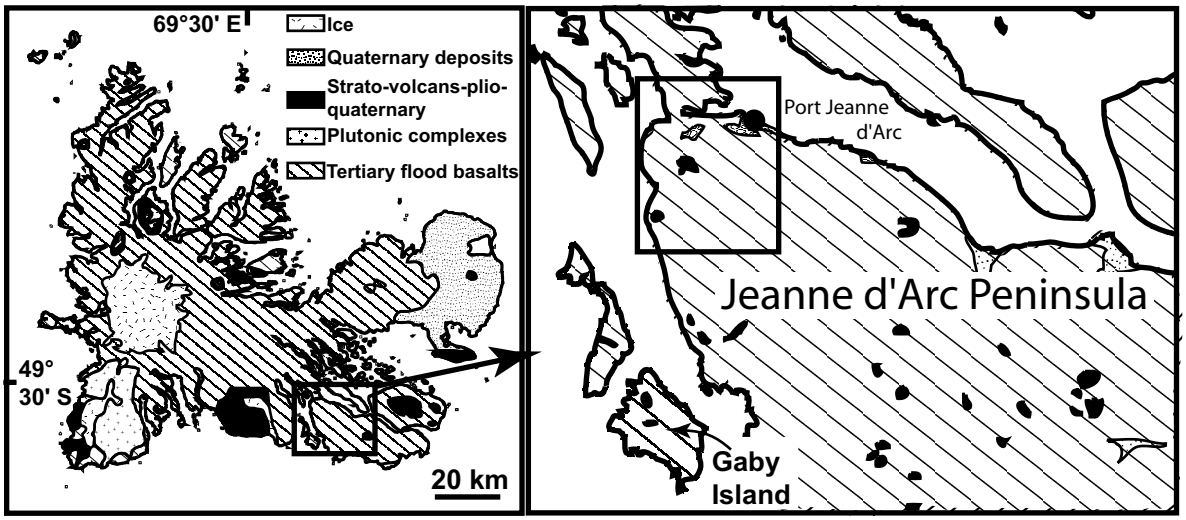

FIG. 2.8 – Localisation de la section de Port Jeanne d'Arc.

originale visait à vérifier si des unités volcaniques, séparées par une couche conglomératique épaisse, étaient, malgré une période importante séparant leur mise en place, issues d'un même centre éruptif ou au contraire provenaient de zones d'émission bien distinctes.

Les résultats partiels encourageants de cette étude nous ont poussés à mesurer par la suite l'ASM de la section du Mont de la Tourmente. Contrairement aux autres sections échantillonnées durant la même campagne de prélèvement et qui présentaient des pendages sub-horizontaux, cette séquence volcanique présentait un pendage de 15° avec un azimut de plus grande pente de 88°. Nous avons donc voulu déterminer la fabrique magnétique de cette section pour vérifier si le basculement était d'origine tectonique, nécessitant alors une correction de pendage, ou bien préalable à l'épanchement des coulées, impliquant alors une direction d'écoulement proche de la direction du pendage. Les résultats de cette analyse intéressant directement l'étude des directions paléomagnétiques ont été présentés dans le premier chapitre de cette thèse. Le lecteur est donc invité à relire la section traitant des corrections tectoniques avant d'entamer le deuxième chapitre de cette partie.

Suite aux interrogations soulevées par l'étude de la section du Mont de la Tourmente, nous avons voulu analyser le reste des coulées prélevées sur l'archipel. Le principal objectif de cette étude était de contrôler les directions d'écoulement déduites d'observations géomorphologiques (Nougier, 1970a) en combinant l'approche paléomagnétique à l'analyse de l'orientation préférentielle de forme (OPF) de phases minérales observées en lames minces pour contrôler nos interprétations. Ce deuxième chapitre présente les résultats obtenus pour les sections échantillonnées pendant la campagne d'été 1999-2000, auxquels s'ajoutent ceux de deux sections prélevées durant la campagne de 1997-98. Ce manuscrit a été soumis très récemment au *Geophysical Journal International*.

Bibliographie

Borradaile, G., Henry, B., 1997. Tectonic applications of magnetic susceptibility and its anisotropy. Earth-Science Reviews 42, 49–93.

Bouchez, J., 2000. Magnetic susceptibility anisotropy and fabrics in granites. C.R. Acad. Sci. Paris 330, 1–14.

Cañón Tapia, E., Walker, G., Herrero-Bervera, E., 1995. Magnetic fabric and flow direction in basaltic pahoehoe lava of Xitle volcano, Mexico. J. Volcanol. Geotherm. Res. 65, 249–263.

Cañón Tapia, E., Walker, G., Herrero-Bervera, E., 1997. The internal structure of lava flows – insights from AMS measurements II : Hawaiian pahoehoe, toothpaste lava and 'a'$\bar{a}$. J. of Volcanol. and Geother. Res. 76 (1-2), 19–46.

Ferré, E. C., Bordarier, C., Marsh, J., 2002. Magma flow inferred from AMS fabrics in a layered mafic sill, Insizwa, South Africa. Tectonophys. 354, 1–23.

Geoffroy, L., Callot, J., Aubourg, C., Moreira, M., 2002. Magnetic and plagioclase linear fabric discrepancy in dykes : a new way to define the flow vector using magnetic foliation. Terra Nova 14, 183–190.

Hargraves, R., Johnson, D., Chan, C., 1991. Distribution anisotropy : The cause of AMS in igneous rocks ? Geophys. Res. Lett. 18, 2193–2196.

Hrouda, F., 1982. Magnetic anisotropy of rocks and its application in geology and geophysics. Geophys. Surv. 5, 37–82.

Knight, M., Walker, G., 1988. Magma flow directions in flows of the Koolau Complex, Oahu, determined from magnetic fabric studies. J. Geophys. Res. 93, 4308–4319.

Merle, O., 1998. Internal strain within lava flows from analogue modelling. J. of Volcanol. and Geother. Res. 81, 189–206.

Morris, A., 2000. Magnetic fabric and palaeomagnetic analyses of the Plio-Quaternary calc-alkaline series of Aegina Island, South Aegean volcanic arc, Greece. Earth Planet. Sci. Letts. 176, 91–105.

Nougier, J., 1970. Contribution a l'étude géologique et géomorphologique des iles Kerguelen. Bull. Com. Nation. Fr. Rech. Antarct. Paris 27, 696pp.

Rochette, P., Aubourg, C., Perrin, M., 1999. Is this magnetic fabric normal ? A review and case studies in volcanic formations. Tectonophys. 307, 219–234.

Rochette, P., Jackson, M., Aubourg, C., 1992. Rock magnetism and the interpretation of anisotropy of magnetic susceptibility. Rev. Geophys. 30 (3), 209–226.

Tarling, D., Hrouda, F., 1993. The Magnetic Anisotropy of Rocks. Chapman&Hall, London, 217pp.

Tauxe, L., Gee, J., Staudigel, H., 1998. Flow directions in dikes from AMS data : The bootstrap way. J. Geophys. Res. 103, 17,775–17,790.

Chapitre 3

Magnetic fabric of Oligocene lavas in the Jeanne d'Arc peninsula (Kerguelen Islands)

B. Henry, G. Plenier & P. Camps

Soumis au J. Volcano. Geotherm. Res.

Statistical analysis of the magnetic fabric of samples from several successive lava flows emplaced in the same conditions can allow determination of the mean flowing direction when data from individual flows does not lead to reliable results. For 22 flows of the Jeanne d'Arc peninsula, the difference of the obtained flowing direction with that of the present dip points out a weak tilting after lava emplacement. Paleomagnetic data from this area can therefore be corrected for this weak tilting. The magnetic fabric data allow here the reconstitution of the different conditions of the emplacement of two series of lava flows and of formation of the local thick conglomerate interbedded between these series.

Keywords : Lava flows, magnetic susceptibility, anisotropy, Kerguelen Archipelago.

3.1 Introduction

Kerguelen Islands («Terres Australes et Antarctiques Françaises »in the southern Indian Ocean - 49° 30'S, 69° 30'E) are mainly constituted of volcanic rocks and of some plutonic complexes. Jeanne d'Arc peninsula is located on the southeastern border of the main island (Fig. 3.1). At Port Jeanne d'Arc, on the northwestern border of this peninsula, outcrops a conglomeratic unit (Aubert de la Rüe, 1932), thick but without very large lateral extension, interbedded in Oligocene basalts ($\sim$ 25Ma - H. (1992); Nicolaysen et al. (2000); Frey et al. (2000)). This conglomerate includes as well relatively large volcanic pebbles as coal levels. That suggests rather a deposition in a delta area, or an alluvial depression, relatively close to the source of the pebbles (Nougier, 1965). Presence of such isolated conglomerate asks about the event at the origin of its deposition. It could corresponds, either to a long period of erosion between two volcanic phases, or to a tectonic event. South of Port Jeanne d'Arc (Fig 1), the lava flows present a weak dip of about 4° towards the NNW (Nougier,

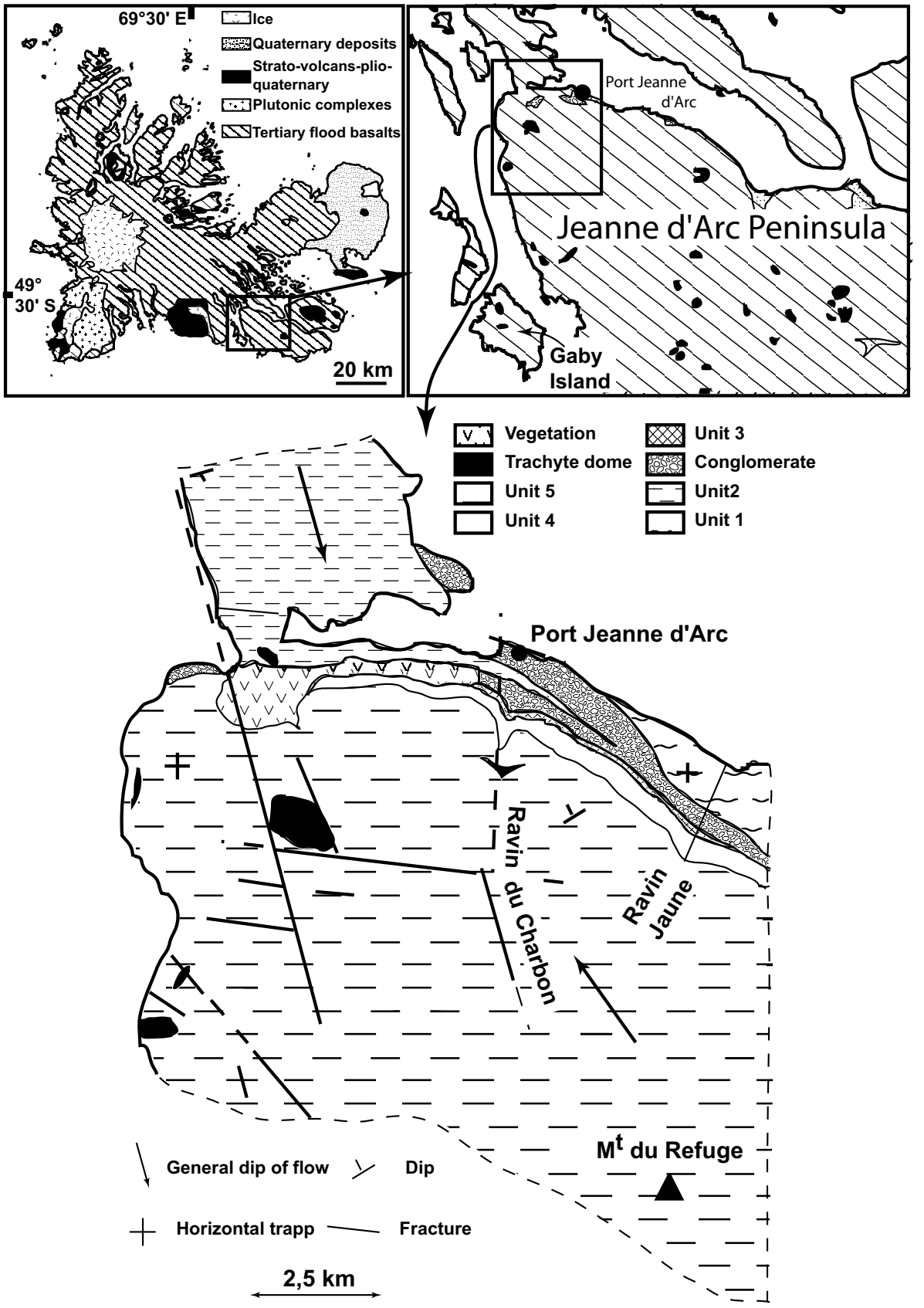

FIG. 3.1 – Location and geological map of the studied area (Ravin Jaune and Ravin du Charbon sections) in the Kerguelen islands (modified from Frey et al. (2000).

1970a). Though bad outcrop conditions, this dip appears comparing different sections. For example, petrographic (Leyrit et al., 1990; H., 1992) and paleomagnetic (Henry and Plessard, 1997; Camps et al., 1999) studies pointed out, in two parallel sections (2 km far one to the other - Fig. 3.1) close to Port Jeanne d'Arc, difference in elevation (of the order of 60 to 80 m) of the conglomerate and of basaltic flows (Frey et al., 2000), in particular for two flows clearly identified because emplaced respectively before and after a reversal of the earth magnetic field. North of the peninsula, the closest lava outcrops correspond to another flow (Unit 3 in Fig. 3.1) with, on the contrary, weak southward dip. Again, a possible tectonic event, having occurred before or after the flow emplacement, is questioned. Dip variation related to post-emplacement tiltings should imply significant deformation at least in the southern part of the Kerguelen Islands. For the interpretation of paleomagnetic data, it is also important to know if the flows were affected by some tiltings after emplacement or if the present dip is of topographic origin. This information is of capital importance but unfortunately rarely available, in particular in the case of volcanic islands. According to the present dip, the lava presently under and over the conglomerate flowed south of Port Jeanne d'Arc from the SSE to the NNW. The probable eruption center was in the north flank of the Gaby island (Leyrit et al., 1990), located SSW of the studied flows, i.e. implying irregular topography if the flowing direction is SSE-NNW. The main aim of this work is to determine the actual flowing direction by means of the magnetic fabric data. An agreement of this flowing direction with the azimuth of the present dip should be a strong argument for a lack of significant tilting after the lava emplacement. A secondary aim is to search possible change of flowing conditions before and after the conglomerate deposition. That should give also interesting information about the event at the origin of the conglomeratic formation.

3.2 Geological setting

Nougier (1965, 1970a) studied in detail two cross-sections in this area. At the «Ravin du Charbon», he described the lower part of the section, with mainly conglomerate and volcanic tuffs and few interbedded and overlying lavas flows. The second section at the «Dôme Rouge»is much more limited, with conglomerate and a single flow. H. (1992) detailed the petrography of the whole section of the Ravin du Charbon. He also studied a third section at the «Ravin Jaune»where additional flows crop out under the conglomerate. A synthesis (Frey et al., 2000) of these previous works has distinguished in this area 5 main units, numbered from the bottom to the top. The thick (until at least 110 m) conglomerate (unit 2) and trachytic breccia-tuff (unit 4) have only a limited extension (about 8 km). At the Ravin du Charbon and Ravin Jaune, the conglomerate is interbedded between lavas flows : at Ravin Jaune, it

overlies a series of at least 8 visible flows (unit 1), and it is overlain by more than 14 outcropping flows (unit 5) at the Ravin du Charbon. There are also 2 or 3 flows (unit 3) interbedded within the conglomerate, but, because the magnetic fabric results are actually exploitable only for a sufficient number of flows emplaced in the same conditions, they are not considered here. Only units 1 and 5 include sufficient number of flows and will be studied. The oldest lavas (unit 1) correspond to flows of aphyric alkalic basalts. The youngest ones (unit 5) range from aphyric trachyandesites to alkalic basalts (H., 1992; Frey et al., 2000). Several flows have vesicles filled with clays, calcite and zeolites. The whole series emplaced around 25 Ma (H., 1992; Nicolaysen et al., 2000; Frey et al., 2000), units 1 and 3 during a period of reversed polarity of the Earth magnetic field, and the unit 5 during period of normal polarity (Henry and Plessard, 1997; Camps et al., 1999).

3.3 Magnetic fabric and volcanic flows

Magnetic fabric data of volcanic rocks (Violat, 1972; Kolofikova, 1976; Ellwood, 1978; Knight and Walker, 1988; Cañón Tapia et al., 1995, 1996, 1997; Dragoni et al., 1997) mostly presents relatively scattered orientation of the principal susceptibility axes and low anisotropy percentage. During flowing, the main stresses undergone by lava (Merle, 1998) are related to the gravity (including from the overlying part of the flow, effect of the contact with the underlying surface,...). All these stresses are in relation with the orientation of the slope, and therefore of the flowing direction. However, because of high viscosity (Murase and Mc Birney, 1973), flowing conditions in lava flows are actually complex. This gives local disturbances of flowing, which have a major effect on the fabric at the scale of a sample. Moreover direction of flowing of a flow can be locally modified because of the irregular topography of the underlying surface. The single manner to actually point out an effect of the gravity (i.e. the flowing direction) is therefore to analyze a large number of specimens sampled in several different flows emplaced in the same conditions. The effects of local disturbances (essentially an increase of the confidence zones of all the principal susceptibility axes) are then averaged out and do not affect the mean direction. Two approaches are possible. The flowing direction could be determined either by averaging the flowing direction obtained at the level of a single flow, or by studying data gathered from several successive flows. The first approach is often difficult or impossible to implement because of very large uncertainty on mean magnetic fabric of each flow. Moreover, it needs mostly collection of samples much larger (Cañón Tapia et al., 1997) than that generally chosen for paleomagnetic studies. The second one is only usable for a sufficient number of flows emplaced in the same conditions. It can be applied with a reduced number of samples per flow and could be used as a routine in paleomagnetic works. For a nor-

mal fabric, mean magnetic foliation (perpendicular to the minimum axis) is mostly close to the flow plane (Brown et al., 1964; Symons, 1967). It presents sometimes a small difference in orientation (imbrication angle) relative to the flow plane (Knight and Walker, 1988), and, according to the part of the flow, could be dipping toward upstream (lower part) or downstream direction (upper part) of the flow (Cañón Tapia et al., 1996, 1997) relatively to the flow plane. Mean maximum axis has been found (Khan, 1962; Leong and Stacey, 1966; Halvorsen, 1974; Cañón Tapia and Pinkerton, 2000) mainly either parallel (flow emplaced on significant slope) or perpendicular (flow emplaced on very weak slope) to the flowing direction (Cañón Tapia et al., 1995). There are four main statistical methods concerning the principal directions of the magnetic fabric. The Hext (1963)-Jelinek (1978) statistics and the bootstrap method (Constable and Tauxe, 1990) are both based on the variability of the mean normalized tensor, and the elliptical confidence zones obtained by these approaches are more or less similar. The results of the bootstrap method will be here therefore presented without transformation of the empirical confidence zone as an elliptical confidence zone (Henry, 1997a) to obtain complementary information relative the Hext-Jelinek statistics. The method (Henry and Le Goff, 1995) based on bivariate extension of the Fisher (1953) statistics considers independently the distribution of the maximum, intermediate and minimum axes. This method not only allows integrating the measurement uncertainty on the directions, but also permits, as used here, to underline the effect of the best specified data by weighting them using the precision parameter k related to this uncertainty. Because of possible high scattering of the susceptibility axes, this vectorial approach has to be considered with care and its results have to be compared with those of the other statistical methods. Ending, the determination of the magnetic zone axis with its confidence zone (Henry, 1997b) is made by analyzing the variability of the magnetic foliation and yields the best direction of intersection of the magnetic foliation of the minerals carrying the magnetic fabric. Concerning the uncertainty of the intensity P' and shape T parameters (Jelinek, 1981), bootstrap approach has been applied (Henry, 1997a) for P'-T diagram on the data from the whole collection of samples. The results will be also presented using density contours diagrams which allow better visualization of the axes distribution.

3.4 Magnetic fabric of Port Jeanne d'Arc volcanic flows

Derder (1989) and Henry and Plessard (1997) studied the magnetic mineralogy of the Oligocene lavas of the Kerguelen archipelago. The main magnetic mineral is a titanomagnetite with low Ti-contents, of pseudo-single-domain size (PSD). This mineral is the carrier of the primary remanent magnetization, and therefore crys-

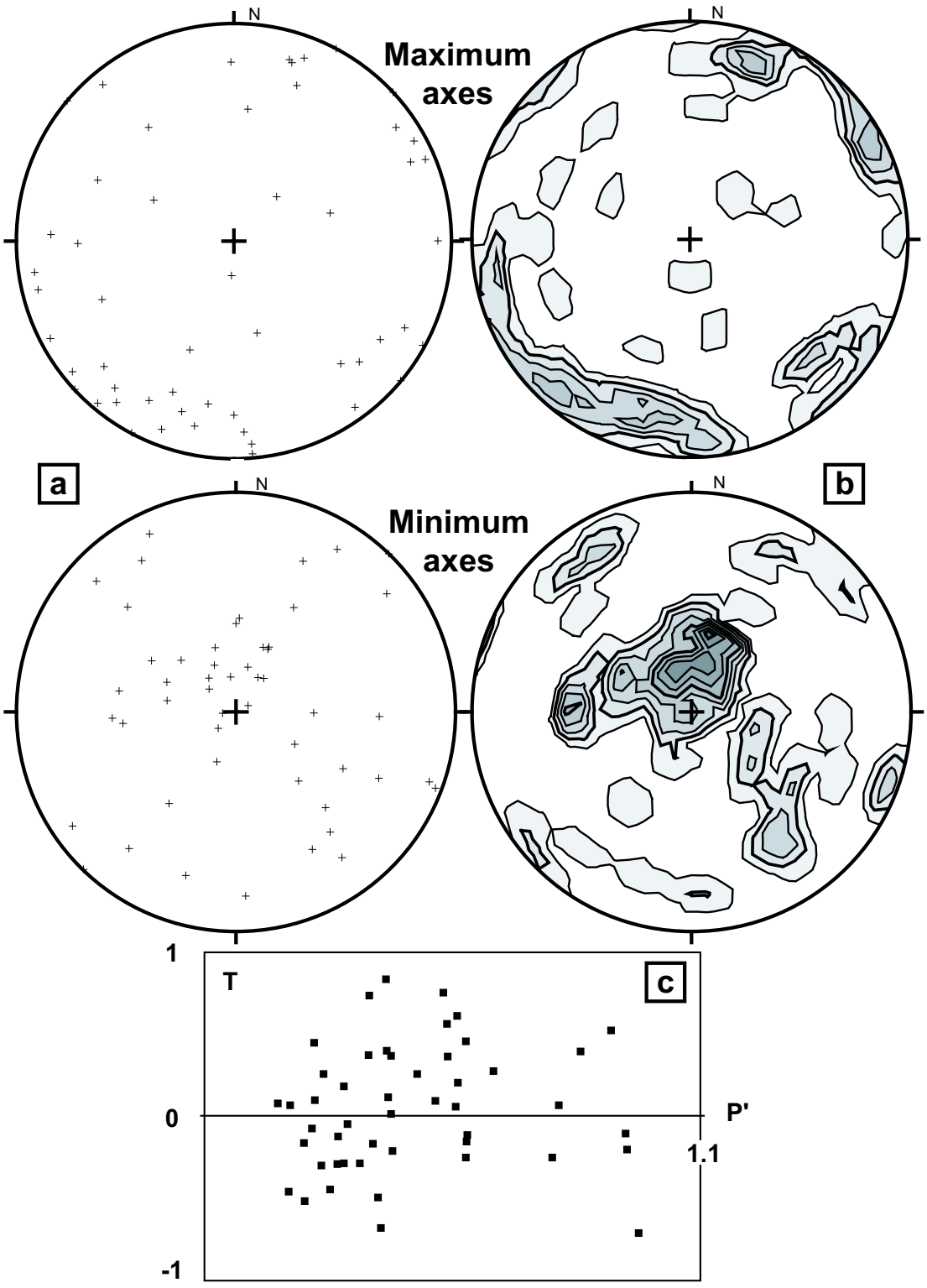

FIG. 3.2 – JU1 samples : a) Maximum (squares) and minimum (circles) axes (stereographic projection in the lower hemisphere). b) Corresponding density contours diagrams. c) P'-T diagram (Jelinek, 1981).

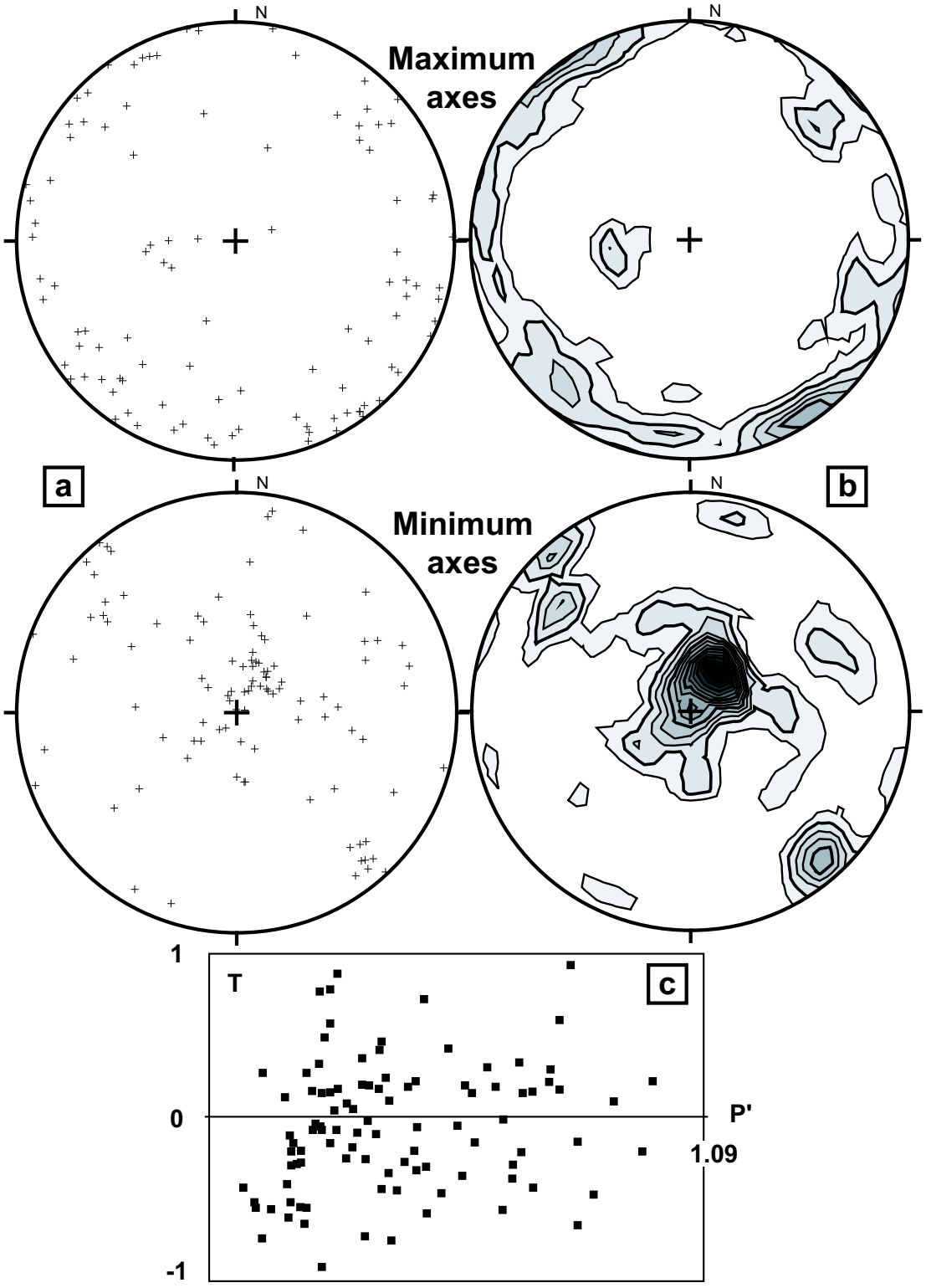

FIG. 3.3 – JU5 samples (see Fig. 3.2).

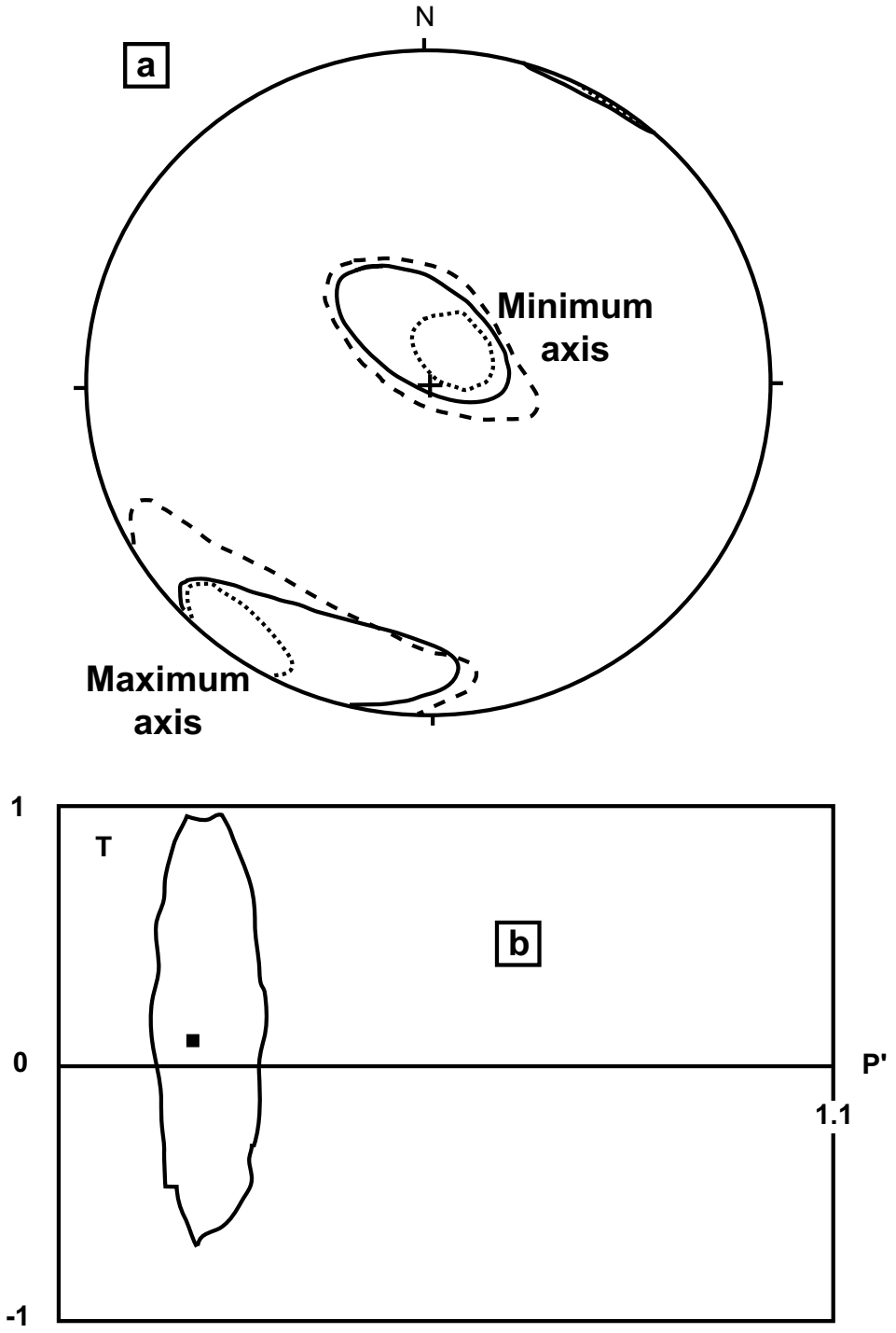

FIG. 3.4 – JU1 samples : a) Confidence zone (stereographic projection in the lower hemisphere) for maximum and minimum axes using Hext (1963) - Jelinek (1978) statistics (continuous line), bootstrap (Constable and Tauxe, 1990; Henry, 1997a) method (dashed line) and bivariate (Henry and Le Goff, 1995) statistics (dotted line). b) Confidence zone (Henry, 1997a) on P'-T diagram (Jelinek, 1981).

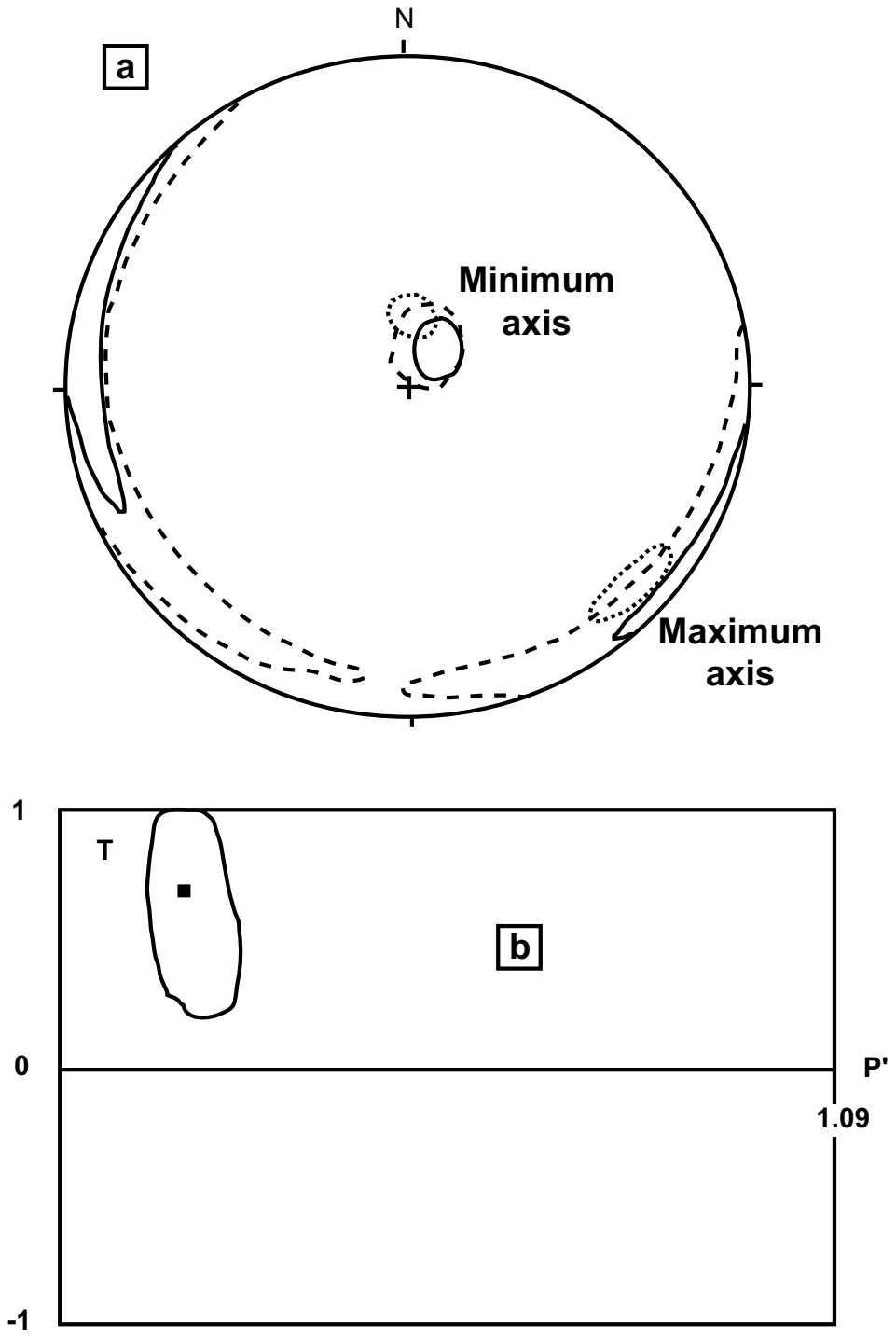

FIG. 3.5 – JU5 samples (see Fig. 3.4).

tallized very early in the magma evolution. Very few large grains of titanomagnetite, which formed after emplacement (Gautier, 1987; H., 1992), have higher Ti-contents and are paramagnetic at the room temperature. Magnetic mineralogy is therefore strongly dominated by the PSD titanomagnetite with low Ti-contents, and we can expect normal magnetic fabric directly related to the lava emplacement. Magnetic fabric was measured using KLY-3 Kappabridges (Agico, Brno) in NIPR (Tokyo) and IPGP (Saint-Maur) laboratories. The studied samples have been collected for paleomagnetic analysis (Henry and Plessard, 1997; Camps et al., 1999) in 22 lava flows (6 to 8 samples per flow, mostly taken in the lower part of the flows) in the Ravin Jaune and Ravin du Charbon sections (Fig. 3.1). Obtained data for each flow are not actually here usable to determine flowing direction, because of too large uncertainties on the mean axes orientation. The statistical analyses were thus applied to data from group of flows. Assuming possibly different conditions of flowing before and after deposition of the conglomerate, the lava flows outcropping in the Port Jeanne d'Arc area were separated in two series : JU1 data corresponds to 8 flows (50 samples) of the unit 1 and JU5 results to 14 flows (102 samples) of the unit 5. In both the cases, anisotropy percentages are mostly low, and the principal directions scattered (Fig. 3.2 and 3.3). Such results are not surprising in volcanic rocks, and only statistical data can yield actually usable information. The confidence zones obtained using the bivariate statistics (Fig. 3.4 and 5) are coherent with the confidence zones from the other statistical methods (except for the intermediate axis of the JU5 flows), but are much smaller. This shows that the scattering of the principal directions is mainly due to samples with very low anisotropy. The magnetic fabric results, though this dispersion, are therefore suitable for statistical analyses. For the different axes, the confidence zones for the whole data of JU1 flows (Fig. 3.4) are relatively large, but not overlapping for the Hext-Jelinek and bootstrap methods. They are of neighboring size and shape, presenting an elongation close to the flow plane for the maximum and intermediate axes. For the minimum axis, this lengthening is around a plane strongly dipping towards NNE. The confidence zones are much smaller for the bivariate approach. Mean maximum axis is along a SSW weakly dipping direction (D=211° ; I=10° from Hext-Jelinek and bootstrap methods, D=218° ; I=6° from bivariate statistics). The mean intermediate axis (D=120° ; I=7° from Hext-Jelinek and bootstrap methods, D=133° ; I=17° from bivariate statistics) is slightly SSE dipping. The magnetic zone axis (D=228° ; I=6°) is relatively close to the mean maximum axis, but has a low significance because of a very large confidence area. Mean minimum axis present a strong dip towards the NNW to NE (D=347° ; I=78° from Hext-Jelinek and bootstrap methods, D=35° ; I=80° from bivariate statistics). For the mean tensor, the shape is slightly oblate (T=0.10) and the anisotropy per-

centage very low (P'=1.017). The confidence zone on P'-T diagram (Fig. 3.4) appears very large, including also values characteristic of a prolate shape. For the JU5 flows (Fig. 5), the confidence zones for the maximum and intermediate axes are elongated for Hext-Jelinek and bootstrap methods (these confidence zones being larger and partly overlapping for the bootstrap). They present an elongation close to the flow plane. For the minimum axis, the confidence zone is small and almost circular for these two statistical approaches. The confidence zone is much smaller (because of the larger weight of the best specified axes) for the bivariate statistics, with the same orientation. Mean maximum axis is close to the horizontal plane (D=294° ; I=1° from Hext-Jelinek and bootstrap methods, and D=133° ; I=12° from bivariate statistics). The magnetic zone axis (D=218° ; I=13°) is almost perpendicular to the mean maximum axis, and, contrary to that obtained in the JU1 flows, with a relatively small confidence area (roughly corresponding to an ellipse with half-axis of 21° parallel to the flow plane and 9° in a vertical plane). Mean intermediate axis (D=204° ; I=11° from Hext-Jelinek and bootstrap methods) appears partly biased using bivariate analysis (D=219° ; I=27°) because of the very strong scattering. Such a bias does not affect mean maximum axis because of a scattering mainly in a part of girdle. Mean minimum axis presents a strong dip towards the N to NNE (D=26° ; I=79° from Hext-Jelinek and bootstrap methods, D=5° ; I=73° from bivariate statistics). For the mean tensor, the shape is oblate (T=0.69) and the anisotropy percentage again very low (P'=1.014). The confidence zone on P'-T diagram (Fig. 5) appears less large than for JU1 flows, including only values corresponding to an oblate shape.

3.5 Discussion

For JU1 as for JU5 flows, minimum axis presents a strong dip. The magnetic foliation is therefore close to the flow plane. Application of a dip correction (mean dip is of the order of 4° toward NNW) increases the angle between vertical and mean minimum axis. Even assuming that the present dip is due to post-emplacement tilting, the minimum axis is deviated from the pole of the flow plane (imbrication). Because of possible maximum axes parallel or perpendicular to the flowing direction, two possibilities have to be considered for determination of the flowing direction from magnetic fabric data. - For JU1 flows, SSW-NNE and ESE-WNW flowing directions are then possible. However, as shown by the bivariate statistics, the best specified minimum axes have an imbrication angle towards the NNE. The confidence zone for the minimum axis obtained by the other statistics is around a girdle perpendicular to the mean maximum axis which has a SSW azimuth. The best vertical symmetry plane of the axes distribution is then this SSW-NNE plane. It also clearly appears on density diagrams (Fig. 3.2b). In addition, this symmetry is underlined by the orientation of the magnetic zone axis to-

wards SW. Such a vertical plane of symmetry mostly includes in non-deformed lava flows the flowing direction (Henry, 1980). The flowing direction was therefore along a direction about SSW-NNE. - For JU5 flows, again SSW-NNE (perpendicular to mean maximum axis) and ESE-WNW (parallel to mean maximum axis) flowing directions are possible. In this case, minimum axes are strongly dipping towards NNE to N. The criterion of the best vertical symmetry plane of the axes distribution again argues for choice of the flowing direction SSW-NNE. This plane also appears on the density diagrams (Fig. 3.2b). The coincidence of this SSW-NNE directions with the flowing direction determined in the JU1 flows is unlikely a mere chance. Moreover, the orientation of the magnetic zone axis is again towards SW. In addition, the mean intermediate axis from bivariate statistics, though partly biased by the strong scattering, is an indicator of the symmetry of the distribution of these axes. It has an azimuth close to the SSW, arguing then also for a best vertical symmetry plane about SW-NE. The flowing direction was therefore along a direction about SSW-NNE. The mean maximum axis is therefore here perpendicular to the flowing direction. It is also perpendicular to the magnetic zone axis, indicating that it is not zone axis of planar grains, but related to lengthened grains.

The flowing direction has a same SSW-NNE azimuth in JU1 and JU5 flows. According to Cañón Tapia et al. (1996, 1997), the orientation of the imbrication angle of our samples, collected in the lower part of the flows, should indicate a flowing towards the NNE. Such a flowing direction towards the NNE perfectly agrees with the location of the eruption center, which should be, SSW of the studied flows, in the north flank of the Gaby island (Leyrit et al., 1990). The flowing direction then does not correspond to that suggested by the present dip. There was therefore a significant tilting since the emplacement of the flows. The single available information about the orientation of this tilting is that the dip was towards NNE during lava emplacement (flowing towards the NNE). This implies that the tilting was towards a direction between SSW and NNW. Owing to the fabric of the JU5 flows with scattered maximum axes in mean perpendicular to the flowing direction, the slope during emplacement was probably very weak (Cañón Tapia et al., 1995). Assuming a slope during lava flowing lower than 4°, the tilting should be of the order of 4 to 5° towards NNW to W. The main tectonic local event since the Oligocene was mainly limited to a weak tilting. Paleomagnetic directions obtained in the Port Jeanne d'Arc sections have thus to be slightly corrected for a tilting.

It is also interesting to compare the results of JU1 and JU5 flows. General distribution of the axes is relatively similar, as clearly shown by the density diagrams (Fig. 3.2 and 3.3). However, some differences appear looking at the statistical results. The maximum axis has a much smaller confidence zone and the mean fa-

bric is less oblate in JU1 flows than in JU5 flows. For JU1 flows, the confidence zones for minimum axis from Hext-Jelinek and bootstrap statistics is around a partial girdle perpendicular to the mean maximum axis. The minimum axis for the JU5 flows has much smaller corresponding confidence zones. The very large size of the confidence zone of the magnetic zone axis points out relatively incoherent variations of the magnetic foliation in the JU1 flows. On the contrary, JU5 flows, though reduced confidence zone for the minimum axis, have coherent variations giving small confidence zone for the magnetic zone axis. All these observations show that the dominant element of the magnetic fabric is rather the maximum axis in JU1 flows and the minimum axis in JU5 flows. Though a same flowing direction, the emplacement conditions were therefore different in JU1 and JU5 units. Cañón Tapia et al. (1995) showed that scattered maximum axes, even sometimes perpendicular to the flowing, generally corresponds to a very weak slope during emplacement while they are less scattered and rather parallel to the flowing for a stronger slope. This suggests that the JU1 flows likely emplaced on a significant slope and JU5 flows on a very weak slope. The main event between the flowing of these two series of lava is the emplacement of conglomerate and trachytic breccia-tuff. The following history can therefore be suggested for this area : - Emplacement of JU1 flows, - deposition of the conglomerate and breccia-tuff, mainly on the bottom part of the existing slope, thus giving a surface with a weaker slope, - emplacement of the JU5 flows, - tilting of the section. The flowing direction, and then the slope direction, is the same before and after the deposition of conglomerate and breccia-tuff. Tectonic event between emplacement of JU1 and JU5 flows, if existing, should be limited to a vertical displacement.

3.6 Conclusion

In the Jeanne d'Arc peninsula, the difference of the flowing direction relatively to the present dip points out the occurrence of a weak tilting after lava emplacement. The paleomagnetic data have then to be slightly corrected before use for applications like secular variation analysis (Camps et al., 1999). In addition, the magnetic fabric data allow to reconstitute the evolution of this area during the emplacement of the lava flows : flowing of first series of lava on a significant slope, deposition of conglomerate and breccia-tuff leading to a decrease of the slope, and emplacement of the second series of flows, weak tilting of the section

3.7 Acknowledgments

We are very grateful to the «Institut Français pour la Recherche et les Technologies Polaires»for providing all transport facilities and for the support of this project. Special thanks to A. Lamalle and all our field friends. We are grateful to C. Aubourg for constructive comments. Main part of this work was realized during a stay of one

of us (B.H.) at National Institute of Polar research (Tokyo). Thanks to the staff of this Institute, and especially to M. Funaki, for kind invitation and to Excellence Committee of Japan for financial support of this stay.

Bibliographie

Aubert de la Rüe, E., 1932. Etude géologique et géographique de l'archipel de Kerguelen. Rev. Géogr. Géol. Dyn. 5, 231 pp.

Brown, H., Khan, M., Stacey, F., 1964. A search for flow structure in columnar basalts using magnetic anisotropy of rocks. Pure Appl. Geophys. 57, 61–65.

Cañón Tapia, E., Pinkerton, H., 2000. The anisotropy of magnetic susceptibility of lava flows : an experimental approach. J. Volcanol. Geotherm. Res. 98, 219–233.

Cañón Tapia, E., Walker, G., Herrero-Bervera, E., 1995. Magnetic fabric and flow direction in basaltic pahoehoe lava of Xitle volcano, Mexico. J. Volcanol. Geotherm. Res. 65, 249–263.

Cañón Tapia, E., Walker, G., Herrero-Bervera, E., 1996. The internal structure of lava flows – insights from AMS measurements I : Near-vent a'a. J. Volcanol. Geotherm. Res. 70, 21–36.

Cañón Tapia, E., Walker, G., Herrero-Bervera, E., 1997. The internal structure of lava flows – insights from AMS measurements II : Hawaiian pahoehoe, toothpaste lava and 'a'ā. J. of Volcanol. and Geother. Res. 76 (1-2), 19–46.

Camps, P., Henry, B., Prévot, M., 1999. Paleomagnetism of volcanic rocks from Kerguelen archipelago (24-30 Ma) : Implications for the palaeosecular variation in the southern Indian Ocean. In : XXII UGGI Gener. Assemb. Birmingham.

Constable, C., Tauxe, L., 1990. The bootstrap for magnetic susceptibility tensors. J. Geophys. Res. 95 (8), 383,395.

Derder, M., 1989. Contribution à la paléointensité du champ magnétique terrestre d'après l'étude de roches magmatiques quaternaires, miocènes et jurassiques. Ph.D. thesis, Orsay, France.

Dragoni, M., Lanza, R., Tallarico, A., 1997. Magnetic anisotropy produced by magma flow : theoritical model and experimental data from Ferrer dolerite sills (Antarctica). Geophys. J. Int. 128, 230–240.

Ellwood, B., 1978. Flow and emplacement direction determined for selected basaltic bodies using magnetic anisotropy measurement. Earth Planet. Sci. Lett. 41, 254–264.

Fisher, R., 1953. Dispersion on a sphere. Proc. R. Soc. London Ser A (217), 295–305.

Frey, F., Weis, D., Yang, H.-J., Nicolaysen, K., Leyrit, H., Giret, A., 2000. Temporal geochemical trends in Kerguelen Archipelago basalts : evidence for decreasing magma supply from the Kerguelen plume. Chem. Geol. 164, 61–80.

Gautier, I., 1987. Les basaltes des îles Kerguelen (Terres Australes et Antarctiques Françaises. Ph.D. thesis, Paris, France.

H., L., 1992. Kerguelen : cartographie et magmatologie des presqu'îles Jeanne

d'Arc et Ronarc'h. Ph.D. thesis, Orsay, France.

Halvorsen, E., 1974. The magnetic fabric of some dolerite intrusions, northeast Spitsbergen : implications for the emplacement. Earth Planet. Sci. Lett. 21, 127–133.

Henry, B., 1980. Contribution à l'étude des propriétés magnétiques de roches magmatiques des Alpes : Consequences structurales, régionales et générales. Ph.D. thesis, Paris, 528 pp.

Henry, B., 1997a. Bootstrap and magnetic fabric. In : EUG 9 meeting. Strasbourg, France.

Henry, B., 1997b. The magnetic zone axis : a new element of magnetic fabric for the interpretation of the magnetic lineation. Tectonophys. 271, 325–329.

Henry, B., Le Goff, M., 1995. Application of the bivariate extension of Fisher's statistics to the magnetic susceptibility anisotropy data : integration of the measurment uncertainties on the orientation of the principal directions. C.R. Acad. Sci. Paris 320 (IIa), 1037–1042.

Henry, B., Plessard, C., 1997. New palaeomagnetic results from the Kerguelen Islands. Geophys. J. Int. 128 (1), 73–83.

Hext, G., 1963. The estimation of second-order tensors, with related tests and designs. Biometrika 50, 353–373.

Jelinek, V., 1978. Statistical processing of magnetic susceptibility measured in groups of specimens. Stud. Geophys. Geod. 22, 50–62.

Jelinek, V., 1981. Characterization of the magnetic fabric of rocks. Tectonophys. 79, T63–T67.

Khan, M., 1962. The anisotropy of magnetic susceptibility of some igneous and metamorphic rocks. J. Geophys. Res. 67, 2873–2885.

Knight, M., Walker, G., 1988. Magma flow directions in flows of the Koolau Complex, Oahu, determined from magnetic fabric studies. J. Geophys. Res. 93, 4308–4319.

Kolofikova, O., 1976. Geological interpretation of measurement of magnetic properties of basalts on example of the chribsky les lava flow of the Veljy Roudny volcano (Nizky Jesenik Mts.)(in Czech.). Cas. Mineral. Geol. 21, 387–396.

Leong, W., Stacey, F., 1966. Magnetic anisotropy of laboratory materials in which magma flow is simulated. Pure Appl. Geophys. 64, 78–80.

Leyrit, H., Bardintzeff, J., Verdier, O., Giret, A., Brousse, R., 1990. Les presqu'îles Jeanne d'Arc et Ronarc'h : zone test pour une cartographie géologique au 1/100 000 des îles Kerguelen. Compt. Rend. Acad. Sci. Paris 311 (II), 561–566.

Merle, O., 1998. Internal strain within lava flows from analogue modelling. J. of Volcanol. and Geother. Res. 81, 189–206.

Murase, T., Mc Birney, A., 1973. Properties of some common igneous rocks and their melts at high temperatures. Geol. Soc. Amer. Bull. 84, 3563–92.

Nicolaysen, K., Frey, F., Hodges, K., Weis, D., Giret, A., 2000. $^{40}Ar/^{39}Ar$ geochro-

nology of flood basalts from the Kerguelen Archipelago, southern Indian Ocean : implications for Cenozoic eruption rates of the Kerguelen plume. Earth Planet. Sci. Letts. 174, 313–328.

Nougier, J., 1965. Etudes des formations de Port Jeanne d'Arc (Archipel des Kerguelen. Bull. Com. Nation. Fr. Rech. Antarct. Paris 11, 29–55.

Nougier, J., 1970. Contribution a l'étude géologique et géomorphologique des iles Kerguelen. Bull. Com. Nation. Fr. Rech. Antarct. Paris 27, 696pp.

Symons, D., 1967. The magnetic and petrologic properties of a basalt column. Geophys. J. Roy. Astron. Soc. 12, 473–490.

Violat, C., 1972. Contribution à l'étude de l'anisotropie magnétique des roches volcaniques. Ph.D. thesis, Paris.

Chapitre 4

Determination of Flowing directions for volcanic sections from the Kerguelen Archipelago (southern Indian Ocean)

G. Plenier, P. Camps, B. Henry & B.Ildefonse

Soumis au Geophys. J. Int.

We report AMS study carried out on six Oligocene volcanic sections from the Kerguelen Archipelago in order to infer their direction of emplacement and possibly precise the corresponding location of the eruptive centers. Because of permutation axis frequently observed for lava flows, the results at flow scale and at section scale are checked with density diagrams and thin section analysis. Imbrication, also pointed out by discrepancy of the strongly dipping principal axis relative to the vertical, and axes distribution allowed to determine the flowing direction of each lava pile. Therefore, specifying the observations made by Nougier (1970a), it helps to sharpen the location of the different eruptive centers.

Keywords : Lava flows, PSO, AMS, magnetic susceptibility, anisotropy, Kerguelen Archipelago.

4.1 Introduction

The magnetic susceptibility of a rock is function of the number of minerals in presence and of their individual characteristics. It generally displays a directional variability referred as anisotropy of magnetic susceptibility (AMS). AMS is well represented by a second rank tensor of eigenvectors K_{min}, K_{int} and K_{max} (see Hrouda (1982); Borradaile (1988); Rochette et al. (1992); Tarling and Hrouda (1993); Borradaile and Henry (1997); Bouchez (2000) among others). For undeformed volcanic rocks, the global AMS is usually controlled by titanomagnetites and reflects either their distribution anisotropy, after they lately crystallized in interstitial zones oriented in the same way than a preexisting silicate phase during lava flowing (Hargraves et al., 1991), or more directly their orientation acquired during emplacement (Hrouda, 1982; Cañón Tapia et al., 1995; Morris, 2000). It is mostly weak suggesting possibility of not very effective orientation mechanism. This should be

particularly true for lava flow where conditions of magma emplacement are much less constrained than for dyke intrusions. The magnetic lineation (K_{max}) is either parallel or perpendicular to the flow direction (Cañón Tapia et al., 1995; Glen et al., 1997; Morris, 2000; Herrero-Bervera et al., 2002; Henry et al., 2003) and the magnetic foliation (pole given by K_{min}) close to the flow plane (Kolofikova, 1976; Cañón Tapia et al., 1996). By analogy with the use of imbrication to determine the flow direction within a dyke (Knight and Walker, 1988; Tauxe et al., 1998; Geoffroy et al., 2002), AMS was also proposed to infer the flowing direction within a lava flow (Cañón Tapia et al., 1997).

The first aim of this study is to check the reliability of the flowing directions obtained by AMS studies with the results of thin sections analyse. The second part of the paper will summarized the lava flow directions of emplacement for the Kerguelen islands. In particular, these directions will be compared to that proposed by Nougier (1970a) from observations of the present dips, of the thickness of the lava piles and of the orientations of the fractures affecting them.

4.2 Geology and sampling

The Kerguelen archipelago (Nougier, 1970a; Giret, 1986) is located at 70°E and 49°S in the southern Indian Ocean. It lies on the northern part of the Kerguelen-Gaussberg plateau and represents the last 30 Ma aerial continuation of the Kerguelen plume magmatic activity (Yang et al., 1998; Weis et al., 1998; Nicolaysen et al., 2000). Some magmatic contributions from the Southeast Indian Ridge during the early Cenozoic is also suspected (Doucet et al., 2002). Consequently, volcanic rocks are preponderant in the archipelago. They outcrop at more than 85% of the surface and form 400 to 900m high tabular relief incised by glacial erosion. Gabbro, granite and syenite intrusions from 1 to 15km in diameter are also present locally. These plutons, issued from later Kerguelen plume melts (Giret, 1990; Weis and Giret, 1994), compose, with quaternary sediments, the rest of the rocks observed in the archipelago.

Our samples (about seven per flow, oriented using magnetic and solar compass), devoted for paleosecular variation and paleointensity purposes (Plenier et al., 2002, 2003) were drilled in the bottom part of the least altered flows. Fortunately the lower part of the flows are recommended for AMS studies (Glen et al., 1997; Herrero-Bervera et al., 2002). The samples were collected, as far as possible from dykes and close to previously-dated sections (Yang et al., 1998; Nicolaysen et al., 2000; Doucet et al., 2002) across Mont des Ruches (18 flows), Mont des Tempêtes (20 flows), Mont de la Rabouillère (19 flows) Mont Amery (8 top flows), Port Christmas(16 flows) and Port Raymond sections (Fig. 4.1). For the Mont Amery section, about 50 samples from the 8 bottom flows, previously collected by Henry and Plessard

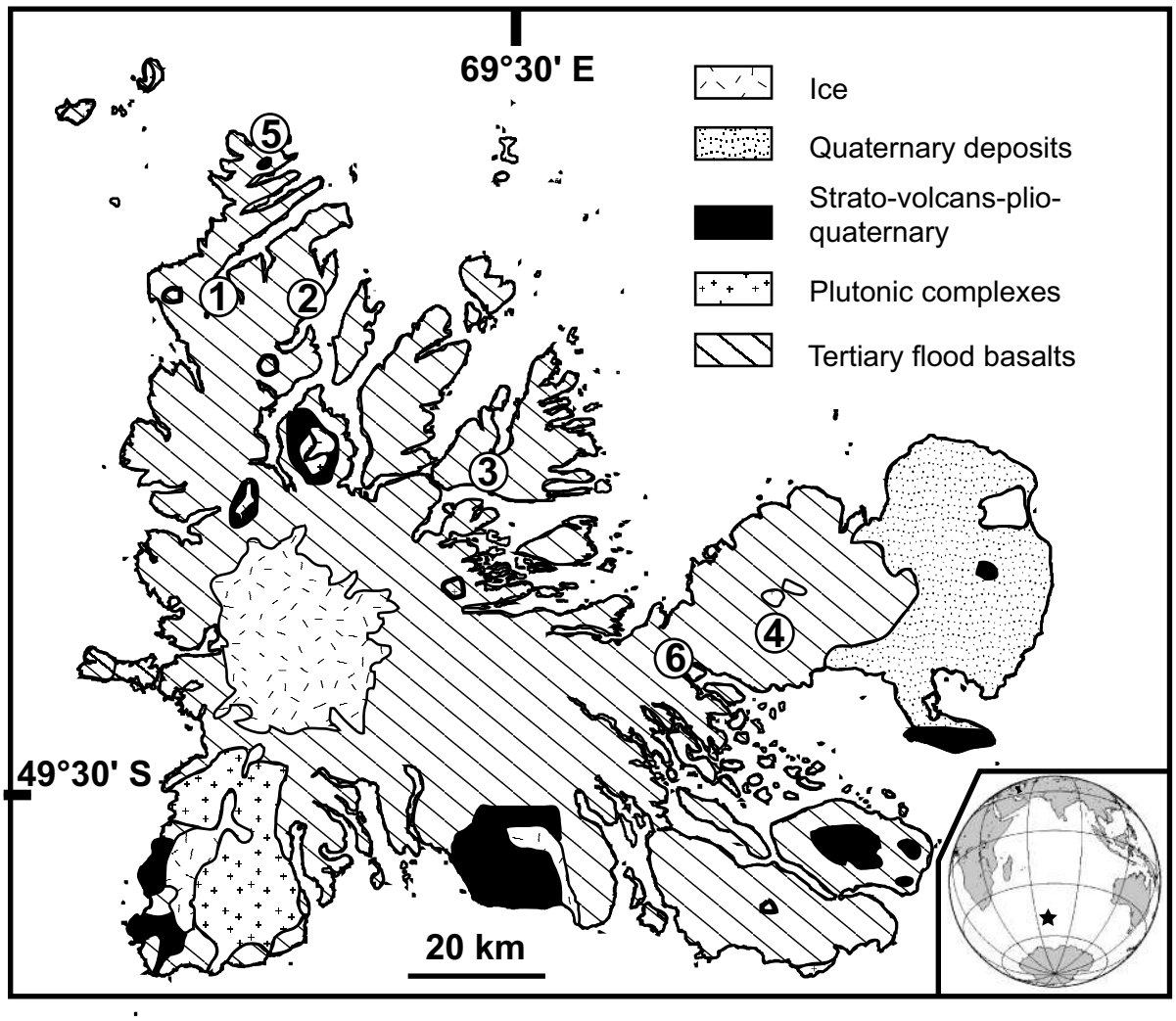

FIG. 4.1 – Geological map of the Kerguelen Archipelago after Frey et al. (2000). Numbers indicate the locations of sampled sections : **1** Mont des Ruches : 18 flows, **2** Mont des Tempêtes : 20 flows, **3** Mont de la Rabouillère : 19 flows, **4** Mont Amery : 16 flows, **5** Port Christmas : 16 flows, **6** Port Raymond : 9 flows.

(1997), were also analyzed. No significant dip has been observed for all of these lava sequences, except for the Port Raymond section with a dip of 4° toward the ESE.

4.3 Rock magnetism

For paleointensity study purpose (Plenier et al., 2003), the magnetic carriers of the Mont des Ruches, Mont des Tempêtes and Mont de la Rabouillère sections have been identified using low-field susceptibility thermal evolution curves (K-T curves). Two distinct behaviors were observed. Irreversible and complex K-T curves correspond to an assembly of original titanomagnetites or slightly oxidized titanomaghemites with higher Curie temperature titanomaghemites due to low temperature oxidation at a stronger level. The second behavior presenting reversible K-T curves comprises poor-Ti titanomagnetites produced by high temperature oxyexsolution during the flow emplacement of the original titanomagnetite. The thin sections observation with an oil immersion objective confirmed these interpretations. We found an isotropic phase associated with a pleochroic ilmenite that we preferably interpreted as a titanomaghemite for samples displaying irreversible K-T curves, and exsolved ilmenite or titanohematite lamellae resulting from deuteric oxidation of a residual titanomagnetite for samples presenting reversible K-T curves.

4.4 AMS study

AMS of 629 standard samples was measured using KLY2 and KLY3 Kappabridges at IPGP (St Maur) and Montpellier paleomagnetic laboratories respectively. The confidence zone for the mean direction of each axis was calculated using both linear perturbation analysis (Hext, 1963; Jelinek, 1978; Lienert, 1991) and bootstrap method (Constable and Tauxe, 1990). These two statistics providing approximately the same results, only the bootstrap ellipses are displayed on the following figures.

Because small number of strongly anisotropic samples can deflect the orientation of the mean principal directions away from that of the majority of samples (Borradaile, 2001), the data were filtered using the 3σ limit on $A = 100(1-[(K_{min}+K_{int})/2K_{max}])$ and $B = 100([(K_{min} - 2K_{int})/K_{max}] + 1)$ parameters (Cañón Tapia et al., 1995) to discard the samples presenting an abnormal fabric compared to the others from the same section. This selection leads to noticeably decrease the confidence ellipses around the mean eigenvectors in a previous study (Plenier et al., 2002). Secondly, the Fisher statistics was used to eliminate samples displaying statistically indistinct principal directions. These filters allowed removing of 19 samples on the total collection. Owing to the occurrence of conglomerate at the base of the third flow from the Mont des Ruches section and the weak number of samples in the underlying units, these bottom flows have been rejected as they can result from different emplacement conditions as previously observed in a simi-

lar case for another section (Henry et al., 2003).

4.4.1 Flow scale analysis

The flows displaying overlapping confidence regions for the different axes or corresponding to less than three measured samples were discarded for the analysis at the flow scale. Measurement of less than 10 specimens per flow often yields large statistical uncertainty of the susceptibility principal directions (Cañón Tapia et al., 1997). Our sampling was initially restricted to only about 7 samples by flow because it was devoted for paleosecular variation and paleointensity purposes (Plenier et al., 2002, 2003). Thus, less than half of the flows gave reliable results (Table B.1 and left part of Fig. 4.2 and Fig. 4.3).

TAB. 4.1 – Directions of the mean principal susceptibilities and sizes of the confidence regions around them for the suitable flows.

Flow	n/N		$\bar{s}$	$\delta\bar{s}$	Dec	Inc	ζ	d_ζ	i_ζ	η	d_η	i_η
Mont des Ruches section (48.87°S, 68.91°E)												
Ruc6	7/8	Max	1.017	0.0021	164.7	5.7	9.8	255.9	11.6	16.3	49.2	77.1
		Int	0.999	0.0009	257.1	22.7	10.3	162.1	11.7	15.6	46.8	64.1
		Min	0.984	0.0015	61.5	66.5	13.0	302.5	11.9	18.4	208.1	19.9
Ruc8	8/8	Max	1.023	0.0039	148.9	9.5	10.2	18.7	75.6	79.4	240.7	10.8
		Int	1.014	0.0042	240.8	11.2	13.2	49.4	78.6	83.1	150.4	2.2
		Min	0.966	0.0048	19.6	75.3	8.4	125.5	4.1	14.5	216.6	14.1
Ruc9	9/11	Max	1.014	0.0033	164.0	12.4	10.0	264.2	38.9	21.8	59.6	48.4
		Int	0.996	0.0033	65.5	33.6	20.8	158.1	3.8	44.9	253.9	56.1
		Min	0.990	0.0018	271.3	53.5	11.8	161.4	14.1	43.6	62.1	32.8
Ruc12	7/7	Max	1.014	0.0018	123.9	20.0	7.8	237.0	47.1	16.4	18.5	36.0
		Int	1.002	0.0030	30.4	9.6	15.8	122.1	10.3	31.6	258.3	75.9
		Min	0.984	0.0033	276.2	67.6	7.2	114.7	21.3	32.3	22.2	6.5
Ruc14	6/7	Max	1.017	0.0060	197.1	58.7	10.9	72.8	18.9	33.2	334.0	23.9
		Int	0.999	0.0027	320.8	18.6	14.9	87.9	60.8	43.4	223.1	21.7
		Min	0.984	0.0039	59.5	24.2	13.1	197.2	58.8	28.8	320.8	18.6
Ruc15	6/7	Max	1.014	0.0030	230.9	19.0	11.1	98.1	63.2	49.8	327.4	18.2
		Int	1.005	0.0018	140.9	0.1	10.0	50.6	78.1	48.5	230.9	11.9
		Min	0.978	0.0042	50.7	71.0	10.6	187.8	14.1	17.5	280.9	12.4
Whole section	6/18	Max	1.014	0.0015	160.8	13.3	7.9	19.4	73.2	16.1	253.2	10.1
		Int	1.002	0.0018	253.4	11.0	12.3	144.2	59.5	18.8	349.3	28.1
		Min	0.984	0.0024	21.8	72.7	7.6	153.1	11.6	15.6	245.7	12.7
Mont des Tempêtes section (48.88°S, 69.11°E)												
Temp1	6/7	Max	1.017	0.0033	162.4	12.5	7.6	19.2	74.5	26.6	254.5	9.0
		Int	1.011	0.0012	254.9	10.9	6.8	29.0	74.6	26.7	162.8	10.8
		Min	0.972	0.0033	24.6	73.3	5.0	208.3	16.7	8.8	118.0	1.0
Temp4	7/7	Max	1.005	0.0015	327.3	1.0	15.4	236.5	41.2	26.6	58.4	48.7
		Int	0.999	0.0006	57.6	15.5	22.9	319.8	26.2	44.1	174.9	58.9
		Min	0.996	0.0009	233.8	74.5	14.7	141.0	0.8	42.8	50.8	15.5
Temp6	5/5	Max	1.002	0.0003	18.7	8.3	27.2	268.4	67.1	54.6	111.9	21.2
		Int	0.999	0.0003	109.6	6.0	26.6	225.6	76.6	55.1	18.3	12.0

Flow	n/N		$\bar{s}$	$\delta\bar{s}$	Dec	Inc	ζ	d_ζ	i_ζ	η	d_η	i_η
		Min	0.999	0.0006	234.8	79.7	21.7	56.3	10.3	31.3	326.2	0.3
Temp8	7/7	Max	1.002	0.0006	292.7	43.7	22.3	133.9	44.2	51.9	33.2	10.8
		Int	1.002	0.0009	200.7	2.0	13.3	107.1	60.8	50.4	291.9	29.1
		Min	0.996	0.0006	108.6	46.2	13.2	217.9	17.6	26.7	322.5	38.5
Temp11	7/7	Max	1.008	0.0033	199.8	9.9	31.5	90.0	62.6	43.1	294.5	25.2
		Int	0.999	0.0027	290.5	4.4	35.2	178.3	78.5	42.3	21.4	10.6
		Min	0.990	0.0033	44.2	79.1	33.2	177.1	7.5	35.3	268.1	7.9
Temp12	5/7	Max	1.032	0.0120	172.2	2.7	9.1	264.5	40.5	23.4	79.2	49.4
		Int	0.996	0.0045	81.0	24.3	16.1	301.6	59.3	22.3	179.3	17.6
		Min	0.972	0.0087	268.1	65.5	3.3	24.8	11.6	20.7	119.3	21.3
Temp17	7/7	Max	1.002	0.0009	163.8	8.0	20.6	260.7	40.2	62.1	64.6	48.7
		Int	1.002	0.0009	71.0	19.0	25.7	210.0	65.5	67.9	335.8	15.0
		Min	0.996	0.0012	275.6	69.3	23.6	172.3	5.0	38.0	80.5	20.1
Temp18	8/8	Max	1.005	0.0012	337.3	8.1	11.5	77.5	51.5	22.9	241.1	37.3
		Int	0.999	0.0009	243.1	27.1	22.9	342.3	17.3	44.5	101.0	57.1
		Min	0.996	0.0009	82.4	61.6	11.8	339.0	7.2	43.6	245.2	27.3
Temp20	8/8	Max	1.029	0.0054	167.5	14.3	10.3	261.8	16.1	11.5	38.1	68.2
		Int	0.993	0.0027	275.4	50.4	12.8	168.0	13.9	44.4	67.6	36.2
		Min	0.981	0.0048	66.9	36.0	8.9	164.2	10.0	45.3	267.3	52.2
Whole section	9/20	Max	1.011	0.0018	168.7	7.8	5.8	275.3	64.4	7.7	75.2	24.2
		Int	0.999	0.0012	259.8	8.3	7.0	169.7	0.9	18.2	73.3	81.6
		Min	0.990	0.0015	36.1	78.6	6.4	165.8	7.4	18.1	256.9	8.7
Mont Rabouillère section (49.09°S, 69.44°E)												
Rab6	7/7	Max	1.005	0.0012	135.0	50.2	11.0	14.6	22.9	46.6	270.1	30.6
		Int	0.999	0.0012	252.4	21.0	33.5	10.0	50.4	50.6	148.6	31.8
		Min	0.993	0.0009	356.3	32.0	7.1	151.7	55.5	37.6	259.0	11.5
Rab7	7/7	Max	1.008	0.0012	252.0	82.8	12.7	17.1	4.2	61.4	107.5	5.9
		Int	1.002	0.0009	94.6	6.7	27.5	184.8	1.6	58.8	287.9	83.1
		Min	0.990	0.0015	4.3	2.7	14.6	270.2	55.8	27.1	96.1	34.1
Rab10	6/7	Max	1.011	0.0024	103.9	24.4	4.5	194.0	0.2	41.8	284.6	65.6
		Int	0.999	0.0024	243.5	59.2	32.7	347.0	7.9	41.7	81.5	29.5
		Min	0.990	0.0021	5.6	17.6	11.7	105.6	28.7	33.5	248.2	55.4
Rab11	6/7	Max	1.014	0.0024	152.9	69.5	4.3	52.2	4.0	22.3	320.7	20.1
		Int	0.999	0.0012	288.0	14.9	11.8	39.4	54.0	24.4	188.5	31.9
		Min	0.987	0.0027	21.8	13.8	5.5	125.5	44.0	21.5	278.6	42.8
Rab13	7/7	Max	1.011	0.0009	124.7	19.1	5.0	337.3	67.6	21.4	218.7	11.1
		Int	1.002	0.0006	215.8	3.2	7.6	116.7	70.9	26.5	306.9	18.8
		Min	0.987	0.0012	314.9	70.6	4.4	108.4	17.5	17.3	200.9	8.1
Rab15	4/7	Max	1.020	0.0027	152.5	85.0	14.7	339.7	5.0	34.9	249.6	0.6
		Int	0.999	0.0030	259.1	1.4	22.5	349.7	23.3	35.1	165.8	66.6
		Min	0.984	0.0024	349.2	4.8	16.1	94.0	71.7	23.0	257.7	17.6
Rab16	6/8	Max	1.008	0.0015	112.0	28.3	4.3	268.7	59.6	47.4	16.4	10.2
		Int	1.002	0.0015	15.2	12.3	23.1	258.6	64.1	48.7	110.4	22.4
		Min	0.990	0.0027	264.3	58.7	2.3	115.2	27.6	22.7	17.9	13.7
Rab19	6/7	Max	1.008	0.0048	189.3	75.1	21.5	338.7	12.9	31.6	70.4	7.3
		Int	0.996	0.0024	91.4	2.1	24.1	346.2	82.1	40.9	181.7	7.7
		Min	0.993	0.0024	0.9	14.7	23.3	249.3	54.3	38.3	100.2	31.6
Whole section	8/19	Max	1.005	0.0009	119.8	51.9	8.4	14.5	11.7	21.9	276.0	35.6
		Int	0.999	0.0009	261.6	31.6	16.2	31.8	46.3	23.7	153.6	26.7
		Min	0.993	0.0009	3.8	19.0	8.0	107.6	34.7	19.5	250.6	49.0

Flow	n/N		$\bar{s}$	$\delta\bar{s}$	Dec	Inc	ζ	d_ζ	i_ζ	η	d_η	i_η
Mont Amery section (49.29°S, 70.06°E)												
VA	6/6	Max	1.023	0.0057	84.3	25.7	15.0	204.3	46.1	16.6	336.3	32.7
		Int	0.993	0.0030	334.4	35.2	16.8	83.2	24.4	55.8	199.9	44.8
		Min	0.981	0.0051	201.8	43.8	13.0	94.3	17.4	57.2	348.4	41.1
VE	6/6	Max	1.011	0.0039	15.3	6.2	13.5	116.3	60.2	62.0	281.8	29.0
		Int	1.005	0.0015	281.2	32.9	24.4	133.9	52.5	65.2	22.0	16.0
		Min	0.984	0.0036	114.8	56.4	12.4	8.9	10.3	24.5	272.4	31.6
VF	6/6	Max	1.017	0.0036	10.3	2.2	11.1	107.0	71.6	30.8	279.5	18.2
		Int	1.005	0.0036	279.9	9.6	17.3	169.3	64.4	33.8	14.1	23.5
		Min	0.978	0.0024	113.3	80.2	8.5	13.4	1.7	21.2	283.1	9.7
Ame1	4/7	Max	1.026	0.0075	150.7	2.7	16.9	241.4	14.4	24.9	50.2	75.4
		Int	1.002	0.0063	241.0	7.3	17.0	149.3	13.3	58.6	359.2	74.8
		Min	0.972	0.0102	40.5	82.2	25.8	152.9	3.0	58.6	243.3	7.2
Ame2	5/7	Max	1.011	0.0030	326.3	16.8	16.4	234.0	7.5	90.0	120.9	71.5
		Int	0.999	0.0030	107.5	68.8	50.3	279.9	21.0	90.0	10.9	2.6
		Min	0.990	0.0033	232.4	12.5	17.5	136.0	26.7	90.0	345.1	60.1
Ame3	7/7	Max	1.026	0.0048	346.8	10.5	6.1	222.9	71.6	19.3	79.7	15.0
		Int	1.014	0.0015	79.9	16.2	7.2	285.9	72.1	20.3	172.1	7.4
		Min	0.963	0.0039	225.1	70.5	6.1	349.6	11.3	9.3	82.8	15.6
Ame4	6/7	Max	1.032	0.0051	127.1	65.7	6.8	236.2	8.4	16.9	329.7	22.6
		Int	0.993	0.0051	337.7	21.2	9.1	99.3	53.4	56.9	235.6	28.3
		Min	0.975	0.0042	243.3	11.2	7.2	129.4	63.8	52.4	338.2	23.3
Ame5	5/7	Max	1.014	0.0066	322.0	9.7	15.0	70.9	62.4	53.9	227.3	25.6
		Int	0.999	0.0024	55.1	17.9	41.1	149.4	13.0	46.2	273.4	67.7
		Min	0.987	0.0045	204.8	69.5	20.3	111.9	1.1	58.4	21.5	20.4
Ame6	6/7	Max	1.023	0.0033	151.8	10.4	5.5	242.8	5.8	11.4	1.5	78.1
		Int	0.996	0.0027	12.1	76.5	11.5	147.5	9.7	22.6	239.1	9.3
		Min	0.981	0.0051	243.3	8.6	4.9	152.8	3.2	22.6	42.6	80.9
Ame7	5/7	Max	1.032	0.0051	345.4	4.4	3.6	252.1	37.0	7.8	81.3	52.7
		Int	0.993	0.0009	254.6	10.9	4.5	164.1	2.4	15.8	61.7	78.9
		Min	0.972	0.0057	97.2	78.2	6.3	333.0	6.7	16.1	241.9	9.6
Ame8	7/7	Max	1.011	0.0012	315.7	9.4	8.2	50.5	26.7	12.8	208.0	61.4
		Int	1.002	0.0009	222.2	20.4	7.1	118.6	32.2	13.2	338.9	50.4
		Min	0.987	0.0009	69.2	67.3	7.0	266.7	21.7	13.2	174.3	6.2
Whole section	11/16	Max	1.011	0.0018	332.9	3.1	7.4	236.4	64.6	15.1	64.4	25.2
		Int	0.999	0.0018	63.8	16.3	14.3	157.2	11.6	24.4	281.2	69.8
		Min	0.990	0.0021	232.5	73.4	7.4	336.7	4.2	23.8	67.9	16.0
Port Christmas section (48.67°S, 69.02°E)												
ca1	7/7	Max	1.009	0.0045	292.5	1.9	7.7	201.9	18.9	9.4	28.0	71.0
		Int	0.999	0.0018	23.4	24.8	9.3	291.0	5.2	18.1	189.9	64.5
		Min	0.992	0.0033	198.4	65.1	5.6	96.4	5.5	19.3	3.9	24.2
ca2	7/7	Max	1.004	0.0015	111.8	17.1	5.5	231.9	58.4	36.3	13.2	25.7
		Int	1.000	0.0009	18.2	11.3	29.8	230.2	76.7	35.0	109.6	6.8
		Min	0.997	0.0012	256.4	69.3	12.1	112.3	17.0	28.4	18.7	11.4
ca6	7/7	Max	1.008	0.0009	330.3	1.7	8.2	228.8	81.5	20.7	60.6	8.3
		Int	0.999	0.0012	60.8	15.0	16.1	287.4	68.6	21.0	154.9	14.8
		Min	0.993	0.0006	234.1	74.9	7.9	137.5	1.8	16.7	47.0	15.0
ca7	7/7	Max	1.007	0.0015	209.7	21.6	8.1	355.9	64.5	31.4	114.5	12.9
		Int	1.001	0.0009	300.2	1.3	27.2	208.3	56.9	38.6	31.0	33.1
		Min	0.992	0.0015	33.4	68.3	8.9	222.3	21.4	35.1	131.1	3.1
ca14	7/7	Max	1.003	0.0006	320.1	12.1	8.7	51.6	6.9	12.6	170.5	76.0

Flow	n/N		$\bar{s}$	$\delta\bar{s}$	Dec	Inc	ζ	d_ζ	i_ζ	η	d_η	i_η
		Int	1.001	0.0006	218.7	42.6	10.5	314.3	6.1	19.9	50.8	46.8
		Min	0.996	0.0003	62.5	44.9	8.5	302.3	26.7	20.8	193.1	33.2
ca15	4/7	Max	1.062	0.0090	306.4	11.5	4.8	64.3	66.5	16.0	212.0	20.2
		Int	0.999	0.0030	214.3	10.0	5.3	79.3	76.0	15.8	306.0	9.7
		Min	0.938	0.0102	84.4	74.6	4.8	346.9	2.0	5.9	256.4	15.2
ca16	7/7	Max	1.009	0.0030	160.8	1.3	6.4	66.0	74.9	20.9	251.2	15.0
		Int	1.001	0.0009	251.3	19.7	9.1	65.0	70.2	20.9	160.6	2.0
		Min	0.990	0.0021	67.2	70.3	6.2	325.4	4.2	9.3	233.9	19.2
Whole	7/16	Max	1.010	0.0027	312.6	6.5	4.8	62.8	71.9	15.4	220.6	16.8
section		Int	1.001	0.0009	221.5	9.7	8.9	49.1	80.2	15.3	311.7	1.3
		Min	0.990	0.0030	75.7	78.3	4.9	326.6	3.9	9.1	235.9	11.0
Port Raymond section (49.34°S, 69.80°E)												
ra1	7/7	Max	1.023	0.0045	108.1	10.3	10.3	217.2	61.0	22.2	12.8	26.8
		Int	0.995	0.0042	14.2	20.8	23.2	109.3	13.2	50.8	229.6	65.0
		Min	0.982	0.0027	222.9	66.6	8.2	99.3	13.5	51.0	4.6	18.8
ra2	7/7	Max	1.026	0.0069	110.4	5.6	1.7	17.1	30.3	5.3	209.9	59.1
		Int	0.992	0.0042	15.7	39.9	1.8	108.9	3.8	16.4	203.5	49.9
		Min	0.982	0.0027	207.0	49.6	5.2	111.6	4.6	16.4	17.7	40.1
ra3	7/7	Max	1.023	0.0048	114.5	0.3	8.2	23.9	64.7	28.2	204.6	25.3
		Int	1.005	0.0057	204.6	20.5	29.8	294.6	0.0	46.9	24.7	69.5
		Min	0.972	0.0063	23.8	69.5	7.8	114.1	0.1	45.9	204.2	20.5
ra5	7/7	Max	1.028	0.0045	113.8	8.7	7.5	23.6	0.9	10.7	287.7	81.2
		Int	0.990	0.0033	13.4	49.4	9.9	117.1	11.4	56.9	216.2	38.3
		Min	0.982	0.0027	211.0	39.2	8.9	114.5	7.9	56.8	15.1	49.7
ra6	7/7	Max	1.026	0.0036	274.4	2.1	10.3	7.4	55.0	32.8	182.9	34.9
		Int	1.012	0.0027	183.4	23.5	13.8	32.3	63.6	31.8	278.5	11.3
		Min	0.962	0.0030	9.2	66.3	6.9	229.9	18.4	17.2	135.0	14.4
ra7	7/7	Max	1.012	0.0021	278.2	13.5	11.2	38.4	64.5	42.2	182.8	21.2
		Int	1.006	0.0033	181.1	26.9	15.5	58.8	46.5	43.9	289.1	31.2
		Min	0.982	0.0027	32.1	59.4	13.2	298.1	2.4	18.5	206.6	30.5
ra8	7/7	Max	1.018	0.0024	272.5	10.2	7.0	26.0	65.6	14.1	178.4	21.9
		Int	1.005	0.0015	175.3	34.8	4.5	38.1	46.6	14.2	282.1	22.5
		Min	0.977	0.0021	16.5	53.3	5.4	194.7	36.7	7.8	285.3	0.9
ra9	7/7	Max	1.015	0.0027	146.6	14.6	19.1	355.0	73.5	58.7	238.5	7.5
		Int	1.000	0.0024	56.1	1.7	23.5	316.6	80.1	59.4	146.4	9.8
		Min	0.985	0.0042	319.8	75.3	17.2	126.6	14.3	24.5	217.4	3.2
Whole	8/9	Max	1.020	0.0018	111.8	4.3	4.6	7.6	72.8	6.8	203.1	16.6
section		Int	0.999	0.0021	203.4	19.6	6.8	113.3	0.0	11.0	23.3	70.4
		Min	0.981	0.0018	9.9	69.9	4.5	115.4	5.6	11.0	207.3	19.2

n/N is the number of sample per data-set/total number of samples collected or the number of flow used/total number of flows collected. $\bar{s}$ is the eigenvalue of normalized mean susceptibility tensor. $\delta\bar{s}$ corresponds to the 95% confidence region for $\bar{s}$. *Dec* and *Inc* are the declination and the inclination of the mean susceptibility axis, respectively. ζ and η are the semiangles of minor and major axis of the 95% confidence ellipse, respectively. $d_{\zeta,\eta}$ is the declination of minor, major axis direction. $i_{\zeta,\eta}$ is the inclination of minor, major axis direction.

Combination of the obtained principal directions allowed determining mean magnetic fabric for each of the six sections (Table B.1 and right part of Fig. 4.2 and Fig. 4.3).

The three northern sections, Port Christmas, Mont des Ruches and Mont des Tempêtes, and the Mont Amery and

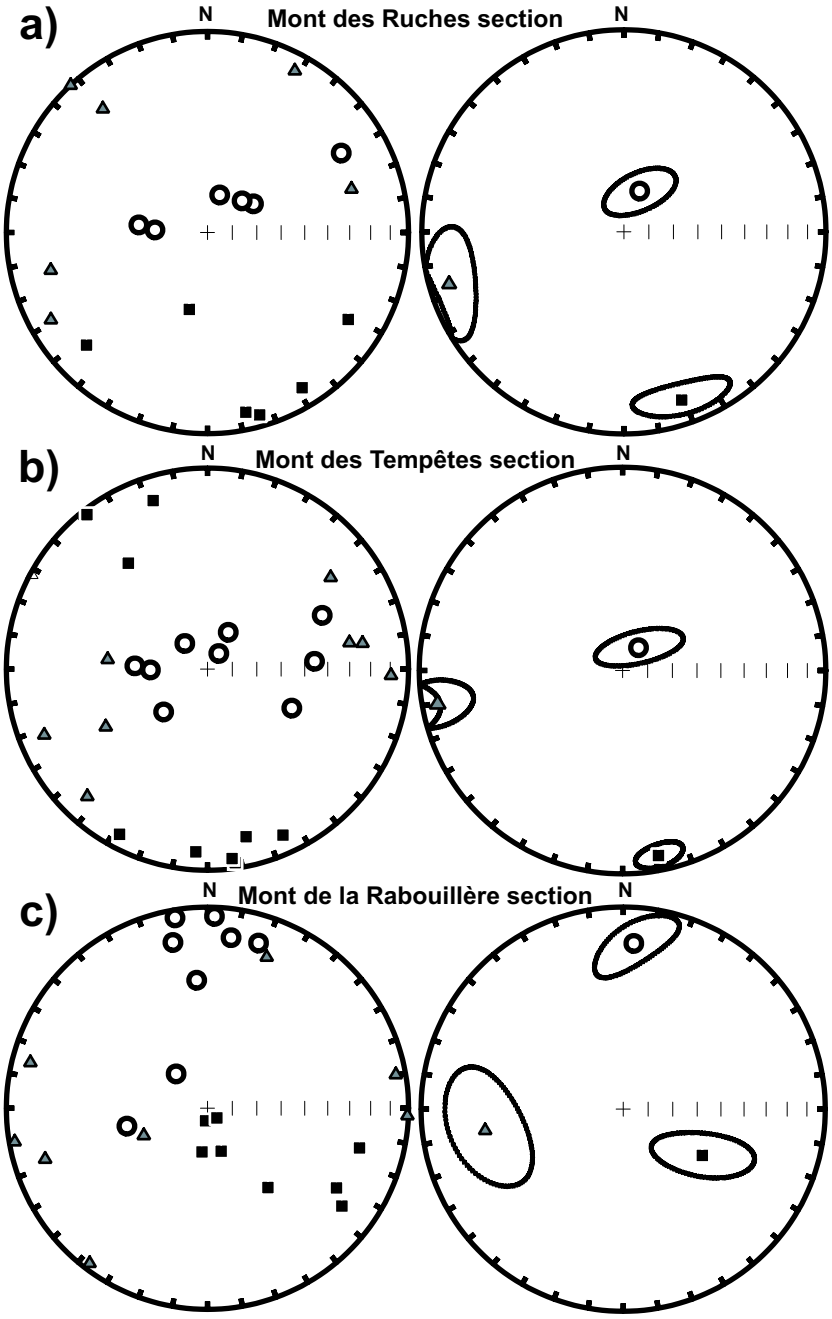

FIG. 4.2 – Flow scale analysis : left, mean principal axis of the suitable flows, right, resulting mean principal axis of each section and their 95% confidence ellipses (Constable and Tauxe, 1990). Black squares K_{max}, gray triangles K_{int} and white circles K_{min}. The equal area projections are lower hemispheres in geographic coordinates.

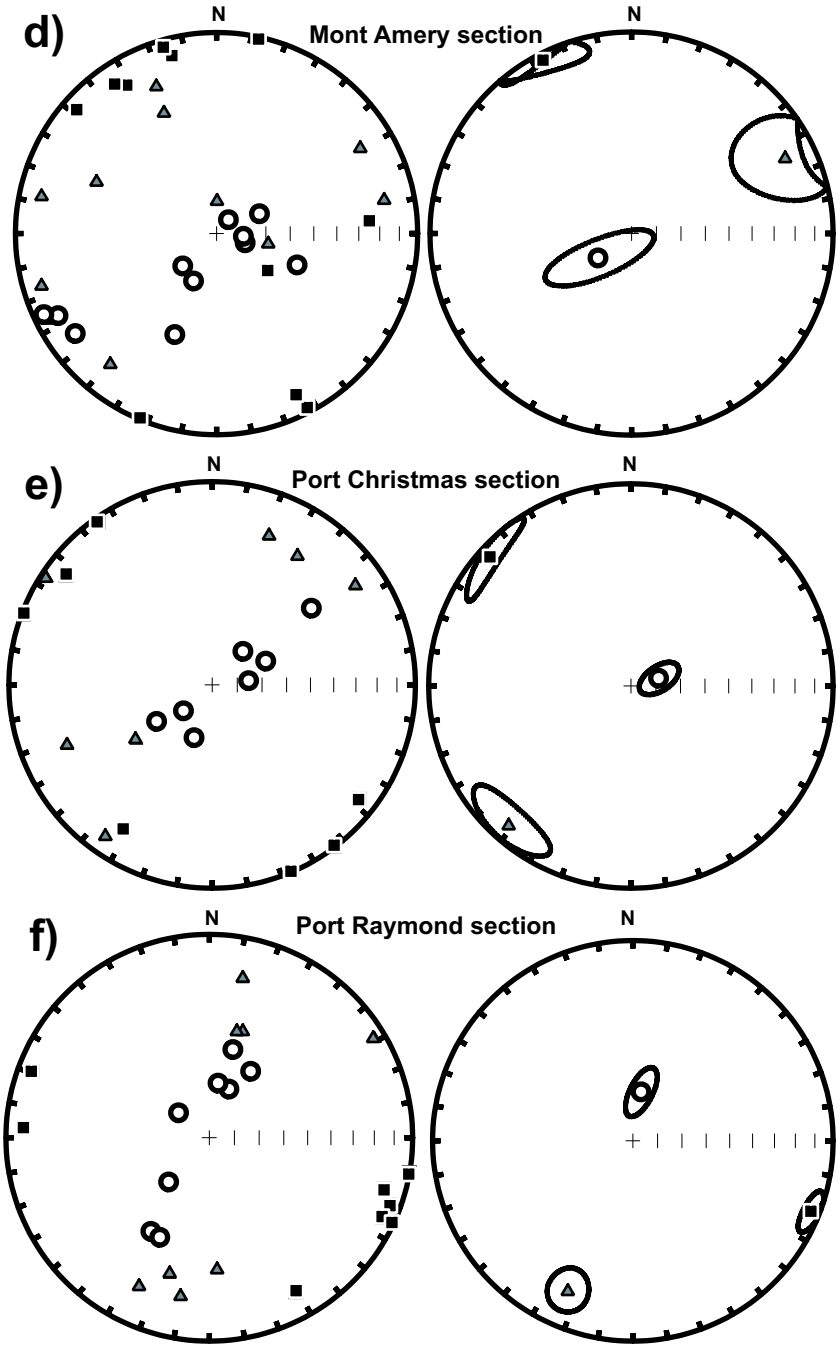

FIG. 4.3 – Flow scale analysis : left, mean principal axis of the suitable flows, right, resulting mean principal axis of each section and their 95% confidence ellipses (Constable and Tauxe, 1990). Black squares K_{max}, gray triangles K_{int} and white circles K_{min}. The equal area projections are lower hemispheres in geographic coordinates.

Port Raymond section present very similar magnetic fabric K_{max} around horizontal NNW-SSE direction and K_{min} almost vertical. Confidence zone are of variable size, from small for Port Raymond section to relatively large for Mont Amery flows. The confidence ellipse for K_{min} is elongated in a plane perpendicular to K_{max} and slightly elongated in the horizontal plane for K_{max}. For the Mont de la Rabouillère section (Fig. 4.2c), the fabric is very different : K_{max} is far from the horizontal plane, dipping of 56°towards ESE and K_{min} has a moderate plunge northwards. K_{max} confidence ellipse is elongated in a plane perpendicular to K_{min} and the one of K_{min} in a plane perpendicular to K_{max}.

4.4.2 Lumping of the flows

The preceding flow scale analysis led to reject more than half of the studied flows. However, AMS records the end of the flow emplacement (Ventura, 2001) and may relates local disturbances related for example to irregularities of the underlying flowing surface. In such a case, the more the considered flows are numerous, the more the effects of disturbed flows on the mean are limited by stacking. Thus, on the condition that the dip from flow to flow remains identical and after verification of the absence of significant evolution of the mean axes for groups of 3 to 5 lava flows, Plenier et al. (2002) and Henry et al. (2003) merged all the AMS data from successive flows of a same volcanic sequence. This method allows an increase of the reliability of the mean axes and of their confidence zones.

For the different sections analysed in the present study, no significant dip variations have been observed. The mean principal axes and their 95% confidence zones parameters have been then calculated for each lava groups (Fig. 4.4 and Fig. 4.5). For the Mont des Ruches, Mont des Tempêtes and Port Raymond sections, though in the two latter the mean directions of the last lava group are a little more scattered, the successive groups of flow recorded an almost identical mean signal. For the Mont de la Rabouillère, Mont Amery sections, the signal recorded by each group seems less consistent at the section scale, but the mean axes are not statistically different from subset to subset. For the Port Christmas section, owing permutations of K_{max} and K_{int}, the 9-12 lava group displays more scattered mean directions and these two axes are exchanged. However, the resulting mean directions display the same signal as the other lava group if their value are not taken into account. The consistency of the mean directions verified, the AMS samples data of each whole section were merged.

The mean axes orientation obtained for each section (Table B.2, Fig. 4.6 and Fig. 4.7) is very similar to that determined by flow scale analysis.

TAB. 4.2 – Directions of the mean principal susceptibilities and sizes of the confidence regions around them for the merged flows.

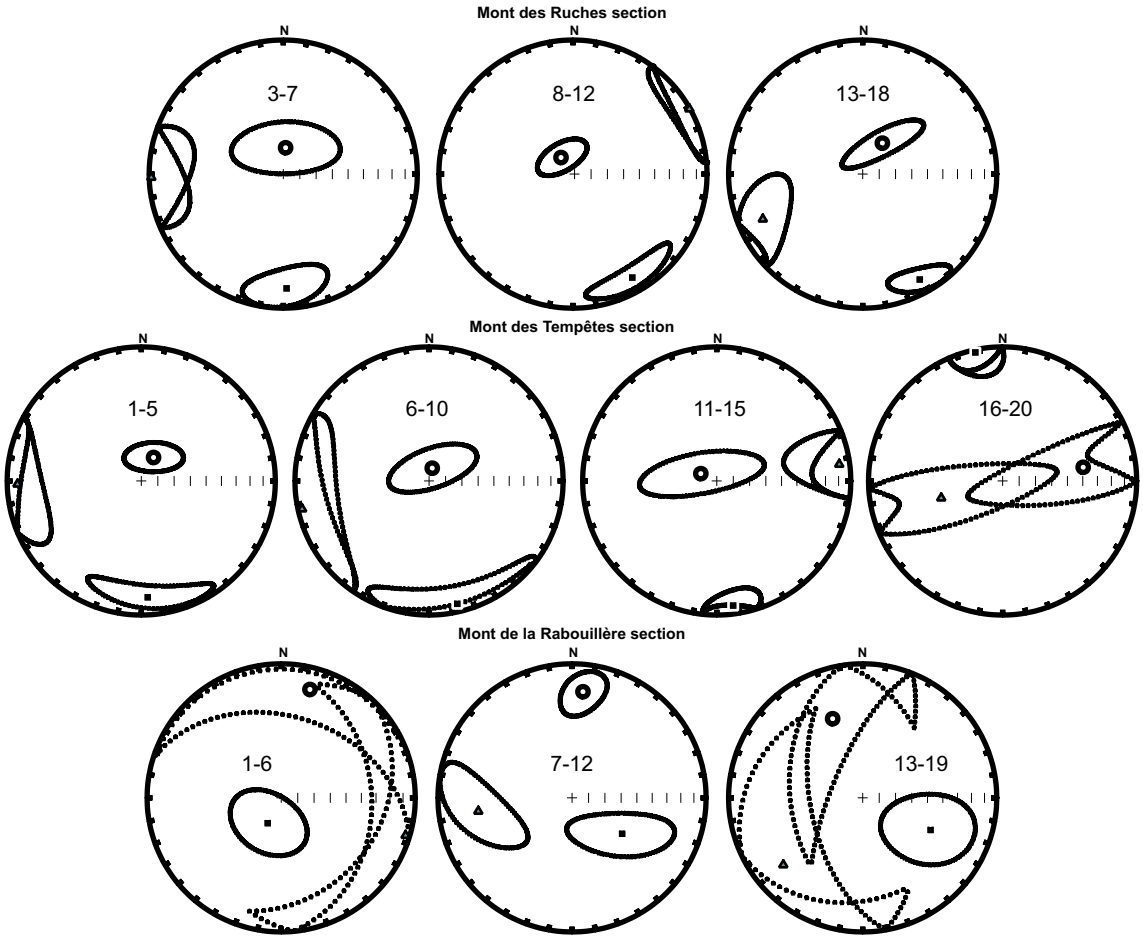

FIG. 4.4 – Successive mean principal axis and their 95% confidence ellipses (Constable and Tauxe, 1990) for the different flow groups considered at each section. Black squares K_{max}, gray triangles K_{int} and white circles K_{min}. The equal area projections are lower hemispheres in geographic coordinates.

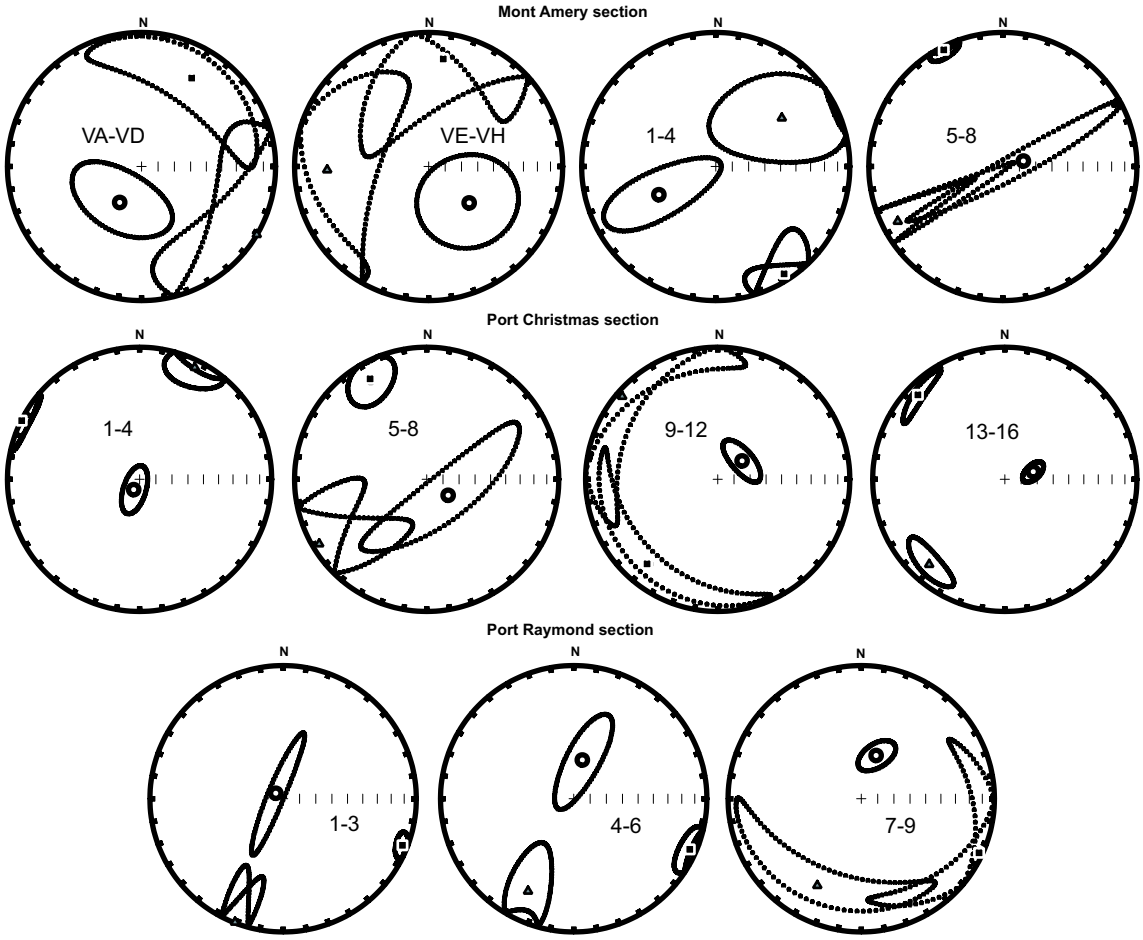

FIG. 4.5 – Successive mean principal axis and their 95% confidence ellipses (Constable and Tauxe, 1990) for the different flow groups considered at each section. Black squares K_{max}, gray triangles K_{int} and white circles K_{min}. The equal area projections are lower hemispheres in geographic coordinates.

n/N		$\bar{s}$	$\delta\bar{s}$	Dec	Inc	ζ	d_ζ	i_ζ	η	d_η	i_η
Mont des Ruches section (48.87°S, 68.91°E)											
15/18	Max	1.011	0.0015	158.0	13.0	6.3	4.6	75.5	12.4	249.5	6.3
	Int	0.999	0.0012	249.5	6.3	10.3	144.3	67.3	13.3	342.0	21.7
	Min	0.990	0.0015	4.6	75.5	6.3	153.4	12.5	11.4	245.1	7.3
Mont des Tempêtes section (48.88°S, 69.11°E)											
20/20	Max	1.008	0.0012	170.3	5.9	6.5	46.6	79.4	10.3	261.2	8.7
	Int	0.999	0.0009	261.1	7.6	10.3	169.6	11.0	15.6	25.0	76.6
	Min	0.993	0.0012	42.8	80.4	6.5	166.3	5.4	15.6	257.1	8.0
Mont Rabouillère section (49.09°S, 69.44°E)											
17/19	Max	1.005	0.0006	139.9	60.9	10.0	15.9	17.3	22.9	278.5	22.7
	Int	0.999	0.0006	266.7	18.5	12.4	11.8	37.9	23.1	156.3	46.3
	Min	0.996	0.0006	4.4	21.7	9.5	110.5	34.9	14.4	249.0	47.1
Mont Amery section (49.29°S, 70.06°E)											
16/16	Max	1.011	0.0015	340.3	9.5	10.0	228.3	65.9	16.3	74.1	21.9
	Int	0.999	0.0015	73.3	17.7	16.3	341.5	5.5	22.0	235.0	71.5
	Min	0.990	0.0018	223.3	69.8	10.1	342.5	10.2	21.9	75.7	17.2
Port Christmas section (48.67°S, 69.02°E)											
16/16	Max	1.008	0.0015	320.3	5.8	8.0	68.4	71.8	90.0	228.5	17.2
	Int	1.004	0.0012	228.7	15.5	7.4	71.0	73.3	90.0	320.4	6.0
	Min	0.988	0.0018	70.3	73.4	6.0	248.5	16.6	8.0	338.6	0.5
Port Raymond section (49.34°S, 69.80°E)											
9/9	Max	1.019	0.0015	113.3	4.0	4.4	11.8	70.4	7.1	204.7	19.1
	Int	0.998	0.0018	204.8	20.7	7.2	112.5	6.2	11.3	6.7	68.3
	Min	0.983	0.0018	12.8	68.8	4.3	116.5	5.3	11.4	208.5	20.4

n/N is the number of flow used/total number of flows collected. $\bar{s}$ is the eigenvalue of normalized mean susceptibility tensor. $\delta\bar{s}$ corresponds to the 95% confidence region for $\bar{s}$. *Dec* and *Inc* are the declination and the inclination of the mean susceptibility axis, respectively. ζ and η are the semiangles of minor and major axis of the 95% confidence ellipse, respectively. $d_{\zeta,\eta}$ is the declination of minor, major axis direction. $i_{\zeta,\eta}$ is the inclination of minor, major axis direction.

Their associated confidence zones being smaller, these mean axes are thus more precisely defined. Another difference is that the confidence zones for K_{max} and K_{min} are of neighboring size. The only exception is for the Port Christmas section because of the axes permutations between K_{max} and K_{int} evoked before. Bootstrap for Jelinek (1981) diagram (Henry, 1997a) shows (Fig. 4.6) similar mean parameters for The Mont des Ruches, Mont des Tempêtes, Mont de la Rabouillère, Mont Amery and Port Raymond sections, with a shape intermediate between prolate and oblate cases and P' between 1.01 and 1.04. For the Port Christmas section, the bootstrapped data favors an oblate shape which may explain the axes permutations observed in the horizontal plane.

4.4.3 Density diagrams

A difficulty in AMS study of volcanic flows is the possible occurrence of permutation of the principal susceptibility axes at the sample scale as well as at the flow scale. Such permutations, often observed, can be ascribed to (i) local strain changes (Merle, 1998) owing to the paleotopography or the position of the samples in the flow, (ii) composition and size of the magnetic minerals (Rochette et al., 1992), (iii) magnetic interactions of the grains (Grégoire et al.,

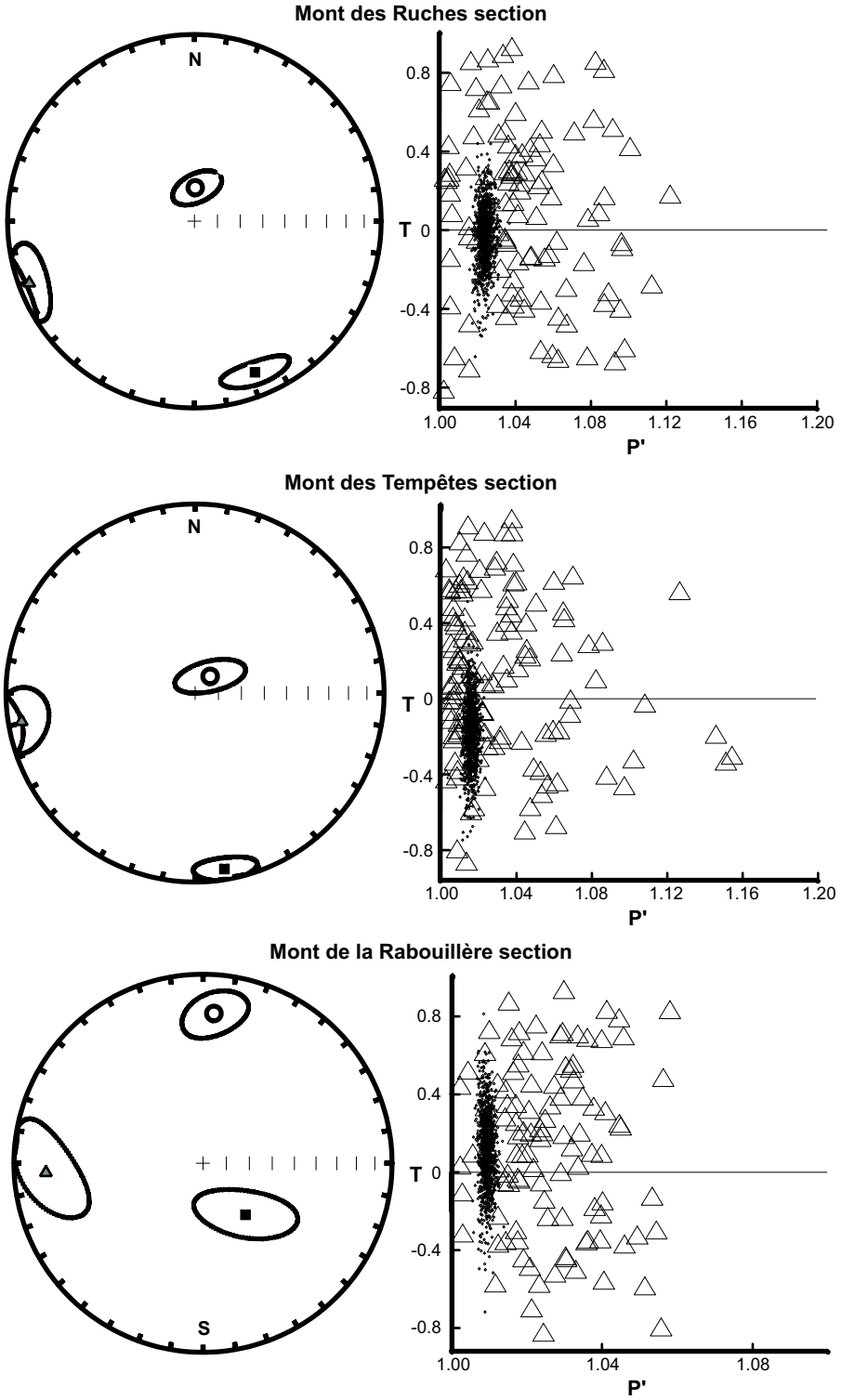

FIG. 4.6 – Section scale analysis : Mean principal axis and their 95% confidence ellipses (Constable and Tauxe, 1990) associated with Jelinek plot (Jelinek, 1981) for each section after merging of all the data together. The equal area projections are lower hemispheres in geographic coordinates, black squares represent K_{max}, gray triangles K_{int} and white circles K_{min}. For the Jelinek plots, open triangles correspond to measurements and black circles are bootstrapped data.

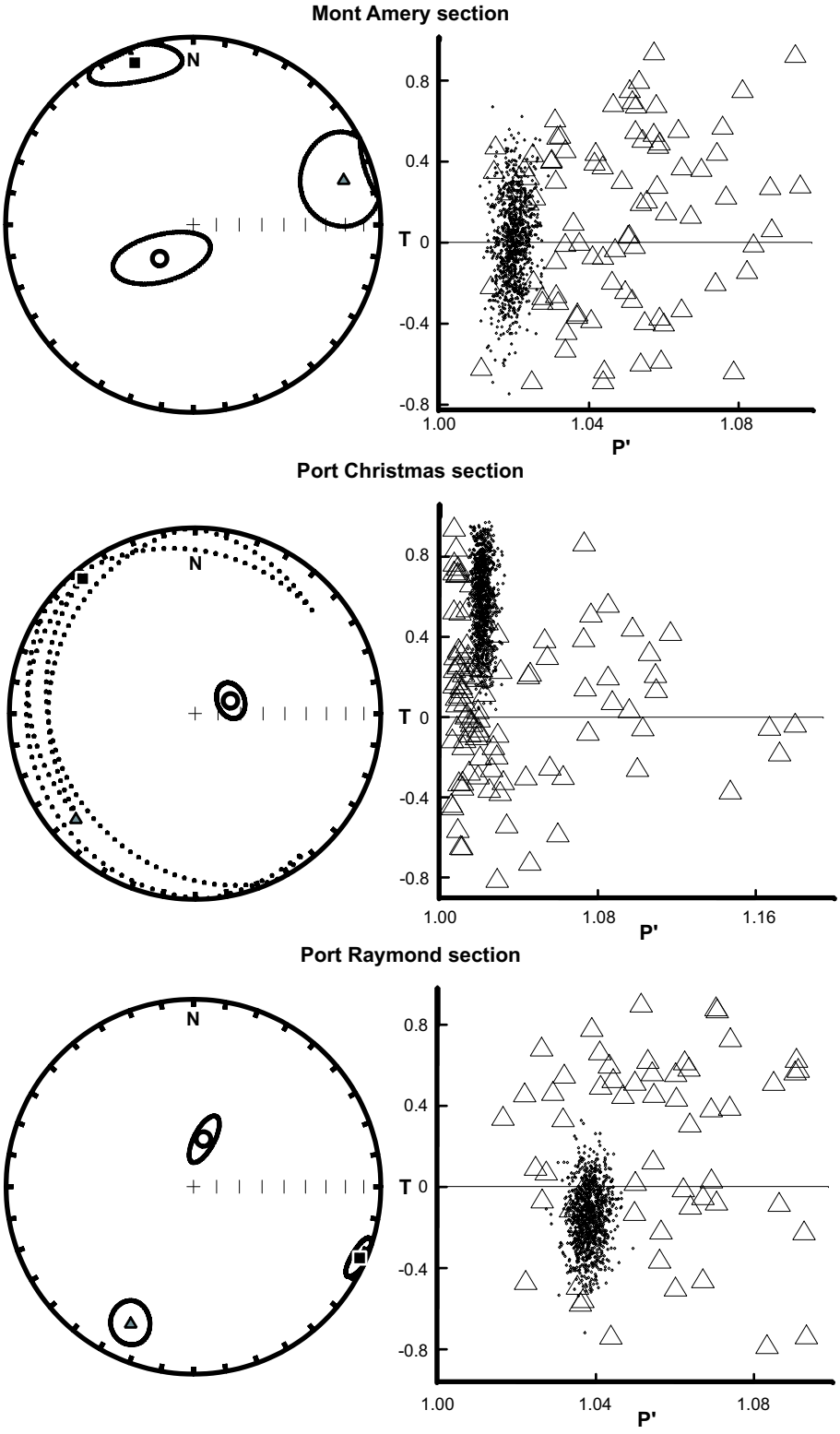

FIG. 4.7 – Section scale analysis : Mean principal axis and their 95% confidence ellipses (Constable and Tauxe, 1990) associated with Jelinek plot (Jelinek, 1981) for each section after merging of all the data together. The equal area projections are lower hemispheres in geographic coordinates, black squares represent K_{max}, gray triangles K_{int} and white circles K_{min}. For the Jelinek plots, open triangles correspond to measurements and black circles are bootstrapped data.

1995), (iV) rolling of the elongated particles in strong velocity gradients by analogy with sediments (Jeffery, 1922; Tarling and Hrouda, 1993) and (V) grain settling (Cañón Tapia et al., 1996). These permutations lead to perpendicular clusters for a same principal axis. This clearly appears using density contours on a stereonet for a large set of samples (Rochette et al., 1992). Such diagrams also often allow to better estimate the distribution symmetry relative to vertical plane of the eigenvectors. Density plots of K_{max}, K_{min} and K_{max}-K_{min} for all the AMS data of each section have been calculated.

The distribution of the principal axes (Fig. 4.8 and Fig. 4.9) are very similar for five of the studied sections (Mont des Ruches, Mont des Tempêtes, Mont Amery, Port Christmas and Port Raymond), with mostly K_{min} of high inclination and K_{max} more or less scattered around the horizontal plane. The axes for the Mont de la Rabouillère section present exactly an opposite distribution, with K_{max} of high inclination and K_{min} more or less scattered around the horizontal plane, and then clearly correspond to an inverse fabric (Rochette, 1988). Except for this latter section displaying a 30°clockwise rotation in the horizontal plane, the three mean directions isolated on the density diagrams are very similar to the three global mean eigenvectors of the section scale analysis. This indicates that permutations do not significantly affects the mean tensor directions.

The minimum axes (maximum for the Mont Rabouillère section) are however not regularly scattered around their mean direction, but mostly around a strongly dipping plane, towards NNW for the Mont des Ruches, Mont des Tempêtes and Port Raymond sections, the SSE for the Mont Amery and Port Christmas sections and the SSW for the Mont Rabouillère section. The best vertical symmetry plane of the distribution of this axis is then NNW-SSE for five sections and NNE-SSW for the sixth one and probably represents the flowing direction (Henry, 1980; Thompson et al., 1986).

The maximum axes systematically display a bimodal distribution indicating that perpendicular permutations occur frequently in the horizontal plane for all the sections. It is noteworthy that the clearest defined horizontal mean axis is always near from the intersection of the best vertical symmetry plane of the distribution of K_{min} with the horizontal plane, and probably also represents the flowing direction.

4.5 Thin sections analysis

The maximum axis of AMS (minimum axis in case of inverse fabric) being mostly either parallel or perpendicular to the flowing direction, the latter cannot be always determined from the magnetic lineation. In that case, the choice between the two possible directions can be made using the imbrication angle. Unfortunately, its orientation, taking into account the confidence zone, does not yield the choice between the two possible orientations (Fig. 4.6), except may be for the Mont des Ruches sec-

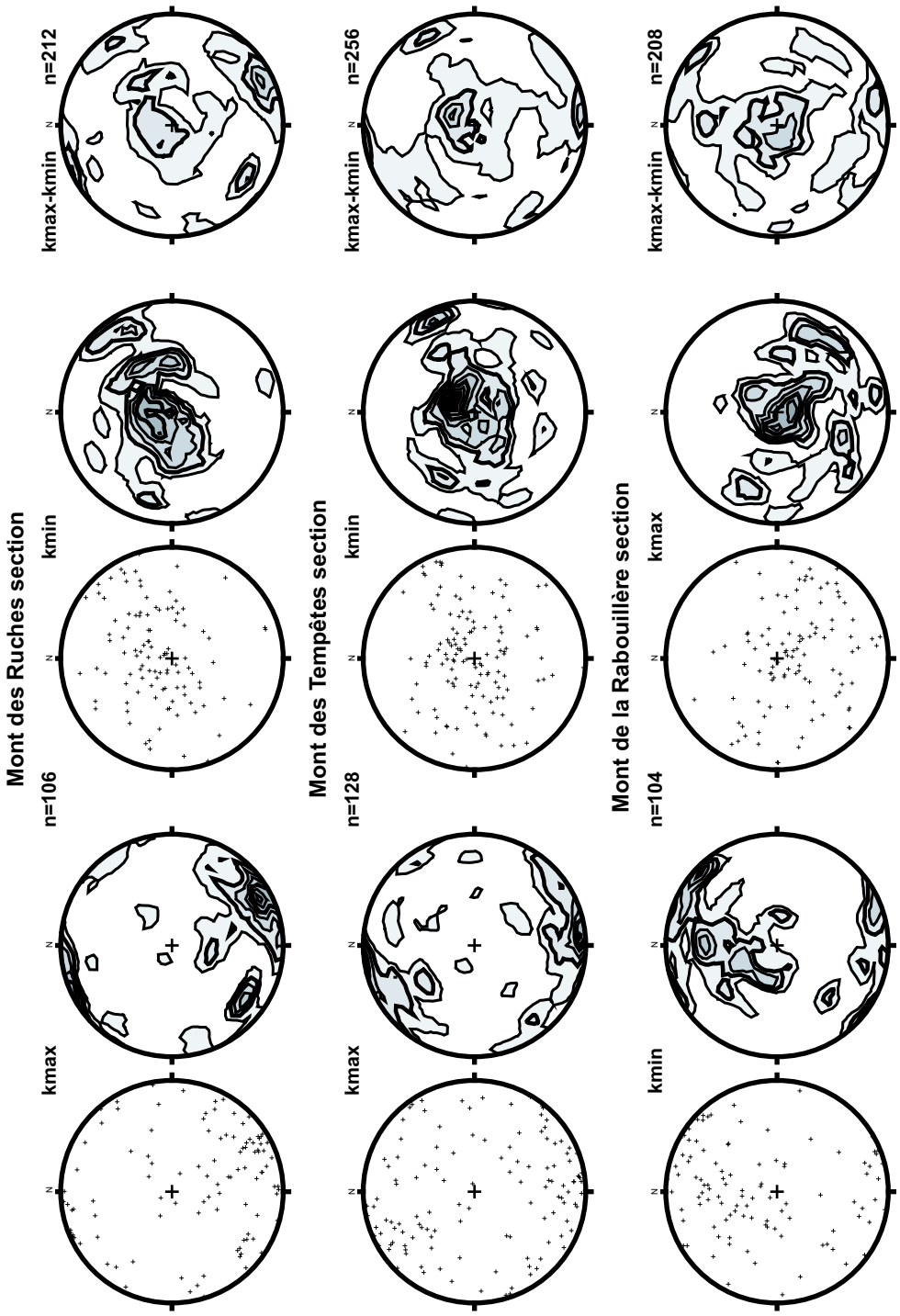

FIG. 4.8 – Horizontal (left) and vertical (center) axes associated with their density contours (stereographic projection in the lower hemisphere) for each section. The density diagrams of the maximum and minimum axes combined (left) are also displayed for each volcanic sequence.

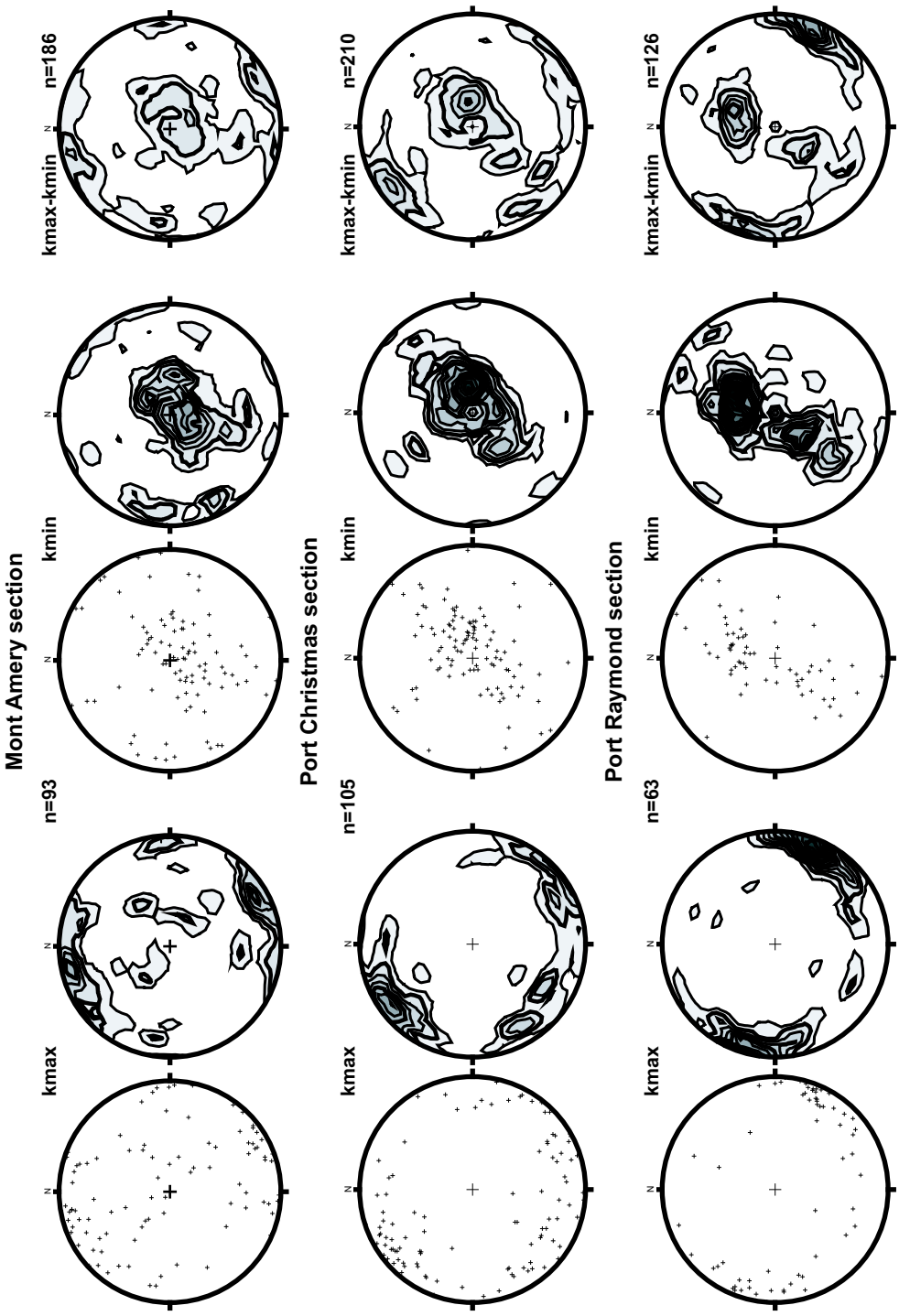

FIG. 4.9 – Horizontal (left) and vertical (center) axes associated with their density contours (stereographic projection in the lower hemisphere) for each section. The density diagrams of the maximum and minimum axes combined (left) are also displayed for each volcanic sequence.

tion, where maximum and minimum axes are in a same NNW-SSE vertical plane. Thus the choice has to be made by means of an independent flowing direction indicator (Henry, 1980; Callot et al., 2001) represented by image analysis of thin sections in this study.

We prepared polished thin sections parallel to the magnetic foliation plane (K_{max}-K_{int}) for two samples from the Mont des Tempêtes section (Fig. 4.10a and b) and two others from the Mont Amery section (Fig. 4.10d and Fig. 4.11e). We included in addition three other samples from a previous study (Plenier et al., 2002) at the Mont de la Tourmente section (Fig. 4.10c and Fig. 4.11f and g). One of these samples (Fig. 4.11f) has magnetic lineation (K_{max}) perpendicular to the interpreted flowing direction.

Depending on the grain size, one main thin section to four zoomed numeric microphotographs were taken for each thin section. After redrawing each feldspar lath, the cosine director method of Harvey and Laxton (1980) was firstly used to determine the preferred elongation axis of the plagioclases. In the absence of imbrication and for a low velocity gradient, this axis is assumed to reflect the flow direction. However, only two thin sections possessing plagioclase phenocrysts were suitable. We performed systematic analysis using the intercept method (Launeau and Bouchez, 1992), which allows random shapes to be treated (see Callot et al. (2001)). After image filtering to sharpen their bounds, the plagioclase and opaque phases were individualized in two black and white (B&W) pictures for each microphotograph. The intercept software (Launeau and Robin, 1996) yielded the direction of maximum orientation of the grain boundaries, which corresponds to the preferred elongation axis of the considered phase. The coherence between the two methods has been verified with the two thin sections (Fig. 4.10d and f) where they have been used. Results are plotted as a rose diagram with a line indicating the preferred elongated axis researched and a bold line corresponding to the long axis of a mean ellipse. The mean maximum orientation defined with the method of Harvey and Laxton (1980), when it was usable, is represented by a dashed bold line.

The thin sections presented in Fig. 4.10, display a poorly anisotropic distribution of the preferred elongated axis of each phase (shape ratio SR on the order of 1.05). The maximum direction nearest to the mean orientation is thus interpreted as indicating the flowing direction. Therefore, a relatively good agreement between the orientation of the minerals and the magnetic lineation (arrows) is observed.

For the sample e (Fig. 4.11), the contrast of color between the plagioclase laths was not enough pronounced to be able to individualize them with image filtering. The N-S maximum orientation found after analyzing the filtered B&W picture supposed to correspond to the plagioclase phase then corresponds to an artefact of the digital treatment of the microphotograph. It can be due to noise included by

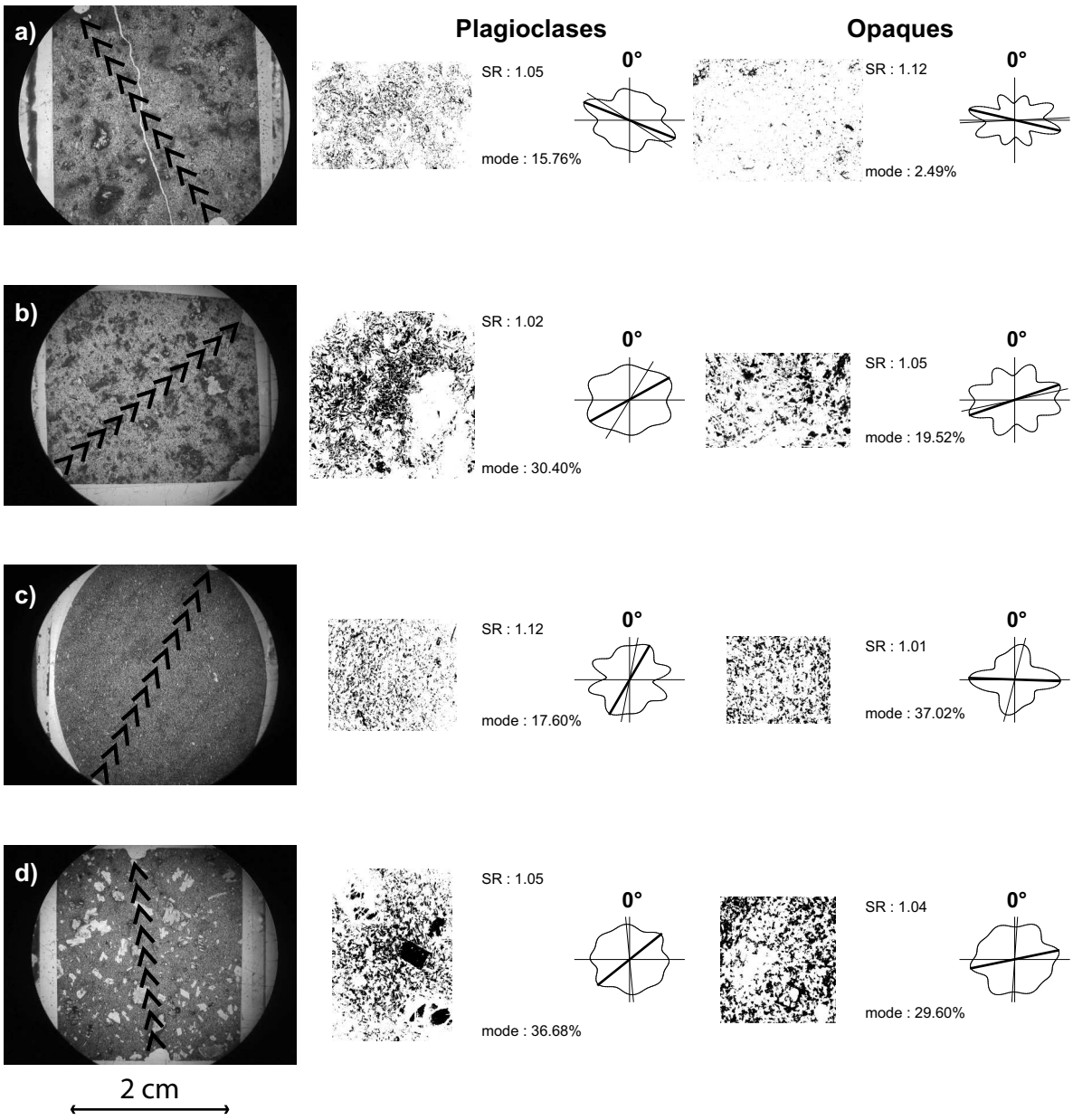

FIG. 4.10 – Shape preferential orientation (SPO) analysis of plagioclase and opaques phases : a) and b) samples from the Mont des Tempêtes section, c) from the Mont de la Tourmente lava pile and d) from the Mont Amery section. From left to right : global pictures of the thin section (not oriented), extracted black and white pictures after image filtering and their corresponding rose of direction of the plagioclase boundaries, same thing for the opaque phase. For d) and f) thin sections, the redrawn plagioclase laths pictures are given in the bottom with the corresponding rose of direction diagram. Black arrows indicate K_{max} (direction and way). For the rose diagrams, lines correspond to the long axis of the mean ellipse and bold lines are the maximum direction of the distribution.

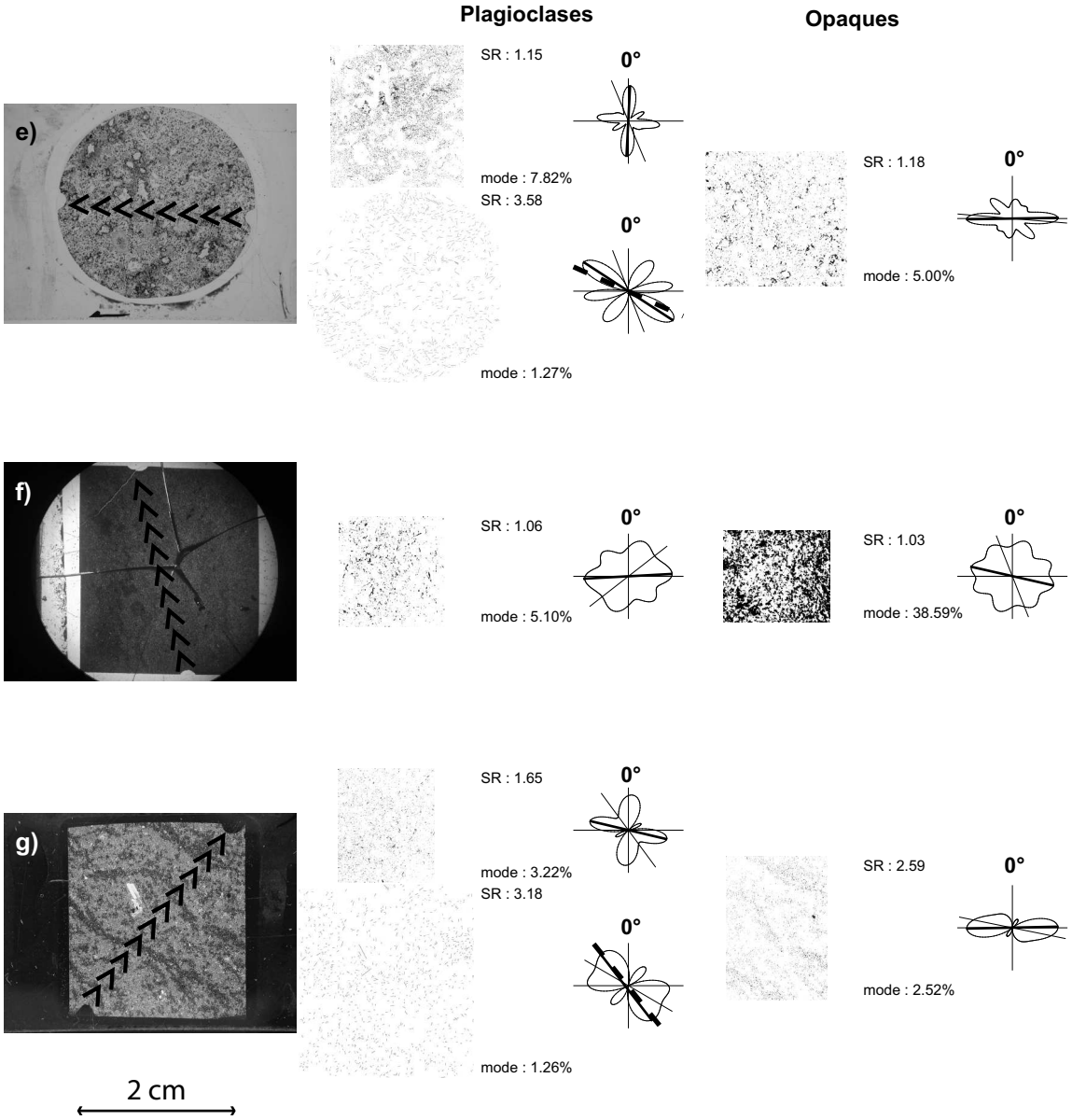

FIG. 4.11 – Shape preferential orientation (SPO) analysis of plagioclase and opaques phases : e) from the Mont Amery volcanic sequence, f) and g) samples from the Mont de la Tourmente section. From left to right : global pictures of the thin section (not oriented), extracted black and white pictures after image filtering and their corresponding rose of direction of the plagioclase boundaries, same thing for the opaque phase. For e) and g) thin sections, the redrawn plagioclase laths pictures are given in the bottom with the corresponding rose of direction diagram. Black arrows indicate K_{max} (direction and way). For the rose diagrams, lines correspond to the long axis of the mean ellipse, bold lines are the maximum direction of the distribution and dashed bold lines represent the mean orientation given by the method of Harvey and Laxton (1980).

the picture treatment as well as several groupings of plagioclase laths together with global shapes not systematically related to the flow emplacement. In that case again we interpreted the preferred elongated direction of the phases analyzed as parallel to the magnetic lineation.

On the contrary, the thin section f (Fig. 4.11), furnish a maximum elongated axis perpendicular to the magnetic lineation (arrows) for both phases. Precisely, this sample was indicated to present a magnetic lineation perpendicular to the interpreted flowing direction. Combined with the analysis of the thin section c (Fig. 4.10), this observation strongly strengthen the emplacement direction evoked for the Mont de la Tourmente section (Plenier et al., 2002).

The third sample g (Fig. 4.11) from the Mont de la Tourmente section is more problematic. For this thin section, K_{max} is parallel to the interpreted flowing direction but the elongated axes are again perpendicular to the magnetic lineation. This observation should refute the possibility of the thin section analysis to furnish a systematic answer for a given flowing direction. However, the rose of direction of the opaque phase clearly mimic the signal of the redrawn plagioclase phenocrysts picture (bottom). An anisotropy of distribution of the ferromagnetic grains crystallized along the plagioclase phenocrysts boundaries is then strongly suspected (Hargraves et al., 1991; Callot et al., 2001; Ferré et al., 2002).
We can also observe that the B&W picture of the plagioclase phase issued from image filtering furnish a bimodal distribution. This bimodality results from the superimposition in the analyzed microphotograph of plagioclases with perpendicularly oriented laths for the phenocrysts and in the groundmass, not sampled in the redrawn picture. A "rolling effect" (Jeffery, 1922; Tarling and Hrouda, 1993), which is known to influence preferentially the phenocrysts, can be expected for a 15°dip as determined for the Mont de la Tourmente section. Hence, we interpret the secondary maximum corresponding to the groundmass as a better indicator of the flowing direction. This secondary maximum direction is then in good agreement with the magnetic lineation of the sample.

4.6 Discussion and interpretation

Four different approaches were attempted to obtain the flowing direction in the different studied sections. For the flow scale analysis, the number of suitable flows, less than a half for almost all the sections, were too low to sufficiently sharpen the uncertainty zones and point out a clear indication between the two possible directions of flowing.
Without considering the Port Christmas section affected by axes permutations, lumping all the data together allowed to strongly reduce the confidence zones and, by considering all the flows, to more confidently represent the flowing direction of the lava piles. However, only the Mont des

Ruches section displayed a maximum or intermediate axis significantly distinct from the horizontal plane to indicate an unambiguous NNW-SSE flowing direction.

The analysis of density diagrams yielded symmetry of the axes distribution around a vertical plane in the six sections, therefore allowing flowing direction to be determined. For the Mont des Ruches, this direction coincides with the direction determined by analysis of the lumping of all the data. The density diagrams of the Mont de la Rabouillère section also pointed out an inverse fabric for this volcanic sequence. The predominant irreversible behavior observed in the K-T curves of this section, explain that only one flow gave a suitable paleointensity estimate and leaded to interpret this inverse magnetic fabric as related to magnetic mineralogy (Rochette et al. (1992, 1999), and references therein). Hysteresis loops were used to constrain the grain size of 4 samples from this volcanic sequence. They were comprised in the pseudo-single domain (PSD) range in a remanence versus coercivity ratios plot (Day et al., 1977). However, this PSD behavior probably results from a combination of multidomain and single domain grains, the latter producing the observed inverse magnetic fabric.

The thin sections study, furnished a shape preferential orientation (SPO) of the opaque and plagioclase phases parallel to the magnetic lineation for all the samples from the Mont des Tempêtes and Mont Amery lava piles. The three thin sections from the Mont de la Tourmente volcanic sequence incorporated in this analysis checked that the SPO is always parallel to the flowing direction, as it was interpreted in a previous study (Plenier et al., 2002).

When all the data are issued from the same part of the flow (bottom part in our case), knowing the dip of the section, it is theoretically possible to deduce its direction of flowing by imbrication (Cañón Tapia et al., 1997). Then, the departure direction of the strongly dipping mean axis from the vertical, related to imbrication, can be used alternatively to select the way of flowing between the two possible interpretations for each section. The flowing should have been towards the NNW for the Mont des Ruches, Mont des Tempêtes and Port Raymond volcanic sequences, SSW for the Mont de la Rabouillère lava pile and SSE for the Mont Amery and Port Christmas sections. However, computed flowing experience (Dragoni et al., 1997) with rotating rigid ellipsoidal magnetite in a viscous material subjected to a velocity gradient displays normal or reverse imbrication depending on the strain value for a given elongation ratio. Therefore, the magnetic imbrication cannot be used confidently to help in the interpretation. We are thus reduced to use geological and geomorphological observations to choose between the two possible ways of flowing for each interpreted direction.

For the Mont des Ruches, Mont des Tempêtes and Port Christmas sections, several observations argue for an independent volcanic province with an eruptive center located westerly or northwes-

terly to the Loranchet Peninsula (Nougier, 1970a) : western mountain axis, abrupt western coast affected by intense regressive marine erosion, shallow western submarine plateau evidenced by the isobath -200 m and surrounding the Nuageuses islands, global shallow dip toward the East or Southeast and a main morphology of ending flow at the eastern coast. Flowing direction is NNW-SSE in our sections, thus, in the absence of geological evidence for a volcanic center SSE of these two volcanic sequences, their flowing direction is interpreted from NNW to SSE, contrarily to WSW-ENE as proposed by Nougier (1970a). This flowing interpretation is also in opposite direction of that deduced from imbrication (Cañón Tapia et al., 1997) for the Mont des Ruches and Mont des Tempêtes sections and confirm that this criterion is not always reliable for deducing way of flowing. The eruptive center should be then expected under the sea level and located close to the Nuageuses islands, NNW of the Loranchet Peninsula.

The main eruptive center of the archipelago is located under the Cook glacier. It unambiguously produces the lavas forming the Mont de la Tourmente section and also probably the Mont de la Rabouillère lava pile. The flowing direction of the Mont de la Rabouillère section is then SSW to NNE interpreted, again in the opposite way than proposed with imbrication.

For the Mont Amery section, another independent eruptive center is defined in the western mountainous part of the Courbet Peninsula with clear geomorphological arguments (thickness of the lava pile, contrast with the eastern flat part,...). Even though it is not very pronounced, a divergence of the dip from a center located at Montagnes Vertes is described. Numerous dykes also are observed in this area. A well defined flowing direction oriented toward the Montagnes Vertes strengthens the interpretation of flowing from NNE to SSW with a section located very close to the supposed eruptive center.

The Port Raymond section is located at the limit between the Courbet peninsula and Cook glacier volcanic provinces. The flowing direction determined for this section favors to consider the Cook glacier as being the eruptive center and then to interpret a flowing from NNW to SSE for this section.

Figure 4.12 displays the supposed eruptive center and volcanic province limits and summarizes the flowing interpretation of each section including the results from the Mont de la Tourmente (Plenier et al., 2002) and the Port Jeanne d'Arc (Henry et al., 2003) sections. Although the lavas did not follow a straight line during emplacement, the flowing directions interpreted at each section allow refining the location of the corresponding eruptive center. This is particularly true for the northern sections, which may indicate a more northwestern eruptive center than expected by Nougier (1970a). The combination of the Mont de la Rabouillère, Mont de la Tourmente and Port Raymond sections results favors an eruptive center under the Cook glacier. The Mont Amery section strongly indicates

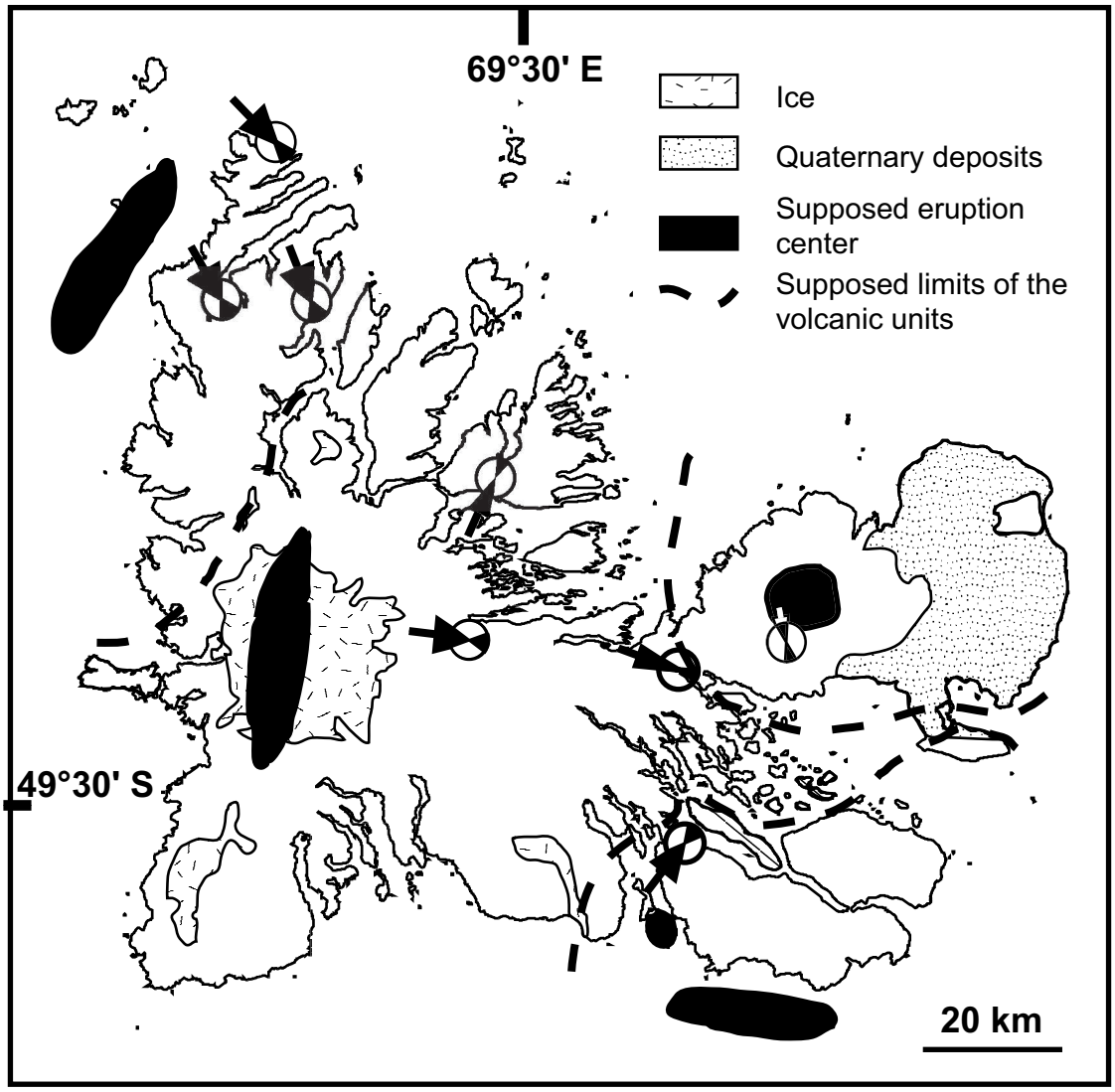

FIG. 4.12 – Summary of the interpreted flowing directions of all the sections studied so far, including the Mont de la Tourmente (Plenier et al., 2002) and the Port Jeanne d'Arc (Henry et al., 2003) sections. The volcanic province limits (dashed bold lines) and the corresponding supposed eruptive center location (in black) are also displayed after Nougier (1970a) and Leyrit et al. (1990).

a source located at the Montagnes Vertes and finally, the flowing evoked for the Port Jeanne d'Arc section defines an eruptive center in the Gaby Island direction for the sixth volcanic unit.

4.7 Conclusion

Magnetic fabric can be a useful tool for studying emplacement conditions of lava flows. Because flowing is not constrained by two walls, its interpretation is not as simple as for dykes. It implies the use of different statistical approaches and therefore has to be based on a large number of samples. Owing to local flowing deviations relative to the mean slope, these samples have to be taken in several different flows to average the effects of these disturbances. Merging of the samples from each section helps to determine the flowing direction even for a limited number of samples per flow as usually chosen for paleomagnetic or paleointensity purposes. The density diagrams, because of frequent axes permutations, are useful to observe the often complicated actual distribution of the axes. The imbrication, underlined in particular by a difference between the strongly dipping axis and the vertical, was systematically observed for all the sections. It represents, with the symmetry around a vertical plane of the axes distribution, key information to interpret the magnetic fabric data in lava flows. The thin sections study allows an independent way to infer flowing direction, but they are sometimes affected by the same indetermination as the magnetic fabric. Additionally, geomorphological and geological arguments were used at the very end of this study to infer the direction of flowing : NNW to SSE for the Mont des Ruches, Mont des Tempêtes, Mont Amery, Port Christmas and Port Raymond sections and SSW to NNE for the Mont de la Rabouillère lava pile. Even though the lavas may not flowed straight from their eruptive center during emplacement, they allowed to more precisely locate their source.

4.8 Acknowledgments

We are grateful to the "Institut Polaire Paul Emile Victor" for providing all transport facilities and for the support of this project. Special thanks to Alain Lamalle, Roland Pagny and all our field friends. We thank Mireille Perrin for her help during sampling, Michel Prévot for scientific discussions, and Charles Aubourg for reading the first version of this manuscript and for helpful comments. We also thank Christophe Nevado for preparing the thin sections. This work was partially supported by CNRS-INSU programme intérieur Terre.

Bibliographie

Borradaile, G., 1988. Magnetic susceptibility, petrofabric and strain–a review. Tectonophys. 156, 1–20.

Borradaile, G., 2001. Magnetic fabrics and petrofabrics : their orientation distributions and anisotropies. J. Struct. Geol. 23, 1581–1596.

Borradaile, G., Henry, B., 1997. Tectonic applications of magnetic susceptibility and its anisotropy. Earth-Science Reviews 42, 49–93.

Bouchez, J., 2000. Magnetic susceptibility anisotropy and fabrics in granites. C.R. Acad. Sci. Paris 330, 1–14.

Cañón Tapia, E., Walker, G., Herrero-Bervera, E., 1995. Magnetic fabric and flow direction in basaltic pahoehoe lava of Xitle volcano, Mexico. J. Volcanol. Geotherm. Res. 65, 249–263.

Cañón Tapia, E., Walker, G., Herrero-Bervera, E., 1996. The internal structure of lava flows – insights from AMS measurements I : Near-vent a'a. J. Volcanol. Geotherm. Res. 70, 21–36.

Cañón Tapia, E., Walker, G., Herrero-Bervera, E., 1997. The internal structure of lava flows – insights from AMS measurements II : Hawaiian pahoehoe, toothpaste lava and 'a'$\bar{a}$. J. of Volcanol. and Geother. Res. 76 (1-2), 19–46.

Callot, J., Geoffroy, L., Aubourg, C., Pozzi, J., Mege, D., 2001. Magma flow directions of shallow dykes from the east greenland volcanic margin inferred from magnetic fabric studies. Tectonophys. 335, 313–329.

Constable, C., Tauxe, L., 1990. The bootstrap for magnetic susceptibility tensors. J. Geophys. Res. 95 (8), 383,395.

Day, R., Fuller, M., Schmidt, V., 1977. Hysteresis properties of titanomagnetites : Grain size and composition dependence. Phys. Earth Planet. Int. 13, 260–267.

Doucet, S., Weis, D., Scoates, J., Nicolaysen, K., Frey, F., Giret, A., 2002. The depleted mantle component in Kerguelen Archipelago basalts : Petrogenesis of tholeiitic-transitional basalts from the Loranchet Peninsula. J. Petrol. 43 (7), 1341–1366.

Dragoni, M., Lanza, R., Tallarico, A., 1997. Magnetic anisotropy produced by magma flow : theoritical model and experimental data from Ferrer dolerite sills (Antarctica). Geophys. J. Int. 128, 230–240.

Ferré, E. C., Bordarier, C., Marsh, J., 2002. Magma flow inferred from AMS fabrics in a layered mafic sill, Insizwa, South Africa. Tectonophys. 354, 1–23.

Frey, F., Weis, D., Yang, H.-J., Nicolaysen, K., Leyrit, H., Giret, A., 2000. Temporal geochemical trends in Kerguelen Archipelago basalts : evidence for decreasing magma supply from the Kerguelen plume. Chem. Geol. 164, 61–80.

Geoffroy, L., Callot, J., Aubourg, C., Moreira, M., 2002. Magnetic and plagioclase linear fabric discrepancy in dykes : a new way to define the flow vector using magnetic foliation. Terra Nova 14, 183–190.

Giret, A., 1986. Géologie des Terres Australes Françaises. Bull. Com. Nation. Fr. Rech. Antarct. Paris 58, 17–41.

Giret, A., 1990. Typology, evolution, and origin of the Kerguelen plutonic series, Indian ocean : a review. Geol. J. 25, 239–247.

Glen, J., Renne, P., Milner, S., Coe, R., 1997. Magma flow inferred from anisotropy of magnetic susceptibility in the coastal Paranà-Etendeka igneous province : Evidence for rifting before flood volcanism. Geology 25 (12), 1131–1134.

Grégoire, V., de Saint Blanquat, M., Nédélec, A., Bouchez, J., 1995. Shape anisotropy versus magnetic interactions of magnetite grains : experiments and application to AMS in granitic rocks. Geophys. Res. Lett. 22 (20), 2765–2768.

Hargraves, R., Johnson, D., Chan, C., 1991. Distribution anisotropy : The cause of AMS in igneous rocks ? Geophys. Res. Lett. 18, 2193–2196.

Harvey, P., Laxton, P., 1980. The estimation of finite strain from the orientation distribution of passively deformed linear markers : eigenvalue relationships. Tectonophys. 70, 285–307.

Henry, B., 1980. Contribution à l'étude des propriétés magnétiques de roches magmatiques des Alpes : Consequences structurales, régionales et générales. Ph.D. thesis, Paris, 528 pp.

Henry, B., 1997. Bootstrap and magnetic fabric. In : EUG 9 meeting. Strasbourg, France.

Henry, B., Plenier, G., Camps, P., 2003. Magnetic fabric of Oligocene lavas in the Jeanne d'Arc peninsula (Kerguelen Islands). J. of Volcanol. and Geother. Res. submitted.

Henry, B., Plessard, C., 1997. New palaeomagnetic results from the Kerguelen Islands. Geophys. J. Int. 128 (1), 73–83.

Herrero-Bervera, E., Cañón Tapia, E., Walker, G., Tanaka, H., 2002. Magnetic fabrics study and inferred flow directions of lavas of the Old Pali Road, O'ahu, Hawaii. J. of Volcanol. and Geother. Res. , in press.

Hext, G., 1963. The estimation of second-order tensors, with related tests and designs. Biometrika 50, 353–373.

Hrouda, F., 1982. Magnetic anisotropy of rocks and its application in geology and geophysics. Geophys. Surv. 5, 37–82.

Jeffery, G., 1922. The motion of ellipsoidal particles immersed in a viscous fluid. Proc. R. Soc. London 102, 161–179.

Jelinek, V., 1978. Statistical processing of magnetic susceptibility measured in groups of specimens. Stud. Geophys. Geod. 22, 50–62.

Jelinek, V., 1981. Characterization of the magnetic fabric of rocks. Tectonophys. 79, T63–T67.

Knight, M., Walker, G., 1988. Magma flow directions in flows of the Koolau Complex, Oahu, determined from magne-

tic fabric studies. J. Geophys. Res. 93, 4308–4319.

Kolofikova, O., 1976. Geological interpretation of measurement of magnetic properties of basalts on example of the chribsky les lava flow of the Veljy Roudny volcano (Nizky Jesenik Mts.)(in Czech.). Cas. Mineral. Geol. 21, 387–396.

Launeau, P., Bouchez, J., 1992. Mode et orientation préférentielle de forme des granites par analyse d'images numériques. Bull. Soc. géol. France 163 (6), 721–732.

Launeau, P., Robin, P., 1996. Fabric analysis using the intercept method. Tectonophys. 267, 91–119.

Leyrit, H., Bardintzeff, J., Verdier, O., Giret, A., Brousse, R., 1990. Les presqu'îles Jeanne d'Arc et Ronarc'h : zone test pour une cartographie géologique au 1/100 000 des îles Kerguelen. Compt. Rend. Acad. Sci. Paris 311 (II), 561–566.

Lienert, B., 1991. Monte Carlo simulation of errors in the anisotropy of magnetic susceptibility : a second-rank symmetric tensor. J. Geophys. Res. 96, 19,539–19,544.

Merle, O., 1998. Internal strain within lava flows from analogue modelling. J. of Volcanol. and Geother. Res. 81, 189–206.

Morris, A., 2000. Magnetic fabric and palaeomagnetic analyses of the Plio-Quaternary calc-alkaline series of Aegina Island, South Aegean volcanic arc, Greece. Earth Planet. Sci. Letts. 176, 91–105.

Nicolaysen, K., Frey, F., Hodges, K., Weis, D., Giret, A., 2000. $^{40}Ar/^{39}Ar$ geochronology of flood basalts from the Kerguelen Archipelago, southern Indian Ocean : implications for Cenozoic eruption rates of the Kerguelen plume. Earth Planet. Sci. Letts. 174, 313–328.

Nougier, J., 1970. Contribution a l'étude géologique et géomorphologique des iles Kerguelen. Bull. Com. Nation. Fr. Rech. Antarct. Paris 27, 696pp.

Plenier, G., Camps, P., Coe, R., Perrin, M., 2003. Absolute palaeointensity of Oligocene (24-30 Ma) lava flows from the Kerguelen Archipelago (southern Indian Ocean). Geophys. J. Int. , submitted.

Plenier, G., Camps, P., Henry, B., Nicolaysen, K., 2002. Palaeomagnetic study of Oligocene (24-30 Ma) lava flows from the Kerguelen Archipelago (southern Indian Ocean) : directional analysis and magnetostratigraphy. Phys. Earth Planet. Int. 133, 127–146.

Rochette, P., 1988. Inverse magnetic fabric in carbonate bearing rocks. Earth Planet. Sci. Lett. 90, 229–237.

Rochette, P., Aubourg, C., Perrin, M., 1999. Is this magnetic fabric normal ? A review and case studies in volcanic formations. Tectonophys. 307, 219–234.

Rochette, P., Jackson, M., Aubourg, C., 1992. Rock magnetism and the interpretation of anisotropy of magnetic susceptibility. Rev. Geophys. 30 (3), 209–226.

Tarling, D., Hrouda, F., 1993. The Magnetic Anisotropy of Rocks. Chapman&Hall, London, 217pp.

Tauxe, L., Gee, J., Staudigel, H., 1998. Flow directions in dikes from AMS data : The bootstrap way. J. Geophys. Res. 103, 17,775–17,790.

Thompson, J., Guillaume, A., Daly, L., 1986. Paleomagnetism of the Permian volcanic rocks of Moissey (French Jura) : implications for the paleofield and tectonic evolution. Geophys. J. Roy. Astr. Soc. 86, 103–117.

Ventura, G., 2001. The strain path and emplacement mechanism of lava flows : an example from Salina (southern Tyrrhenian Sea, Italy). Earth Planet. Sci. Letts. 188, 229–240.

Weis, D., Damasceno, D., Frey, F., Nicolaysen, K., Giret, A., 1998. Temporal isotopic variations in the Kerguelen plume : evidence from the Kerguelen Archipelago. Miner. Mag. 62A, 1643–1644.

Weis, D., Giret, A., 1994. Kerguelen plutonic complexes : Sr, nd, pb isotopic study and inferences about their sources, age and geodynamic setting. Mem. Soc. Géol. Fr. 166, 47–59.

Yang, H.-J., Frey, F., Weis, D., Giret, A., Pyle, D., Michon, G., 1998. Petrogenesis of the flood basalts forming the northern Kerguelen Archipelago : Implications for the Kerguelen plume. J. Petrol. 39 (4), 711–748.

Conclusion Générale

Ces trois années d'étude m'ont permis de répondre de façon satisfaisante aux objectifs fixés en début de thèse. En ce qui concerne l'étude des fluctuations du champ magnétique terrestre, la désaimantation minutieuse (essentiellement par traitement thermique) de chacun des échantillons issus des sections oligocènes des Monts des Ruches, des Tempêtes, de la Tourmente, Amery et de la Rabouillère nous a permis de définir convenablement les directions d'aimantation primaires de chacune des coulées prélevées. C'est ce qu'attestent la dispersion intra-coulée relativement faible et la réponse positive au test d'inversion exposés dans le premier chapitre. Ce résultat positif du test d'inversion indique par ailleurs que pour l'intervalle de temps de mise en place des sections, nos données moyennent bien la variation séculaire. L'estimation que nous en avons faite est en accord avec le modèle G de variation séculaire entre 22.5 et 45 Ma proposé par McFadden et al. (1991), lequel considère un champ paléomagnétique de symétrie axiale et équatoriale. L'archipel des Kerguelen étant localisé dans l'hémisphère Sud, cette concordance avec le modèle G confirme l'hypothèse de symétrie équatoriale assumée par celui-ci. Cependant, ce dernier modèle était le seul à notre disposition pour des âges oligocènes. Il manque en particulier pour cette époque des familles de modèles de variation paléoséculaire anisotropes, tels que ceux présentés par Constable and Johnson (1999) pour les 5 derniers Ma. Il serait intéressant à l'avenir de développer ce genre de modèles afin de tester leur compatibilité avec les fluctuations de direction mais aussi d'intensité enregistrées par les laves de Kerguelen.

Malheureusement, la prospection d'enregistrements détaillés de renversements du champ magnétique terrestre n'a pas été aussi fructueuse que nous l'aurions souhaité. Bien que des successions de polarité magnétique différentes soient observées, seules quelques coulées intermédiaires, définies par un pôle géomagnétique virtuel (PGV) avec un écart de plus de 45° avec l'axe de rotation de la terre, ont été obtenues et toujours entre des coulées présentant une même polarité du champ. Celle décrite pour la section du Mont des Ruches, troublante de part la position de son pôle géomagnétique virtuel à l'aplomb d'une zone supposée de localisation préférentielle des PGVs durant des renversements (Hoffman, 1996), est interprétée comme un rebond lors du passage d'une polarité normale à inverse du CMT. Cette observation tend à indiquer que la section du Mont des Ruches au moins aurait enregistré l'enchainement de l'ensemble des périodes de polarité fixe s'étant produit durant sa mise en place. Le nombre important de coulées intermédiaires observées pour les sections des Monts de la Tourmente et de la Rabouillère pourrait cependant traduire l'existence de hiatus dans l'enregistrement de la polarité pour ces dernières sections.

En prévision de l'étude de paléointensité qui devait suivre, une analyse de la variation de susceptibilité magnétique en température (k-T) mesurée sous vide nous a permis d'estimer la minéralogie magnétique des laves échantillonnées. Deux types de comportements distincts ont été identifiés : soit l'assemblage non stable thermiquement d'une titanomagnétite originale avec des titanomaghémites issues de son oxydation à basse température

(maghémitisation), soit des titanomagnétites faiblement enrichies en Titane, stables thermiquement au contraire et produites par une oxyexolution à haute température de l'ensemble des titanomagnétites originales. Une estimation de la part d'aimantation visqueuse pouvant être portée par chacun des échantillons a aussi été réalisée. Il en ressort que l'ensemble des sections présente une aimantation visqueuse du même ordre de grandeur que celle attendue pour les roches volcaniques de surface (6.1% d'après Prévot (1981)), à l'exception de la section du Mont de la Tourmente pour laquelle des coefficients de viscosité anormalement élevés, et encore mal expliqués, ont été trouvés.

L'étude de paléointensité proprement dite a ensuite été menée sur les sections des Monts des Ruches, des Tempêtes et de la Rabouillère. Elle s'est déroulée en deux étapes avec tout d'abord la sélection, à l'aide de différents critères *a priori* , des coulées pouvant potentiellement fournir des résultats fiables, dans le but de constituer une série d'échantillons pilotes. Un à deux échantillons des 32 coulées ainsi sélectionnées (parmi les 57 initiales) ont constitué une première série de détermination de la paléointensité du CMT. Suite à cette analyse pilote, douze coulées ont ensuite été analysées en intégralité et finalement, 102 échantillons auront été traités au total. S'appuyant sur des critères *a posteriori* relativement stricts, 49 d'entre eux ont fournit des estimations supposées fiables et 12 estimations moyennes à l'échelle de la coulée ont été définies. Ces données constituent les premières estimations de bonne qualité technique obtenues pour l'archipel des Kerguelen. La moyenne arithmétique de leurs moments dipôlaires virtuels (VDM), s'élève à $6.15 \pm 2.1\ 10^{22} Am^2$. Après sélection, ces nouvelles estimations doublent le nombre de données oligocènes de qualité comparable disponibles dans la base internationale de paléointensité de l'IAGA (Perrin and Schnepp, 2003) et contribuent à augmenter de façon sensible la moyenne arithmétique des VDMs pour cette période (de 4.1 ± 0.5 à $5.4 \pm 2.3\ 10^{22} Am^2$). Les estimations de paléointensité à partir d'une aimantation rémanente de type cristalline étant théoriquement beaucoup plus faibles que pour une aimantation thermo-rémanente, les déterminations élevées obtenues dans cette étude pourrait indiquer que l'aimantation primaire enregistrée par les laves de Kerguelen est bien une aimantation de type thermo-rémanente, peu ou pas perturbée par une aimantation secondaire cristalline. Quoi qu'il en soit, l'estimation de paléointensité du CMT à l'oligocène reste dans le même ordre de grandeur que celle déterminée pour des âges compris entre 0.3 et 300 Ma (Selkin and Tauxe, 2000) et renforce l'idée de valeurs anormalement élevées obtenues pour le champ magnétique récent ($8\ 10^{22} Am^2$).

L'apport des nouvelles directions et intensités du CMT enregistrées depuis l'oligocène à Kerguelen et présentées dans ce travail est important mais bien loin de combler le manque de données expérimentales dont nous faisions part dans l'introduction. Des études sys-

tématiques similaires, en plus grand nombre et reparties de façon uniforme à la surface du globe pour des intervalles de temps aussi étroits que possibles sont donc encore nécessaires. Pour la seule région de Kerguelen, l'analyse des sections échantillonnées au cours de la dernière campagne de prélèvement dans la partie Sud de l'archipel (Plaine Ampère) est à réaliser ainsi que l'étude de paléointensité des sections des Monts Amery et de la Tourmente, que je n'avais pas eu le temps matériel de traiter ici. Les résultats des sections échantillonnées durant la campagne d'été 1997-1998, non encore publiés à ce jour, viendront aussi se rajouter à cette masse de nouveaux enregistrements oligocènes à venir (Camps et al., 2003).

Concernant l'apport de ce travail aux connaissances de la géologie de Kerguelen, la magnétostratigraphie établie suite à l'étude des directions magnétiques nous a permis de mieux contraindre les intervalles de temps de mise en place de chaque section et par conséquent mieux estimer les taux d'extrusions de chacune d'elles. En effet, en considérant l'ensemble des intervalles de polarité (chrons) du CMT comme enregistré durant la mise en place de ces sections, notre interprétation de corrélation avec une échelle magnétostratigraphique globale (Huestis and Acton, 1997), à l'aide de datations absolues et d'observations géochimiques (Yang et al., 1998; Nicolaysen et al., 2000; Doucet et al., 2002), nous a permis de limiter la durée de mise en place des sections du Mont des Ruches entre 28.7 et 28.1 Ma, du Mont des Tempêtes entre 28.6 et 28.1 Ma, des Monts Amery et de la Tourmente entre 25.3 et 24.9 Ma ainsi que du Mont de la Rabouillère entre 29.7 et 28.7 Ma. Les taux d'éruption correspondant à cette meilleure estimation des temps de mise en place de chacune des sections sont respectivement de 0.35, 0.43, 0.96, 1.31 et 0.3 km/Ma. Ils présentent donc des variations non négligeables de section à section avec la confirmation d'une tendance à l'augmentation pour les sections les plus récentes. Cette observation est en désaccord avec l'hypothèse de taux d'extrusions constants durant la période éocène-oligocène qui avait été proposée au préalable (Nicolaysen et al., 2000).

Le principal apport à ce dernier objectif provient cependant de l'étude de la fabrique magnétique effectuée pour chacune des sections. L'étude préliminaire de la section de Port Jeanne d'Arc a permis de retracer l'historique probable de l'emplacement de celle-ci : épanchement de la première unité volcanique depuis le centre éruptif localisé sur l'île de Gaby, remaniement de la paléosurface topographique et dépôt en bas de pente de tuffs bréchiatiques et de conglomérats, mise en place de la seconde unité volcanique issue du même centre éruptif et léger basculement de l'ensemble de la section dû très probablement à l'activité volcanique plus tardive exprimée dans cette région de l'archipel.

Ces premiers résultats concluants nous ont alors poussés à mener plus avant ces analyses d'anisotropie de susceptibilité magnétique, avec l'étude de la section du Mont de la Tourmente tout d'abord. Nous avons pu montrer que le pendage observé actuellement à l'affleurement était en fait très probablement préexistant à la mise en place des coulées de cette section. Par conséquent, aucune correction tectonique ne fut appliquée lors de l'étude des directions paléomagnétiques. Cette seconde étude, bien qu'ayant soulevé des problèmes propres à l'utilisation de l'anisotropie de susceptibilité magnétique seule pour retrouver la direction et le sens de mise en place d'empilements de coulées de laves, a elle aussi contribué à ce que nous continuions ces études de fabrique magnétique pour les autres sections prélevées dans l'archipel. Il s'agissait de mieux contraindre la localisation des différents centres éruptifs supposés auparavant par des observations de terrain uniquement (Nougier, 1970a). D'un point de vue méthodologique, l'utilisation d'une méthode indépendante de détermination des directions d'écoulement, à savoir l'orientation préférentielle de forme (OPF) de certaines phases minérales, nous a permis de conforter les interprétations de mise en place que nous avions faites après analyse de l'anisotropie de susceptibilité. Il semblerait d'autre part que nous ayons mis en évidence une caractéristique systématique de la position de l'axe minimal de susceptibilité magnétique par rapport à la direction d'écoulement. Ce dernier aurait tendance à être dispersé dans la direction perpendiculaire à nos interprétations d'écoulement et ce pour l'ensemble des sections étudiées à ce jour.

Les perspectives impliquées par ces dernières études sur des laves sont donc plutôt alléchantes. Si il s'avère que l'analyse de l'anisotropie de susceptibilité magnétique, rapide et non destructrice, permet à elle seule de définir convenablement la direction de mise en place d'une section, celle-ci pourrait être réalisée de façon systématique pour les études directionnelles d'empilements de laves basculés à condition d'avoir limité l'échantillonnage à la partie inférieure des coulées. Cela permettrait, comme nous l'avons vu pour la section du Mont de la Tourmente, d'indiquer si des corrections de pendages sont judicieuses à effectuer plutôt que de les appliquer automatiquement lorsque de tels cas se présentent actuellement. Ces études relativement faciles et rapides à mettre en oeuvre permettraient en outre en indiquant la direction du centre éruptif de mettre en évidence une possible évolution de la localisation des sources, information utile dans le cadre d'une étude géologique locale, comme celle menée pour la section de Port Jeanne d'Arc. Cependant, le caractère systématique de la position de l'axe de susceptibilité minimum par rapport à la direction d'écoulement doit être validé au préalable afin de ne pas avoir nécessairement recours à d'autres méthodes plus lourdes et plus coûteuses en temps pour estimer de façon sûre la direction de mise en place d'une section. Pour cela, une étude de référence qui porterait sur des coulées de différent type, pour contrôler la relation entre cette observation

et le changement de minéralogie magnétique ou de dynamique de mise en place, et dont la direction et le sens d'écoulement sont connus, est nécessaire. En attendant, les résultats des analyses de fabrique magnétique, menées sur d'autres sections prélevées au préalable sur Kerguelen et qui seront étudiées prochainement, devraient s'ajouter à ceux présentés dans le quatrième chapitre de cette thèse dans le but de localiser de façon plus précise encore les centre éruptifs. Ils devraient aussi permettre d'infirmer ou au contraire nous l'espérons de confirmer nos premières interprétations.

Bibliographie

Arai, Y., 1963. Secular variation in the intensity of the past geomagnetic field. Master's thesis, Univ. of Tokyo, Tokyo, Japan.

Aubert de la Rüe, E., 1932. Etude géologique et géographique de l'archipel de Kerguelen. Rev. Géogr. Géol. Dyn. 5, 231 pp.

Bol'shakov, A., Scherbakova, V., 1979. Thermomagnetic criterion for determining the domain structure of ferrimagnetics. Izvest. Earth Phys. 15, 111–116.

Borradaile, G., 1988. Magnetic susceptibility, petrofabric and strain–a review. Tectonophys. 156, 1–20.

Borradaile, G., 2001. Magnetic fabrics and petrofabrics : their orientation distributions and anisotropies. J. Struct. Geol. 23, 1581–1596.

Borradaile, G., Henry, B., 1997. Tectonic applications of magnetic susceptibility and its anisotropy. Earth-Science Reviews 42, 49–93.

Bouchez, J., 2000. Magnetic susceptibility anisotropy and fabrics in granites. C.R. Acad. Sci. Paris 330, 1–14.

Brown, H., Khan, M., Stacey, F., 1964. A search for flow structure in columnar basalts using magnetic anisotropy of rocks. Pure Appl. Geophys. 57, 61–65.

Brunhes, B., 1906. Recherches sur la direction d'aimantation des roches volcaniques. J. Phys. 5, 705–724.

Buffet, B., 2000. Earth's core and the Geodynamo. Science 288, 2007–2012.

Cañón Tapia, E., Pinkerton, H., 2000. The anisotropy of magnetic susceptibility of lava flows : an experimental approach. J. Volcanol. Geotherm. Res. 98, 219–233.

Cañón Tapia, E., Walker, G., Herrero-Bervera, E., 1995. Magnetic fabric and flow direction in basaltic pahoehoe lava of Xitle volcano, Mexico. J. Volcanol. Geotherm. Res. 65, 249–263.

Cañón Tapia, E., Walker, G., Herrero-Bervera, E., 1996. The internal structure of lava flows – insights from AMS measurements I : Near-vent a'a. J. Volcanol. Geotherm. Res. 70, 21–36.

Cañón Tapia, E., Walker, G., Herrero-Bervera, E., 1997. The internal structure of lava flows – insights from AMS measurements II : Hawaiian pahoehoe, toothpaste lava and 'a'ā. J. of Volcanol. and Geother. Res. 76 (1-2), 19–46.

Callot, J., Geoffroy, L., Aubourg, C., Pozzi, J., Mege, D., 2001. Magma flow directions of shallow dykes from the east greenland volcanic margin inferred from magnetic fabric studies. Tectonophys. 335, 313–329.

Calvo, M., Prévot, M., Perrin, M., Riisager, J., 2002. Investigating the reasons for the failure of palaeointensity experiments : A study on historical lava flows from Mt. Etna (Italy). Geophys. J. Int. 149 (1), 44–63.

Camps, P., Henry, B., Plenier, G., 2003. Statistical properties of paleomagnetic directions in Kerguelen lava flows. Geochem. Geophys. Geosystems in preparation.

Camps, P., Henry, B., Prévot, M., 1999. Paleomagnetism of volcanic rocks from Kerguelen archipelago (24-30 Ma) : Implications for the palaeosecular variation in the southern Indian Ocean. In : XXII UGGI Gener. Assemb. Birmingham.

Carvallo, C., Camps, P., Ruffet, G., Henry, B., Poidras, T., 2002. Mono lake or Laschamp geomagnetic event recorded from lava flows in Amsterdam Island (southeastern Indian Ocean). Geophys. J. Int. submitted.

Coe, R., 1967a. The determination of paleointensities of the earth's magnetic field with emphasis on mechanisms which could cause non-ideal behaviour in thellier's method. J. Geomag. Geoelect. 19, 157–179.

Coe, R., 1967b. Paleointensities of the earth's magnetic field determined from tertiary and quaternary rocks. J. Geophys. Res. 72, 3247–3262.

Coe, R., Grommé, S., Mankinen, E., 1978. Geomagnetic paleointensities from radiocarbon-dated lava flows on Hawaii and the question of the Pacific nondipole low. J. Geophys. Res. 83, 1740–1756.

Coe, R., Grommé, S., Mankinen, E., 1984. Geomagnetic paleointensities from excursion sequences in lavas on oahu, hawaii. J.Geophys.Res. 89, 1059–1069.

Constable, C., Johnson, C., 1999. Anisotropic paleosecular variation models : implications for geomagnetic field observables. Phys. Earth Planet. Int. 115, 35–51.

Constable, C., Tauxe, L., 1990. The bootstrap for magnetic susceptibility tensors. J. Geophys. Res. 95 (8), 383,395.

Cox, A., 1969. Confidence limits for the precision parameter k. Geophys. J. R. astr. Soc. 18, 545–549.

David, P., 1904. Sur la stabilité de la direction d'aimantation dans quelques roches volcaniques. C. R. Acad. Sci. Paris 138, 41–42.

Day, R., Fuller, M., Schmidt, V., 1977. Hysteresis properties of titanomagnetites : Grain size and composition dependence. Phys. Earth Planet. Int. 13, 260–267.

Derder, M., 1989. Contribution à la paléointensité du champ magnétique terrestre d'après l'étude de roches magmatiques quaternaires, miocènes et jurassiques. Ph.D. thesis, Orsay, France.

Derder, M., Plessard, C., Daly, L., 1990. Mise en évidence d'une transition de polarité du champ magnétique terrestre dans les basaltes miocènes des îles Kerguelen. C. R. Acad. Sci. Paris 310 (II), 1401–1407.

Dormy, E., Valet, J., Courtillot, V., 2000. Numerical models of the geodynamo and observational constraints. Geochem. Geophys. Geosystems 1 (2000GC000062).

Doucet, S., Weis, D., Scoates, J., Nicolaysen, K., Frey, F., Giret, A., 2002. The depleted mantle component in Kerguelen Archipelago basalts : Petrogenesis of tholeiitic-transitional basalts from the Loranchet Peninsula. J. Petrol. 43 (7), 1341–1366.

Dragoni, M., Lanza, R., Tallarico, A., 1997. Magnetic anisotropy produced by magma flow : theoritical model and experimental data from Ferrer dolerite sills (Antarctica). Geophys. J. Int. 128, 230–240.

Duncan, R., 2002. A time frame for construction of the Kerguelen Plateau and Broken Ridge. J. Petrol. 43, 1109–1119.

Dunlop, D., Özdemir, O., 2001. Beyond Néel's theories : thermal demagnetization of narrow-band partial thermoremanent magnetizations. Phys. Earth Planet. Int. 126, 43–57.

Ellwood, B., 1978. Flow and emplacement direction determined for selected basaltic bodies using magnetic anisotropy measurement. Earth Planet. Sci. Lett. 41, 254–264.

Fabian, K., 2001. A theoritical treatment of paleointensity determination experiments on rocks containing pseudo-single or multi domain magnetic particles. Earth Planet. Sci. Letts. 188, 45–58.

Ferré, E. C., Bordarier, C., Marsh, J., 2002. Magma flow inferred from AMS fabrics in a layered mafic sill, Insizwa, South Africa. Tectonophys. 354, 1–23.

Fisher, R., 1953. Dispersion on a sphere. Proc. R. Soc. London Ser A (217), 295–305.

Frey, F., Weis, D., Yang, H.-J., Nicolaysen, K., Leyrit, H., Giret, A., 2000. Temporal geochemical trends in Kerguelen Archipelago basalts : evidence for decreasing magma supply from the Kerguelen plume. Chem. Geol. 164, 61–80.

Frey, F., Nicolaysen, K., Kubit, B.K., Weis, D., Giret, A., 2002. Flood basalt from Mont Tourmente in the central Kerguelen Archipelago : the change from transitional to alcalic basalt at ≈25 Ma. J. Petrol. 43, 7, 1367-1387.

Gautier, I., 1987. Les basaltes des îles Kerguelen (Terres Australes et Antarctiques Françaises. Ph.D. thesis, Paris, France.

Gautier, I., Weis, D., Mennessier, J., Vidal, P., Giret, A., Loubet, M., 1990. Petrology and geochemistry of the Kerguelen Archipelago basalts (south Indian Ocean) : evolution of the mantle sources from ridge to intraplate position. Earth Planet. Sci. Letts 100, 59–76.

Geoffroy, L., Callot, J., Aubourg, C., Moreira, M., 2002. Magnetic and plagioclase linear fabric discrepancy in dykes : a new way to define the flow vector using magnetic foliation. Terra Nova 14, 183–190.

Giret, A., 1986. Géologie des Terres Australes Françaises. Bull. Com. Nation. Fr. Rech. Antarct. Paris 58, 17–41.

Giret, A., 1990. Typology, evolution, and origin of the Kerguelen plutonic series, Indian ocean : a review. Geol. J. 25, 239–247.

Glen, J., Renne, P., Milner, S., Coe, R., 1997. Magma flow inferred from anisotropy of magnetic susceptibility in the coastal Paranà-Etendeka igneous province : Evidence for rifting before flood volcanism. Geology 25 (12), 1131–1134.

Goguitchaichvili, A., Alva-Valdivia, L., Urrutia-Fucugauchi, J., Zesati, C., Caballero, C., 2001. Paleomagnetic and paleointensity study of Oligocene volcanic rocks from Chihuahua (northern Mexico. Phys. Earth Planet. Int. 124, 223–236.

Goguitchaichvili, A., Prévot, M., Camps, P., 1999a. No evidence for strong fields during the R3-N3 icelandic geomagnetic reversal. Earth Planet. Sci. Lett. 167, 15–34.

Goguitchaichvili, A., Prévot, M., Thompson, J., Roberts, N., 1999b. An attempt to determine the absolute geomagnetic field intensity in Southwestern Iceland during the Gauss-Matuyama reversal. Phys. Earth Planet. Int. 115, 53–66.

Grégoire, V., de Saint Blanquat, M., Nédélec, A., Bouchez, J., 1995. Shape anisotropy versus magnetic interactions of magnetite grains : experiments and application to AMS in granitic rocks. Geophys. Res. Lett. 22 (20), 2765–2768.

Gubbins, D., 1999. The distinction between geomagnetic excursions and reversals. Geophys. J. Int. 137 (1), F1–F3.

H., L., 1992. Kerguelen : cartographie et magmatologie des presqu'îles Jeanne d'Arc et Ronarc'h. Ph.D. thesis, Orsay, France.

Halvorsen, E., 1974. The magnetic fabric of some dolerite intrusions, northeast Spitsbergen : implications for the emplacement. Earth Planet. Sci. Lett. 21, 127–133.

Hargraves, R., Johnson, D., Chan, C., 1991. Distribution anisotropy : The cause of AMS in igneous rocks ? Geophys. Res. Lett. 18, 2193–2196.

Harvey, P., Laxton, P., 1980. The estimation of finite strain from the orientation distribution of passively deformed linear markers : eigenvalue relationships. Tectonophys. 70, 285–307.

Henry, B., 1980. Contribution à l'étude des propriétés magnétiques de roches magmatiques des Alpes : Consequences structurales, régionales et générales. Ph.D. thesis, Paris, 528 pp.

Henry, B., 1997a. Bootstrap and magnetic fabric. In : EUG 9 meeting. Strasbourg, France.

Henry, B., 1997b. The magnetic zone axis : a new element of magnetic fabric for the interpretation of the magnetic lineation. Tectonophys. 271, 325–329.

Henry, B., Le Goff, M., 1995. Application of the bivariate extension of Fisher's statistics to the magnetic susceptibility anisotropy data : integration of the measurment uncertainties on the orientation of the principal directions. C.R. Acad. Sci. Paris 320 (IIa), 1037–1042.

Henry, B., Plenier, G., Camps, P., 2003. Magnetic fabric of Oligocene lavas in the Jeanne d'Arc peninsula (Kerguelen Islands). J. of Volcanol. and Geother. Res. submitted.

Henry, B., Plessard, C., 1997. New palaeomagnetic results from the Kerguelen Islands. Geophys. J. Int. 128 (1), 73–83.

Herrero-Bervera, E., Cañón Tapia, E., Walker, G., Tanaka, H., 2002. Magnetic fabrics study and inferred flow directions of lavas of the Old Pali Road, O'ahu, Hawaii. J. of Volcanol. and Geother. Res. , in press.

Hext, G., 1963. The estimation of second-order tensors, with related tests and designs. Biometrika 50, 353–373.

Hoffman, K., 1996. Transitional paleomagnetic field behavior : Preferred paths or patches ? Surv. Geophys. 17 (2), 207–211.

Hrouda, F., 1982. Magnetic anisotropy of rocks and its application in geology and geophysics. Geophys. Surv. 5, 37–82.

Huestis, S., Acton, G., 1997. On the construction of geomagnetic timescales from nonprejudicial treatment of magnetic anomaly data from multiple ridges. Geophys. J. Int. 129 (1), 176–182.

Jacobs, J., 1994. Reversals of the Earth's magnetic field, Cambridge University Press Edition. the Press Syndicate of the University of Cambridge.

Jeffery, G., 1922. The motion of ellipsoidal particles immersed in a viscous fluid. Proc. R. Soc. London 102, 161–179.

Jelinek, V., 1978. Statistical processing of magnetic susceptibility measured in groups of specimens. Stud. Geophys. Geod. 22, 50–62.

Jelinek, V., 1981. Characterization of the magnetic fabric of rocks. Tectonophys. 79, T63–T67.

Juarez, M., Tauxe, L., 2000. The intensity of the time-averaged geomagnetic field : the last 5Myr. Earth Planet. Sci. Lett. 175, 169–180.

Juarez, M., Tauxe, L., Gee, J., Pick, T., 1998. The intensity of the Earth's magnetic field over the past 160 million years. Nature 394, 878–881.

Khan, M., 1962. The anisotropy of magnetic susceptibility of some igneous and metamorphic rocks. J. Geophys. Res. 67, 2873–2885.

Kirschvink, J., 1980. The least-squares line and plane and the analysis of paleomagnetic data. Geophys. J. R. Astr. Soc. 62, 699–718.

Knight, M., Walker, G., 1988. Magma flow directions in flows of the Koolau Complex, Oahu, determined from magnetic fabric studies. J. Geophys. Res. 93, 4308–4319.

Kolofikova, O., 1976. Geological interpretation of measurement of magnetic properties of basalts on example of the chribsky les lava flow of the Veljy Roudny volcano (Nizky Jesenik Mts.)(in Czech.). Cas. Mineral. Geol. 21, 387–396.

Kosterov, A., Prévot, M., 1998. Possible mechanism causing failure of the Thellier paleointensity experiments in some basalts. Geophys. J. Int. 134, 554–572.

Launeau, P., Bouchez, J., 1992. Mode et orientation préférentielle de forme des granites par analyse d'images numériques. Bull. Soc. géol. France 163 (6), 721–732.

Launeau, P., Robin, P., 1996. Fabric analysis using the intercept method. Tectonophys. 267, 91–119.

Le Mouël, J., 1984. Outer core geostrophic flow and secular variation of Earth's geomagnetic field. Nature 311, 734–735.

Leong, W., Stacey, F., 1966. Magnetic anisotropy of laboratory materials in which magma flow is simulated. Pure Appl. Geophys. 64, 78–80.

Levi, S., 1977. The effect of magnetite particle size on paleointensity determinations of the geomagnetic field. Phys. Earth Planet. Int. 13, 245–259.

Leyrit, H., Bardintzeff, J., Verdier, O., Giret, A., Brousse, R., 1990. Les presqu'îles Jeanne d'Arc et Ronarc'h : zone test pour une cartographie géologique au 1/100 000 des îles Kerguelen. Compt. Rend. Acad. Sci. Paris 311 (II), 561–566.

Lienert, B., 1991. Monte Carlo simulation of errors in the anisotropy of magnetic susceptibility : a second-rank symmetric tensor. J. Geophys. Res. 96, 19,539–19,544.

Love, J., 2000. Statistical assessment of preferred transitional vgp longitudes based on paleomagnetic volcanic data. Geophys. J. Int. 140, 211–221.

McElhinny, M., Lock, J., 1996. IAGA paleomagnetic databases with access. Surv. Geophys. 17 (5), 575–591.

McFadden, P., Merrill, R., McElhinny, M., Sunhee, L., 1991. Reversals of the Earth's magnetic field and temporal variations of the dynamo families. J. Geophys. Res. 96 (B3), 3923–3933.

Merle, O., 1998. Internal strain within lava flows from analogue modelling. J. of Volcanol. and Geother. Res. 81, 189–206.

Merrill, R., McElhinny, M., Stevenson, D., 1979. Evidence for long-term asymmetries in the Earth's magnetic field and possible implications for dynamo theories. Phys. Earth Planet. Inter. 20, 75–82.

Merrill, R., McFadden, P., 1999. Geomagnetic polarity transitions. Rev. Geophys. 37 (2), 201–226.

Morris, A., 2000. Magnetic fabric and palaeomagnetic analyses of the Plio-Quaternary calc-alkaline series of Aegina Island, South Aegean volcanic arc, Greece. Earth Planet. Sci. Letts. 176, 91–105.

Murase, T., Mc Birney, A., 1973. Properties of some common igneous rocks and their melts at high temperatures. Geol. Soc. Amer. Bull. 84, 3563–92.

Nagata, T., Arai, Y., Momose, K., 1963. Secular variation of the geomagnetic total force during the last 5,000 years. J. Geophys. Res. 68, 5277–5282.

Nicolaysen, K., Frey, F., Hodges, K., Weis, D., Giret, A., 2000. $^{40}Ar/^{39}Ar$ geochronology of flood basalts from the Kerguelen Archipelago, southern Indian Ocean : implications for Cenozoic eruption rates of the Kerguelen plume. Earth Planet. Sci. Letts. 174, 313–328.

Nougier, J., 1965. Etudes des formations de Port Jeanne d'Arc (Archipel des Kerguelen. Bull. Com. Nation. Fr. Rech. Antarct. Paris 11, 29–55.

Nougier, J., 1970a. Contribution a l'étude géologique et géomorphologique des iles Kerguelen. Bull. Com. Nation. Fr. Rech. Antarct. Paris 27, 696pp.

Nougier, J., 1970b. Terres Australes et Antarctique Françaises (T.A.A.F.), Kerguelen Islands reconnaissance map, 1 :200 000. Instit. Geograph. Nat'l., Paris .

Özdemir, O., 1987. Inversion of titanomaghemites. Phys. Earth Planet. Int. 46, 184–196.

Perrin, M., 1998. Paleointensity determination, magnetic domain structure, and selection criteria. J. Geophys. Res. 103, 30591–30600.

Perrin, M., Schnepp, E., Shcherbakov, V., 1998. Paleointensity database updated. EOS 79 (16), 198.

Perrin, M., Schnepp, L., 2003. IAGA paleointensity database. in preparation .

Perrin, M., Shcherbakov, V., 1997. Paleointensity of the Earth's magnetic field for the past 400 ma : Evidence for a dipole structure during the mesozoic low. J. Geomag. Geoelect. 49, 601–614.

Plenier, G., Camps, P., Coe, R., Perrin, M., 2003. Absolute palaeointensity of Oligocene (24-30 Ma) lava flows from the Kerguelen Archipelago (southern Indian Ocean). Geophys. J. Int. , submitted.

Plenier, G., Camps, P., Henry, B., Nicolaysen, K., 2002. Palaeomagnetic study of Oligocene (24-30 Ma) lava flows from the Kerguelen Archipelago (southern Indian Ocean) : directional analysis and magnetostratigraphy. Phys. Earth Planet. Int. 133, 127–146.

Prévot, M., 1981. Some aspects of magnetic viscosity on subaerial and submarine volcanic rocks. Geophys. J. R. Astr. Soc. 66, 169–192.

Prévot, M., Mankinen, E., Coe, R., Grommé, C., 1985. The Steens Mountain (Oregon) geomagnetic polarity transition. 2. field intensity variations and discussion of reversal models. J. Geophys. Res. 90, 10417–10448.

Prévot, M., Mankinen, E., Grommé, C., Lecaille, A., 1983. High paleointensities of the geomagnetic field from thermomagnetic studies on rift valley pillow basalts from the mid-Atlantic ridge. J. Geophys. Res. 88, 2316–2326.

Riisager, J., 1999. Variation en direction et en intensité du champ magnétique terrestre a la fin du Mesozoique et au Cenozoique. Ph.D. thesis, University of Montpellier, 168 pp.

Riisager, P., Riisager, J., 2001. Detecting multidomain magnetic grains in Thellier palaeointensity experiments. Phys. Earth Planet. Int. 125, 111–117.

Rochette, P., 1988. Inverse magnetic fabric in carbonate bearing rocks. Earth Planet. Sci. Lett. 90, 229–237.

Rochette, P., Aubourg, C., Perrin, M., 1999. Is this magnetic fabric normal ? A review and case studies in volcanic formations. Tectonophys. 307, 219–234.

Rochette, P., Jackson, M., Aubourg, C., 1992. Rock magnetism and the interpretation of anisotropy of magnetic susceptibility. Rev. Geophys. 30 (3), 209–226.

Schlich, R., Giret, A., 1994. Géologie, géochimie et géophysique des Kerguelen. Mem. Soc. Géol. Fr., 108p, 11 contributions.

Selkin, P., Tauxe, L., 2000. Long-term variations in palaeointensity. Phil. Trans. R. Soc. Lond. 358 (A), 1065–1088.

Shcherbakov, V., Shcherbakova, V., Vinogradov, Y., Heider, F., 2001. Thermal stability of pTRMs created from different magnetic states. Phys. Earth Planet. Int. 126, 59–73.

Shcherbakova, V., Shcherbakov, V., Heider, F., 2000. Properties of partial thermoremanent magnetization in pseudosingle domain and multidomain magnetite grains. J. Geophys. Res. 105 (B1), 767–781.

Symons, D., 1967. The magnetic and petrologic properties of a basalt column. Geophys. J. Roy. Astron. Soc. 12, 473–490.

Tanaka, H., Kono, M., 1984. Analysis of the thelliers' method of paleointensity determination, 2. applicability to high and low magnetic fields. J. Geomag. Geoelect. 36, 285–297.

Tanaka, H., Kono, M., Uchimura, H., 1995. Some global features of paleointensity in geological time. Geophys. J. Int. 120, 97–102.

Tarling, D., Hrouda, F., 1993. The Magnetic Anisotropy of Rocks. Chapman&Hall, London, 217pp.

Tauxe, L., 1998. Paleomagnetic Principles and Practice. Kluwer, Dordrecht.

Tauxe, L., Gee, J., Staudigel, H., 1998. Flow directions in dikes from AMS data : The bootstrap way. J. Geophys. Res. 103, 17,775–17,790.

Tauxe, L., Kylstra, N., Constable, C., 1991. Bootstrap statistics for paleomagnetic data. J. Geophys. Res. 96, 11723–11740.

Thellier, E., 1938. Sur l'aimantation des terres cuites et ses applications géophysiques. Ann. Inst. Physique du Globe, Univ. Paris 16, 157–302.

Thellier, E., Thellier, O., 1944. Recherches géomagnétiques sur des coulées volcaniques d'Auvergne. Ann. Geophys. 1, 37–52.

Thellier, E., Thellier, O., 1959. Sur l'intensité du champ magnétique terrestre dans le passé historique et géologique. Ann. Geophys. 15, 285–376.

Thompson, J., Guillaume, A., Daly, L., 1986. Paleomagnetism of the Permian volcanic rocks of Moissey (French Jura) : implications for the paleofield and tectonic evolution. Geophys. J. Roy. Astr. Soc. 86, 103–117.

Ventura, G., 2001. The strain path and emplacement mechanism of lava flows : an example from Salina (southern Tyrrhenian Sea, Italy). Earth Planet. Sci. Letts. 188, 229–240.

Violat, C., 1972. Contribution à l'étude de l'anisotropie magnétique des roches volcaniques. Ph.D. thesis, Paris.

Weis, D., Damasceno, D., Frey, F., Nicolaysen, K., Giret, A., 1998. Temporal isotopic variations in the Kerguelen plume : evidence from the Kerguelen Archipelago. Miner. Mag. 62A, 1643–1644.

Weis, D., Giret, A., 1994. Kerguelen plutonic complexes : Sr, nd, pb isotopic study and inferences about their sources, age and geodynamic setting. Mem. Soc. Géol. Fr. 166, 47–59.

Wilson, R., 1962. The paleomagnetism of baked contact rocks and reversals of the earth's magnetic field. Geophys. J. Roy. Astron. Soc. 7, 194–202.

Yang, H.-J., Frey, F., Weis, D., Giret, A., Pyle, D., Michon, G., 1998. Petrogenesis of the flood basalts forming the northern Kerguelen Archipelago : Implications for the Kerguelen plume. J. Petrol. 39 (4), 711–748.

Liste des tableaux

Table des figures

Annexes

Avant propos

La première partie de ces annexes vise à expliquer en quelques lignes la méthode bootstrap que nous avons été amenés à utiliser durant le test d'inversion présenté en première partie et les études de la fabrique magnétique.

En seconde partie de ces annexes sont regroupées succinctement les informations glanées sur le terrain durant l'échantillonnage des différentes sections prélevées dans le cadre du programme Paléomagne 310.

Vous trouverez ensuite la reproduction exacte d'un article paru dans *Marine Geophysical Researches*. Celui-ci expose les résultats obtenus durant mon stage de D.E.A. encadré par Mireille Perrin et Michel Prévot, intitulé : «Paléomagnétisme de laves du Nord de l'ophiolite d'Oman ». Des analyses complémentaires réalisées durant les premiers mois de ma thèse ainsi que des résultats provenant du D.E.A. d'Emmanuel Cocuaud encadré lui aussi par Mireille PERRIN auparavant, ont été ajoutés pour compléter cette étude.

L'ensemble des données acquises durant cette thèse est disponible sur le site :

ftp.univ-montp2.fr/pub/paleomag/These-plenier/

Leur mise à disposition vise à permettre au lecteur de juger de leur qualité en toute objectivité. Il s'agit des données non interprétées qui pourraient éventuellement servir si des recherches postérieures à ces travaux remettaient totalement ou partiellement nos résultats en cause. La compilation de données antérieures qu'il m'a été donné de réaliser durant l'étude de paléointensité m'a appris à quel point nos interprétations peuvent être relatives et que seule la qualité des mesures et la disponibilité des résultats comptent réellement.

Le nombre important de données à traiter durant cette étude m'a par ailleurs amené à développer, avec l'aide de Pierre Camps, une interface graphique des programmes fournis par Tauxe et al. (1998). Le code multi plate-forme TCL-TK, encore loin d'être optimisé, est disponible dans le même répertoire.

Annexe A

Méthode bootstrap

La méthode bootstrap est un outil numérique qui permet de déterminer la moyenne et la dispersion d'un ensemble de N données dont on ne connaît pas la fonction de densité de probabilité. Cette méthode consiste à sélectionner aléatoirement N enregistrements parmi ces données, certaines pouvant être réutilisées plusieurs fois et d'autres jamais, et d'en calculer la moyenne dite bootstrappée (littéralement programmée). En répétant cette opération un très grand nombre de fois (10 000 par exemple) on dispose d'un ensemble de moyennes bootstrappées qui, une fois classées par ordre croissant, permet de déterminer un interval de confiance à 95% autour de la moyenne calculée pour les données initiales. Si l'ensemble de données initial possède une distribution gaussienne, ce type de statistique n'a évidemment pas grand intérêt, mais il permet dans le cas de distributions quelconques pour lesquelles les calculs d'écart type n'ont plus de sens, d'estimer la dispersion des données par rapport à la moyenne. Il est à noter que cette estimation de l'intervalle de confiance à 95% autour de la moyenne est asymptotique, *i.e.* qu'elle tend vers la valeur exacte de l'intervalle de confiance plus le nombre de moyennes bootstrappées calculé est important.

Cependant la méthode bootstrap simple qui vient d'être exposée dépend largement du nombre de données contenues dans l'ensemble considéré initialement. Pour un nombre de données trop petit (<20), les limites de confiance se retrouvent sous estimées (Tauxe et al., 1991). Si les données expérimentales initiales sont assorties d'une incertitude, il est alors possible de remédier à ce problème en utilisant la méthode bootstrap paramétrée. Dans ce cas, on substitue chaque donnée sélectionnée aléatoirement comme auparavant par une donnée «fictive» prise dans une distribution possédant la même moyenne et le même écart type que l'erreur associée à la donnée considérée. Les sous ensembles de N données de substitution reflètent mieux alors la distribution initiale limitée à quelques données et les intervalles de confiance s'en trouvent mieux définis qu'avec la méthode bootstrap simple.

Cette méthode de bootstrap peut par exemple être utilisée en paléomagnétisme pour estimer la moyenne et la dispersion par rapport à cette moyenne d'un ensemble de direc-

tions. Elle permet aussi de distinguer deux directions moyennes en vérifiant si les limites de confiance à 95% de la moyenne d'au moins une de leurs coordonnées cartésiennes ne se recouvrent pas. Le test bootstrap d'inversion, utilisé dans le premier chapitre de cette thèse, consiste alors à comparer la direction moyenne des coulées de polarité normale avec celle des coulées de polarité inverse basculées de 180°. Si ces deux directions moyennes sont distinctes, le test bootstrap d'inversion est négatif, et il est positif dans le cas contraire.

Pour les études de la fabrique magnétique, la méthode bootstrap a aussi été adaptée pour définir des ellipses de confiance autour des vecteurs propres du tenseur d'anisotropie (Constable and Tauxe, 1990). Les ensembles de données sélectionnés aléatoirement parmi les données initiales servent à déterminer trois vecteurs propres bootstrappés. En répétant cette sélection un grand nombre de fois, les lignes de contour regroupant 95% de l'ensemble de chacun des vecteurs propres bootstrappés permet de définir leurs ellipses de confiance à 95%.

Deux types de bootstrap paramétrés sont cette fois disponibles. A l'échelle de l'échantillon tout d'abord, en assumant que les incertitudes de mesure sont normalement distribuées. Pour chaque tenseur de susceptibilité selectionné aléatoirement, les éléments sont substitués individuellement par d'autres éléments pris dans une distribution normale qui aurait le même écart type que celui de l'échantillon considéré. Les ellipses de confiance à 95% sont alors définies comme précédemment. A l'échelle d'un site ensuite, en considérant cette fois que les données provenant d'une même roche de composition supposée homogène sont normalement distribuées. Pour chaque tenseur de susceptibilité sélectionné aléatoirement, les éléments qui se substituent sont cette fois pris dans une distribution normale qui aurait le même écart type que celui déterminé par toutes les données du site.

Par analogie avec la comparaison des directions magnétiques moyennes, celle des vecteurs propres moyens K_{max}, K_{int} et K_{min}, déterminés par la méthode bootstrap, permet par exemple de déterminer la forme de l'ellipsoïde d'anisotropie de susceptibilité magnétique. Celui-ci est sphérique si les trois axes sont confondus, oblate si K_{max} et K_{int} seulement sont confondus, prolate si il s'agit de K_{int} et K_{min} et enfin triaxial si les trois axes sont distincts.

Annexe B

Echantillonnage

Campagne d'été 1997-1998

TAB. B.1 – Section de Port Christmas

Coulée	épaisseur (m)	affl. Coulée (m)	N	Remarques	Alt (m)
Ca1	2	-	7	Coulée relativement massive.	35
Ca2	-	-	7	-	45
Ca3	3	-	6	Située au niveau du lac.	55
Ca4	3	-	7	-	58
Ca5	-	-	6	Pas de limite franche avec Ca4. Echantillonnée à la base d'une zone massive.	61
Ca6	1-2	-	7	Présence de zéolites et de géodes de Quartz. Base de la coulée observée.	80
Ca7	-	-	7	Petite coulée affleurant de façon discontinue.	90
Ca8	2	-	7	Petite coulée.	100
Ca9	10	-	7	Coulée massive.	110
Ca10	-	-	7	Coulée épaisse et massive.	130
Ca11	>5	-	7	Coulée épaisse et massive.	140
Ca12	-	-	7	Série de petits ressauts correspondant à autant de petites coulées. Echantillonnage dans les trois coulées les plus marquées.	165
Ca13	-	-	7	-	180
Ca14	-	-	7	-	185
Ca15	7-8	50	7	Coulée massive qui se suit dans le paysage.	195
Ca16	3	>10	7	Coulée massive, base observée.	230

TAB. B.2 – Section du Mont Bureau

Coulée	épaisseur (m)	affl. Coulée (m)	N	Remarques	Alt (m)
Fa1	3	-	7	-	-
Fa2	-	-	7	-	-
Fa3	-	-	7	-	-
Fa4	-	-	7	-	100
Fa5	8	-	7	Faciès massif, dure à carotter.	120
Fa6	15	-	7	Faciès massif.	155
Fa7	4	-	7	Faciès massif, grenu, riche en zéolites. Au dessus d'un niveau volcano-clastique.	-
Fa8	8	-	7	Coulée très altérée non échantillonnée entre Fa7 et Fa8. Coulée massive, traces d'échantillonnage de Watkins.	230
Fa9	3	-	7	Deux coulées non échantillonnées entre Fa8 et Fa9. Correspond au sommet de la falaise, coulée assez altérée et zéolitisée.	
Fa10	3	-	7	Faciès altéré.	275
Fa11	4	-	7	Changement de rive. Faciès massif, dure à carotter, sans continuité de l'autre côté de la vallée.	280
Fa12	10	-	7	Faciès massif, dure à carotter.	305
Fa13	8	-	7	Faciès massif, dure à carotter.	330
Fa14	2-3	40	7	Petite coulée massive, base observée et sommet deviné. Nombreuses fractures présentes mais pas de zéolites.	350
Fa15	3-4	15	8	Petite coulée massive, aphyrique et fracturée. Base observée et faciès bulleux au sommet.	360
Fa16	10	-	7	Petite coulée massive, très fracturée (carottage difficile) reposant sur un niveau rouge.	370
Fa17	20	20-30	7	Coulée très massive et fracturée avec un niveau rouge à la base.	400
Fa18	20	20-30	8	caractéristiques identiques à Fa17. Il reste 8 coulées non échantillonnées après Fa18.	420

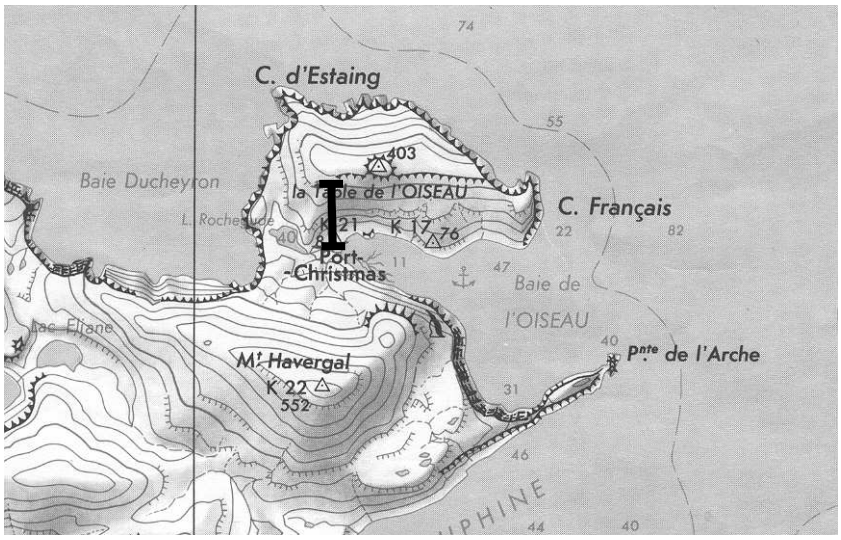

FIG. B.1 – Localisation de la section de Port Christmas.

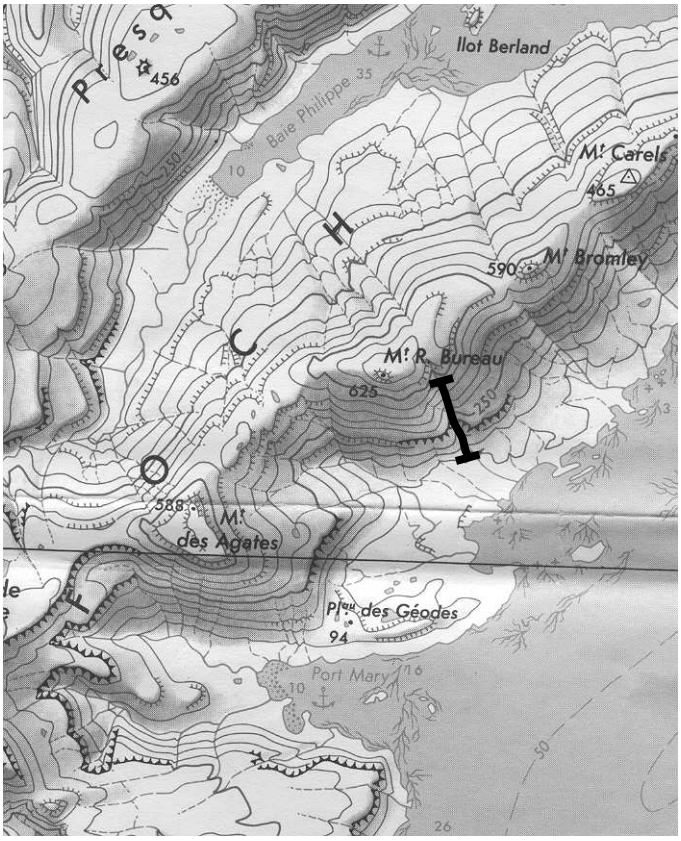

FIG. B.2 – Localisation de la section du Mont Bureau.

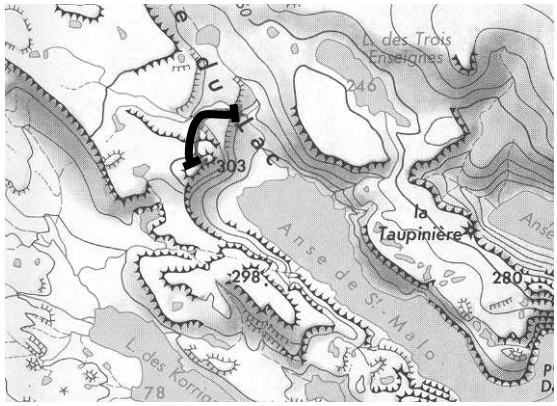

FIG. B.3 – Localisation de la section de Port Raymond.

TAB. B.3 – Section de Port Raymond

L'ensemble de la section se trouve sur la rive droite du ruisseau.

Coulée	épaisseur (m)	affl. Coulée (m)	N	Remarques	Alt (m)
Ra1	5	-	7	Faciès massif reposant sans discontinuité nette sur une zone plus bulleuse (5 m).	65
Ra2	5	>10	7	Coulée massive.	75
Ra3	10	>8	7	Coulée massive.	90
Ra4	15	30	7	Coulée massive, au dessus d'un niveau rouge. Forme la première grosse barre observée 200m plus au S. Constituée de blocs qui semblent en place.	115
Ra5	15	60	7	Coulée massive pouvant correspondre à la coulée située à la base de la section de l'Ile Haute. Reprise de la coupe 300m au SE.	180
Ra6	15	-	7	Coulée massive pouvant correspondre à la coulée située à la base de la section de l'Ile Haute.	205
Ra7	8	-	7	Coulée massive.	232
Ra8	5	40	7	Coulée massive.	265
Ra9	3	40	7	Coulée sommitale peu altérée à patine blanche sur un niveau rougeâtre. Existence possible de coulées se terminant en biseau entre Ra8 et Ra9.	290

TAB. B.4 – Sections de l'Ile Haute

Coulée	épaisseur (m)	affl. Coulée (m)	N	Remarques	Alt (m)
Ha1	6	10	7	Coulée épaisse et massive sous un niveau volcano-clastique.	0
Ha2	10	30	7	Coulée épaisse et massive, très fissurée et altérée donnant des boues grises. Située au dessus d'un niveau rougeâtre	15
Ha3	3	20	8	Située 200 m plus à l'E. de HA1 et HA2, la base de la coulée est bien visible.	35
Ha4	3.5		7	Faciès très bulleux, zéolitisée et altérée.	45
Ha4_d			3	Dyke recoupant HA4 à HA6 au moins et situé à 5 m à l'E. de HA4 (98C025) et 5 m à l'O de HA5 (98C033).	45
Ha5	2	10	7	Echantillonage serré car cette coulée est très altérée (boue marron) d'où un carottage difficile.	49
Ha6	6-7	30	7	Jolie coulée massive et prismée qui se suit dans le paysage sur plusieurs centaines de mètres. Très fracturée, elle donne une boue grise au carottage. Niveau de zéolites présent à la base.	51
Ha7	8	65	8	Repose sur un faciès altéré représentant le sommet de HA6. Coulée altérée avec présence de zéolites, elle forme le plateau qui correspond au point culminant. Les 4 derniers échantillons sont prélevés à environ 30 m au N.	60
Hb1	-	35	7	Prélevée dans la crique aux crânes. Equivaut à la coulée HA1.	0
Hb2	5	40	9	Coulée massive et épaisse. Equivalente à la coulée HA2 et sans doute à la coulée H15 de Plessard.	20
Hb3	3	-	7	Coulée altérée visible très localement.	50
Hb4	3-4	30	7	Jolie petite coulée présentant de nombreuses fractures et donnant des boues grises. Base observée.	55
Hb5	10	-	7	Coulée épaisse avec une zone plus altérée au sommet.	80
Hb5_r	-	-	3	Zone rouge entre HB5 et HB6.	82.5
Hb6	-	-	8	Coulée prismée, localement assez bizarrement.	85
Hb7	4	-	4	Faciès bulleux pour toute la partie supérieure.	100
HB8	-	-	-	Petite coulée non échantillonnée du fait de la présence d'un dyke.	-
Hb9	3	55	9	Coulée massive située sous un niveau d'argiles cuites. Echantillonnage répartit en deux endroits séparés de 50m.	115
Hb10	10	+10	7	Présence d'un niveau cuit à la base. Coulée très fracturée, avec présence de zéolites par endroit.	130

Coulée	épaisseur (m)	affl. Coulée (m)	N	Remarques	Alt (m)
Hb11	10	+10	7	Coulée massive située au dessus d'un niveau rouge rubéfié. Echantillonnage réalisé à 5m d'un couloir vertical (plan 90 vers 260) coupant la coulée sur environ 3m de large.	155
Hb12	15	75	8	Coulée massive dure au carottage. Echantillonnage répartit de part et d'autre d'un ravin.	205
Hb13	1.5	-	4	Petite coulée visible très localement, très altérée et zéolitisée. Présente un faciès bulleux.	235
Hb14	5	70	8	Coulée épaisse relativement difficile à carotter.	237
Hb15	9	40+-	7+4	Coulée massive située au dessus d'un niveau d'argiles cuites. Entre les échantillons 98C146 et 98C147, présence d'une fracture de 3 à 4 m de largeur que l'on peut suivre vers l'O. et qui n'affecte pas les coulées suivantes. Echantillonnage répartit sur deux zones.	250
Hb16	3	55+-	7+6	Coulée très altérée et zéolitisée. Echantillonnage répartit sur deux zones.	260
Hb17	-	40	7	Echantillonnage réalisé de part et d'autre d'un ruisseau.	270
Hb18	-	-	7	Petite coulée assez massive.	282
Hb19	-	-	7	Petite coulée assez altérée avec un faciès bulleux.	295
Hb20	-	-	4	Petite coulée.	300
Hb21	-	25	7	Coulée sommitale qui doit correspondre à celle formant la table des Mouflons.	315

TAB. B.5 – Sections de Port Jeanne d'Arc

Coulée	épaisseur (m)	affl. Coulée (m)	N	Remarques	Alt (m)
JA1	-	-	7	Seul affleurement disponible le long de la rivière. Faciès assez massif.	-
JA2	-	5	7	Coulée aphyrique peu épaisse et altérée avec un affleurement très réduit en largeur. Carottage difficile de part et d'autre d'un ruisseau.	-
JA3	-	2-3	7	Faciès bulleux correspondant probablement au sommet de la coulée. Présence de phénocristaux d'olivine et de pyroxène,	-
JA4	1.5	-	7	Faciès très altéré.	32
JA5	1.5	-	7	Faciès très altéré. Coulée échantillonnée dans le ruisseau à l'E.	33.5
JA6	1	-	7	Faciès très altéré.	35
JA7	1.5	25	7	Petite coulée altérée à la base. Possibilité de basculement des blocs localement.	36
JA8	3		7	Faciès très altéré. Coulée plus massive que les précédentes.	37.5
JA9	1	50	7	Coulée relativement altérée située au dessus du niveau conglomératique. Echantillonnage répartit en deux endroits espacés de 50m avec un faciès plus massif pour les 4 derniers échantillons.	140
JA10	-	15	7	Coulée peu épaisse et très zéolitisée.	141
JA11	10	55	8	Grosse coulée massive mise en place au dessus de Tuffs, très dure au carottage. Premier échantillon probablement foudroyé.	200
JB1	7	45	7	Coulée très massive et dure au carottage, échantillonnée au niveau du ruisseau formant le ravin du charbon. Base et sommet observés. 20 m au dessus de la coulée D de Henry et Plessard.	160
JB2	4-5	40	7	Jolie coulée massive (base et sommet observés) dure au carottage, qui ne parait pas altérée.	170
JB3	3-5	35	7	Jolie petite coulée très massive et peu épaisse, directement au contact sur JB2.	182
JB4	1	15	7	Ensemble de coulées métriques sur un niveau conglomératique. Ces coulées sont très altérées, zéolitisées et avec des contours flous. Seule la première unité est échantillonnée.	198
JB5	3	30	7	Correspond à la barre supérieure de la cascade à angle droit. Coulée massive, peu altérée sans zéolites visibles, repose sur un ensemble très altéré.	205
JB6	3	30	7	Coulée massive, peu altérée sans zéolites visibles.	215

Coulée	épaisseur (m)	affl. Coulée (m)	N	Remarques	Alt (m)
JB7	-	15	7	Ensemble très chaotique constitué sans doute de plusieurs coulées très zéolitisées. Affleurement très réduit en largeur.	225
JB8	-	-	7	Au sommet de la zone perturbée de JB7, changement radical de faciès : massif et peu bulleux.	240
JB9	7	30	7	Coulée fracturée, très dure au carottage. Affleurement à 50 m à l'E. de JB8.	250
JB10	-	>10	7	Coulée peu épaisse à faciès massif reposant au dessus de pyroclastites. Echantillonnage au niveau du ruisseau.	280
JB11	-	>10	7	Coulée massive après une absence relativement longue d'affleurement. Echantillonnage au niveau du ruisseau.	325
JB12	2-3	30	7	Coulée massive, très dure au carottage, située au dessus de JB11. Echantillonnage au niveau du ruisseau.	330

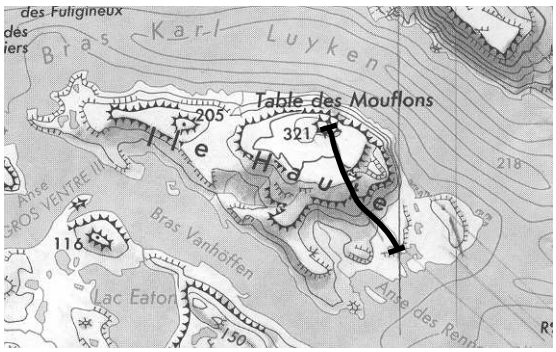

FIG. B.4 – Localisation de la section de l'Ile Haute.

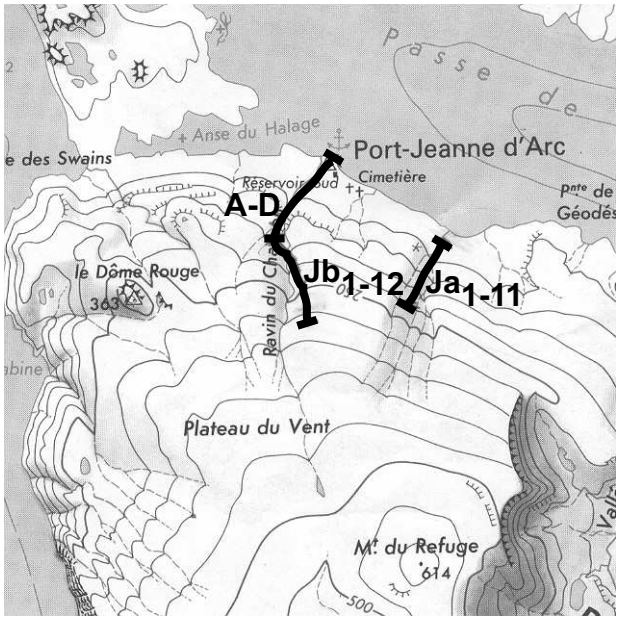

FIG. B.5 – Localisation des sections de Port Jeanne d'Arc.

Campagne d'été 1999-2000

TAB. B.6 – Section du Mont des Ruches

Coulée	épaisseur (m)	affl. Coulée (m)	N	Remarques	Alt (m)
Ruc1	3-5	10	8	Située dans le ruisseau au niveau de la mer. Vésicules remplies de Quartz. Base non visible.	10
Ruc2	3	20	7	Entre Ruc1 et Ruc2, une coulée non échantillonnée.	25
Ruc3	15	15	8	A la base de Ruc3, un niveau conglomératique (3-5 m) sous un niveau de charbon (10 cm, prélevé). Coulée massive et fracturée au niveau d'une cascade.	40
Ruc4	7	15	7	-	50
Ruc5	2-5	10	7	Echantillonnage réalisé sur un replat entre deux cascades. Base de coulée observée.	55
Ruc6	<3	15	8	A 100 m de Ruc5 vers le S. Exceptionnellement échantillonnée vers le sommet.	60
Ruc7	7-8	30	7	50 m au S. de Ruc6, prélevée de part et d'autre d'une cascade.	70
Ruc8	10	25	8	Jolie coulée massive avec prismes à la base, se prolonge très bien dans le paysage sur plus de 100 m vers l'E.	80
Ruc9	7-10	-	11	Echantillonnage répartit sur deux sites de part et d'autre de la rivière (100 m E puis 300 O).	85
Ruc10	5	25	7	-	90
Ruc11	5-10	50	7	Remplissage rouge à la base dont l'épaisseur peut atteindre 50 cm.	100
Ruc12	>10	-	7	8 10 m au dessus de Ruc11 après un replat. Base de la coulée visible.	120
Ruc13	5-7	-	7	Prise d'un échantillon pour d'éventuelles datations.	140
Ruc14	5	100	7	-	150
Ruc15	-	-	7	-	160
Ruc16	-	-	4	Entre Ruc15 et Ruc16, 4-5 coulées altérées non échantillonnées.	180
Ruc17	-	-	7	Entre Ruc16 et Ruc17 une coulée non échantillonnée.	220
Ruc18	2 à 7-10	30	7	Epaisseur variable de la coulée.	230

TAB. B.7 – Section du Mont des Tempêtes

Coulée	épaisseur (m)	affl. Coulée (m)	N	Remarques	Alt (m)
Tem1	3-4	15	7	Coulée échantillonnée au niveau de la mer dans l'Anse des Phoques.	5
Tem2	10	50	7	Coulée échantillonnée côté Baie Caillé.	30
Tem3	5	30	7	-	50
Tem4	5	40	7	-	60
Tem5	2	5	5	-	68
Tem6	1-2	-	5	Coulée très altérée.	75
Tem7	3	30	7	-	80
Tem8	4	10	7	-	90
Tem9	5-6	20	7	-	100
Tem10	4-5	10	7	Niveau très fin de sédiments (10 cm) entre Tem9 et Tem10.	105
Tem11	4-5	30	7	-	110
Tem12	10	30-40	7	-	120
Tem13	3	-	7	Section décalée vers le N. Entre Tem12 et Tem13. Petit niveau de sédiments rouges à la base de Tem13.	130
Tem14	2	-	7	Base de la coulée rougeâtre.	140
Tem15	1-2	5	4	Niveau rouge entre Tem15 et Tem16.	145
Tem16	2	10	7	-	152
Tem17	<1	-	7	Entre Tem17 et Tem18, 2 coulées non échantillonnées et un niveau sédimentaire jaune orange. Cette coulée correspond au sommet du replat avant la dernière falaise.	160
Tem18	2	10	8	Belle coulée prismée correspondant à la base de la dernière grosse falaise du Mont des Tempêtes.	172
Tem19	8-10	30	7	-	224
Tem20	7-8	30	8		246

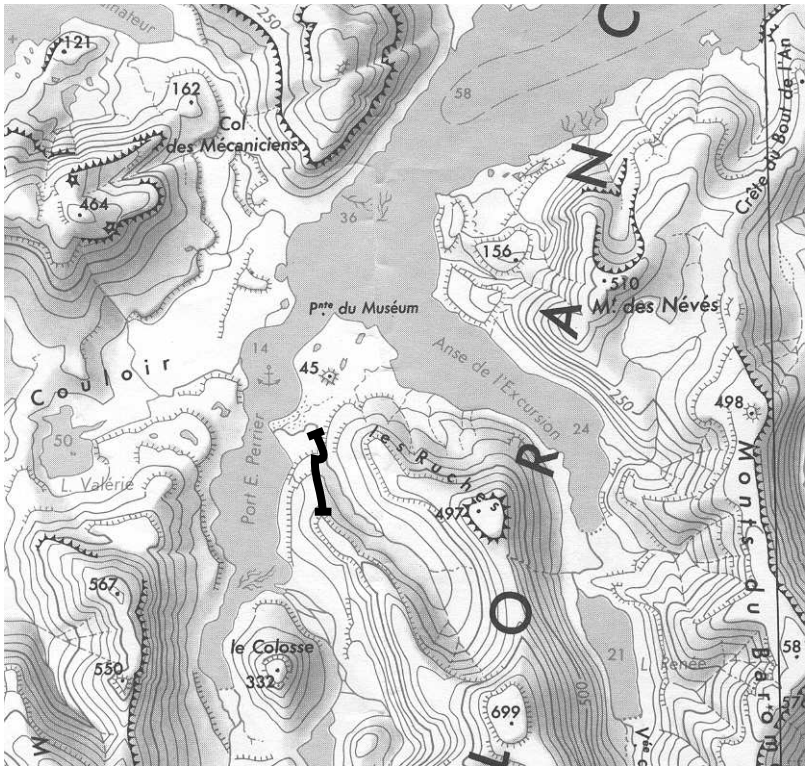

FIG. B.6 – Localisation de la section du Mont des Ruches.

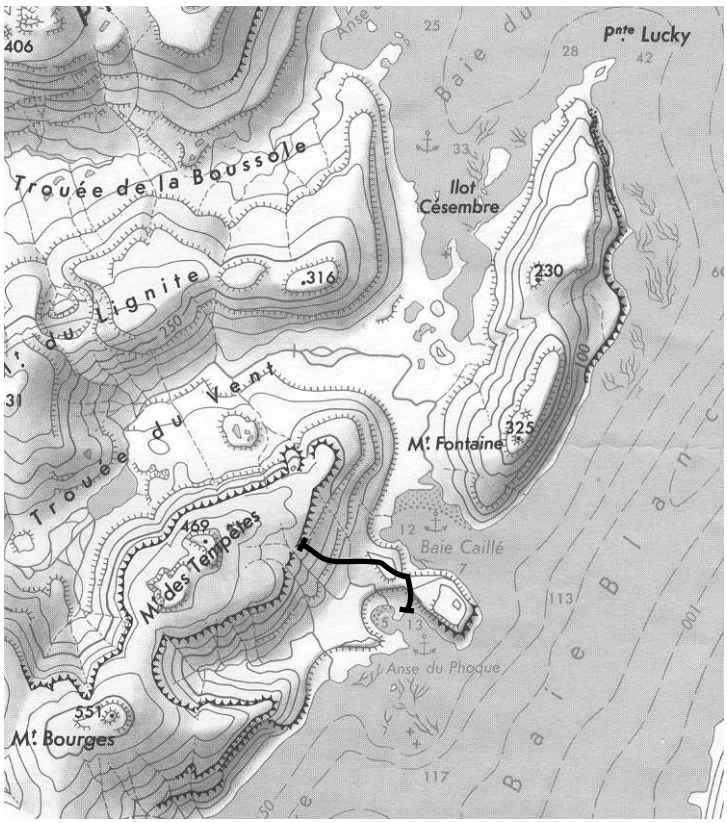

FIG. B.7 – Localisation de la section du Mont des Tempêtes.

TAB. B.8 – Section du Mont de la Tourmente

Coulée	épaisseur (m)	affl. Coulée (m)	N	Remarques	Alt (m)
Tou1	-	-	7	Grosse coulée du sommet du Mont de la Tourmente avec à la base un niveau de sédiments rouges(40 cm)..	580
Tou2	1.5	-	7	Entre Tou1 et Tou2, replat avec plusieurs petites coulées relativement altérées. Là encore, niveau rouge à la base.	525
Tou3	2	-	7	-	520
Tou4	2	-	7	-	510
Tou5	4	-	9	Niveau rouge observé à la base (20 cm).	505
Tou6	2-4	-	7	-	495
Tou7	2	-	4	-	490
Tou8	7-8	-	7	-	480
Tou9	4-6	>10	7	Belle coulée peu altérée avec un niveau rouge (20 cm) à la base et un niveau hyaloclastique au sommet.	465
Tou10	5-7	>10	7	Jolie coulée massive, fracturée sans phénocristaux.	430
Tou11	10	-	6	Jolie coulée massive, sans zéolites ni phénocristaux.	420
Tou12	2-3	-	7	Base de la coulée rougeâtre.	410
Tou13	4-5	10	7	-	390
Tou14	2	-	4	Coulée relativement altérée.	380
Tou15	6	-	7	-	370
Tou16	1-4	-	7	Coulée massive d'épaisseur variable, à grins fins (carrotier cassé).	360
Tou17	6	-	7	Coulée massive à grains fins avec un niveau rouge à la base.	340
Tou18	5-6	-	7	Coulée massive à grains fins avec un niveau rouge à la base.	330
Tou19	10	-	7	Coulée massive à grains fins, beaucoup plus fracturée que les précédentes avec un niveau rouge à la base. Présence de géodes de Quartz.	320
Tou20	4	-	7	Niveau rouge observé à la base.	305
Tou21	6	-	7	Echantillonnage concentré à la base.	290
Tou22	6	-	7	Echantillonnage réalisé de part et d'autre du ruisseau.	280
Tou23	4-6	-	7	Présence de grosses géodes de Quartz. Niveau rougeâtre observé à la base.	250
Tou24	6-8	-	7	Echantillonnage réalisé de part et d'autre du ruisseau. Niveau rouge à la base.	240
Tou25	8-10	-	7	Echantillonnage réalisé de part et d'autre du ruisseau. Niveau rouge à la base.	220

Coulée	épaisseur (m)	affl. Coulée (m)	N	Remarques	Alt (m)
Tou26	6-8	-	8	Fin de la coupe prélevée plus au SE. au dessus de la cabane. Carottes prélevées en base de coulée au dessus d'un niveau rouge (40-60 cm à 1 m).	210
Tou27	6-8	-	7	Coulée massive à grains fins, sans grosses zéolites avec un niveau bulleux plus ou moins rougeâtre à la base.	200
Tou28	6-8	-	7	Coulée massive à base conglomératique formée de gros galets de basaltes.	190
Tou29	2	-	5	Nouveau décalage vers le SE. Faciès beaucoup plus bulleux qu'avant. De nombreuses petites coulées sont intercalées entre Tou28 et Tou30 mais trop altérées pour pouvoir être échantillonnées.	180
Tou30	-	-	7	Coulée plus massive mais plus fracturée et altérée. Niveau rougeâtre à la base (5-10 cm).	160
Tou31	6	-	7	Coulée reposant sur un niveau rougeâtre très épais (1 m) situé au dessus du sommet altéré bulleux de la coulée sous-jacente. Le sommet de cette coulée correspond à un replat.	135
Tou32	6	-	7	Niveau rouge grossier d'épaisseur variable observé à la base (5-40 cm).	120
Tou33	4-6	-	7	Nombreuses petites géodes de Quartz.	110

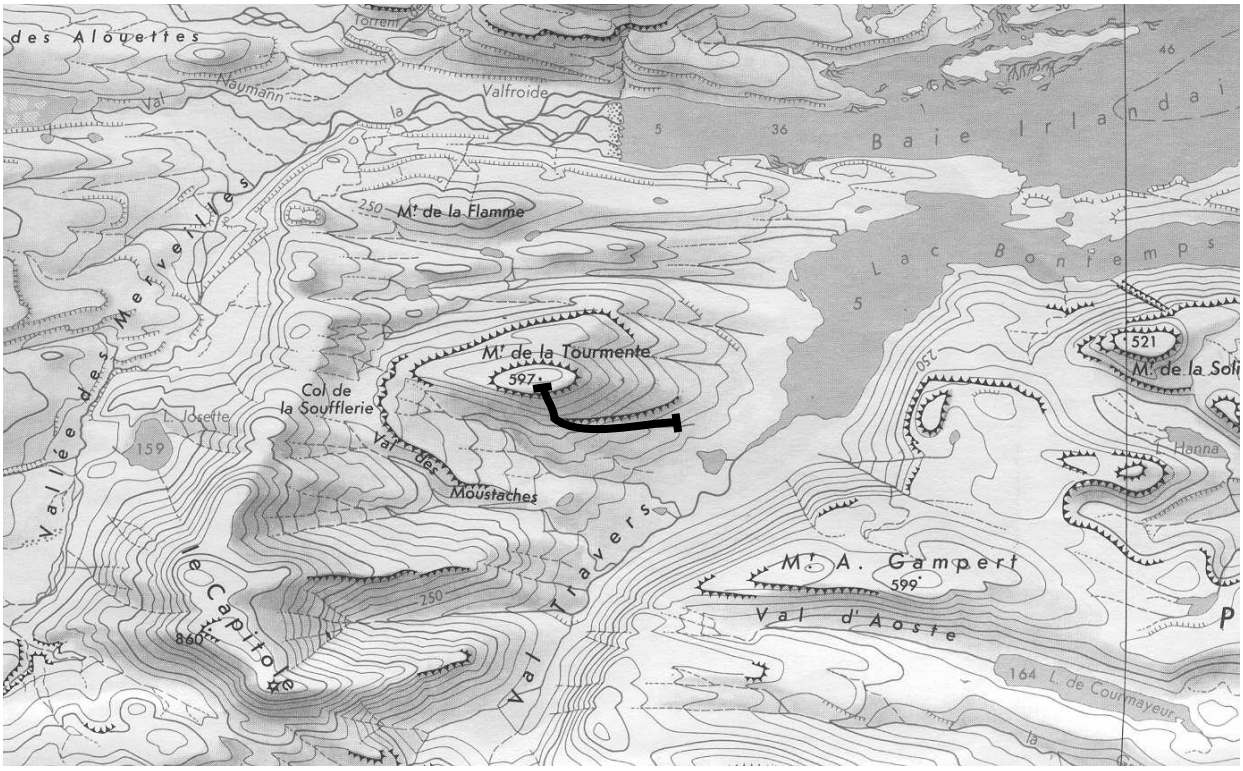

FIG. B.8 – Localisation de la section du Mont de la Tourmente.

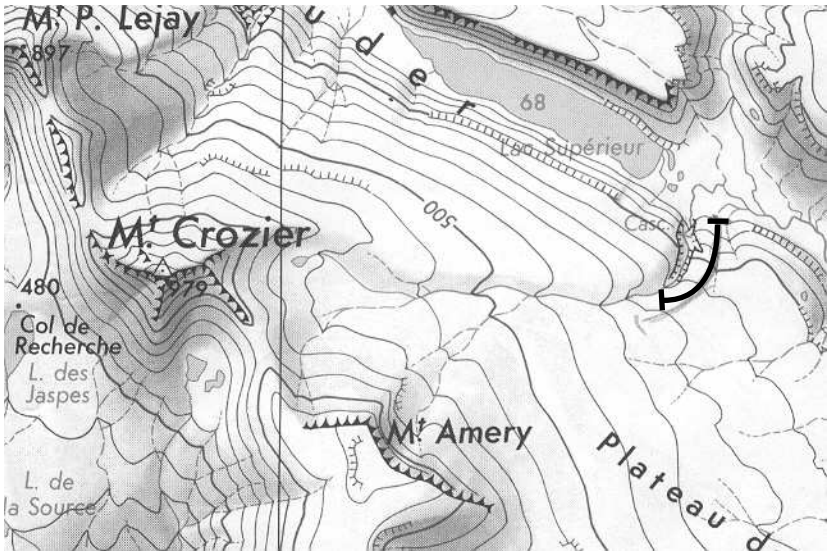

FIG. B.9 – Localisation de la section du Mont Amery.

TAB. B.9 – Section du Mont Amery

Coulée	épaisseur (m)	affl. Coulée (m)	N	Remarques	Alt (m)
Ame1	6	-	7	Directement au dessus de la dernière coulée échantillonnée par Henry et Plessard.	200
Ame2	6-8	-	7	-	225
Ame3	6-8	-	7	-	250
Ame4	>2	-	7	Vents très forts durant l'échantillonnage. Pas de limite de coulée évidente.	270
Ame5	3	7-8	7	Vents très forts durant l'échantillonnage.	280
Ame6	>4	-	7	-	330
Ame7	>2	-	7	Epaisseur de la coulée difficile à estimer. De nombreux petits affleurements sont séparées par des faux plats très longs.	340
Ame8	>1	-	7	Coupe continuée au SE de la rivière tombant dans la cascade cachée. On abandonne la coupe après avoir observé des dykes s'entrecoupant au niveau de la rivière.	345

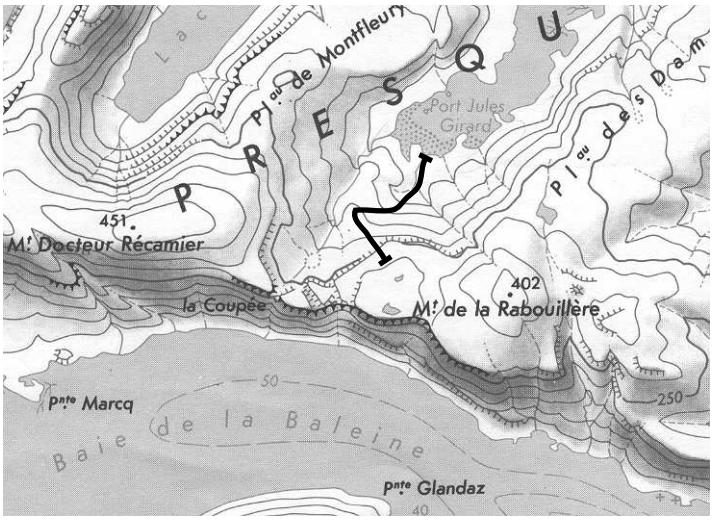

FIG. B.10 – Localisation de la section du Mont de la Rabouillère.

TAB. B.10 – Section du Mont de la Rabouillère

Coulée	épaisseur (m)	affl. Coulée (m)	N	Remarques	Alt (m)
Rab1	6-8	-	7	Au SE. de la rivière.	2
Rab2	6	-	7	-	8
Rab3	1-2	-	8	-	14
Rab4	6	-	8	Grosses géodes de Quartz observées à l'affleurement.	20
Rab5	6-8	-	7	Niveau rouge (5 cm) observé à la base.	30
Rab6	2	-	7	-	45
Rab7	4-6	-	7	-	60
Rab8	6-8	-	7	-	80
Rab9	6-8	-	7	Coulée beaucoup plus dure.	100
Rab10	4-5	-	7	-	120
Rab11	6-8	10	7	Niveau rouge (40 cm à 1 m) observé à la base.	130
Rab12	6-8	-	7	-	50
Rab13	4-6	-	7	Niveau rouge à la base. Extension horizontale très importante, la coulée se suit très facilement dans le paysage. Le sommet forme un plateau avant d'atteindre la coulée Rab14.	160
Rab14	4-6	-	7	Encore une coulée massive de grande extension latérale. La roche est dure à carotter.	170
Rab15	2	-	7	Entre Rab14 et Rab15, une coulée très altérée non prélevée.	190
Rab16	6-8	-	8	Entre Rab15 et Rab16, une coulée métrique (ou peut-être 2 ou 3) non prélevée.	230
Rab17	10	-	7	Entre Rab16 et Rab17, une coulée un peu moins épaisse que Rab17 n'a pas été prélevée.	250
Rab18	4	-	7	-	270
Rab19	>4	-	7	Niveau rouge observé à la base.	280

Campagne d'été 2001-2002

TAB. B.11 – Section des Trois Ménestrels

Coulée	épaisseur (m)	affl. Coulée (m)	N	Remarques	Alt (m)
MenA1	10	10	9	Base non visible sous une faible épaisseur de moraines ou de cendres marrons. Roche dure au carottage.	25
MenA2	3	10	8	entre MenA1 et MenA2, niveau de conglomérat rouge, oxydé et composé de clastes arrondis (3 m). Coulée massive et fraîche.	35
MenA3	-	15	8	Contact incertain mais semble reposer directement sur MenA2 avec un niveau de sédiments rouges cuits intercalé entre les deux.	47
MenA4	2-3	10	5	Coulée massive au sommet vésiculaire et altéré dans lequel on peut voir du Quartz.	60
MenA5	2	5	4	Une coulée non échantillonnée entre MenA4 et MenA5. Sommet bulleux aux vésicules aplaties (5-6 cm de diamètre).	70
Seconde partie de la section séparée de la première par une discordance mettant en évidence une paléovallée. Les coulées au contact n'ont pas été prélevées afin de s'assurer qu'elles soient bien plus jeunes que celles de la première partie. La section débute à environ 50-70 m au dessus de la discordance, au niveau d'un replat. Elle est limitée à l'O par une faille importante, et à l'E par une fracture qui se suit clairement dans le paysage et qui ne semble pas avoir de jeux vertical.					
MenB1	3	30	7	Coulée relativement altérée, échantillonnée à la base.	85
MenB2	4	15	7	Coulée partiellement altérée.	90
MenB3	5	15	7	Coulée conglomératique (aiguilles et clastes oxydés) entre MenB2 et MenB3. Faciès massif avec niveau vésiculaire observé à la base.	95
MenB4	-	10	7	2 coulées (?) non prélevées entre MenB3 et MenB4. Coulée altérée et fracturée, contact basal peu clair. Petit dyke coupant la section sur le flanc opposé de la fracture.	115
MenB5	7-8	20	7	Coulée massive, aphyrique, fortement fracturée et affectée par quelques veines (Calcite et/ou Quartz).	130
MenB6	1	10	7	Au dessus de 5 m de débris et trois coulées altérées non échantillonnées (4 m, 4 m, 1m), coulée massive, dure à carotter, avec quelques vésicules. Présence d'un petit sill affectant le sommet de la coulée.	145

Coulée	épaisseur (m)	affl. Coulée (m)	N	Remarques	Alt (m)
MenB7	1-2	10	7	Entre MenB6 et MenB7, on passe un sill et des coulées détritiques d'épaisseur variable. MenB7 repose directement sur une coulée détritique. Tous les échantillons sont prélevés à la base.	165
MenB8	12	10	7	Coulée prismée avec quelques phénocristaux de plagioclases et de pyroxènes, reposant sur un niveau de sédiments oxydés (10 cm). Entre MenB8 et MenB7, nous avons passé un fin niveau détritique et une coulée peu exposée (4 m).	185
MenB9	10	25	7	Directement sur MenB8, cette coulée aphyrique forme le dernier plateau avant la fin de cette partie.	200
MenB10	4	15	7	Correspond à la partie basale, massive et peu bulleuse, de la coulée en contact avec le sommet altéré de MenB9.	210
MenB11	17	10	8	Coulée fracturée, affectée localement de veines (Calcite et/ou Quartz). Les échantillons sont prélevés à la base qui est en contact direct avec le sommet de MenB10.	230
MenB12	3	20	7	Coulée fraîche et massive mais très fracturée. Présence de petites vésicules arrondies (jusqu'à 10 cm de diamètre) remplies d'agate et de calcite. Contact basal ondulant.	240
MenB13	2.5	15	7	Coulée très vésiculaire avec de multiples minéraux d'altération. Présence de phénocristaux de plagioclases et de clinopyroxènes. Base non observée. Correspond très probablement au sommet de la coulée.	255
Cette dernière partie de la section est située à l'O. des deux autres, après avoir traversé la faille évoquée dans la partie précédente.					
MenC1	1-5	15	7	Coulée vésiculaire altérée avec un contact basal oxydé bien observé.	265
MenC2	3	25	9	Coulée très vésiculaire (vésicules remplies de zéolites) à phénocristaux de plagioclases, fracturée et érodée. Base clairement observée. Tous les échantillons sont prélevés à la base (1m).	268
MenC3	<1	30	8	Coulée vésiculaire (remplies de zéolites) de type pahoehoe au sommet érodé. Repose directement sur les brèches oxydées du sommet de MenC2.	270
MenC4	<2	15	7	Une coulée peu exposée non prélevée entre MenC3 et MenC4. Coulée aphyrique à matrice altérée pervasivement. Base difficilement identifiable mais les échantillons sont prélevés à 1m de celle-ci au maximum.	275

Coulée	épaisseur (m)	affl. Coulée (m)	N	Remarques	Alt (m)
MenC5	>1	15	7	Repose sur le sommet vésiculaire (remplies de zéolites) oxydé de MenC4. Coulée vésiculaire (remplies de zéolites) de type pahoehoe ayant subit une altération pervasive (sommet érodé) et dans laquelle on peut observer des microphénocristaux de plagioclases. Tous les échantillons sont prélevés à la base (10 cm).	278
MenC6	-	20	7	Petit plateau sans affleurement entre MenC5 et MenC6, mais le contact entre les deux est clair. Coulée relativement fraîche, aphyrique, massive avec quelques vésicules dans la partie centrale.	285
MenC7	2.5	20	7	Base visible en contact avec un sommet de coulée vésiculaire oxydé. Présence de phénocristaux et de glomérocristaux de plagioclase (jusqu'à 0.3 cm) altérés la plupart du temps, ainsi que d'olivine largement altérée. Les échantillons sont prélevés à la base (1 m).	305
MenC8	6-7	20	6	Environ 6-7 m au dessus de menC7. Présence de microphénocristaux de plagioclase et de quelques zéolites. Echantillonnage dans des blocs probablement en place. Base observée.	320
MenC9	10	10	7	Base bien visible en contact avec un conglomérat (1 m) oxydé avec des clastes arrondis de taille variable. Présence de moins de 1% de phénocristaux de plagioclase et d'olivine altérée (2 mm de diamètre). Echantillonnée à la base (50 cm).	330
MenC10	2	25	8	Contact à la base avec un sédiment grossier oxydé. Comprend 5% de vésicules arrondies remplies d'un minéral vert d'altération. On distingue moins de 1% de phénocristaux de plagioclase (frais) et quelques clinopyroxènes. Les échantillons sont prélevés à la base (1 m).	335
MenC11	6	30	8	Contact bien visible avec un sédiment oxydé (2 m). Coulée massive et fracturée, aphyrique avec quelques vésicules (<1%).	340
MenC12	1.5	35	10	Environ 3-4 m au dessus de MenC11. Coulée aphyrique, relativement fraîche, érodée, comprenant moins de 1% de vésicules remplies d'argiles. Une coulée (?) n'a pas été échantillonnée.	370

Coulée	épaisseur (m)	affl. Coulée (m)	N	Remarques	Alt (m)
MenC13	1.8	30	8	Deux coulées non échantillonnées entre MenC12 et MenC13. Coulée massive et fraîche au centre, de type pahoehoe, et aphyrique (sauf quelques pyroxènes <2 mm). Contact basal très ondulant sur des sédiments. La direction d'écoulement pourrait éventuellement être déterminée à l'aide de vésicules assez grosses remplies de zéolites.	380
MenC14	1.5	10	7	Coulée fracturée avec un contact basal ondulant.	395
MenC15	2.5	15	7	Contact basal peu exposé. Présence de vésicules arrondies remplies d'argiles ou de zéolites.	400
MenC16	3-4	10-15	5	2 coulées au dessus de MenC15 après avoir traversé un ruisseau correspondant à la fracture située à l'E. de la deuxième partie. Base bien visible avec un niveau rouge correspondant à un paléosol recuit.	410
MenC17	2	15	7	Une coulée non prélevée entre MenC16 et MenC17. Sommet et base avec un petit niveau rouge bien visibles. Echantillonnée à la base.	428
MenC18	5-6	50	7	Une coulée non prélevée entre MenC17 et MenC18. A environ 10 m au dessus de MenC17. Base bien visible sur une couche volcano-détritique (50 cm-1 m).	440
MenC19	10-15	40	7	Base bien visible avec présence de sédiments rouges. A environ 30 m au dessus de MenC18. Une coulée non prélevée entre MenC18 et MenC19.	480
MenC20	2-3	10	5	Coulée pahoehoe, vésiculaire au sommet (15% remplies zéolites vertes et noires) et reposant sur des sédiments rouges fins (15 cm).	495
MenC21	3	15	7	Une coulée non prélevée entre MenC20 et MenC21. Coulée finement vésiculaire (avec des minéraux d'altération verts dans la matrice), très fracturée et reposant sur un niveau volcano-détritique oxydé.	520
MenC22	4	20	7	Base visible reposant sur un niveau rouge correspondant au sommet de MenC21.	530
MenC23	10-15	30	6	4-5 m au dessus de MenC22. Base bien visible sur un niveau de sédiments volcano-détritiques rouges. Echantillonnée à la base.	540
MenC24	3-4	30	7	Juste au dessus de MenC23, base bien visible avec présence de sédiments volcano-détritiques fins.	555
MenC25	3-3.5	25-30	7	Au dessus de MenC24, base et sommet non visibles. Echantillonnée au plus bas.	560

Coulée	épaisseur (m)	affl. Coulée (m)	N	Remarques	Alt (m)
MenC26	1.5	20	6	Décallé d'environ 60 m vers le NO. on se retrouve juste au dessus de MenC25 dont le sommet est bien visible ici. Repose sur un niveau de sédiments rouges (50-70 cm).	578
MenC27	2-2.5	25	7	Au dessus de MenC26, base bien visible.	580

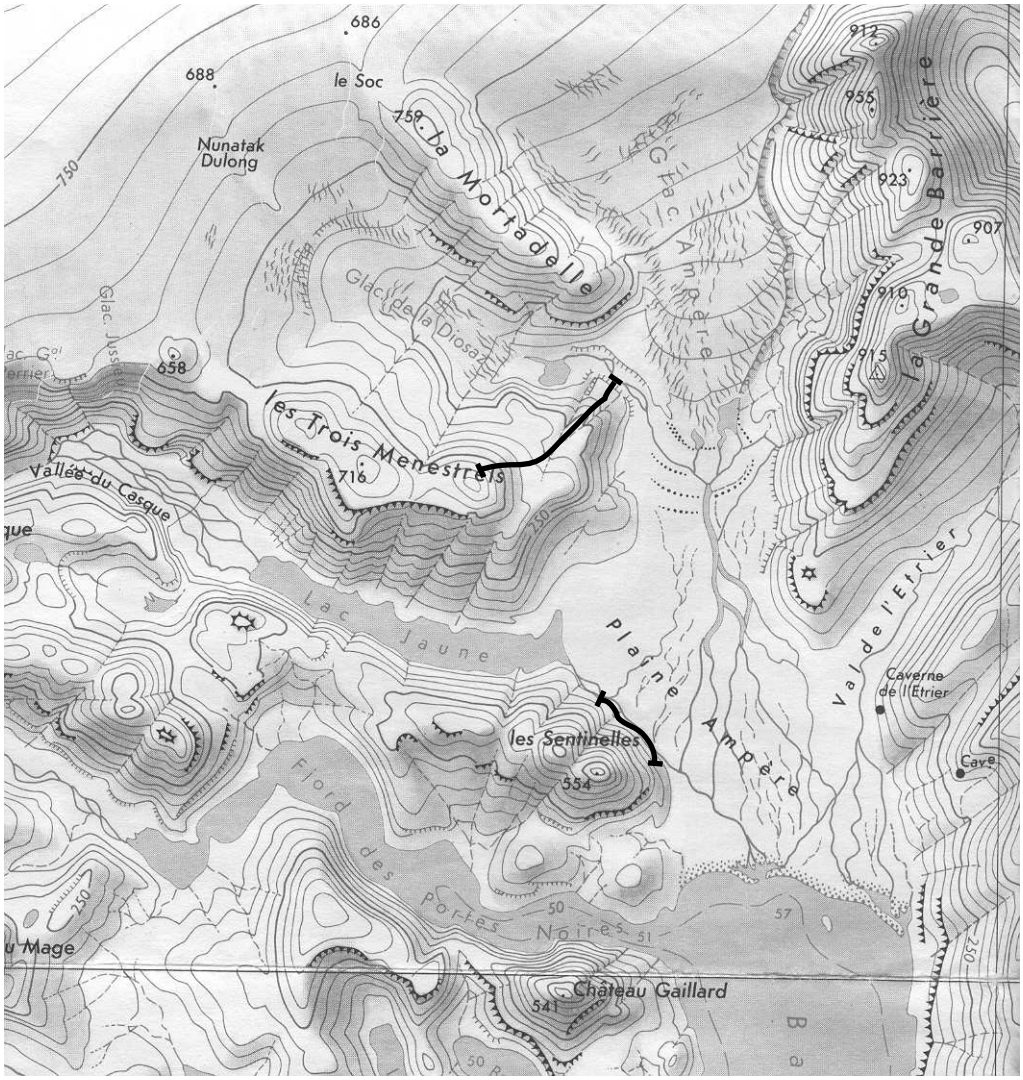

FIG. B.11 – Localisation des sections des Trois Ménestrels et des Sentinelles.

TAB. B.12 – Section des Sentinelles

Section prélevée le long de la rivière du Lac Jaune.

Coulée	épaisseur (m)	affl. Coulée (m)	N	Remarques	Ep. (m)
Sen1	6-7	-	7	Coulée massive, aphyrique et fracturée. Petite coulée à la base qui surmonte un niveau de sédiments rouges.	0
Sen2	3-4	20	7	Base observée mais irrégulière. Repose presque directement sur Sen1. Echantillonnage dans la partie massive centrale.	10
Sen3	-	4-5	5	Petite coulée située à une vingtaine de mètres au dessus de Sen2. Il peut éventuellement s'agir d'un sill.	20
Sen4	4-5	-	7	Jolie petite coulée massive prélevée à une centaine de mètres à l'E. de Sen3.	35
Sen5	3-4	10-15	7	Située juste au dessus de Sen4. Jolie petite coulée massive avec un niveau de brèches à la base.	40
Sen6	5-6	-	9	Située à l'aplomb de Sen1 au bord du ruisseau. Jolie coulée massive, très fracturée.	60
Sen7	3	40	8	A environ 500 m vers le S., juste au dessus de la continuation de la coulée Sen6 (alt. 40 m). Affleurement non vertical mais joli cependant. Base de la coulée observée.	65
Sen8	15	20	7	Coulée très massive située à 20-30 m à l'aplomb de Sen7. Niveau conglomératique observé à la base.	95
Sen9	3	5	8	A environ 200 m vers le S., escarpement où 4-5 coulées affleurent dont la première correspond au sommet de Sen8. La deuxième ne peut être prélevée car trop verticale et est donc sautée. Jolie coulée massive à la base très irrégulière.	105
Sen10	4-5	-	7	A environ 200 m vers le S., affleurement très altéré surmontant un niveau volcano-détritique très épais.	135
Sen11	5-6	-	7	Juste au dessus de Sen10. Jolie coulée massive au dessus d'un niveau d'argiles cuites (20 cm), décallée de 2 m environ par une faille où passe un ruisseau.	140
Sen12	3-4	35	7	A plusieurs centaines de mètres vers le S. (200 m du camping, alt. 10 m). Jolie coulée massive. Base observée.	170
Sen13	5	-	7	Coulée très altérée dont la base est observée par endroit. Au sommet se trouve un niveau volcano-détritique (50 cm).	175

Coulée	épaisseur (m)	affl.	Coulée (m)	N	Remarques	Ep. (m)
Sen14	10		50	7	Jolie coulée massive mais inaccessible d'où un échantillonnage réduit à 20-30 m au S. de Sen13. Ici le niveau conglomératique entre Sen13 et Sen14 est plus épais (1.5 m) et est composé de galets ronds décimétriques s'affinant de la base au sommet. Il se pourrait qu'il s'agisse d'un énorme sill alimentant deux dykes recoupant le niveau conglomératique (10 m) au dessus de Sen14.	182

Annexe C

Rotation of the Semail ophiolite (Oman): Additional Paleomagnetic data from the volcanic sequence

Marine Geophysical Researches **21:** 181–194, 2000.

Rotation of the Semail ophiolite (Oman): Additional Paleomagnetic data from the volcanic sequence

Mireille Perrin[1], Guillaume Plenier[1], Jean-Marie Dautria[2], Emmanuel Cocuaud[1] & Michel Prévot[1]

[1]*Géophysique, Tectonique et Sédimentologie, UMR CNRS 5573, Université Montpellier II, CC 060, 34095 Montpellier Cedex 5, France;* [2]*Laboratoire de Tectonophysique, UMR CNRS 5568, Université Montpellier II, 34095 Montpellier Cedex 5, France*

Received 1 March 2000; accepted 31 July 2000

Key words: oman, ophiolite, paleomagnetism, volcanic sequence

Abstract

Thirty-two flows (247 cores) were sampled in the V1 (Geotimes) and V2 (Lasail) volcanic units of the Semail ophiolite, Oman (Aswad, Fizh, Hilti, Sarami, Wuqbah, and Tayin massifs). Paleomagnetic analysis of the samples was complicated by a large overlap of the two components of magnetization carried by the rocks: a crystalline remanent magnetization (CRM) acquired in the present day field, probably during weathering, and an older CRM probably produced by oxidation of the original titanomagnetites during hydrothermal event(s). If the magnetization carried by the V1 samples was acquired during the hydrothermal event related to the emplacement of these lava, e.g., during and/or shortly after cooling, the tectonic unity of the northern domain has to be questioned and a differential rotation considered between the Aswad and Hilti-Sarami massifs but, by the time of emplacement of the V2 series, this northern area seems to behave as one large unit. As only one set of data is available for the southern Tayin-Sumail massif, it is premature but a possible relative rotation on the order of 90° can be suspected between the Hilti-Sarami and Tayin-Sumail massifs, rotation which would have occurred after emplacement of the V2 series.

Introduction

Many rock types of the Semail ophiolitic complex have been studied paleomagnetically. These are : gabbros (Luyendyk and Day, 1982; Shelton, 1984; Thomas et al., 1988; Weiler, 2000), sheeted dikes (Luyendyk et al., 1982; Shelton, 1984), sedimentary rocks and a few lavas (Thomas et al., 1988). Although large rotations during intraoceanic thrusting have been proposed, due to uncertainties about the acquisition of the different groups of magnetic directions and their polarity, the sense of rotation of the nappe remained questionable (Thomas et al., 1988).

An extensive study (Perrin et al., 1994) was then conducted on the volcanic sequence of the ophiolite because lavas are usually better paleomagnetic recorders than intrusive or sedimentary rocks. This study concentrated on the Salahi area of the Hilti massif (Figure 1) because it is the only area where the sequence of volcanic rocks is complete, going from pillow basalt extruded at the oceanic ridge before the detachment of the nappe, up to lava extruded before the end of the obduction (e.g., Alabaster et al., 1982). Moreover, the occurrence of sediments interbedded with and overlying the lavas allowed a good control of the paleohorizontal. The paleomagnetic Euler pole analysis, which could luckily be conducted there, has shown that the movement of the Salahi area could be modeled by a single, large rotation of about 145–150° around an Euler pole located close to the nappe (less than 200 km away). Combining plate tectonic concepts, a mantle-anchored hotspot reference frame, and paleomagnetic data the initial paleolatitude (around 10° N) and paleolongitude (around 45° E) as well as the paleorientation (NNW/SSE to N/S) of the ridge in hotspot coordinates was determined for Salahi, with

182

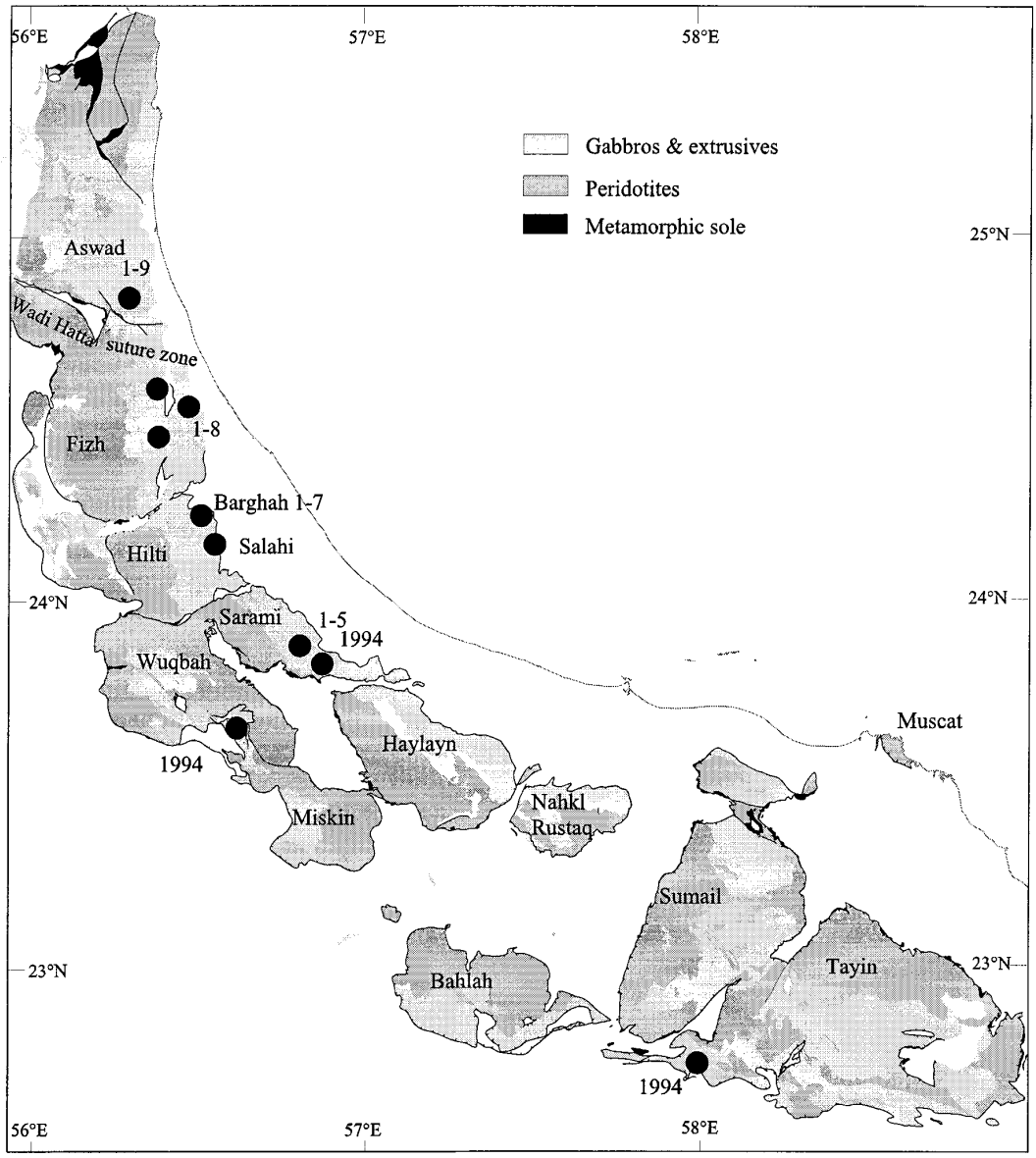

Figure 1. Geologic map showing sampling locations (full dots).

a linear velocity of the nappe between the period of accretion at the ridge and the end of the obduction onto the Arabian peninsula slightly less than 2 cm per year.

As the Semail nappe is divided into structural massifs (e.g., Nicolas et al., 2000b), each several tens of kilometers long (Figure 1), the question is whether the Salahi results are representative for the entire Hilti Massif, for the northern part of the ophiolite nappe, or for the entire ophiolite nappe. In order to test this, additional volcanic rocks were sampled in various massifs.

Volcanic units and sampling

Three episodes of submarine volcanism can be distinguished on petrologic and geochemical grounds (Alabaster et al., 1980; Pearce et al., 1981; Lippard et al., 1986; Ernewein et al., 1988). The first episode V1 (Geotimes), interpreted as ridge-axis volcanism, consists mainly of large pillow basalt with some massive flows that directly overly the sheeted dike complex. The second volcanic episode V2 (Lasail) consists of small pillows or sheet flows in the top part and clearly post-dates the V1 episode but absence of a continuous sedimentary layer between these two episodes indicates no substantial interruption in volcanic activity. Biostratigraphic ages determined from radiolarian faunas present in the pelagic sediments interbedded with the volcanic sequence also indicate that the two first volcanic episodes occurred within a very short time interval. According to Ernewein et al. (1988), the V1 episode took place from late Albian to early Cenomanian (approximately 100 Ma ago) at mid-ocean ridge and the V2 episode occurred shortly afterwards at the start of oceanic thrusting during Cenomanian to Turonian times (possibly before ∼95–96 Ma, e.g., Hacker et al., 1996). The third volcanic episode V3 is characterized by thick flows showing columnar jointing and doleritic texture. A thick pelagic sedimentary layer (up to 15 m) of Campanian age is observed between the V2 and V3 units. The age of the V3 episode remains unclear. Ernewein et al. (1988) suggested formation as due to intraplate seamount volcanism, produced some 15–20 Ma after the beginning of oceanic thrusting but preceding the end of the obduction of the ophiolite onto the Arabian continental margin. This last episode is now found only in the Hilti massif. Hydrothermal circulations, contemporaneous with the various phases of volcanic activity, appear to have induced some recrystallization in the lava and interbedded sediments (Karpoff et al., 1988; Pflumio, 1988).

Results from two successive samplings will be presented in this paper. A preliminary sampling was kindly made in 1994 by Edwin Gnos, on the side of his geologic work. One V1 flow (9 cores) and one V2 flow (11 cores) were sampled in the Sarami massif (23.84° N, 56.87° E), three V1 flows (20 cores) in the Wuqbah massif (23.66° N, 56.59° E) located on the western front of the ophiolite, and one V1 flow (11 cores) in the Tayin massif (22.76° N, 58.01° E). To complete this sampling, a second field campaign was organized in 1999 with the aim to cover as well the northern than the southern parts of the ophiolite. However, most of the sampling had to be done in the northern part of the ophiolite because of the extreme difficulty to find outcrops suitable for a paleomagnetic sampling in the southern part of the nappe (high degree of alteration of the rocks and common absence of sediments which precludes estimation of the paleohorizontal). Nine V2 flows (76 cores) were sampled in the Aswad massif (between 24.82 and 24.83° N, and between 56.32 and 56.33° E), six V2 flows (44 cores) in the Fizh massif (between 24.55 and 24.58° N, and between 56.39 and 56.47° E), seven V1 flows (50 cores) in the Wadi Barghah area of the Hilti massif (24.23° N, 56.52° E), and four V2 flows (26 cores) in the Sarami massif (23.87° E, 56.82° E). All cores were drilled directly in the field using a gasoline-powered core drill and oriented using both magnetic and sun compasses. In the laboratory, each core was cut in one to eight half-standard size specimens (2.5 cm in diameter and 1.1 cm in height). Location of the different sampling areas is shown in Figure 1. Distinction between V1 and V2 units was made according to the 1:50 000 geological maps produced by the Ministry of Petroleum and Minerals of Oman (1993).

Trace and major element analysis

In the field, the V1 and V2 volcanic units are hardly distinguishable and to find discrimination criteria beyond all question is one of the challenges of the study of the Semail volcanic unit. Field criteria such as sample colour (dark brown for V1, greenish for V2), flow jointing (large pillow for V1, small pillow or sheet for V2) and erosion resistance (relatively high for V1, low for V2) have been successfully used in the location of massive sulfide deposits (Alabaster et al., 1980). However application of these criteria is often insufficient and even error bearing, as we will see in this study. Even petrologic criteria used classically for lava discrimination, such as texture and clinopyroxene composition, are here inefficient because both V1 and V2 basalts are hyalopilitic and contain identical low Ti and Na endiopside. Furthermore their groundmasses cannot be used because hydrothermal alteration have cancelled their possible initial specificity : they are in both cases identically altered to chlorite, quartz, hematite, Fe hydroxyde, epidote, prehnite and zeolite. The best approach to discriminate the two series is a geochemical analysis, as shown by Albaster et al. (1982), Pearce et al. (1981), Lippard et al. (1986),

184

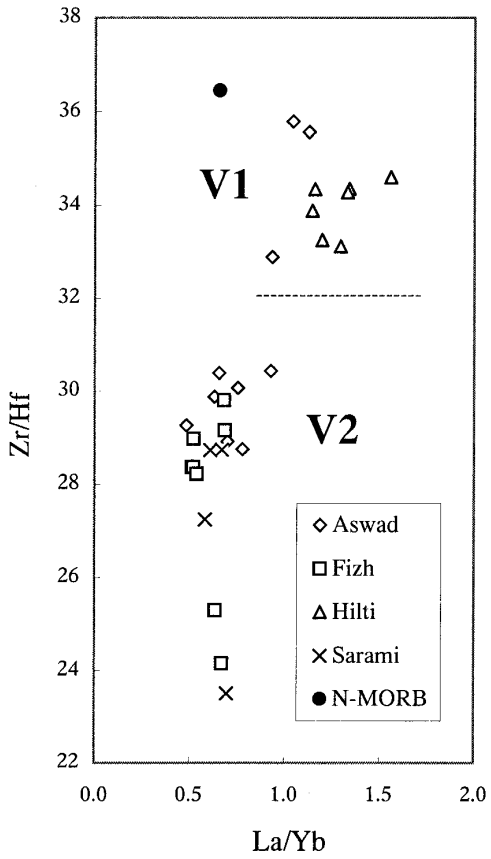

Figure 2. La/Yb versus Zr/Hf diagram. N-MORB from Sun and McDonough (1989).

Ernewein et al. (1988) and recently confirmed by Godard et al. (submitted). Titanium, Rare Earth Element (REE), Zirconium and Hafnium appear to be the most discriminant elements. For example, the V1 lavas display TiO_2, La and Zr amounts systematically higher than V2 lavas. The La/Yb ratio of V1 is systematically nearly 1 (or slightly higher) while that of V2 is significantly lower (< 0.8); the Zr/Hf ratio of V1 is near 35 and that of V2 lower than 30. Moreover, the V1 lava display N-MORB REE chondrite-normalized patterns while the V2 are more depleted, particularly in light REE.

On this base, we carried out major and trace element analysis on one specimen from each flow sampled in 1999. The La, Yb, Zr, Hf and TiO_2 amounts are listed in Table 1 and the La/Yb vs. Zr/Hf diagram is given in Figure 2. Clearly, all flows from the Hilti massif belong to the V1 series while those from Sarami and Fizh are typically V2, as shown on the 1:50 000 geological maps. Only the V2 unit has been mapped in the Aswad massif whereas surprisingly our geochemical analysis show that both V1 and V2 series were sampled there: flows 1, 5, and 7 display unquestionable V1 geochemical characteristics, while flows 2, 3, 4, 6, 8, and 9 have a V2 signature similar to those of Sarami and Fizh. This geochemical stratigraphy is always in agreement with the relative position of the flows in the field when it can be estimated. This emphasizes the suitability of the geochemical method on its own to discriminate the volcanic units of the Semail ophiolite.

Paleomagnetic analysis

Remanent magnetization of the rocks was measured with commercial devices (JR5 spinner and CTF cryogenic magnetometers), while both the zero-field oven and the AF demagnetizer are home-made. Most of the samples (90%) were thermally demagnetized, however alternating fields (AF) demagnetization up to 140 mT was also performed with 5, 10, 15, 20 or 30 mT steps. Stepwise thermal treatments up to 655 °C were applied with 10 to 150 °C steps. After each heating step, the magnetic susceptibility K was measured at room temperature with a Bartington bridge to detect possible mineralogic changes in the specimens. Components of magnetization were estimated through principal component analysis (Kirschvink, 1980). Characteristic directions were corrected for local tilt using the attitude of the interbedded sediments.

Most samples showed two components of magnetization whose relative strength varies strongly depending on the samples (e.g., Figures 3a and 3b versus 3c and 3d). The most difficult aspect of the paleomagnetic analysis was the extremely large overlapping of the unblocking temperature spectra for the two components. Complete overlap was observed in the worse cases. Thermal demagnetization (Figures 3a to 3c) was generally found more efficient than AF demagnetization to isolate the characteristic components of magnetization, as also noticed by Perrin et al (1994). The only exception was the Tayin flow for which excellent results were obtained with AF demagnetization (Figure 3d).

In a few cases, the lower temperature (LT) component could be estimated by principal component analysis below 300 °C but, most of the time, the orthogonal diagrams are curved right from the start,

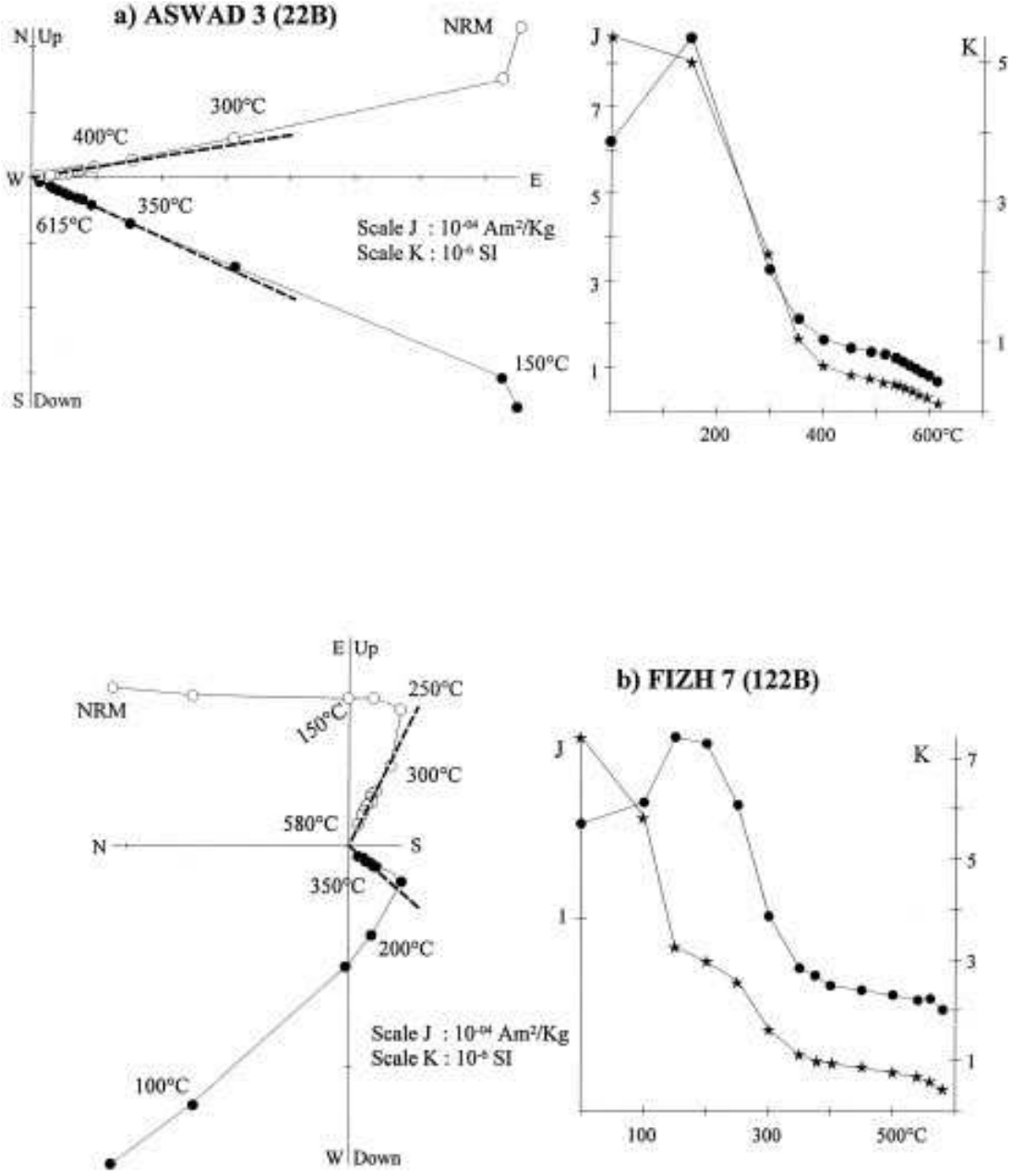

Figure 3. Representative orthogonal demagnetization diagrams (in situ coordinates) on the left side of the figure (open and full circles correspond respectively to the horizontal and vertical plane), with the corresponding variation of the intensity of magnetization J (stars) and the room temperature susceptibility K (circles) on the right side of the figure.

186

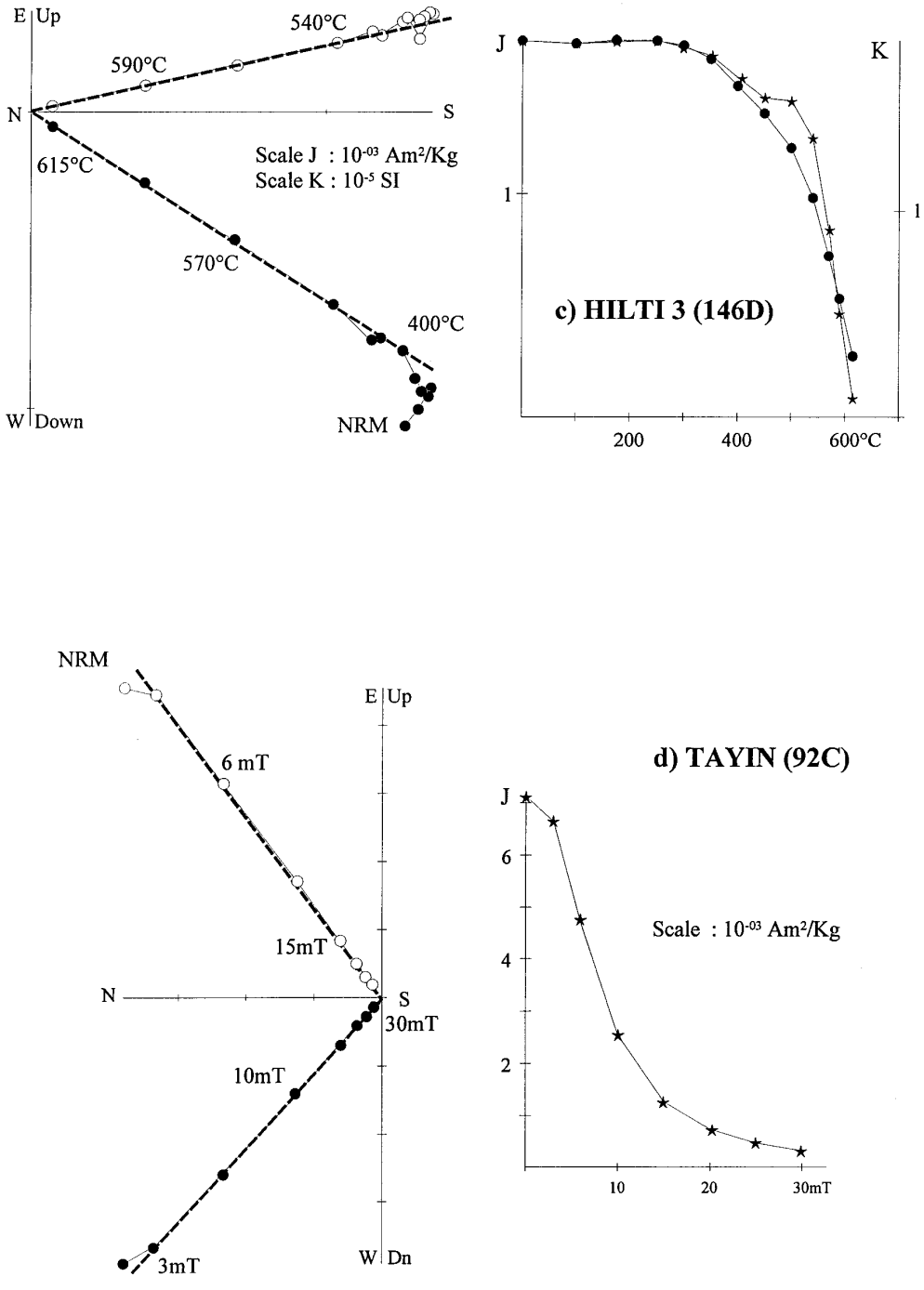

Figure 3. Continued.

Table 1. TiO_2, La, Yb, Zr and Hf concentrations in the studied lavas from Oman. Titanium was analyzed on the ICP-AES at C.R.P.G (Nancy), the other elements on the ICP-MS at I.S.T.E.E.M (Montpellier). Complete analyses are available from dautria@dstu.univ-montp2.fr.

	TiO_2 (wt %)	La (ppm)	Yb (ppm)	Zr (ppm)	Hf (ppm)	La/Yb	Zr/Hf	
ASWAD								
Flow 1	0.73	1.34	2.04	39.50	1.30	0.7	30.4	V2
Flow 1	0.74	1.32	2.09	39.43	1.32	0.6	29.9	V2
Flow 2	1.83	4.30	4.12	113.47	3.17	1.0	35.8	V1
Flow 3	0.47	0.64	1.32	21.36	0.73	0.5	29.3	V2
Flow 4	0.66	1.97	2.12	36.82	1.21	0.9	30.4	V2
Flow 5	1.73	4.57	4.05	110.27	3.10	1.1	35.6	V1
Flow 6	0.60	1.61	2.13	30.67	1.02	0.8	30.1	V2
Flow 7	1.41	3.15	3.37	75.97	2.31	0.9	32.9	V1
Flow 8	0.47	1.17	1.67	22.55	0.78	0.7	28.9	V2
Flow 9	0.51	1.45	1.86	24.72	0.86	0.8	28.7	V2
FIZH								
Flow 2	0.38	1.12	1.64	17.88	0.60	0.7	29.8	V2
Flow 3	0.32	1.01	1.47	16.03	0.55	0.7	29.1	V2
Flow 4	0.73	1.07	2.05	31.57	1.09	0.5	29.0	V2
Flow 4	0.74	1.06	2.06	30.91	1.09	0.5	28.4	V2
Flow 5	0.56	0.86	1.65	26.09	0.92	0.5	28.4	V2
Flow 5	0.56	0.90	1.67	26.24	0.93	0.5	28.2	V2
Flow 6	0.79	1.54	2.29	29.47	1.22	0.7	24.2	V2
Flow 7	0.78	1.42	2.23	25.80	1.02	0.6	25.3	V2
HILTI								
Flow 1	1.15	6.46	5.57	164.20	4.78	1.2	34.4	V1
Flow 2	1.20	7.94	5.09	151.58	4.38	1.6	34.6	V1
Flow 3	1.23	7.09	5.29	155.98	4.54	1.3	34.4	V1
Flow 4	1.16	6.29	5.49	160.96	4.75	1.1	33.9	V1
Flow 5	1.30	5.23	4.37	127.39	3.83	1.2	33.3	V1
Flow 6	1.21	4.61	3.56	105.33	3.18	1.3	33.1	V1
Flow 7	1.30	6.80	5.11	150.85	4.40	1.3	34.3	V1
SARAMI								
Flow 1	0.87	1.36	2.33	34.60	1.27	0.6	27.2	V2
Flow 2	0.74	1.38	1.98	19.04	0.81	0.7	23.5	V2
Flow 3	0.80	1.30	2.13	35.04	1.22	0.6	28.7	V2
Flow 4	0.83	2.05	3.05	53.30	1.85	0.7	28.8	V2

indicating an early overlapping of the two components. However, the few LT directions which could be obtained (Figure 4), when plotted in situ (e.g., without tilt correction), have declinations close to zero and a mean inclination around 40°, the large dispersion being mainly due to imprecise determinations in many cases. These LT directions are thus in good agreement with the 41° inclination of the present dipole field in the area. Even when the overlap precludes a principal component analysis of the LT component, the first steps of the thermal treatments usually followed a great circle going through the dipole direction. These observations clearly evidence the recent nature of this remagnetization.

Because of the large overlapping of the unblocking temperatures, the characteristic components of magnetization could only be estimated at high temperatures, above 400-550 °C. Nevertheless, the determina-

188

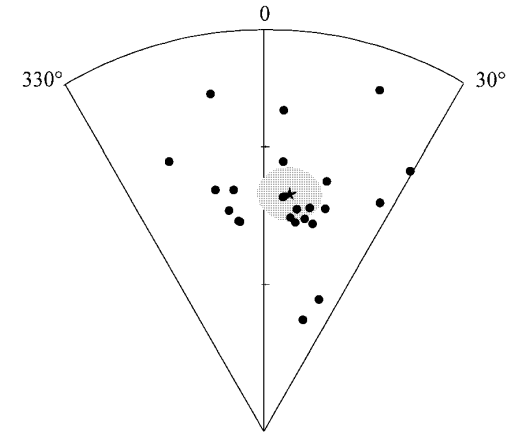

Figure 4. Distribution of the recent remagnetization (in-situ coordinates) on a polar equal-area projection. The shaded area corresponds to the confidence limit α_{95} around the mean direction.

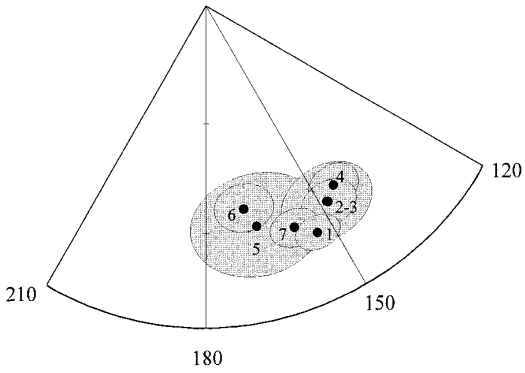

Figure 5. Barghah mean directions of magnetization (stratigraphic coordinates) per flow, Hilti massif. Polar equal-area projection.

tions are usually good (e.g., Figure 3), with maximum angular deviations (Kirschvink, 1980) mainly below 1 and always less than 3. Half of all samples allowed definition of a final direction. As also noticed by Perrin et al (1994), the V1 samples usually have a better paleomagnetic behavior, mainly related to a stronger resistance to alteration under present surface conditions.

Hilti massif

In order to check if the Salahi results are representative of the whole Hilti massif, a new V1 section (7 flows) was sampled in a small canyon oriented ESE–WNW and located close from Wadi Barghah in the northern part of the Hilti massif. Analysis of these samples was usually straightforward and well-defined mean direc-

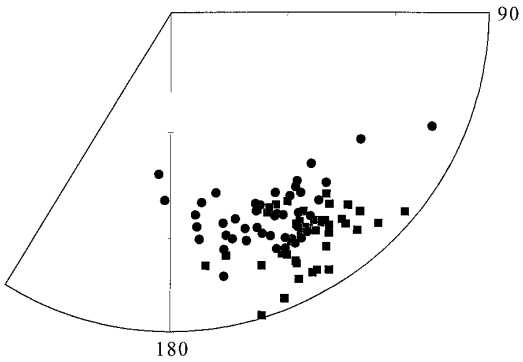

Figure 6. Hilti V1 directions (stratigraphic coordinates): circles and squares correspond respectively to the Barghah (this study) and the Salahi (Perrin et al., 1994) areas. Polar equal-area projection.

tions of magnetization per flow could be estimated in all cases (Table 2; Figure 5).

These Barghah V1 results were compared with previous results from Salahi (Perrin et al., 1994). The two data sets show good agreement, with a tighter distribution when the 84 individual directions are corrected ($\kappa = 36$; $\alpha_{95} = 2.6$) than uncorrected ($\kappa = 24$; $\alpha_{95} = 3.2$) for local tilt. Even though the difference between the respective statistical parameters is not large enough for a robust fold test (passage of F-test only at 95% confidence), it is a clear indication of the ancient nature of this component of magnetization. The Barghah's results tend to have a slightly steeper inclination than the Salahi's results (Figure 6). This is likely due to uncertainties on the paleohorizontal estimation and was not considered as significant. The mean V1 direction from the Hilti massif was therefore calculated using all available data (Table 3) and is only a few degree away from the Salahi V1 mean direction.

Aswad massif

Analysis of these samples was not as straightforward as the previous ones and it was not possible to estimate characteristic components for most samples of flows 6 to 9. It was noticed in the field that the series tend to be steeper, almost vertical near the Wadi Hatta suture zone (Figure 1), a WNW–ESE shear zone and fault with borders the southern part of the Aswad massif (Nicolas et al., 2000a). Magnetization of flows 6 to 9 may have been disturbed by hydrothermal alteration, thought to have affected the upper crustal part (dikes and lava) in relation with the shear zone (Reuber, 1988).

Table 2. **Mean paleomagnetic directions per flow.** N/N_0: number of samples used for calculation/total number of samples; (Inc, Dec): characteristic mean inclination and declination corrected for tilt; (kappa, α_{95}): Fisher statistic parameters.

Massif	Unit	Site	N/N_0	Inc.	Dec.	α_{95}	κ
Aswad	V2	*1999-1*	*7/9*	*53.1*	*69.1*	*14.7*	*18*
		1999-3	4/5	17.5	101.9	11.8	62
		1999-4	10/10	11.6	119.4	8.5	33
Aswad	V1	1999-2	6/9	8.4	88.3	10.1	45
		1999-5	5/7	30.2	86.7	11.7	44
Fizh	V2	1999-5	3/9	25.5	131.2	–	459
		1999-7	5/7	36.4	108.3	9.4	67
Hilti	V1	1999-1	7/7	22.4	153.6	5.0	147
		1999-2	6/7	28.8	148.2	10.6	41
		1999-3	5/6	28.8	148.0	6.4	142
		1999-4	6/6	31.7	144.6	6.0	126
		1999-5	5/8	30.1	166.7	15.0	27
		1999-6	7/8	36.2	169.3	6.8	79
		1999-7	6/8	26.5	158.1	5.5	150
Sarami	V2	1999-1	6/7	2.0	88.3	14.9	21
		1999-2	3/7	14.9	71.9	–	36
		1999-3	4/5	2.3	71.4	16.9	31
		1999-4	3/7	−9.8	77.4	–	49
Sarami	V2	1994	9/11	−5.7	121.9	9.4	31
Sarami	V1	1994	3/9	9.2	166.7	–	162
Wuqbah	V1	1994-1&3	6/8	15.0	104.8	7.2	88
Tayin	V1	1994	10/11	−9.6	48.8	4.3	129

Table 3. **Mean paleomagnetic directions per volcanic unit for each massif.** N: number of specimens used in the calculation; (Inc, Dec): characteristic mean inclination, declination corrected for tilt; (kappa, α_{95}): Fisher statistic parameters; (V1-V2): angle between V1 and V2 directions, positive (negative) if clockwise (counterclockwise) rotation.

Massif	Sampling	Unit	N	Inc	Dec	α_{95}	κ	V1-V2
Aswad	1999	V1	11	18.3	87.7	9.3	25	26°
	1999	V2	14	13.4	114.5	7.6	28	
Fizh	1999	V2	8	32.8	117.5	9.6	34	
Hilti	1999	V1	84	23.9	151.7	2.6	36	−43°
	Perrin et al., 1994	V2	18	17.6	106.5	4.9	51	
Sarami	1994	V1	3	9.2	166.7	–	162	−47°
	1994	V2	9	−5.7	121.9	9.4	31	
	1999	V2	*16*	*2.3*	*78.9*	*8.2*	*21*	
Wuqbah	1994	V1	6	15.0	104.8	7.2	88	
Tayin- Sumail	1994	V1	10	−9.6	48.8	4.3	129	−36°
	Thomas, 1991	∼V2	6	7.4	17.2	7.7	77	

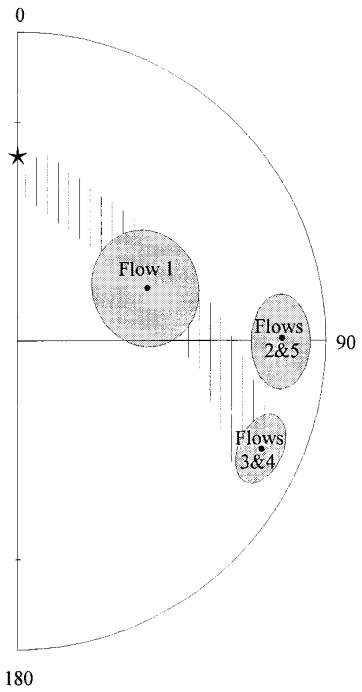

Figure 7. Aswad mean directions of magnetization (stratigraphic coordinates) on a polar equal-area projection.

Flow 1 has a significantly different mean value (Figure 7) compared to the other flows. The definition of flow 1 components was not as good as the others, with larger maximum angular deviations (up to 2.1) and a larger dispersion at the flow level ($\kappa = 18$ compared to 25 up to 62 for the others, Table 2). Finally the directions estimated for flow 1 are located close to the great circle (Figure 7) which connects the two components defined by the rest of the V2 samples. These observations indicate that flow 1 directions likely result from an unresolved overlapping of components, impossible to detect if the conjugated destruction of components occurs with a constant ratio for a certain temperature interval. For this reason, flow 1 values were not used in the calculation of the mean V2 direction for the Aswad massif.

Initially we thought that all flows sampled in the Aswad massif belong to the V2 series. However, the geochemical analysis revealed that three flows (2, 5, and 7) are in fact V1 volcanics. Considering the limited number of determinations available as well for V1 than for V2, individual directions were averaged to define an Aswad mean direction for both series. Even though the directions defined for the V1 and V2 flows (Table 3) are not extremely different, the V1 directions have significantly lower declinations and the absence of overlap between the $\alpha 95$ confidence limits associated with the mean V1 and V2 directions (Figure 7) confirms the statistical difference between these directions.

Fizh massif

Only the V2 series was sampled there and results were very disappointing, with less than one-third of the samples allowing definition of characteristic components of magnetization. For only one flow a significant mean direction could be calculated (flow 7, Table 2). The difficulty to define the components of magnetization does not seem to be related to a simple overlap of two components but to a multi-component remanent magnetization. Furthermore the orientation of the interbedded sediments is extremely variable and no regional tilt correction can be estimated. However, the complex nature of the crustal sequence in the Fizh massif (Reuber, 1988) may preclude a much better definition of the magnetization of the volcanic sequence. Here again, because of the very limited number of determinations, the mean V2 direction (Table 3) was calculated at the sample level.

Sarami massif

Rocks from this massif were sampled during both field trips: one flow in each V1 and V2 series in 1994, and 4 flows in the V2 series in 1999. During the second campaign, a complete survey of the massif was made to check the sediments for paleohorizontal estimates and most of the areas had to be abandoned because of the extreme variability of their attitudes maybe related to paleotopography. Furthermore, the tectonic unity of this massif can also be questioned. These various factors very likely explained the different results obtained from both V2 samplings (Table 2). Even the V1 samples behave poorly and no more than a crude estimate of the V1 mean direction could be obtained (Table 2).

Wuqbah massif

This is an important area because it is the only one where relatively good volcanic outcrops are found on the west side of the nappe. However, this massif is complicated by thrusting with a strong local tilt (80° SE) for the sampled flows. Only two out of the three flows sampled in the V1 unit of this massif gave paleomagnetic results and the mean V1 direction was again calculated at the sample level (Table 2). Because

of the limited number of determinations and the tectonic complexity, this direction has to be considered with caution.

Tayin massif

This V1 flow also deserves special attention because is the only one we have from the southern part of the ophiolite. Luckily, the analysis was here very straightforward, with excellent determinations even with AF treatment (e.g., Figure 3d) and a very good grouping of the mean direction at the flow level (Table 2). During the 1999 field trip, an extensive survey of the whole southern area was made in order to locate more V1 flows. Unfortunately no additional outcrops suitable for a paleomagnetic sampling were found, either because of the weathering of the rocks or because of the absence of sediments to estimate the paleohorizontal.

Magnetic carriers and nature of the components

Prior to demagnetization, magnetic viscosity of some samples was estimated by comparing the remanent magnetization carried by the samples after a one-month storage in zero-field with the remanent magnetization carried by the same samples after a two-week stay with the present Earth's magnetic field applied along the Z-axis of the cores. The viscosity index thus defined is very low, with an average value of 4%, similar to values found by Perrin et al. (1994). Therefore viscous remanent magnetization, which may have been acquired by these rocks, is expected to be fairly low and easily removed in the early steps of the thermal treatment. The intensity and the unblocking temperature spectra of the actual field component defined in the study are thus much too large for the LT component to be only of viscous origin and this remagnetization has to be a recent crystalline remanent magnetization, likely acquired during weathering of the rocks.

In order to characterize the magnetic carriers and their Curie temperatures, the susceptibility of some samples was continuously measured during heating-cooling cycles. A Bartington bridge coupled with a furnace was used, with the samples placed in vacuum to minimize oxidation of the rocks during the experiments. Two to four heating-cooling cycles have been done to detect the onset of the transformation. Three characteristic K/T curves were found, two of them strongly irreversible. The first type of curves (Figure 8a) is reversible during the 200 °C cycle but already irreversible during the 400 °C cycle. The change in the magnetic parameter is afterwards progressive, up to at least 600 °C. This is in agreement with the room temperature measurements of susceptibility K made after each heating steps of the thermal demagnetization, which show a stable behavior of K up to 300–400 °C followed by a decrease of K. The second type of curves (Figure 8b) shows an unusually large and irreversible increase of susceptibility up to 250 °C (possibly related in part to some strain release), followed by a sharp decrease between 250–350 °C, and an almost reversible phase for which a pseudo Curie point of about 580 °C was estimated using Prevot et al. (1983) method. The last type of curves (Figure 8c) is almost entirely reversible, with a Curie point around 580 °C. The magnetic phase, stable up to about 300 °C, is likely to be a titanomaghemite which is typical in sub-marine basalt and well-known for its thermal instability above 300–400 °C. The magnetic phase with a 580 °C Curie point corresponds to a pure magnetite.

For the first two types of K/T curves, the classic question is whether the magnetite forms from titanomaghemite during the laboratory experiments, leading to the question of the reliability of the directions defined at high temperatures. The facts that some samples contain only magnetite, that the type of K/T curves and the number of components are not related, and that similar characteristic directions are obtained for all K/T curves, indicate that the high temperature components are chemical remanent magnetizations acquired during hydrothermalism which accompanied the emplacement of submarine lava flows. It is expected that most of the breakdown of the titanomaghemite had occured during the first hydrothermal event, related to the emplacement of the lavas, but it is possible that later hydrothermalism (V2 hydrothermal event on V1 rocks, for example) may still transform the rocks leading to a later remagnetization. Although newly formed magnetite commonly forms rims on titanomagnetite grains, many tiny grains form from the alteration of clinopyroxene (or olivine in V2), and from volcanic glass.

Discussion

Mean V1 and V2 results per massif are summarized in table 3 and plotted for each volcanic series in Figure 9. In addition to results presented in this paper, the V2 result obtained from Salahi (Perrin et al., 1994) and

192

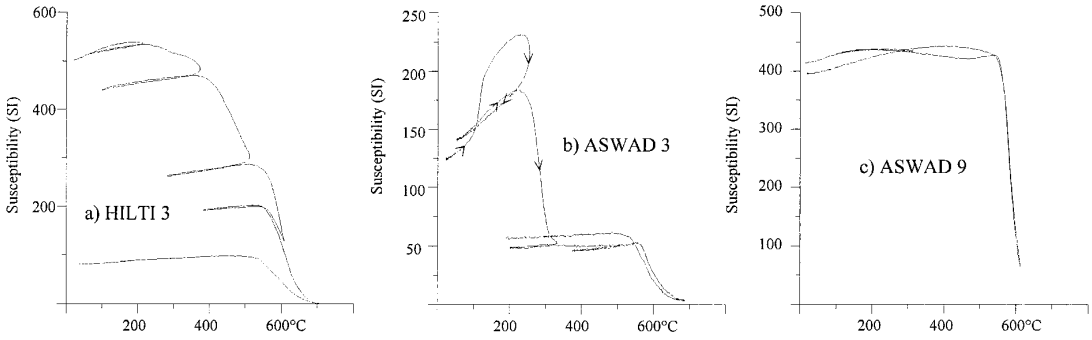

Figure 8. Characteristic K/T curves.

a result obtained by Thomas et al. (1988) on radiolarites (considered as equivalent of V2) from the southern Sumail massif are included. No examples of antipodal directions were found within either the V1 or the V2 units. Both V1 and V2 units were emplaced during the Cretaceous Superchron (long normal polarity interval), which lasted from the early Aptian (around 114 Ma, Odin and Odin, 1990) to the late Santonian (around 83 Ma, Odin and Odin, 1990). As discussed above the magnetization of the lavas is thought to have been acquired shortly after deposition of the lava, we consider therefore their characteristic directions to be of normal polarity.

Except for the Sarami direction found with the 1999 samples, all V2 directions are fairly coherent for the northern part of the ophiolite. This indicates that, prior to V2 magnetization, the northern part of the ophiolite behaves as one tectonic unit. However, difference exists between the V1 directions of the northern area, with the Hilti and Sarami values in good agreement but different from the Aswad and Wuqbah directions. Two hypothesis are possible to explain this difference: (i) the directions found for Aswad and Wuqbah are in fact later remagnetizations, acquired during hydothermal activity related to the V2 emplacement, or (ii) differential rotations occurred between the extreme northern tip, and maybe the western side, and the main center part, with unification of this northern area by the time of emplacement of the V2 units. The large similarity between the magnetic properties of the sampled rocks and the characteristic of the thermal events in the various massifs suggests a comparable mechanism of remanence acquisition in the whole domain. Because of the large difference between the V1 and V2 characteristic directions from Hilti, the CRMs carried by these two sets of directions could not have been acquired during the same hydrothermal event. Because of these two observations, we favored the tectonic hypothesis to explain the directional difference between the various massifs. If the V1 directions are considered to have been acquired early at the ridge, then a clockwise rotation around 26° is necessary to fit the V1 to the V2 directions obtained from the Aswad massif (counterclockwise rotation of the massif) compared to a counterclockwise rotation to fit the V1 to the V2 directions from the Hilti and Sarami massifs, respectively on the order of 43 and 47° (clockwise rotation of the Hilti-Sarami bloc), a movement occurring before the magnetization of the V2 lava. Geologic evidence exist (Nicolas et al., 2000a) for a counterclockwise rotation of the Aswad massif north of the Wadi Hatta suture zone but not for a clockwise rotation south of the suture zone but it could well be that one massif is rotating counterclockwise in a generally clockwise obduction. The absence of V1 results for the Fizh massif may preclude further testing of a model for differential rotations between the Aswad and Hilti-Sarami massifs.

Directions obtained from the Tayin-Sumail massif are very different from those of the northern area, with an angle of 106° between the V1-North and V1-South and 95° between V2-North and V2-South. This indicates a large rotation of the northern relative to the southern parts of the ophiolite. But obviously the only data set available is not enough to propose any general evolution of this extremely complex southern domain. However, it is worse noting that an counterclockwise rotation of about 36° is necessary to fit the V1 to the V2 directions of the Tayin-Sumail massif, on the same order as for Hilti and Sarami. Because of the absence of additional volcanic outcrops suitable for a paleomagnetic sampling in the southern massifs,

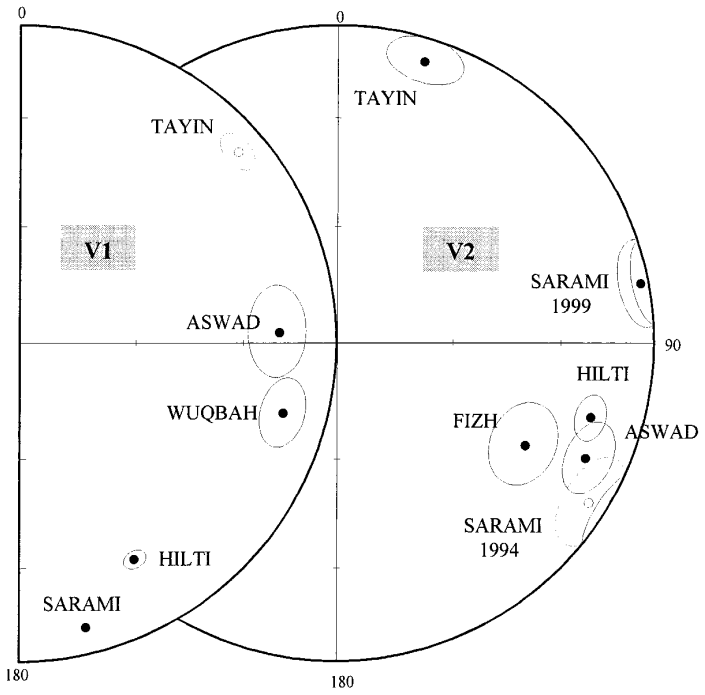

Figure 9. Mean directions of magnetization (stratigraphic coordinates) with confidence circles for V1 and V2 series grouped by massif (full circles and solid lines indicate lower hemisphere, open circles and dashed lines upper hemisphere).

it is very unlikely that the understanding of the relation between the northern and southern parts of the Semail ophiolite will be gained from the volcanic sequence, and a sampling of the gabbros of the southern area (Weiler, 2000) was alternatively carried out during the 1999 campaign.

Conclusion

The interpretation of the paleomagnetic results obtained from the volcanic sequence of the Semail ophiolite is not unambiguous, as the timing of the magnetization of the series cannot be surely estimated. However, if the paleomagnetic results are taken at face value, they tend to question the tectonic unity of the northern part of the Semail ophiolite (Aswad, Fizh, Hilti, Sarami and Wuqbah massifs) at the time of emplacement of the V1 lavas but, by the time of emplacement of the V2 series, this northern domain can be considered as one tectonic unit. On the contrary, the relative movement between this northern part and the southern domain (Tayin-Sumail massif) seems to have happened after emplacement of the two volcanic series.

Acknowledgements

Facilities from the Oman Ministry of Commerce and Industry, Directory of Minerals, extended through Dr H. Al Azri are acknowledged. We thank Françoise Boudier, Edwin Gnos and Peter Weiler for their help in the field; and Jean-Pascal Cogné, Edwin Gnos, and Carlo Laj for very helpful reviews. This work was supported by the Centre National de la Recherche Scientifique partly through grant from ‘Intérieur de la Terre’. Contribution CNRS-INSU-DBT 238.

References

Alabaster, T., Pearce, J. A., Mallivk, D. I. J., and Elboushi, I. M., 1980, The volcanic stratigraphy and location of massive sulphide deposits in the Oman ophiolite, *International Ophiolite Symposium*, Geological Survey Department, Nicosia, Cyprus, 751–757.

Alabaster, T., Pearce, J. A., and Malpas, J., 1982, The volcanic stratigraphy and petrogenesis of the Oman ophiolite complex, *Contrib. Min. Petr.* **81**: 168–183.

Ernewein, M., Pflumio, C. and Whitechurch, H., 1988, The death of an accretion zone as evidenced by the magmatic history of the Sumail ophiolite (Oman), *Tectonophysics* **151**: 247–274.

Geological maps, 1993, 1:50,000 Ministry of Petroleum and Minerals, Directory of Minerals, Muscat, Sultanate of Oman.

Godard, M., Bosch, D., Bodinier, J. L. and Einaudi, F., 2000, A trace element and isotope study of the tholeiitic volcanic sequence of the Salahi block: Implications for the origin and evolution of the Oman ophiolite, *Chem. Geol.*, submitted.

Hacher, B. R., Mosenfelder, J. L. and Gnos, E. , 1996, Rapid emplacement of the Oman ophiolite, *Tectonics* **15**: 1230–1247.

Karpoff, A. M., Walter, A. V. and Pflumio, C., 1988, Metalliferous sediments within lava sequences of the Sumail ophiolite (Oman): Mineralogical and geochemical characterization, origin and evolution, *Tectonophysics* **151**: 223–245.

Kirschvink, J. L., 1980, The least-squares line and plane and the analysis of paleomagnetic data, *Geophys. J. R. Astron. Soc.* **62**: 699–718.

Lippard, S. J., Shelton, A. W. and Gass, I. G., 1986, The ophiolite of northern Oman, *Geol. Soc. Memoir* **11**, Backwell Scientific Publications, London, 178 pp.

Luyendyk, B. P. and Day, R., 1982, Paleomagnetism of the Samail ophiolite, Oman. 2. The Wadi Kadir Gabbro section, *J. Geophys. Res.* **87**: 10903–10917.

Luyendyk, B. P., Laws, B. R., Day, R. and Collinson, T. B., 1982, Paleomagnetism of the Samail ophiolite, Oman. 1. The sheeted dyke complex at Ibra, *J. Geophys. Res.* **87**: 10883–10902.

Nicolas, A., Boudier, F., Michibayashi, K. and Gerbert-Gaillard, L., 2000a, Aswad Massif (United Arab Emirates) archetype of the Oman-UAE ophiolite belt, *Mar. Geophys. Res.*, in press.

Nicolas, A., Boudier, F., Ildefonse, B. and Ball, E., 2000b, Accretion of Oman and United Arab Emirates ophiolite – Discussion of a new structural map, *Mar. Geophys. Res.* **21**, 269–287, this issue.

Odin, G. S. and Odin, C., 1990, Echelle numérique des temps géologiques, *Géochronique* **35**: 12–21.

Pearce, J. A., Alabaster, T., Shelton, A. W. and Searle, M. P., 1981, The Oman ophiolite as a Cretaceous arc-basin complex: evidence and implications, *Phil. Trans. R. Soc. London* **300**: 299–317.

Perrin, M., Prévot, M. and Bruère, F., 1994, Rotation of the Oman ophiolite and initial location of the ridge in hotspot reference frame, *Tectonophysics* **229**: 31–42.

Pflumio, C., 1988, Histoire magmatique et hydrothermale du bloc de Salahi: Implications sur l'origine et l'évolution de l'ophiolite de Sémail (Oman), Thèse de Doctorat, Ecole des Mines de Paris, 243 pp.

Prévot, M., Mankinen, E. A., Grommé, C. S. and Lecaille, A., 1983, High paleointensities of the geomagnetic field from thermomagnetic studies on rift valley pillow basalts from the mid-Atlantic ridge, *J. Geophys. Res.* **88**: 2316–2326.

Reuber, I., 1988, Complexity of the crustal sequence of the northern Oman ophiolite (Fizh and southern Aswad blocks) : the effect of early slicing ? *Tectonophysics* **151**: 137–165.

Shelton, A. W., 1984, Geophysical studies on the northern Oman ophiolite, Ph. D. thesis, The Open University, 353 pp.

Sun, S. S. and McDonough, W. F., 1989, Chemical and isotopic systematics of oceanic basalts: implications for mantle composition and processes, In A. D. Saunders and M. J. Norry (eds), *Magmatism in the Ocean Basins*, Geol. Soc. London, Vol. 42, pp. 313–345.

Thomas, V., Pozzi, J. P. and Nicolas, A., 1988, Paleomagnetic results from Oman ophiolites related to their emplacement, *Tectonophysics* **151**: 297–321.

Weiler, P. D., 2000, Differential rotations in the Oman ophiolite: paleomagnetic evidence from the southern massifs, *Mar. Geophys. Res.* **21**: 195–210, this issue.

Résumé

La compréhension de la dynamique interne du noyau terrestre nécessite l'observation des fluctuations du champ magnétique en des sites répartis uniformément à la surface du globe pour différentes périodes de temps. La première partie de cette thèse présente les résultats d'une étude paléomagnétique, en direction et en intensité, réalisée sur des laves oligocènes de l'archipel des Kerguelen (49°20'S, 70°20'E) en vue de compléter les bases de données internationales. Celle-ci a permis d'évaluer la dispersion angulaire inter-coulées entre 21.2 et 21.8° par rapport au pôle géographique. Cette estimation de la variation paléoséculaire oligocène est en accord avec le Modèle G de McFadden et al. (1991) pour la période 22.5-45 Ma. Les 12 déterminations de paléointensité reportées sont les premières d'une bonne qualité technique obtenues pour cette région. Le moment dipolaire virtuel moyen leur étant associé ($6.15 \pm 2.1\ 10^{22} Am^2$), est plus élevé que la valeur précédemment estimée pour l'oligocène. Néanmoins, il reste bien inférieur a la valeur moyenne obtenue pour les périodes récentes (<0.3 Ma), qui semblent anormalement élevées.

D'autre part, le travail réalisé au cours de cette thèse contribue aux recherches géologiques menées à Kerguelen en apportant des contraintes propres au paléomagnétisme. A partir d'études de la fabrique magnétique, une meilleure localisation des centres éruptifs des différentes provinces volcaniques ainsi qu'une chronologie détaillée de la mise en place d'une section de la partie Sud-Est de l'archipel, sont proposées. Le report sur une échelle magnétostratigraphique globale des successions de polarité observées pour cinq sections a permis par ailleurs de préciser leurs intervalles de temps de mise en place et réviser ainsi l'estimation de leurs taux d'éruption respectifs.

Mots clefs

Paleomagnétisme - variation paléoséculaire - paléointensités - magnétostratigraphie - fabrique magnétique - Kerguelen

Abstract

Numerous observations of the magnetic fi eld variations, uniformly distributed on the Earth's surface for different time windows are needed to improve our knowledge on the inner-core dynamic. The fi rst part of this work reports a paleomagnetic study, direction and intensity, carried out on oligocene lava flows from the Kerguelen archipelago (49°20'S, 70°20'E) in order to implement international databases. A between-flow angular standard deviation of 21.2 to 21.8° from the geographic pole has been computed. This estimation of the oligocene paleosecular variation agrees with McFadden et al. (1991) Model G for paleosecular variation between 22.5-40 Ma. The 12 new paleointensity determinations reported are the fi rst estimations obtained for this archipelago with good technical quality. The mean VDM of $6.15 \pm 2.1\ 10^{22} Am^2$ increases the mean oligocene estimate but is still lower than recent value (<0.3 Ma), which seems abnormaly high.

Moreover, this work brings additional constraints to the geological researches carried out on Kerguelen. We proposed a better location of the eruptive center for the different magnetic provinces and a detailed chronology of emplacement for a southeastern site by means of magnetic fabric studies. Correlation of the polarity successions for fi ve sections with a global geomagnetic polarity scale allowed refi nement of the emplacement time of these volcanic sequences and consequently reevaluation of their extrusion rates.